UNIVERSITY OF CALIFORNIA
SANTA CRUZ

THEORETICAL STUDIES OF MOLECULAR STRUCTURE, DYNAMICS, AND REACTIVITY AT LIQUID INTERFACES

A dissertation submitted in partial satisfaction of the
requirements for the degree of

DOCTOR OF PHILOSOPHY

in

CHEMISTRY

by

John J. Karnes

June 2018

The Dissertation of John J. Karnes
is approved:

Professor Ilan Benjamin, Chair

Professor Jin Zhong Zhang

Professor Yat Li

Dean Tyrus Miller
Vice Provost and Dean of Graduate Studies

Table of Contents

List of Figures

List of Tables

Abstract

Theoretical Studies of Molecular Structure, Dynamics, and Reactivity at Liquid Interfaces

by

John J. Karnes

Computational studies of liquid interfaces were performed to address a series of open questions across several distinct systems. Binary solvent mixtures of methanol and acetonitrile at the hydroxylated silica interface demonstrate that methanol, each molecule able to form two distinct hydrogen bonds with the silica surface, is energetically favored at the liquid/silica interface. The mechanism by which methanol displaces acetonitrile from the interface is a two-step process where the approaching methanol establishes itself at the surface with one hydrogen bond before "locking" into place when the second hydrogen is formed.

Subtle differences in the induced ordering and structure of liquid methanol and ethanol at the silica interface make methanol's interfacial structure invisible to some nonlinear spectroscopic techniques while the similar, expected ordering is detected at the liquid ethanol/silica interface. This difference in spectroscopic response results from methanol's shorter alkyl tail being unable to span the interface at realistic silanol site densities.

The function of β-cyclodextrin (β-CD) as inverse phase transfer catalyst in the reaction $CN^- + CH_3(CH_2)_6CH_2Br \leftrightharpoons CH_3(CH_2)_6CH_2CN + Br^-$ is studied in two

contexts. Thermodynamic calculations on the formation and stability of the β-CD/1-bromooctane host/guest complex reveal the β-CD promotes transport of the organic reagent toward the nucleophile-rich aqueous phase. Using an empirical valence bond approach, β-CD is also shown to act as a conventional catalyst, reducing the free energy barrier to reaction when a model S_N2 reaction takes place near its hydrophobic cavity at the liquid/liquid interface.

The transfer of an ion across the immiscible oil/water liquid/liquid interface is shown to be accompanied by a protrusion of the ion and its hydration shell into the organic phase, into which the ion and part of its hydration shell diffuse. Both energetic and geometric-based reaction coordinates are useful in describing the transfer process. The transfer of a water molecule into an adjacent liquid oil phase proceeds by a slightly different mechanism. The transferring water is accompanied by a smaller local protrusion of the aqueous phase and moves into the organic phase without co-transfer of any of its hydration shell.

To Yi.

Acknowledgments

I want to thank my research advisor, Professor Ilan Benjamin, for training me as a theoretical chemist. Aside from technical guidance, his unwavering professionalism, patience, accessibility, and support over the last five years allowed me the luxury to focus on our research projects and chase ideas that branch out from our main objectives. I also want to thank members of my Qualifying Exam and Dissertation Reading Committees: Professor Nicholas Brummell, who provided valuable insights toward computational parallelization, and Professors Yat Li and Jin Zhong Zhang, both generous with their time and present to keep my computational studies grounded within the framework of modern physical chemistry. Our Graduate Program Coordinator, Karen Meece, whose skill and attention to detail are unmatched, and Steven Hauskins, "Purveyor of Fine Computing Services," provided me with guidance through many situations that I could not have navigated by myself.

I would also like to thank the research groups of Professors Akihiro Morita and Todd Martinez for generously hosting my visits to Tohoku University and Stanford University, both wonderful experiences. I grateful for the advice and support of Dr. Katherine Nelson and Jackson Chief Elk, former members of the Benjamin group. Lastly I would like to thank Jason Kemper for many conversations that yielded both scientific and mathematical insights and for generously providing proofreading assistance.

Professor Yi Karnes, to whom this work is dedicated, is a constant source of good advice. It's been a pleasure to watch her career grow alongside mine and we're

now beginning to navigate parenthood together with the arrival of little JJ in December 2017.

The text of this dissertation includes reprints of the following previously published material:

- J. J. Karnes and I. Benjamin. Mechanism and dynamics of molecular exchange at the silica/binary solvent mixtures interface. *J. Phys. Chem. A*, 119(50):12073–12081, 2015

- J. J. Karnes and I. Benjamin. Geometric and energetic considerations of surface fluctuations during ion transfer across the water-immiscible organic liquid interface. *J. Chem. Phys.*, 145(1):014701, 2016

- J. J. Karnes, E. A. Gobrogge, R. A. Walker, and I. Benjamin. Unusual structure and dynamics at silica/methanol and silica/ethanol interfaces—a molecular dynamics and nonlinear optical study. *J. Phys. Chem. B*, 120(8):1569–1578, 2016

- J. J. Karnes and I. Benjamin. On the local intermolecular ordering and dynamics of liquid chloroform. *J. Mol. Liq.*, 248(Supplement C):121–126, 2017

- J. J. Karnes and I. Benjamin. S_N2 reaction rate enhancement by β-cyclodextrin at the liquid/liquid interface. *J. Phys. Chem. C*, 121(35):19209–19217, 2017

- J. J. Karnes and I. Benjamin. Structure and dynamics of host/guest complexation at the liquid/liquid interface: Implications for inverse phase transfer catalysis. *J. Phys. Chem. C*, 121(9):4999–5011, 2017

- J. J. Karnes and I. Benjamin. Miscibility at the immiscible liquid/liquid interface: A molecular dynamics study of thermodynamics and mechanism. *J. Chem. Phys.*, 148(3):034707, 2018

Introduction

The interface between a liquid and a second phase is an inhomogeneous environment that continues to attract significant attention from theoreticians and experimentalists in many fields. [26, 173, 19, 36, 138, 13] The interesting physical and chemical phenomena that occur at the liquid/solid, liquid/vapor, and immiscible liquid/liquid interfaces that motivate these studies arise from unique properties and behaviors at the liquid interface, which often differ significantly from behaviors seen in a neighboring bulk phase. Some examples of these interfacial phenomena include chromatographic separation and corrosion at the liquid/solid interface, phase-transfer catalysis, liquid-liquid extraction, and ion transfer at the liquid/liquid interface, and the uptake or release of pollutants at the liquid/vapor interface.

The complex local environment itself also inspires more fundamental investigations of the liquid interface but experimental study of liquid interfaces, particularly the "buried" liquid/solid and liquid/liquid interfaces, has proven to be especially difficult. Aside from the challenge of designing an interface-specific probe, the intriguing properties induced by the interface typically only persist for a few molecular lengths (a few nm), [18] requiring the analytical technique to report information from a very small re-

gion of interest. Despite these challenges, several experimental approaches developed in recent decades have provided interesting insight into the liquid interfaces. Two notable examples include: (1) Sum-frequency generation spectroscopy, a non-linear optical technique that exploits the symmetry-breaking inherent at the phase interface [60, 199, 198] and (2) gas-liquid scattering, which couples a molecular beam source with a mass spectrometer to study the liquid/vapor interface. [21, 47, 40, 63]

In part because of the experimental challenges outlined above, computer simulations have been a valuable tool in forming our understanding of liquid interfaces. The proceeding work continues this tradition and consists primarily of molecular dynamics simulations that provide insights into the liquid interface not yet accessible by experimental approaches. The theoretical and computational work in this dissertation consists of studies of the solid/liquid and liquid/liquid interfaces as well as an investigation of local intermolecular ordering in a bulk liquid and is organized as follows.

Chapters 1 and 2 focus on the silica/liquid interface. In Chapter 1 we consider acetonitrile/methanol binary solvent mixtures and investigate both the ordering of each liquid at the hydroxylated silica surface and the mechanism of solvent exchange at the interface. Methanol is more energetically energetically favored to be at the silica surface since it is able to act as both hydrogen bond donor and acceptor, thus forming twice as many interfacial hydrogen bonds as a corresponding acetonitrile molecule at the interface. Chapter 2 is a collaborative effort with Professor Robert Walker's group at Montana State University. In this work we used molecular dynamics simulations of the silica/liquid alcohol interface to investigate the subtleties of induced molecu-

lar order at the silica/alcohol interface. Interfacial hydrogen bonds between the silica and alcohols results in a well-ordered oily region that repels the adjacent polar liquid. However, differences between the interfacial structures of methanol and ethanol result in methanol producing no spectroscopic signal, suggesting no induced ordering at the liquid methanol/silica interface.

Chapters 3 and 4 study inverse phase transfer catalysis (IPTC), in particular β-cyclodextrin's ability to increase the rate of the S_N2 reaction $CN^- + CH_3(CH_2)_6CH_2Br \longleftrightarrow CH_3(CH_2)_6CH_2CN + Br^-$. Although the precise mechanism is still disputed in regard to the shuttling of species across the interface, the fundamental aspects of IPTC are agreed upon: β-cyclodextrin forms a host-guest complex with the organic reagent, enhancing the conversion rate of the reactants. However, the effect of β-cyclodextrin on mass transport or whether β-cyclodextrin also acts as a conventional catalyst by lowering the rate of reaction are open questions. Chapter 3 characterizes the liquid/liquid interface in this reactive system and considers the formation and stability of reagent/β-cyclodextrin host/guest complexes. Chapter 4 builds upon this work to study the effect that the liquid/liquid interface and β-cyclodextrin have on a model S_N2 reaction, providing new insight toward understanding IPTC.

Chapter 5 investigates the local intermolecular ordering in liquid chloroform. Chloroform, a weakly polar organic molecule, is a common organic solvent in liquid/liquid systems. In this chapter, data from recent neutron diffraction experiments is replicated using molecular dynamics simulations to investigate the driving forces responsible for the local intermolecular order in liquid chloroform– insight into which suggests

a more fundamental understanding of how ordering and structure at the chloroform liquid interface may be induced.

Chapters 6 and 7 investigate the transfer of species across the liquid/liquid interface. In Chapter 6 equilibrium thermodynamics studies of a chloride ion moving between two immiscible electrolytes, water and nitrobenzene, reveal the free energy profile of this transfer event. Several constraints are applied to subsequent simulations in an attempt to deconstruct the free energy profile and identify critical parts of the transfer mechanism. Alternative reaction coordinates are proposed and calculated. In Chapter 7 the water/nitrobenzene interface is examined further, considering the transfer of water into the adjacent nitrobenzene phase. The transfer of a water molecule from the bulk aqueous phase to nitrobenzene is compared to transfer of water into liquid hexane and to evaporation, noting that this comparison is reasonable since evaporation also involves the transfer of water to an adjacent phase of lower relative permittivity. To study the mechanism of water's dissolution into nitrobenzene, MD trajectories capturing over 400 discrete transfer events were collected and analyzed. The resulting mechanism is described within the context of ion transfer and evaporation, two similar but more well-studied transfer events.

Chapter 1

Mechanism and dynamics of molecular exchange at the silica/binary solvent mixtures interface

1.1 Introduction

Molecular structure and dynamics at interfaces dictate behavior in many processes of interest. The silica surface is particularly of interest to researchers due to its abundance in nature and general utility. The need for molecular insight into behavior at this surface inspires current work in several disparate fields, including the frontiers of drug delivery, [71, 207, 206, 218] geology, [38, 117] catalysis, [137] high performance liquid chromatography, [209, 53, 78, 134, 133] and astrophysics. [43, 183, 186] Silica is also an excellent model hydrophilic surface for work that specifically focuses on the solid-liquid interface. Experimental difficulty arises due to the buried nature

of the solid-liquid interface, but advances in nonlinear spectroscopy, particularly vibrational sum frequency generation spectroscopy, [60, 199] have resulted in a continued increase in understanding the silica-liquid interface, with significant work devoted to water, [200, 58, 59] alcohol, [60, 119, 185, 204] and alkyl cyanide [52, 75] liquid phases. Molecular dynamics simulations of these systems [185, 41, 65, 113, 205, 118, 80, 163] provide molecularly detailed insight into the system and have been used extensively in conjunction with nonlinear optical experiments to fully elucidate interfacial organization and orientation. Behavior at the silica-liquid interface varies depending on the nature of the liquid. For example, the polar aprotic acetonitrile exhibits antiparallel dipole-dipole pairing in bulk liquid. At a hydroxylated silica surface, acetonitrile molecules are able to accept hydrogen bonds from the silica surface silanol groups, interactions significantly stronger than dipole pairing. This hydrogen bonding causes the interfacial acetonitrile to align approximately perpendicular to the interface. Interstitial acetonitrile molecules then align themselves into a dipole-paired sublayer nearly antiparallel to the interfacial acetonitrile. [80] Saturated straight-chain alcohols have different hydrogen bonding behavior: they may act as both hydrogen bond donors and acceptors. At a solid silica surface, the alcohols' hydroxyl groups hydrogen bond with the silica surface, and their alkane tails align to create a surface-induced hydrophobic region that prohibits neighboring alcohol solvent layers from interacting with the surface. [204] Recent work has investigated binary solvents as silica's adjacent liquid phase. [134, 146, 68, 145] This next level of complexity requires the understanding of both solvent-solvent interactions and allows researchers to observe the interplay between dissimilar solid-liquid interactions

in a situation where active sites at the solid surface are a limited resource. It is well established that interfacial behavior differs from bulk, and, in the case of binary solvents, interfacial mole fractions often differ significantly from the bulk. For example, Melnikov et. al report that a liquid methanol-acetonitrile mixture with a 2/98 (v/v) bulk ratio at a silica interface has over 50% of the silica surface OH groups bonded to methanol molecules. [134] Bulk-interface inhomogeneity in binary solvent systems may be used to enhance separation processes and are inherent in gradient elution, but the same mechanism may also amplify interface contamination in systems. In the present work, we focus on gaining molecular insight into the dynamics and mechanism by which a hydrophilic solid surface segregates a binary solvent mixture. Specifically, we consider the molecularly detailed events associated with the solvent exchange at the interface between methanol/acetonitrile mixtures and a hydroxylated silica surface. This system behaves similarly to a standard configuration of hydrophilic interaction liquid chromatography (HILIC). [78, 74] HILIC is a liquid chromatographic technique that incorporates hydrophilic stationary and mobile phases, the most common mobile phase consisting of an acetonitrile-water mixture. The mobile phase typically has a low (<3%) mole fraction of water. Since water preferentially organizes at the hydrophilic surface of the stationary phase, the resulting inhomogeneous binary solvent performs a pseudo liquid-liquid extraction and is able to separate polar analytes where more conventional liquid chromatography fails. Recent simulation work has investigated the segregation of solvents in model HILIC systems and supported the theory of a water-rich, mostly immobile solvent layer at the solid-liquid interface that extends 1.5 nm from the silica surface

and reduces translational mobility of polar analytes. [133] In this paper, using nonequilibrium molecular dynamics simulations, we examine the energetic and structural characteristics of the silica-methanol-acetonitrile system as it approaches equilibrium and quantify the dynamics associated with the single molecular exchange event at the interface. This provides us with a molecularly detailed mechanism by which hydrogen bonding molecules undergo exchange at a hydrophilic liquid/solid interface. The rest of the paper is organized as follows. In section II we briefly describe the system structure and potential energy used. In section III we describe and discuss the results of several types of molecular dynamics simulations. Conclusions are presented in section IV. In both systems the initial surface peak is lower due to fewer alcohols hydrogen-bonded to the silica surface. More interestingly, we observe that the increased population in the second sublayer acts to further reduce the net orientation. The well-ordered alcohol molecules hydrogen-bonded to the silica surface induce an average orientation in this second sublayer.

1.2 Systems and Methods

Molecular dynamics simulations are performed utilizing a "box" with dimensions $L_x = 45.0$ Å, $L_y = 43.3$ Å, and $L_z = 100$ Å. The box contains a silica surface in the $x-y$ plane in contact with a total of 1023 solvent molecules, with varying compositions as described below, with periodic boundary conditions extending in the x and y directions. The geometry of the silica surface is based on the work of Lee and Rossky [113]

and consists of a fully-hydroxylated β-Cristobalite surface. Our surface differs by incorporating terminal silanol groups with fully flexible bonds at the silica surface, using the CHARMM water contact angle, Lennard-Jones, and bond parameters. [44, 114] Each silica surface consists of 90 silanol sites: a density of 4.62 /nm^2. The acetonitrile and methanol force field parameters are those used in our earlier work [20, 11] that employ a united atom, three-site description of each solvent. Intermolecular potentials are calculated as the sum of Lennard-Jones and Coulomb terms:

$$U_{ij}(r) = \sum_{i<j} 4\epsilon_{ij} \left[\left(\frac{\sigma_{ij}}{r} \right)^{12} - \left(\frac{\sigma_{ij}}{r} \right)^{6} \right] + \frac{q_i q_j}{4\pi r \epsilon_0} \tag{1.1}$$

where i and j denote atoms on different molecules separated by a distance r. Mixed Lennard-Jones interactions between all species are calculated using Lorentz-Berthelot combining rules: $\sigma_{ij} = (\sigma_i + \sigma_j)/2$ and $\epsilon_{ij} = (\epsilon_i \epsilon_j)^{1/2}$. All simulations are performed using our in-house MD code that incorporates the velocity form of the Verlet algorithm and used an integration time step of 0.5 fs. All simulations were performed at 298 K. A key ingredient in characterizing the system is a definition of the solvent-silica hydrogen bonding. We use geometrical definitions of silica-methanol [185] and acetonitrile-silica [162] hydrogen bonds where a bond is considered present if the H–O–acceptor angle is less than 30° and the donor oxygen-acceptor distance is less than 3.4 Å for silica-methanol bonds and less than 3.5 Å for silica-acetonitrile bonds. We perform the following simulations:

1. 16.5 ns simulations starting from 20 independent configurations of randomly pre-

pared mixtures with several different acetonitrile mole fractions in contact with a silica surface. These calculations provide an overall global tracking of the adsorption/desorption process.

2. 1300 trajectories starting from independent configurations where a single methanol is dissolved in acetonitrile near the surface. These simulations provide the single molecule equivalent of the trajectories in part 1 above and are used to collect the initial conditions for extensive "reactive" trajectories by saving system configurations when methanol-silica hydrogen bonds are first detected.

3. These configurations are used to obtain thousands of "reactive" trajectories where the methanol molecule displaces an adsorbed acetonitrile molecule. This is done for the mechanistic studies and for the computation of reactive flux correlation functions (described below). Additional details on the calculations performed are given below.

1.3 Results and Discussion

As a reference for our mixture calculations, in Figure 1.1 we show the center-of-mass density profiles of the two neat liquids in contact with the silica surface. These density profiles illustrate the liquids' different behavior at the hydrophilic silica interface. Methanol is able to hydrogen bond with surface silica sites as both donor and acceptor to form a densely packed, highly ordered monolayer at the solid-liquid interface, seen as the first sharp peak in the density profile, and correspond to approximately

one methanol molecule per silica site. This surface hydrogen bonding induces order in the methanol methyl groups, forming a hydrophobic region that excludes other polar methanol molecules, resulting in the low-density region between the first and second density peaks. Acetonitrile is also polar but is only able to act as a hydrogen bond acceptor. The silica surface induces order by hydrogen bonding with acetonitrile but allows sufficient spacing for a second sublayer of acetonitrile molecules to align themselves interstitially and antiparallel to the hydrogen bonded acetonitrile. This is seen in the much wider first peak (compared with methanol). However, it still corresponds to a full monolayer coverage (note the kink in the blue line). Dipole-dipole pairing is seen in bulk acetonitrile, but surface-induced order leads to formation of a bilayer-like structure at the solid-liquid interface. Beyond the first solvent layer, the density profiles of both neat liquids oscillate for several periods before reaching bulk behavior at $z \approx 25$ Å. For future reference, we define the "bulk region" to be the region 25 Å $< z <$ 34 Å. Consider next the density profiles of the two liquids in a binary mixture at the silica surface, as shown in Figure 1.2 . These density profiles highlight methanol's affinity for the surface. The first solvent peak, representing methanol molecules hydrogen-bonded to the silica surface, is only weakly dependent on the equilibrium bulk mole fraction of acetonitrile as it increases from 0 to 0.94. As the acetonitrile concentration increases, the first acetonitrile density peak, centered at 5.6 Å, appears. This peak consists of acetonitrile molecules that orient their dipoles antiparallel to the methanol O–CH_3 vectors, exhibiting the same behavior as molecules in the second sublayer of the neat acetonitrile-silica system. Integrated methanol densities, shown in Figure 1.2 as molecules per silica site,

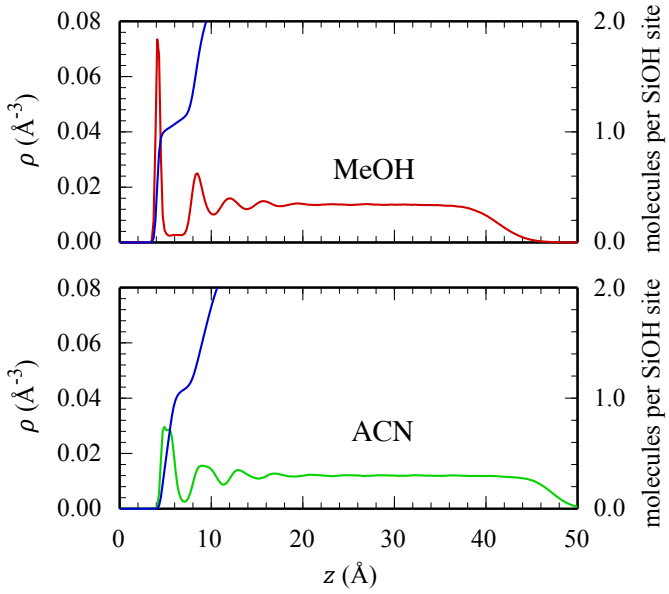

Figure 1.1: Density profiles of neat methanol (top, red) and neat acetonitrile (bottom, green) at the liquid-silica interface. The blue line in each panel represents the cumulative number of liquid molecules per silica site (right axis).

highlight the difference in methanol surface coverage. These values remain quite similar through the first solvent layer before diverging dramatically due to the large differences in mole fraction beyond the hydrogen bonded interfacial layer. To study the nonequilibrium solvent exchange dynamics at the surface, mixtures of methanol-acetonitrile are prepared by either replacing randomly selected acetonitrile molecules by methanol molecules starting from neat acetonitrile or conversely by starting from a neat methanol system and replacing a number of randomly selected methanol molecules by acetonitrile. Twenty independent initial configurations are used. After a short equilibration process to remove high-energy configurations, the binary systems are further allowed to relax to the final equilibrium state. During this process, methanol molecules gradually displace

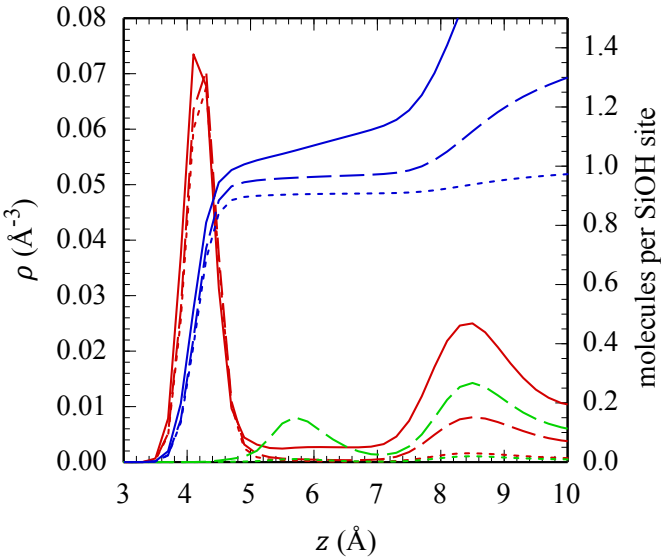

Figure 1.2: Density profiles of methanol (red lines) and acetonitrile (green lines) in several binary acetonitrile-methanol mixtures in contact with a silica surface. The blue lines represent the cumulative number of methanol molecules per silica site (right axis). Shown are representative systems of neat methanol (solid curves) and mixtures in which the acetonitrile bulk mole fractions are $x_{\mathrm{ACN,bulk}}$ =0.64 (dashed curves), and $x_{\mathrm{ACN,bulk}} = 0.94$ (dotted curves).

acetonitrile molecules adsorbed at the silica surface. Figure 1.3 summarizes the dynamics as the system approaches equilibrium. System interaction energies are depicted in Figure 1.3a. As the relaxation proceeds, methanol-silica interaction energy increases (becomes more negative) as methanol molecules move to the interface. As acetonitrile molecules are displaced from the surface, their interaction with the silica surface and with the significant number of methanol molecules migrating to the surface decreases. Relaxation of the interaction energy to its equilibrium value occurs in approximately 12 ns for a system with a bulk acetonitrile mole fraction of 0.94. Silica-solvent hydrogen bonding during these relaxations is shown in Figure 1.3c. As methanol molecules populate the surface, silica sites are able to participate in hydrogen bonds as donor and acceptor, a more energetically favorable configuration than an interface dominated by acetonitrile molecules, which can only accept hydrogen bonds from the silica surface. This binary mixture demonstrates the affinity of the silica surface for methanol over acetonitrile. In this representative binary mixture, with a bulk methanol mole fraction of 0.06, 92% of the silica sites donate hydrogen bonds to methanol molecules (red line in Figure 1.3c) and 85% of these sites accept hydrogen bonds from these same methanol molecules (blue line in Figure 1.3c). A given silanol site has only a 3% likelihood of participating in a hydrogen bond with an acetonitrile molecule. Silica-methanol interaction energy at equilibrium is approximately 6 times greater than silica-acetonitrile. To gain additional insight into the relaxation progress independent of the property examined, Figure 1.3b,d shows the corresponding normalized nonequilibrium correlation functions,

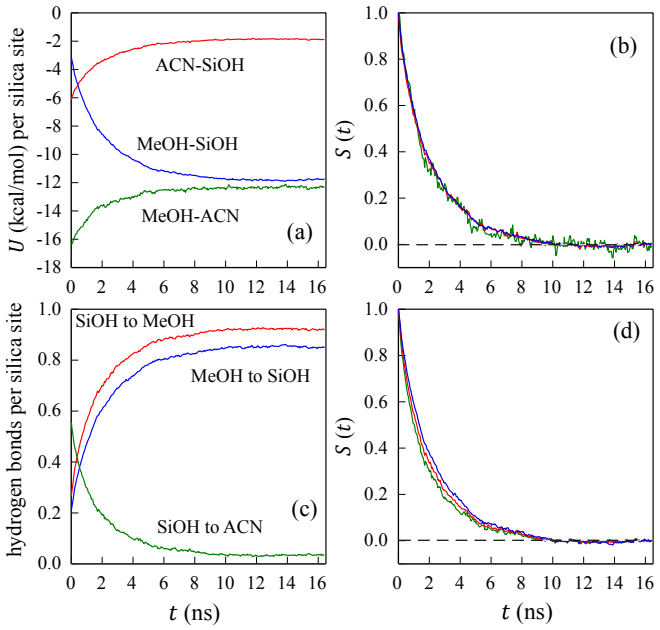

Figure 1.3: Time-dependent relaxation toward equilibrium of a methanol-acetonitrile mixture ($x_{\mathrm{ACN}} = 0.94$) at a silica surface starting from a random molecular composition. (a) Silica-solvent and solvent-solvent interaction energies and (b) the corresponding normalized nonequilibrium correlation function (see eq 1.2 for a definition). (c) Silica-solvent hydrogen bonding probability and (d) the corresponding normalized nonequilibrium correlation function.

which are defined as

$$S(t) = \frac{\overline{\Gamma}(t) - \overline{\Gamma}(\infty)}{\overline{\Gamma}(0) - \overline{\Gamma}(\infty)} \tag{1.2}$$

for any property of interest Γ, where $\overline{\Gamma}(t)$ is the average at time t over all initial configurations. The interaction energies and hydrogen bonding probabilities show very similar time-dependent behavior. It is nearly exponential with a time constant of 2.3 ns. This behavior suggests that the underlying molecular events governing the relaxation are independent replacements of an adsorbed acetonitrile molecule by a methanol molecule, so that the formation of silica-methanol hydrogen bonds is accompanied by the breaking of a silica-acetonitrile hydrogen bond. Acetonitrile molecules subsequently migrate away from the silica surface. It is interesting to compare the nonequilibrium relaxation described above with the relaxation of the fluctuations at equilibrium. To do this, we consider the final 4.5 ns of the trajectories of Figure 1.3 as representative of the system at equilibrium. To avoid confusion between equilibrium and nonequilibrium calculations, we define Γ_e to be the property of interest during the equilibrium portion of the trajectories that correspond to Γ. With these definitions, we may compare the fluctuations of the interaction energies and hydrogen bonding probabilities during this equilibrium period. As a rough measure for the size of the equilibrium fluctuations, we consider the ratio of the standard deviation at equilibrium: $\sigma = \langle(\delta\Gamma_e)\rangle^{1/2} = \langle(\Gamma_e(t) - \langle\Gamma_e\rangle)^2\rangle^{1/2}$ to the total nonequilibrium change $\overline{\Gamma}(0) - \overline{\Gamma}(\infty)$. (Note that $\overline{\Gamma}(\infty) = \langle\Gamma_e\rangle$). This ratio is equal to 0.04 - 0.05 for the hydrogen bonding probabilities and for the solvent-silica interaction energies but considerably greater (0.12) for the methanol-acetonitrile

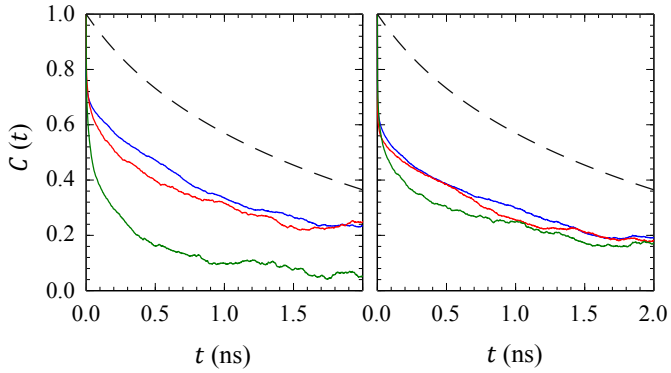

Figure 1.4: Left: Normalized equilibrium correlation functions (eq 1.3) of methanol-silica, acetonitrile-silica, and methanol-acetonitrile interaction energies (blue, red, and green lines, respectively). Right: Silica to methanol, methanol to silica, and silica to acetonitrile hydrogen bonding probability equilibrium correlation functions (blue, red, and green lines, respectively) Dashed lines show the nonequilibrium relaxations.

interaction energy. The methanol-acetonitrile interaction energy is the only parameter not a strong function of the hydrogen bonding at the silica surface, so these results suggest much stronger constraint on the size of the fluctuations associated with the surface hydrogen bonding. It is also interesting to contrast the nonequilibrium correlation functions $S(t)$ of eq 1.2 (shown on the right panels of Figure 1.3) with the equilibrium correlation functions defined as

$$C(t) = \frac{\langle \delta\Gamma_e(t)\delta\Gamma_e(0)\rangle}{\langle \delta\Gamma_e(0)\delta\Gamma_e(0)\rangle} \tag{1.3}$$

These correlations functions are shown in Figure 1.4 together with the exponential fit to the nonequilibrium correlation functions (fit to the average of all six $S(t)$ curves, which essentially fall on top of each other). Figure 1.4 emphasizes the considerably different time scales for the nonequilibrium versus equilibrium decay. The latter

is much faster since it is dominated by the fluctuations of an already existing hydrogen bond, while thenonequilibrium relaxation is dominated by adsorption/desorption events. The fastest equilibrium decay is observed in the interaction energy of the two-solvents; a relaxation essentially independent of the surface dynamics. To gain detailed molecular level understanding of the mechanism and dynamics underlying the process by which a methanol molecule displaces an acetonitrile molecule at the silica surface, we next study a model system of neat acetonitrile at a silica surface where one random acetonitrile molecule in the second solvent layer (8.5 Å $< z <$ 10.5 Å) is replaced by methanol. A harmonic reflecting potential affecting only the methanol is placed at $z = 11$ Å to prevent this molecule from diffusing into the bulk acetonitrile. After a short equilibration process where the methanol reaches an equilibrium with the surrounding acetonitrile molecules, the configuration is saved, and the process is repeated to generate 10 independent configurations. 130 trajectories are generated from each configuration by assigning random velocities to all atoms at time zero. The dynamics for these 1300 trajectories is quantified by detecting methanol-silica hydrogen bonding using the geometrical considerations described above. Since methanol can participate in two hydrogen bonds with the silica site, three possible methanol-silica hydrogen-bonding states are considered: methanol as donor, methanol as acceptor, or methanol participating in two hydrogen bonds with the surface as both donor and acceptor (denoted by $k = d$, a, or b, respectively). Each bonding parameter h_k is assigned a value of 0 if the bond of type k does not exist and 1 if the bond is present. With these definitions, we may quantify the "reaction" progress as the probability that methanol-silica hydrogen

bonding activity is detected:

$$P_k(t) = \frac{1}{N} \sum_{i}^{N} h_k(t) \tag{1.4}$$

where N is the number of trajectories. In computing $P_k(t)$, we use absorbing boundary conditions (ABC), where, after an initial methanol-silica hydrogen bond is detected (either donor or acceptor), the trajectory is terminated if subsequently either no methanol-silica hydrogen bonds are detected for a duration of 2.0 ps ("reactant" side) or if the methanol acts as both donor and acceptor in two distinct methanol-silica hydrogen bonds for 2.0 ps ("product" side). (The 2 ps value is later justified by examining the recrossing dynamics at the "transition state".) Figure 1.5 summarizes the early 70 ps of "reaction" progress, where approximately 17% of the trajectories resulted in methanol being bonded to the silica surface. The progress of the three discrete bonding states track closely together and steadily increase. Silica-methanol interaction energy (values depicted on the right axis), shown as the black curve in Figure 1.5, also tracks well with the reaction progress. The dynamics described in Figure 1.5 include the "uninteresting" effect of the diffusion of the methanol molecule to the surface and, as a result, the wide distribution of arrival times at the surface. To disentangle this part from the actual solvent exchange process, MD trajectories were run starting from configurations obtained from the "reactive" events shown in Figure 1.5. These starting configurations are simulation snapshots collected at the time step when methanol-silica hydrogen bonds were first detected. A total of 120 different configurations, 40 corresponding to each different initial hydrogen bonding state $k = d$, a, or b, were generated for this set

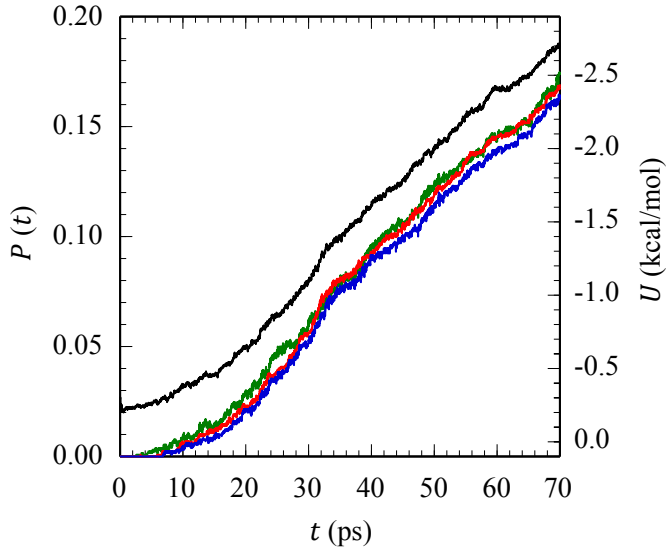

Figure 1.5: Reaction progress of a single methanol molecule adjacent to an acetonitrile-silica interface. Curves represent the probability of methanol hydrogen bonding with the silica surface where methanol acts as donor (blue), acceptor (red), or both donor and acceptor (green). Methanol-silica interaction energy (black) is shown on the right axis.

of simulations. 100 trajectories from each starting configuration were performed with initial random velocities assigned from a Maxwell-Boltzmann distribution and subject to the absorbing boundary conditions described earlier. The results are shown in Figure 1.6. All the curves start at $P_k = 1$ at $t = 0$ and immediately experience a sudden drop since the assignment of random velocities at the initial configuration typically results in the breakup of the bond (see below). In the three starting configurations considered, the probability that the methanol molecule forms stable hydrogen bonds with the silica surface reaches a plateau at about 25 ps. This behavior can be compared to the reaction progress in Figure 1.5, where the probability of stable hydrogen bond formation reached only 0.17 and continues to linearly increase 70 ps into the simulations (due to the wide

distribution of the methanol arrival times at the surface). It is important to keep in mind that the dynamics of hydrogen bond formation described in Figure 1.6 conservatively estimate the bonding progress from first bond detection since the randomized velocities allow for immediate dissociation of the bonds. For example, at the first time step of hydrogen bond detection, the O–O distance may be at the upper limit of the methanol-silica hydrogen bonding definition of 3.4 Å. If these oxygen molecules are assigned velocities in opposing directions, the bond will immediately be broken. The fact that the plateau value in Figure 1.6 is less than 1 is due to the subset of trajectories that did not maintain their hydrogen bonding state and were terminated by the "reactants" ABC. Thus, the utility of this plot is in demonstrating the different relative persistence of the three hydrogen bonding states.

When methanol first interacts with the silica surface as donor, the system is less likely to proceed to the product side than if the methanol first interacts as hydrogen bond acceptor (compare the plateau values of $P(t) = 0.7$ and $P(t) = 0.6$ for acceptor and donor initial states, respectively). This is likely due to the relative immobility and location of the silica oxygen atom relative to the other hydrogen bonding atoms. The methanol hydrogen-silica oxygen bond is less likely to survive because the silica oxygen is bonded to an immobile silicon atom, resulting in a less flexible bond. This same relationship is seen in studies of the neat silica-methanol interface, where methanol-silica hydrogen bond lifetimes are reportedly shorter when methanol acts as donor. [See Appendix A, Figure A.1] However, we also note that methanol is more likely to first hydrogen bond with the silica surface as a donor (61%) than as an acceptor (39%) (data

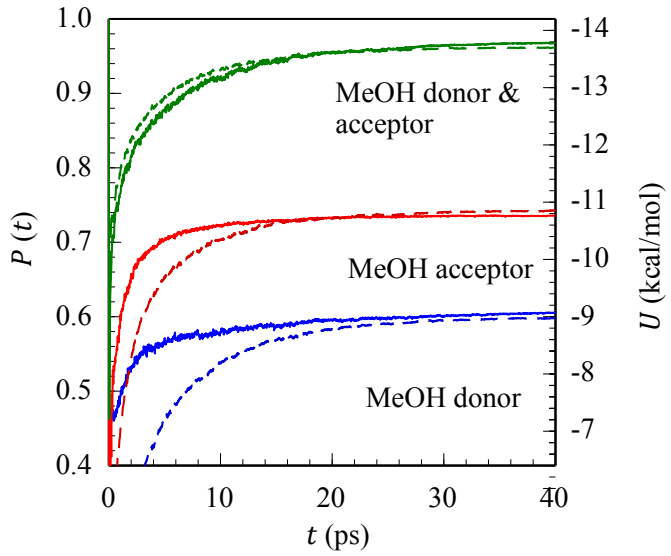

Figure 1.6: Reaction progress when methanol-silica hydrogen bonding is present at $t = 0$. Associated methanol-silica interaction energies (dashed curves) are shown on the right axis.

obtained from the trajectories used to generate Figure 1.5).

Figure 1.6 also depicts the average methanol silica interaction energies for the three types of trajectories. The average energies of the starting configurations are -3.6, -4.3, and -9.2 kcal/mol for methanol acting as donor, acceptor, and both donor and acceptor, while the average silica/methanol interaction energy in the "products" side is $\langle U_p \rangle$ = -14.2 kcal/mol. The average energy scales with $P_k(t)$ near the plateau region so that the interaction energy at the plateau region $\langle U_k(\infty) \rangle$ is approximately equal to the plateau value of $P_k(t)$ times $\langle U_p \rangle$. Thus, the approach to the plateau region may be interpreted as the progress from one weakly bound to two stable methanol-silica hydrogen bonds. We now turn to a detailed examination of the exchange mechanism. To this end, it is useful to define a "reaction coordinate" that tracks the progress from

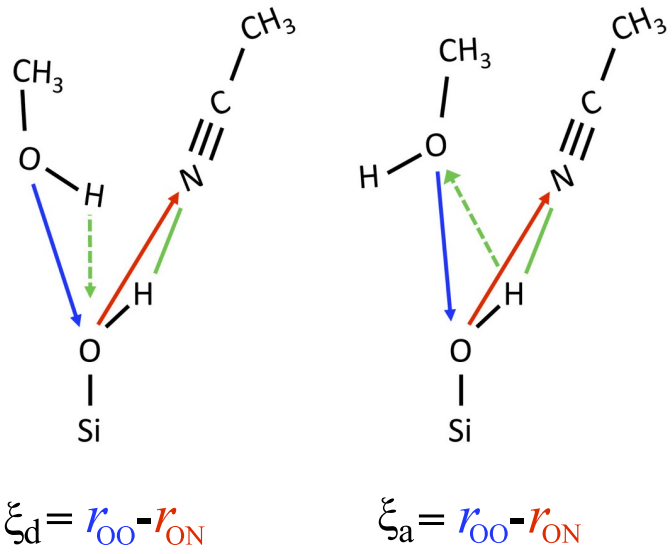

Figure 1.7: Reaction coordinates ξ_d (left) and ξ_a (right) representing methanol's hydrogen bonding relationship with a silica site as either donor or acceptor, respectively.

a methanol molecule far from the surface ("reactants") to a state where this molecule is bonded to the silica surface ("products"). When methanol adsorbs to the silica surface, silica-methanol hydrogen bonds form. Since the silica site is unable to stably donate hydrogen bonds to both a methanol molecule and an acetonitrile molecule, the silica-acetonitrile hydrogen bonds typically break. The distances used to geometrically detect hydrogen bonding may also be used to generate reaction coordinates to monitor the progress of this reactive event. Since methanol forms two hydrogen bonds at the surface, we may define two independent reaction coordinates, illustrated in Figure 1.7. When methanol acts as a hydrogen bond donor, the reaction coordinate ξ_d is defined by locating the silica site whose oxygen atom is closest to the methanol hydrogen. The oxygen-oxygen distance between this silica site and the methanol oxygen is labeled r_{OO}.

The distance between the silica oxygen and the nearest acetonitrile nitrogen atom is labeled r_{ON}. The collective variable ξ_d is then defined as $\xi_d = r_{\mathrm{OO}} - r_{\mathrm{ON}}$. Similarly, we define ξ_a to study the reactive event where the methanol molecule accepts a hydrogen bond from the silica surface. In this case, the relevant silica site is the site whose hydrogen atom is closest to the methanol oxygen atom (see right panel of Figure 1.7). The distances r_{OO} and r_{ON} are defined in the same manner as before; their difference is ξ_a. These definitions depend on identifying during the simulations the proper silica sites and we update these identities every 10 integration steps (5 fs of simulation time).

The values of the reaction coordinates ξ_d and ξ_a are calculated every 25 fs in simulations that resulted in a reactive event. We define this reactive event to be complete when the methanol molecule has been bonded to the silica surface by two hydrogen bonds for an uninterrupted period of 2.0 ps, identical to the product side ABC described above. Once the system reaches this state, the trajectory is terminated. These distances are assembled into probability distributions in Figure 1.8. (The data used to generate these distributions are the subset of all the 1300 trajectories used to generate Figure 1.5 subject to the condition that the trajectory reached the "products" state and was terminated by the ABC). The reaction progress can be followed from left to right on the ξ-axis, where positive values of ξ correspond to methanol far from the silica surface, and negative values represent a state where the acetonitrile has desorbed. When methanol is far from the silica surface, the two curves corresponding to methanol acting as donor or acceptor are nearly identical because the r_{OO} distances (between the silica and methanol oxygens) dominate the values of both ξ_d and ξ_a. As the methanol-

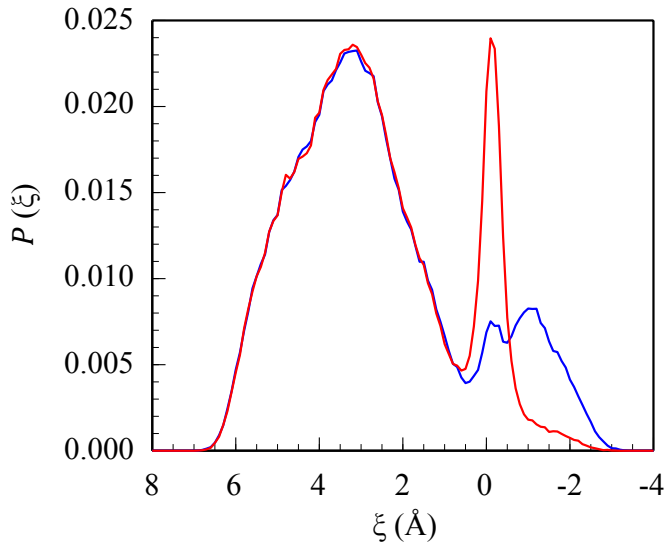

Figure 1.8: Probability distribution (normalized to unit area) of the reaction coordinates ξ_d (red curve) and ξ_a (blue curve).

silica distance approaches the silica-acetonitrile distance, ξ_d and ξ_a both approach zero and the residence time of the system at these distances appears to decrease. We define these local minima as the transition states along these reaction coordinates at 0.5 Å and 0.6 Å for ξ_d and ξ_a, respectively.

The obvious differences between ξ_d and ξ_a are seen once the system is past the transition state and the methanol-silica hydrogen bonds form. When the methanol molecule acts as an acceptor and the silica site acts as donor (ξ_a), a small peak is present at $\xi_a = 0$, where the silica site can potentially serve as hydrogen bond donor to both methanol and the nearby acetonitrile. As the acetonitrile disassociates from the silica site and begins to diffuse away, ξ_a becomes more negative and peaks at -1 Å (representing the products state). In the histogram of this reaction coordinate, ξ_a,

the dissociation of the acetonitrile from the silanol donor site is observed. When the silica site accepts a hydrogen bond from the methanol molecule (ξ_d), no competition for silica's role as donor to the nearby acetonitrile is introduced. The relevant silica site remains hydrogen bonded to an acetonitrile. Since the hydrogen bonds described by r_{OO} and r_{ON} may coexist and their equilibrium distances are similar, ξ_d exhibits a large sharp peak centered at 0 Å. The overlaid histograms in Figure 1.8 also illustrate the mechanism by which methanol displaces acetonitrile from the silica surface: when a methanol molecule interacts with a silica site as hydrogen bond acceptor, the acetonitrile molecule bonded to the same site is displaced. The methanol molecule then hydrogen bonds to an adjacent silanol site as a hydrogen bond donor without affecting the silica-acetonitrile hydrogen bond.

The specifics of this displacement are illustrated further in Figure 1.9a,b. In these plots, the reactive events described above have been time-shifted so that the initial silica-methanol hydrogen bond occurs at $t = 0$. In Figure 1.9a (where methanol acts as an acceptor) the probability of a silica site donating a hydrogen bond to an acetonitrile molecule drops significantly before the silica-methanol hydrogen bond is initiated. In Figure 1.9b (where the methanol acts as a donor) the situation is quite different. The silica-acetonitrile hydrogen bond exhibits no discernible awareness of the formation of a silica-methanol hydrogen bond when methanol acts as donor. The locations of the minima of the reaction coordinates ξ_a and ξ_d, represented as the black dotted lines, add more mechanistic insight. In Figure 1.9a, when methanol acts as hydrogen bond acceptor, the transition state ξ_a is crossed before formation of the silica-methanol hydrogen

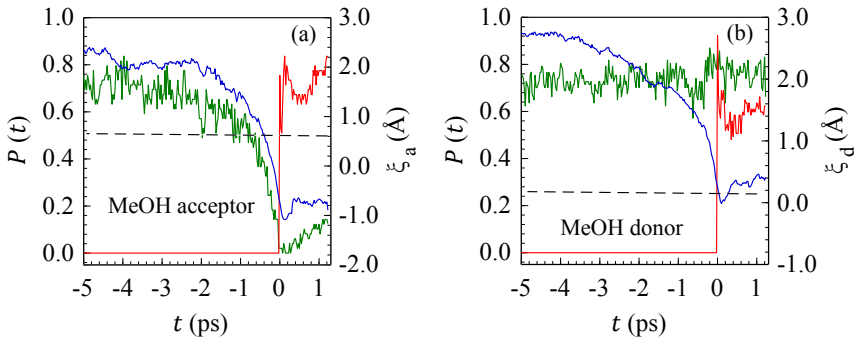

Figure 1.9: Hydrogen bond probabilities for silica-acetonitrile (green curves) and silica-methanol (red curves) when the methanol molecule engages the silica surface. The respective reaction coordinate (blue curves, right axes) are also displayed for events where methanol approaches a given silica site as acceptor (a) or donor (b). The black dotted lines represent the value of the reaction coordinate minima observed in Figure 1.8.

bond. By contrast, when methanol donates a hydrogen bond to silica, this hydrogen bond is detected at the same time the ξ_d transition state is crossed. This difference is further discussed below. The above definitions of transition states based on these geometrical reaction coordinates ξ_d and ξ_a permit investigation of the methanol-silica reactive event. In particular, we consider the deviation from transition state theory, which states that, after reaching the transition state, the trajectory proceeds to the products side without any recrossing. Recrossings of the transition state may be attributed to solvent effects, here the neighboring acetonitrile molecules. To quantify the likelihood of these recrossings, we calculated the reactive flux correlation functions for each of the reaction coordinates. In brief, molecular dynamics simulations are run starting with an initial configuration where the methanol molecule is at the transition state ξ_d or ξ_a. The MD trajectory begins with random velocities assigned from a flux-

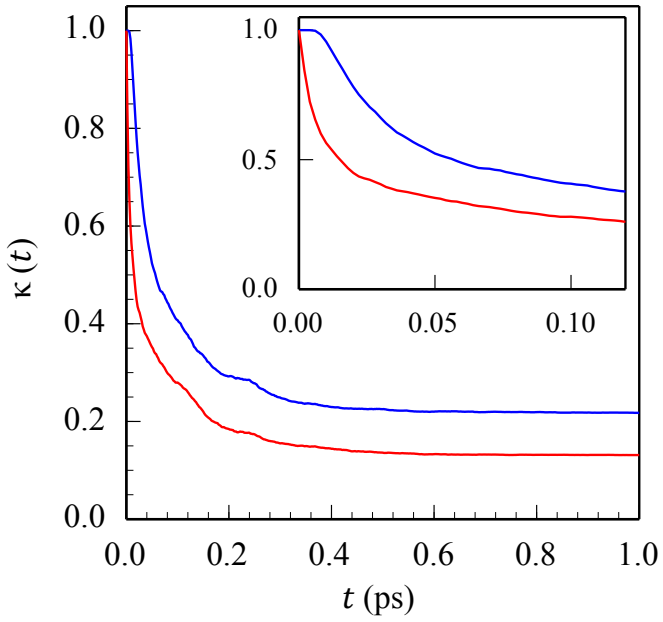

Figure 1.10: Reactive flux correlation functions for the reaction coordinates ξ_d (red curves) and ξ_a (blue curves).

weighted Maxwell-Boltzmann distribution so that the value of $\mathrm{d}\xi/\mathrm{d}t$ is positive at $t = 0$. The normalized reactive flux correlation function for this system was calculated by [230]

$$\kappa(t) = \frac{1}{N} \sum_{i=1}^{N} H[\xi_i(t) - \xi(0)] \tag{1.5}$$

where κ is transmission coefficient, ξ_i is the reaction coordinate value of the ith trajectory at time t, and H is the Heaviside function ($H(x)$ =0 for $x < 0$; $H(x) = 1$ for $x > 0$). These curves are shown in Figure 1.10. The values of $\kappa(t)$ reach a plateau at ~600 fs. We assign the values of these plateaus as transmission coefficients of the respective reaction coordinates, $\kappa_a = 0.22$ and $\kappa_d = 0.13$. These values, as well as the relatively long time needed to reach a plateau suggest extensive recrossings at the transition state.

Closer examination of the initial behavior (Figure 1.10, inset) reveals interesting structural differences in the correlation functions. ξ_a shows a brief plateau, while ξ_d does not. This suggests that ξ_a is a more physically relevant reaction coordinate than ξ_d. This agrees with the above discussion since the two intermolecular distances that define ξ_a also define two hydrogen bond acceptors, methanol, and acetonitrile, competing for the same donor. As ξ_a decreases, methanol becomes the dominant acceptor, and the reactive event moves toward the product side. Conversely, in ξ_d the two hydrogen-bonding distances are relatively impartial to the other's existence, as evidenced by the sharp peak at $\xi_d = 0$ Å in Figure 1.8 and the flat silica-acetonitrile hydrogen bonding probability curve in Figure 1.9b. We conclude by discussing the orientation of the methanol molecule at various locations along the two different reaction coordinate. Far from the surface, methanol's approach to the silica surface is driven by diffusion through acetonitrile liquid in which no particular orientation is preferred. Methanol ultimately attains a very precise orientation when bonded to the silica surface. Of obvious interest is the molecular orientation of the methanol molecule between these two extremes, in particular at the transition states as defined by the histogram in Figure 1.8. Methanol O–CH_3 and O–H molecular vectors are used to describe the orientation of the molecule at the ξ_d and ξ_a transition states. Figure 1.11 shows the orientational distributions of these molecular vectors relative to a vector normal to and pointing away from the silica surface. In both ξ_d and ξ_a, the O–CH_3 vector predominantly points away from the silica interface. We would anticipate that the nonpolar alkyl tail would "dislike" the hydrophilic surface and also that the methanol hydroxyl group should be in position

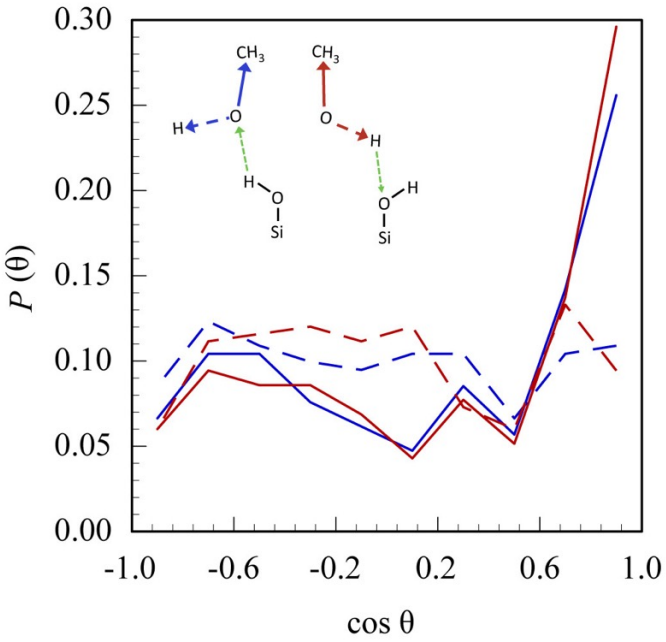

Figure 1.11: Orientational distributions of methanol molecular vectors relative to the surface normal at the reaction transition states ξ_d (red curves) and ξ_a (blue curves). Solid curves represent the methanol O–CH_3 vector, and dashed curves represent the O–H vector.

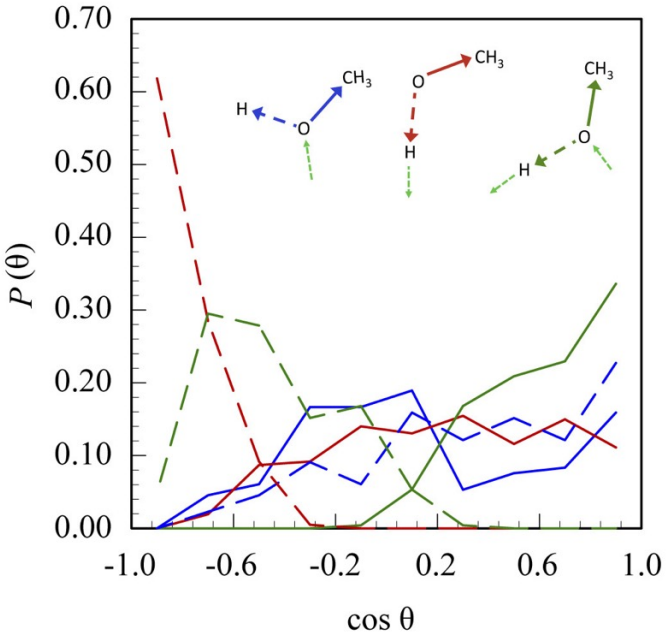

Figure 1.12: Orientational distributions of methanol molecular vectors at initial methanol-silica hydrogen bond formation where methanol participates as donor (red), acceptor (blue), or in two bonds as both donor and acceptor (green). Solid lines represent the O–CH_3 vector. Dashed lines represent the O–H vector.

to engage the silanol groups for hydrogen bonding to occur. We may further describe methanol's orientation during this reactive event by considering the orientation preferred by methanol when hydrogen bonding with silica initially occurs. Figure 1.12 shows the orientational distributions of methanol molecular vectors, O–CH_3 and O–H, relative to a vector normal to and pointing away from the silica surface. We note that orientations for all bonding situations differ significantly from orientations at the transition state (Figure 1.11), where the O–CH_3 vectors predominantly point away from the silica surface and the O–H vectors lack a dominant orientation. When methanol's first hydrogen bonding interaction with silica is as a hydrogen bond donor, the O–H vector

points toward the silica surface. When methanol first accepts a hydrogen bond from a silica site, the O–H vector is parallel to or pointing slightly away from the interface. When methanol is first bonded to two sites as both donor and acceptor, the molecule assumes the anticipated orientation, where the O–H vector points slightly toward the interface so that it may access silica oxygen and hydrogen atoms. The methyl tail, described by the O–CH_3 vector, points away from the polar surface.

1.4 Conclusions

The molecular dynamics simulations described in this work present a detailed view of a mechanism by which a strongly hydrogen bonding solvent molecule (methanol) displaces a weakly hydrogen bonding solvent (acetonitrile) adsorbed at a hydrophilic (silica) surface. At equilibrium, for all the methanol/acetonitrile mixtures investigated here, methanol is much more strongly bonded to the silica surface, as it is able to act as both hydrogen bond donor and acceptor to two neighboring silica sites, compared with acetonitrile, which is able to act only as a hydrogen bond acceptor to one site. When a methanol molecule approaches the silica-acetonitrile system, it is able to effectively leverage its affinity to the silanol oxygen atom, a potential hydrogen bond acceptor ignored by interfacial acetonitrile molecules. This displacement event may be visualized as a "bottle-opener" mechanism, where the methanol anchors itself to the silica surface by donating a hydrogen bond to the silica oxygen and subsequently rotates about its hydroxyl hydrogen atom, accepting a hydrogen bond from a neighboring silica hydrogen

while dislodging the respective acetonitrile. The second possible mechanism is the initial approach of methanol, oriented to accept a hydrogen bond from the silica surface. In this configuration, methanol initially displaces acetonitrile and accepts a hydrogen bond from the silica surface and then donates a hydrogen bond to an adjacent silanol oxygen, ensuring stability at the silica surface.

Acknowledgments

This work has been supported by a grant from the National Science Foundation (CHE-1363076). We are grateful to Rob Walker and Eric Gobrogge for many useful conversations.

Chapter 2

Unusual structure and dynamics at silica/methanol and silica/ethanol interfaces: a molecular dynamics and nonlinear optical study

2.1 Introduction

Solid surfaces often force molecules in an adjacent phase to adopt anisotropic structures and organizations leading to differences between bulk and interfacial properties. Both experimental and computational studies of these surfaces have shown distinctive changes in interfacial density, dynamics, and solvation relative to bulk behavior. [4, 13, 69, 120, 185, 223] These changes have direct consequences for mechanistic descriptions of a wide array of surface phenomena including adhesion, corrosion, chro-

matography, and catalysis. [61, 28, 49, 178, 208] Traditionally these properties have been studied using linear spectroscopic [169] and wet chemical methods, [229] but more recently, nonlinear optical methods have aided in characterizing chemical structure, organization, and reactivity in these asymmetric environments. [4, 138, 56] Acetonitrile is one example of a solvent with well-studied interfacial behavior. Weeks and co-workers studied the silica/acetonitrile interface using both vibrational sum frequency (VSF) spectroscopy and molecular dynamics (MD) simulations. [52] The results of both the experimental and theoretical studies indicated an interfacial structure varying greatly from that of the bulk. Simulations predicted that acetonitrile formed a bilayer structure at the interface, and that this bilayer structure of oppositely oriented acetonitrile molecules extended several nanometers into the bulk. VSF spectroscopy experiments support this picture and imply that the first sublayer interacting directly with the silica surface has a vibrational structure that is slightly different from acetonitrile oriented in the opposite direction and not closely associated with the silica. The silica/water interface has also been well studied. [56, 77, 165, 168] These studies show that interfacial water molecules can exist in two different environments. One environment involves tetrahedrally coordinated water molecules while the other involves water in a more weakly associated hydrogen-bonding environment. Furthermore, these studies showed that the molecules' environment was highly dependent on solution pH. Unique interfacial organization has also been found at the silica/1-alcohol interface. Shen and co-workers determined that for C1-C4 alcohols, the molecules at the silica/vapor interface adsorbed with their methyl groups oriented away from the surface. The decrease in signal observed at the

silica/liquid interface was explained by the formation of a bilayer between oppositely oriented molecules. [119] Alcohol adsorption to solid substrates is of particular interest due to industry's use of oxide catalysts in the production of alkenes, esters, ethers, aldehydes, alkylamines, [232] and blending compounds for reformulated gasoline. [195, 154] Numerous experimental and theoretical studies have investigated both the solid/alcohol and solid/alcohol vapor interfaces. [154, 171, 97, 140] More recently, VSF spectroscopy and other second order nonlinear optical methods have been employed to study molecular-level interactions at buried silica/liquid alcohol interfaces. [119, 68, 236, 7, 204, 237, 30] Using this surface specific technique, vibrational modes of species in asymmetric environments have been observed and used to discern the structure and organization of interfacial molecules. Of all the short chain alcohols, methanol exhibits the most peculiar behavior, with data from experiments and simulations leading to conflicting descriptions of solvent structure at this solid/liquid interface. While VSF studies have reported strong methanol signatures from the silica/methanol vapor interface, virtually no VSF response is observed from the silica/methanol (solid/liquid) interface. [119, 68, 236] Shen and co-workers attributed this observation to the proposed formation of a rigid methanol bilayer at the interface with the first sublayer hydrogen-bonding to the surface silanols, and the second sublayer interacting weakly through the opposing methyl groups. Because opposing methyl groups have antiparallel vibrational dipoles, the SF signal was predicted to disappear. [119] This same cancellation, however, is not seen when the methanol is replaced with ethanol. Ethanol has an observable VSF response at both the silica/vapor and silica/liquid interfaces. [119] While the silica/vapor signal

arises from the same hydrogen-bound monolayer, the bilayer observed at the silica/liquid interface does not result in complete cancelation of the SF signature. This observation is attributed to two main sources. First, the second layer is expected to have a much broader orientational distribution than the first layer; and second, while the methyl symmetric stretches of the two layers are oppositely oriented and result in a severely diminished signal, the antisymmetric stretches remain unaffected. [119] Further attempts at characterizing these surfaces have been made by examining binary mixtures of the alcohol with water, carbon tetrachloride, and acetonitrile. [68, 236] Methanol will give rise to a signal at silica/liquid interfaces under carefully controlled conditions. Zhang et al. have studied both methanol-water and methanol-carbon tetrachloride binary mixtures at the silica interface using VSF spectroscopy. They found that in binary solutions with CCl_4, methanol gave a strong SF signal at methanol mole fractions of 3-30%, but at higher fractions, the signal disappeared. When carbon tetrachloride was replaced with water, however, methanol did not give a signal at any mole fraction. [236] These observations were attributed to the nonpolar nature of carbon tetrachloride allowing the formation of a methanol monolayer at the surface until a high enough mole fraction is reached and a second antiparallel methanol sublayer forms. In water, however, methanol molecules are forced through hydrophobic interactions to associate through the methyl groups at all mole fractions resulting in no SF signal. In a similar experiment, Gobrogge and Walker studied binary mixtures of methanol and acetonitrile and found that any response from methanol was conspicuously absent at all mole fractions, further supporting the proposed model of interfacial methanol pairs consisting of oppo-

sitely oriented monomers. [68] Computational studies have also been used to investigate the silica/alcohol buried interface. Roy et al. confirmed that at the silica/methanol interface, the first sublayer of methanol molecules hydrogen-bonds strongly to the surface silanol groups, but found that the second sublayer tends to associate with the O-H bonds pointing toward the surface. [185] Simulations suggest that the second sublayer forms additional hydrogen bonds with the first sublayer as opposed to interacting through the van der Waals attraction of antiparallel methyl groups. Such organization should lead to enhanced SF intensity given that interfacial solvent molecules are all oriented in approximately the same direction. However, computational support is also found for the antiparallel bilayer model. Simulations by Tallarek and co-workers show that methanol forms a monolayer hydrogen bound to the silanols thereby presenting a hydrophobic surface to the bulk. The methyl-terminated interface then causes the next layer of methanol molecules to orient their methyl groups toward the surface. [134] Such organization should lead to significantly diminished (or absent) signals in VSF spectroscopy experiments consistent with what has been observed experimentally. Differences between these two descriptions of methanol organization are likely to be sensitive to experimental conditions including surface silanol density. Specifically, if the surface silanol density is high and the surface layer of methanol is packed tightly, one might expect the second layer of methanol to adopt an antiparallel arrangement. However, if the silanol surface coverage is lower, adsorbed methanol monomers will have enough space in between so that the second layer can hydrogen bond to the first. In the work presented below, results from molecular dynamics (MD) simulations are

compared with data from VSF spectroscopy experiments in order to develop a better understanding of the structure of methanol and ethanol at the silica interface. Experiments show that while both alcohols provide a strong VSF signal when adsorbed to the silica/vapor interface, only ethanol gives an appreciable signal at the silica/liquid interface. Our MD simulations support the layered methanol system proposed by Roy et al. [185] Striking differences between the two solvents are observed in their organization and dynamics, however. When compared to methanol, ethanol molecules are shown to have longer-lived alcohol-silica hydrogen bonds, and a large ($\sim$ 3 Å) region of near zero density between the first two sublayers. Furthermore, by lowering the number of active sites on the surface and thereby decreasing the number of hydrogen-bonded methanol molecules, the density of the second methanol sublayer is shown to increase as the surface (including the first methanol layer) becomes less hydrophobic. While this predicted result is difficult to test systematically by experiment, surface hydroxyl coverage can be changed by changing the substrate. α-Alumina has surface hydroxyl concentrations 2-3 times higher than silica. VSF data from the methanol/α-alumina liquid-solid interface show a weak but pronounced response from the interfacial solvent. This result suggests that small changes in surface composition have very strong effects on local solvent organization. This paper is organized as follows. In sections II and III we detail the relevant experimental and simulation techniques used to study the silica-methanol and silica-ethanol systems. In section IV we introduce the system through the viewpoint of MD simulations, describe experimentally obtained VSF spectra, and qualitatively explain interesting features of these spectra by directly comparing MD

data from these two systems.

2.2 Experimental methods

Spectroscopic grade methanol and ethanol were obtained from Sigma-Aldrich and used as received. Silica slides (0.5 mm) from SPI, Inc. were first cleaned using a 50/50 (v/v) mixture of sulfuric and nitric acid. The silica slides were then rinsed with deionized water (18.2 MΩ cm) and dried thoroughly to create a fully hydroxylated silica surface that was then affixed to our experimental cell and placed in direct contact with the liquid or saturated vapor phase of interest. The VSF spectroscopy apparatus has been described elsewhere. [69] In brief, a Libra-HE Ti:sapphire laser (Coherent, 3.3 W 85 fs pulse width, 1 kHz repetition rate) was coupled to a visible optical parametric amplifier (Coherent OPerA Solo) to generate the visible and IR beams. The IR wavelength was tuned from 3.2 to 3.7 μm in 0.05 μm increments and the IR field was focused onto the sample at an angle of 73° with respect to normal. The visible beam was spectrally stretched and sliced using an 1800 g/mm grating and variable width slits resulting in a spectrally narrowed visible beam (20 cm^{-1}). After passing through two different delay stages, this beam was focused onto the surface at an angle of 67° with respect to normal. Visible power immediately before the sample was ∼8 μJ while the IR power was ∼5 μJ. IR power was adjusted with neutral density filters to be as high as possible without boiling the sample. The generated sum frequency signal was directed into a monochromator (SpectraPro-300i, Acton Research Corporation) and dispersed onto a

CCD (PIX-IS100B, Princeton Instruments). VSF spectra were combined and corrected for ambient background contributions using inhouse Igor Pro (v.6) routines.

2.3 Simulation details

Molecular dynamics simulations of the neat silica-methanol and silica-ethanol solid-liquid interfaces were performed using an in-house MD code. Our silica surface is a derivative of the fully hydroxylated β-Cristobalite surface used by Lee and Rossky [113] and has recently been described elsewhere. [98] Briefly, we modified the Lee and Rossky surface to include fully flexible silicon-oxygen-hydrogen surface sites that incorporate the CHARMM water contact angle Lennard-Jones and bond parameters. [44, 114] The methanol and ethanol force field parameters are those used in our earlier work, [11] using a united atom 3 or 4 site description of the alcohol. Intermolecular potentials are calculated as the sum of Lennard-Jones and Coulomb terms:

$$U_{ij}(r) = \sum_{i<j} 4\epsilon_{ij} \left[\left(\frac{\sigma_{ij}}{r} \right)^{12} - \left(\frac{\sigma_{ij}}{r} \right)^{6} \right] + \frac{q_i q_j}{4\pi r \epsilon_0} \tag{2.1}$$

where i and j are atoms of different molecules separated by a distance r. Mixed Lennard-Jones interactions were calculated using standard Lorentz-Berthelot combining rules: $\sigma_{ij} = (\sigma_i + \sigma_j)/2$ and $\epsilon_{ij} = (\epsilon_i \epsilon_j)^{1/2}$. To prepare the adjacent alcohol phases, alcohol molecules were placed in a box with periodic boundary conditions in all directions. The x and y dimensions of this simulation box are set equal to the length and width of the silica surface. The alcohol box height z was allowed to vary so that the correct bulk

density of each alcohol is reproduced. The equilibrated box of solvent molecules is then placed adjacent to the silica surface described above. Each silica-alcohol simulation box had dimensions of $L_x = 45.0$Å, $L_y = 43.3$Å, and $L_z = 100$Å with the silica surface placed in the $x-y$ plane at $z = 0.0$ Å. Silica-alcohol MD simulation boxes contained 90 silanol sites per silica surface ($4.62/\text{nm}^2$) and 1023 molecules of methanol or 709 molecules of ethanol. Each simulation was equilibrated for a minimum of 1.5 ns prior to initiating production runs. All simulations utilized a time step of 0.5 fs and were performed at 298 K. Production runs (unless noted otherwise) utilized 10 independently generated configurations, each was used to run a 750 ps MD trajectory at constant $T = 298$ K. Data reported below represent the average over these 7.5 ns of simulation time. Silica-alcohol hydrogen-bond detection utilized a previously described geometrical definition5 where a silica-alcohol hydrogen bond exists when the donor-acceptor oxygen-oxygen distance, r_{OO}, is less than 3.4 Å and the H–O–acceptor angle is less than 30°.

2.4 Results and Discussion

2.4.1 Simulation overview

Center-of-mass density profiles of liquid methanol and ethanol at a solid silica interface share most features. (Figure 2.1) The first major peak represents alcohol molecules hydrogen-bonded to the silica surface, in most cases each alcohol molecule at the interface participates in hydrogen bonds with two neighboring silica sites, acting as a hydrogen-bond donor in one and as acceptor in the other. The cumulative num-

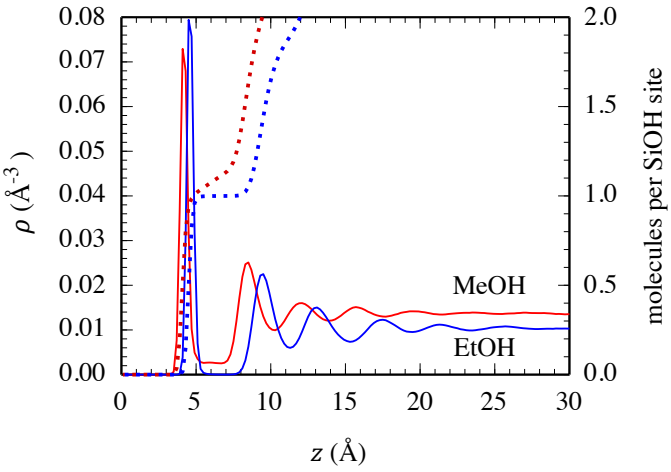

Figure 2.1: Density profiles of neat methanol (red) and ethanol (blue) at a silica interface. The dotted lines represent the respective cumulative number of solvent molecules per silica surface site (right axis).

ber of solvent molecules depicted on the right vertical axis shows that the first peak of the density profile of both liquids corresponds to a complete single-monolayer coverage of the perfect crystal silica surface. This closely packed, highly immobile, and well-ordered monolayer of adsorbed alcohol molecules is followed by a region of near zero density between it and the adjacent bulk liquid. The width of this low population region is approximately equal to the Lennard-Jones methyl-methyl interparticle spacing used in our simulations. We note that this low population region is not observed in polar-nonpolar (e.g., alkane-water) liquid-liquid interfaces due to the inherent capillary broadening effects at the interface of two immiscible liquids. [13] The fluctuating, relatively disordered liquid-liquid interface results in a much larger interfacial width. This low population region induces ordering in the alcohols that oscillates for several periods until bulk density is reached at $z \approx 25$ Å. The density oscillations in Figure

2.1 are out of phase due to the alcohol molecules' different sizes. The most physically interesting difference is in the region between the first and second major density peaks. With methanol as the solvent, this region is populated by a small but certainly nonzero number of molecules, while ethanol exhibits a region of near zero density. This difference is due to the larger alkane-like region formed by ethanol's longer alkyl group. In the silica-methanol system, the surface-induced alkane-like layer is thin enough to not totally shield all methanol molecules in its vicinity from the interface. Methanol molecules are more likely to enter this low population region and interact with the silica surface or surface-adsorbed methanol molecules, resulting in the low but measurable density. These interstitial methanol molecules sometimes displace methanol molecules adsorbed to the silica surface. In contrast, the slightly larger alkane-like region in the ethanol-silica system prevents ethanol molecules from interacting with the interface. This condition results in the adjacent region having a near zero density. The relative mobilities of methanol and ethanol molecules are investigated in detail below. Simulation snapshots in Figure 2.2 show the difference in the low population regions of the two systems. In this work we shall refer to this low population region between the first two major density peaks as the "second sublayer" [185] and note that this second sublayer is distinct from the *second solvent layer*, which we define as the second major density peak in the respective systems, centered at $z \approx 8$ Å and $z \approx 10$ Å for the methanol and ethanol systems, respectively. Interfacial organization at the surface appears qualitatively similar in both systems but the dynamics of these interfaces, particularly residence time of alcohol molecules near the silica interface, are different. Survival probability quantifies

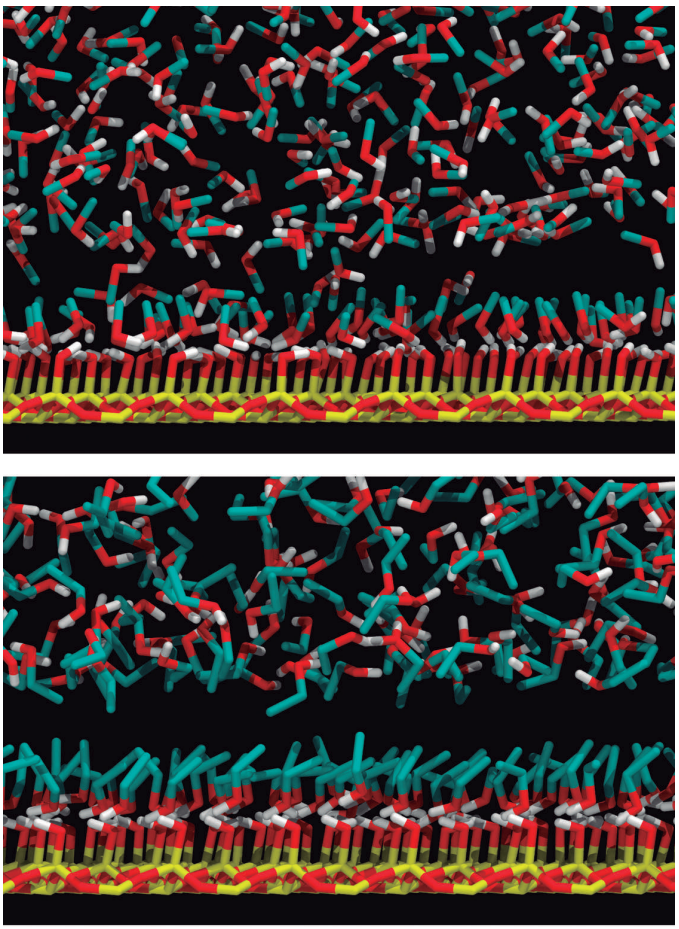

Figure 2.2: Snapshots of the surface region of methanol (top) and ethanol (bottom) in contact with a silica surface.

solvent molecule mobility in the direction normal to the silica surface. We define the survival probability as the probability that a molecule of methanol or ethanol within specified lamella parallel to the interface at a given time remains within the same specified region after an elapsed time t. This quantity is calculated using the time correlation function (TCF) formalism:

$$C(t) = \frac{\langle h(t)h(0)\rangle}{\langle h(0)h(0)\rangle} \tag{2.2}$$

where h represents a random variable of interest. In the case of survival probability, $C_S(t)$, we define h to be 1 if a given molecule is within specified z coordinates and 0 if the molecule is outside of the range. The ensemble average is calculated for all alcohol molecules and for all time origins. These survival probability TCFs, shown in Figure 2.3, illustrate the relative stability of the silica-ethanol surface. Regions where silica-alcohol hydrogen bonds exist, defined as $0.0 < z < 4.5$ Å and $0.0 < z < 7.0$ Å for methanol and ethanol, respectively, show a large difference in solvent mobility. Methanol's second sublayer is defined as $4.5 < z < 6.0$ Å to include the non-hydrogen-bonded molecules adjacent to the methanol molecules hydrogen-bonded to the silica surface. As mentioned above, this second sublayer is distinct from the second solvent layer, which we define as the second density peak in Figure 2.1, $7.0 < z < 10.0$ Å. Methanol molecules move in and out of this second sublayer, which enables more surface activity and rearrangement at the interface. The region of near zero density between the first and second ethanol layers does not allow this exchange. The long residence time of the alcohols at the silica surface is due to the formation of silica-alcohol hydrogen bonds. Each alcohol molecule

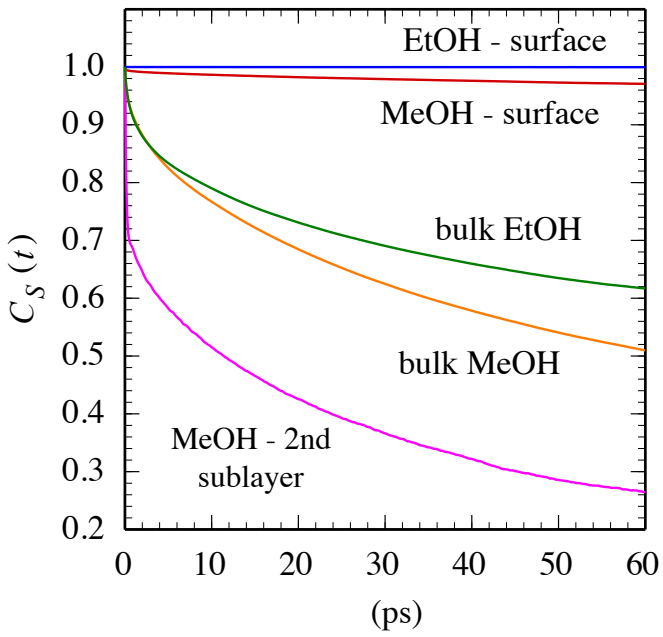

Figure 2.3: Solvent survival probabilities for the methanol-silica and ethanol-silica systems. Curves represent alcohol-silica interface (surface), alcohol bulk, and second sublayer of methanol behaviors.

is able to form two separate hydrogen bonds with adjacent hydroxylated silica surface sites where the alcohol acts as hydrogen-bond donor in one and acceptor in the other. The hydrogen-bond lifetime correlation function, $C_H(t)$, is calculated using Equation 2.2. For hydrogen-bond lifetimes we define the property h to be 1 if a hydrogen bond exists between a given alcohol-silica pair and 0 if no bond exists. The ensemble average is calculated over all possible alcohol-silica pairs and all time origins. Hydrogen-bonding correlation functions for the four silica-alcohol interfacial hydrogen bonds are shown in Figure 2.4. Due to the relatively slow dynamics of this interfacial hydrogen-bonding we ran longer simulations to capture these lifetimes, hence the 0-200 ps $x-$axis in Figure 2.4. These functions exhibit rapid decay on the femtosecond time scale representing reorientational motion of the OH bond, followed by a slow decay due to translational motion of the alcohols. The slow segments highlight different behavior based upon the identity of the alcohol and whether the alcohol or silica acts as hydrogen-bond donor. In both cases, ethanol-silica hydrogen bonds are longer lived than methanol-silica, suggesting more activity and mobility at the methanol-silica interface, consistent with the survival probability data presented in Figure 2.3. Specifically, the lack of ethanol molecules just outside the adsorbed layer lowers the probability for hydrogen-bond breakup since no "replacement" alcohol molecule is available. Further examination of the lifetime decays reveals that, in both systems, hydrogen bonds are longer lived when the alcohol acts as acceptor (note the smaller slope of the long-time tail of the dashed curve compared with the solid curve for each alcohol). This result can be explained by noting that the silica-hydrogen to alcohol oxygen bond consists of more

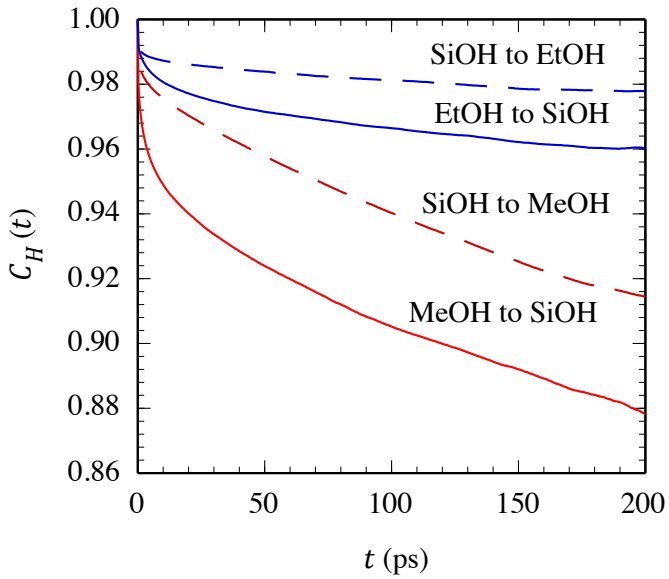

Figure 2.4: Alcohol-silica hydrogen-bond lifetime correlation functions for silica-alcohol hydrogen bonds. The red curves represent methanol-silica and the blue represent ethanol-silica. The respective alcohol acts as hydrogen-bond donor in the solid curves and as acceptor in the dashed curves.

flexible members than the alcohol hydrogen to silica oxygen bond. Thus, the silica oxygen is considerably less able to accommodate alcohol motion than the silica hydrogen while allowing the hydrogen bond to stay intact.

2.4.2 VSF spectra

ssp−Polarized vibrational sum frequency responses at silica-methanol interfaces are shown in Figure 2.5. The *ssp* polarization combination samples those vibrations that have their IR transition dipoles aligned along the surface normal. At the solid-vapor interface (top) two peaks are visible: the methyl symmetric stretch (r^+) centered at 2834 cm^{-1} and a methyl Fermi resonance (r^+-FR) at 2951 cm^{-1}. These data are

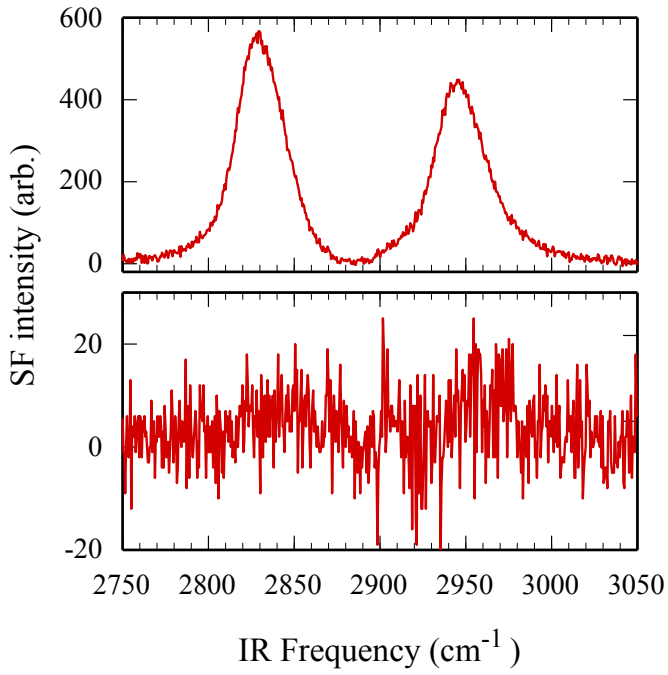

Figure 2.5: VSF spectra of the silica-methanol solid-vapor (top) and solid-liquid (bottom) interfaces.

consistent with what one expects from a methanol monolayer strongly hydrogen-bonded to the silica surface with the methanol methyl groups directed toward the vapor phase. The spectrum obtained at the solid-liquid interface (bottom) exhibits no discernible peaks in the same region. VSF spectra from silica-ethanol interfaces (Figure 2.6) show different behavior. At the silica-ethanol, solid-vapor interface (top) the ethanol CH_3 symmetric stretch (r^+) and its associated Fermi resonance peak (r^+-FR) are observed, centered at 2880 and 2936 cm^{-1}, respectively. In the spectrum from the solid/ liquid interface, the low frequency r^+ band disappears and intensity is observed in a broad feature centered at $\sim$2950 cm^{-1} (bottom). Given the absence of r^+ in the spectrum (and a corresponding source of intensity for Fermi resonance coupling), we tentatively

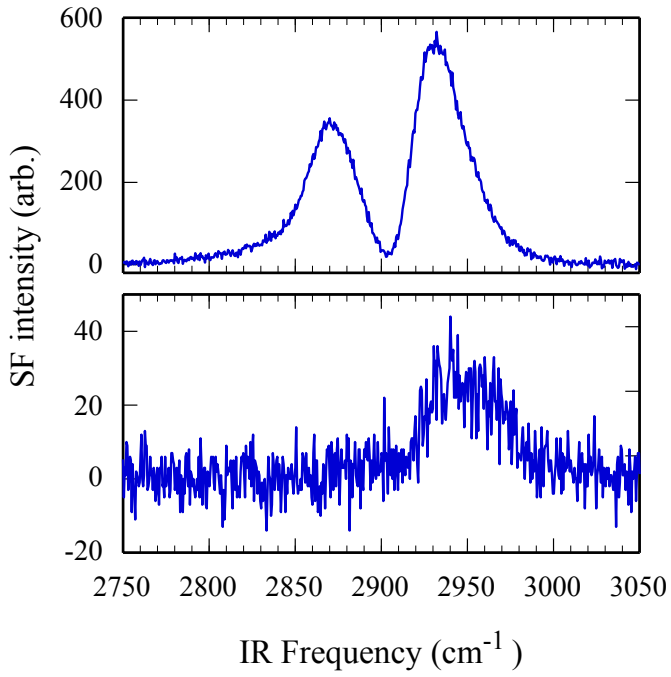

Figure 2.6: VSF spectra of the silica-ethanol solid-vapor (top) and solid-liquid (bottom) interfaces.

assign this broad feature to one of the asymmetric stretches of ethanol's $-CH_3$ group that no longer has C_{3v} symmetry. [227] These data present an interesting comparison of how molecular structure affects organization at solid/liquid interfaces. Methanol and ethanol have similar bulk densities, while the static dielectric constants of these solvents differ by less than 25%. Furthermore, methanol and ethanol associate with the silica surface in similar ways. In terms of elements that will influence interfacial solvent organization, the only obvious difference between these two systems is ethanol's additional methyl group. The effect of this difference is apparent both in the solvent density distributions (Figure 2.1) and in the lifetimes of each solvent's hydrogen bonds (Figure 2.4) although the solvent survival probabilities (Figure 2.3) and surface coverages (Figure

2.1) appear similar. Experimentally, absolute signal intensities drop (in Figure 2.6) by approximately an order of magnitude when moving from the solid/vapor interface to the solid/liquid interface. This general attenuation due to the presence of an adjacent liquid phase can be seen in the case of the ethanol r^- mode in Figure 2.6. Despite this difference in intensities, the absence of any vibrational response from the silica/methanol liquid interface (Figure 2.5) is striking. Lack of a VSF signal from an interface can arise from several sources: the absence of surface species, isotropic organization at the interface, or strong surface anisotropy having inversion symmetry. At the silica/methanol liquid interface, surface species are present and, given the strength of the methanol-silica hydrogen-bonding, a random organization of surface methanol molecules seems unlikely. In the next section, we examine MD simulation results of these systems in an attempt to isolate differences between the silica-methanol and silica-ethanol systems that may illuminate the reason for the suppressed VSF spectroscopy response in the silica-methanol system.

2.5 MD Investigtion of VSF Spectroscopy Response

To examine VSF spectroscopy experiments using molecular insight gained from these MD simulations, we consider that an *ssp*−polarized VSF signal arises when the active mode such as the methyl symmetric stretch has a net orientation of its IR transition moment normal to the silica surface. A cumulative orientational profile for the methyl symmetric stretch vector of each solvent is used to visualize the contribution to

a VSF signal based solely upon the number of molecules present and their orientation with respect to the silica interface. The cumulative orientational profile $S(z)$ is

$$S(z) = \sum_{i=0}^{[[z/\zeta]]} N_i \langle \cos\theta \rangle_i \tag{2.3}$$

where i represents the index of a bin of width ζ perpendicular to the simulation Z axis, $z = i\zeta$, the double brackets indicate the floor function, N_i is the number of alcohol molecules in bin i, and θ is the angle between a vector coincident with each molecule's methyl C_3 axis (in our simulation these vectors are O–CH_3 for methanol and CH_2–CH_3 for ethanol) and a vector normal to and pointing away from the silica surface. All reported cumulative orientational profiles in this work use a bin width (ζ) of 0.5 Å. The molecular vector lies along the transition dipole of the methyl symmetric stretch (r^+) and is perpendicular to the doubly degenerate asymmetric stretch (r^-). In the limit that methyl rotation is hindered, r^- splits into two distinct asymmetric stretches r_a^- and r_b^- with IR transition moments perpendicular to each other and to the molecular vector used to calculate $S(z)$. One of these vibrational modes will have a projection of its IR transition moment along the surface normal and this vibration is the one that appears in the $ssp-$polarized spectrum shown in Figure 2.6. Methanol and ethanol orientational profiles are similarly shaped (Figure 2.7), both dominated by the orientation induced by alcohol molecules hydrogen-bonded to the silica surface. Closer inspection of the two orientational profiles, however, shows subtle differences. Methanol's orientational distribution at the interface is more sharply peaked at normal angle than ethanol's,

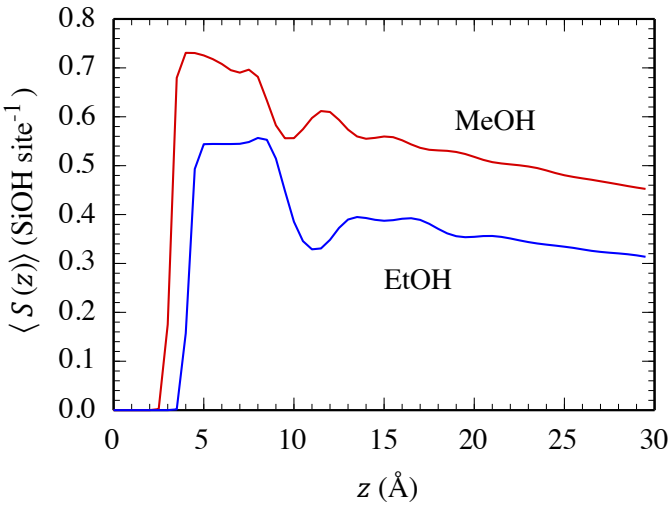

Figure 2.7: Cumulative orientational profiles of molecular vectors parallel to the methyl C_3 axis. See Equation 2.3.

resulting in a profile with larger magnitude despite a similar molecular density at the silica surface. Immediately next to the surface region, (z = 4-8 Å), the curves behave differently. Methanol molecules present in this region (the second sublayer) have negative net orientation, causing a decrease in $S(z)$. For ethanol, this region corresponds to the vacancy between the first and second density peaks that results in a short plateau in $S(z)$. Both curves decrease dramatically at the second density peak and gradually decay as the bulk region is approached, suggesting a weakly induced orientation of the molecules in a direction opposed to the orientation of the surface molecules. We next consider the molecular reorientation dynamics using orientational time correlation functions, $C_O(t)$, [155] defined by

$$C_O(t) = \frac{\langle \hat{u}(t) \cdot \hat{u}(0) \rangle}{\langle \hat{u}(0) \cdot \hat{u}(0) \rangle} \tag{2.4}$$

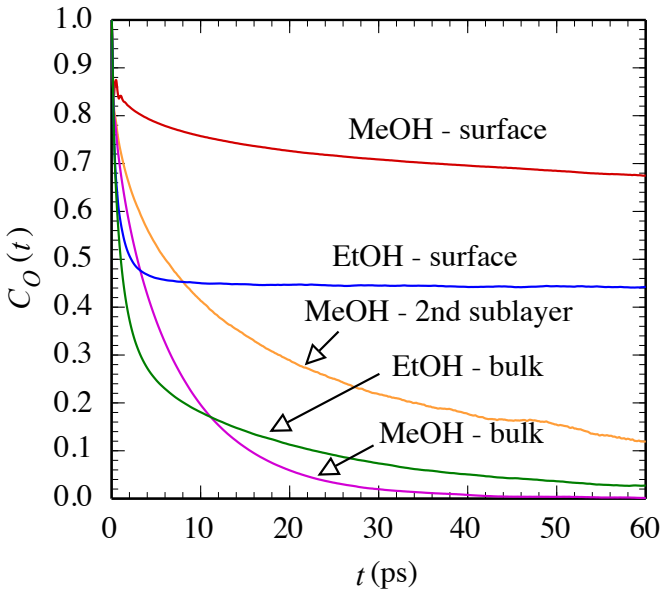

Figure 2.8: Orientational time correlation functions of the molecular vectors parallel to the methyl C_3 axis.

where $\hat{u}$ is a unit vector parallel to the molecular vector of interest. The ensemble average is calculated over all alcohol molecules and all time origins. Orientational correlation functions of vectors parallel to the methyl C_3 axis are shown in Figure 2.8. Alcohol molecules hydrogen-bonded to the silica surface exhibit the most limited orientational dynamics. The methanol O–CH_3 vector's orientational mobility is limited since most interfacial methanol act as both hydrogen-bond donor and acceptor with silica, essentially fixing the O–CH_3 vector. The relevant ethanol vector of interest is affixed to a geometrically similar structure but also able to rotate about the O–CH_2–CH_3 angle. This condition agrees with the shape of the surface ethanol CH_2–CH_3 orientational time correlation function and suggests rapid reorientation within a fixed cone. As expected,

methanol's second sublayer exhibits a faster reorientation than the hydrogen-bonded methanol at the silica surface but slower than that observed in bulk methanol. We now note that the partial cancelation of the interface-induced order (as shown in Figure 2.7) occurs by molecules in the second sublayer that exhibit rapid reorientation dynamics relative to alcohol molecules hydrogen-bonded to the silica surface. The molecular dynamics results with the methanol next to the perfect silica surface suggest that although the methanol molecules directly next to the strongly oriented monolayer are oppositely oriented, the contribution is not dramatic enough to explain the lack of the VSF signal. One possible explanation for this discrepancy is surface structural imperfections that might diminish the signal from the adsorbed monolayer immediately in contact with the silica. To simulate an imperfect silica surface we set the partial charges of every sixth silica site to zero and compared results with the findings previously described. We refer to these surfaces as "deactivated" and "active," respectively. Density profiles of the active and deactivated systems (Figure 2.9) differ in two main ways. As expected, the number of alcohol molecules hydrogen-bonded to the silica surface decreases, as can be seen in the first density peaks and the cumulative numbers in dotted curves. The second difference is a noticeable density increase in the region between the first and second density peaks. The cumulative number of alcohol molecules reveals that the reduced number of surface-bound alcohol molecules is approximately equal to the increased number of molecules present in the "second sublayer." Deactivated silica surfaces change the cumulative orientational profiles of methanol and ethanol systems (see Figure 2.10). In both systems the initial surface peak is lower due to fewer alcohols hydrogen-bonded

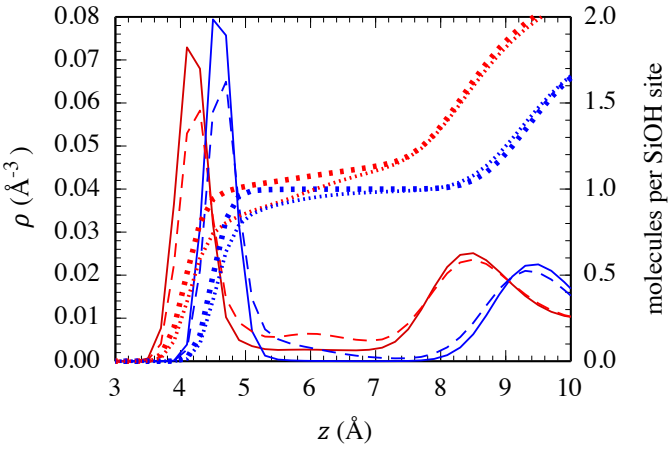

Figure 2.9: Density profiles of methanol (red) and ethanol (blue) at a silica surface. The solid lines are density profiles at an "active" surface. The dashed curves represent density profiles at a "deactivated" surface. Dotted curves (right axis) represent the integrated densities at "active" (large dots) and "deactivated" (small dots) silica surfaces (see text for explanation).

to the silica surface. More interestingly, we observe that the increased population in the second sublayer acts to further reduce the net orientation. The well-ordered alcohol molecules hydrogen-bonded to the silica surface induce an average orientation in this second sublayer that is opposite to the surface orientation. The impact of this second sublayer is more pronounced in methanol. Finally, as we go beyond the second sublayer region, in the methanol system, the difference between the active and deactivated systems extends toward the bulk, suggesting that disorder in the silica surface results in a greater reduction in the $ssp-$polarized VSF signal from the methyl stretch than in the ethanol system, whose "active" and "deactivated" cumulative orientational profiles converge quickly relative to the methanol system. Figure 2.11 supports the above interpretation by showing the orientational distributions of ethanol and methanol molecules

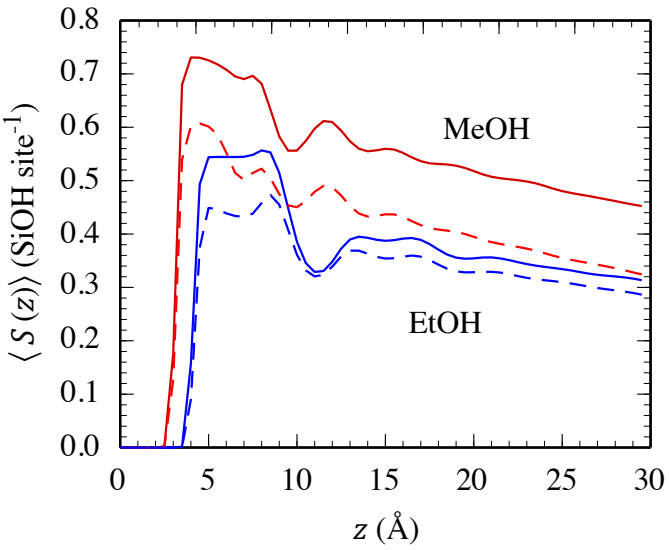

Figure 2.10: Cumulative orientational profile of methanol (red) and ethanol (blue) at a silica surface, see Equation 2.3. The solid curves are the corresponding profiles at an "active" surface; the dashed curves correspond to a "deactivated" surface (see text for explanation).

at the silica surface as a function of z. Each colored "ribbon" in Figure 2.11 represents the normalized orientational distribution of the molecules inside a 0.5 Å thick interval along the z-axis and is essentially an expansion of the $\langle \cos\theta \rangle$ term in Equation 2.3. We note that the molecular vectors reported in these orientational distributions are the vectors parallel to the methyl C_3 axis: O–CH_3 for methanol and CH_2–CH_3 for ethanol. Subsequent references to alcohol orientations refer to the orientation of these molecular vectors. The top left plot in Figure 2.11 shows the orientational distributions of ethanol at the "activated" surface. The region of near zero density in the "activated" ethanol system is noted by making the representative ribbons semitransparent. When the "deactivated" surface is introduced (Figure 2.11, top right) this region sees a rise in population

along with fewer interfacial hydrogen-bonded molecules: the ethanol second sublayer is now populated. This ethanol second sublayer displays a stronger induced inversion than in the methanol system (Figure 2.11, bottom panels). However, unlike the silica-methanol system the orientation of ethanol molecules in the second solvent layer (7.5 $< z <$ 9.0 Å, Figure 2.11, top right) is affected by this population increase. The second solvent layer reorients itself in response to the orientation of the newly populated second sublayer and the net effect is a cumulative orientational profile relatively similar to that of the "activated" system. This induced orientation of the ethanol second solvent layer explains the convergence of the cumulative orientational profiles of ethanol in Figure 2.10. The impact of surface defects on the second sublayer offers a possible explanation for the absence of the VSF response from the silica-liquid methanol interface. Surface imperfections increase the population of methanol molecules in the second sublayer. These molecules are orientationally opposed to the adsorbed molecules, resulting in a diminished signal. Surface defects also increase the population of ethanol molecules in the second sublayer except that in this case–but not for methanol– the ethanol molecules in the second solvent layer adopt an orientation that only partially cancels contributions from molecules in the second sublayer. This effect results in a persistent VSF response generated by the silica-ethanol system. Figure 2.11 describes these induced orientations that result in the different responses seen in Figure 2.10. In summary, deactivating the silica surface only affects the ethanol response in Figure 2.10 while $z <$ 10 Å. Deactivating the silica surface in the methanol system introduces a greater signal reduction, and these effects persist further into the bulk region. Deactivating surface silica sites also

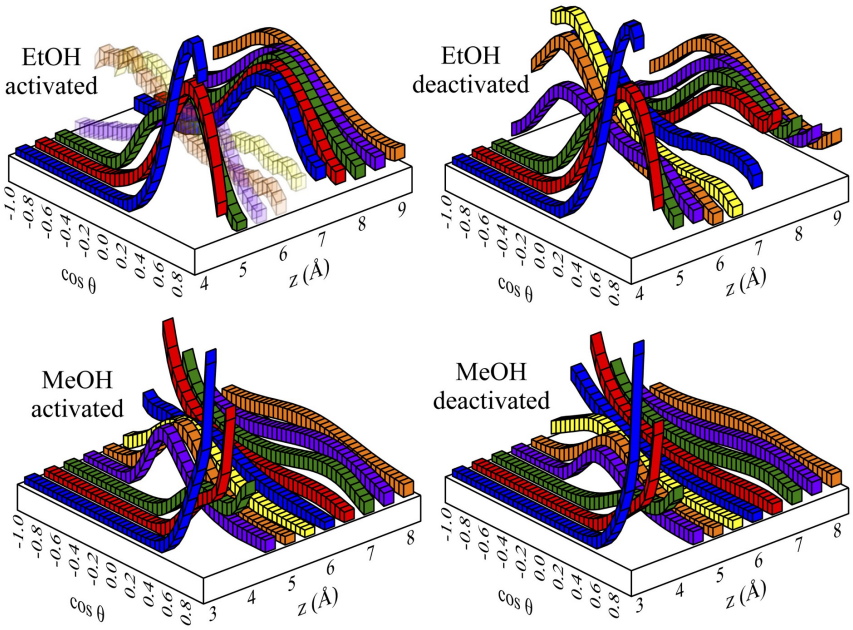

Figure 2.11: Normalized orientational distributions of the molecular vector parallel to the methyl C_3 axis. Ethanol (top) and methanol (bottom) at the "activated" (left) and "deactivated" (right) silica surface.

decreases the lifetime of alcohol-silica hydrogen bonds. Silica-alcohol lifetimes obtained by exponential fits of the slow decay parts of the hydrogen-bond lifetimes are given in Table 2.1. These lifetimes were obtained from fit to hydrogen-bond lifetime correlation functions calculated from trajectories of longer duration, as mentioned in the discussion of Figure 2.3 above. We believe that this reduction in lifetime is due to two factors. The deactivated silica sites reduce the probability of alcohol molecules hydrogen-bonding to two adjacent silica sites, making the same alcohol-silica interactions half as strong. This increases the likelihood of the molecule leaving the surface. The increased population of the second sublayer in turn increases the likelihood that the surface alcohol molecule will be replaced by a mobile alcohol molecule from this second sublayer. Tuning the surface hydroxyl composition of silica is difficult to accomplish experimentally in a controlled and quantitative manner. However, surface hydroxyl group density can be changed by using a different substrate. α-Alumina is another substrate commonly used in chromatographic applications and as a substrate for packed reactor beds. [155, 70, 42] The surface hydroxyl concentration for this metal oxide is estimated to be $\sim$2-3 times higher than for silica. [51, 231, 86] Furthermore, α-alumina is considered to have a basic surface compared to silica's acidic surface, meaning that the α-alumina's surface hydroxyl groups will accept even stronger hydrogen bonds from adjacent methanol (and other alcohols) relative to silica. Given the MD simulation predictions that higher -OH surface coverage should lead to a stronger SFG response from the liquid-solid interface, we measured the VSF response from a liquid alumina-methanol interface. Figure 2.12 shows that unlike the methanol-silica system (Figure 2.5), the methanol-alumina liquid-

solid interface shows a small but clearly distinguishable methanol VSF response. On the basis of insight gained from our experimental and computational studies, we believe this signal is due to the increased surface hydroxyl group density. This increased density of hydroxyl groups manifests itself by diminishing the population and order of the methanol second sublayer. Both of these effects are predicted to lead to an increased SFG signal. This experimental result also raises a host of interesting questions about solvent structure at hydroxyl-terminated surfaces characterized by different acid-base behaviors. Such questions will be the focus of future studies.

Table 2.1: Alcohol-Silica Hydrogen Bond Lifetimes (ns) for "Active" and "Deactivated" Silica Surfaces. (See Text for Explanation.)

donor–acceptor	active	deactivated
SiOH–MeOH	3.3	0.71
MeOH–SiOH	3.3	0.57
SiOH–EtOH	23	3.8
EtOH–SiOH	12	2.9

2.6 Conclusions

Liquid methanol and ethanol interact with a silica surface by similar means, and the silica surface induces a similar molecular order in both liquids. However, VSF spectroscopy experiments suggest that some nontrivial orientational differences between the two liquid-solid interfaces must exist. We use molecular dynamics simulations of the liquid methanol-silica and liquid ethanol-silica interfaces to compare molecular orientational behavior that may account for the differences in recorded VSF spectra. The

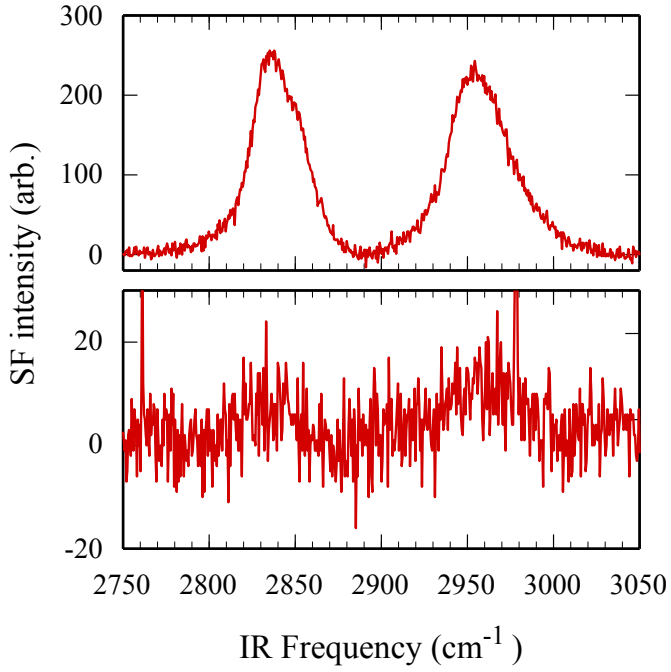

Figure 2.12: VSF spectra of the alumina-methanol solid-vapor (top) and solid-liquid (bottom) interfaces. Spectra were acquired under ssp polarization conditions.

single methyl group difference between the alcohols' alkyl groups results in different surface structures. Beyond the hydrogen-bonded interface, the aligned methyl tails do not create a large enough hydrophobic region to prevent the formation of a low-density second sublayer that aligns itself to partially cancel the VSF signal. This methanol interlayer has been previously reported [185] and considered as a possible cause of VSF signal attenuation at the methanol-silica surface. This second sublayer is not observed in MD simulations of the ethanol-silica system. In further studies we introduced defects into the simulated silica surface. This resulted in an ethanol-silica surface with a populated second sublayer region. In these simulations we found that this sublayer induced orientation of ethanol's second solvent layer, effectively replacing the average orientational anisotropy negated by molecules present in the second sublayer. The second solvent layer of methanol does not respond in this manner. We believe that the lack of induced order in methanol's second solvent layer is largely responsible for the methanol's absent VSF signal as compared to ethanol's weaker but still present VSF spectrum. The addition of surface defects both increased the population in the second sublayer region and increased the dynamics of the alcohol molecules at the interface.

Acknowledgments

Financial support from the National Science Foundation through Grants CHE-1026870 (RAW) and CHE-1363076 (IB) is acknowledged.

Chapter 3

Structure and dynamics of host/guest complexation at the liquid/liquid interface: Implications for inverse phase transfer catalysis

3.1 Introduction

Many chemical reactions of technological interest consist of reactants A and B, where A is located in aqueous solution and B is located in an adjacent, immiscible liquid phase. Since A and B must be in close proximity to react, (1) a reactant must either enter the adjacent phase to find the other species or (2) A and B may meet at the interface for the reaction to proceed. In some cases, workers use aggressive solvents to dissolve both species and avoid this transport-limited reaction. These solvents tend

to be expensive, toxic, and environmentally undesirable. This class of interfacial reactions includes many of interest in the pharmaceutical, agricultural, and material science fields and, due to the inherent environmental and economic benefits, solutions to this transport problem have emerged. [93, 166, 216] Most notably among these solutions, and of particular interest to this work, is the addition of a phase transfer catalyst, Q. This species forms a complex with one of the reactants and shuttles it to the interface or to the adjacent phase where the reaction occurs. Q disassociates from the reactive species, migrates to the other phase, and the cycle continues. In "normal" phase transfer catalysis (PTC), the catalyst Q carries the water-soluble reactant to an adjacent organic phase where it reacts. The alternative, reverse approach is commonly referred to as inverse phase transfer catalysis (IPTC). [129] In IPTC the catalyst complexes with a reactant in the organic phase, facilitating its transport to the aqueous phase for reaction. PTC reactions may also occur at the phase interface, with an interface-active catalyst facilitating contact between a reactant's active site and species in the adjacent immiscible phase. Reactions studied under IPTC include the isomerization of 4-allylanisole,1 hydrogenation of aldehydes, [143] and the hydroformylation and Wacker oxidation of olefins. [141, 142] Trifonov and Nikiforov investigated the S_N2 reaction of 1-bromooctane with CN^-, I^-, and SCN^- at the water/1-bromooctane interface. [217] The experimental results reported by Trifonov and Nikiforov are of particular theoretical interest, since a model S_N2 reaction of similar nature has been extensively studied in solvents of varying polarity and at the liquid/liquid interface by reactive molecular dynamics (MD) simulations. [14, 158]

Such S_N2 IPTC experiments utilize cyclodextrin (CD) molecules as the phase transfer catalyst, a class of cyclic oligomers that consists of α(1,4)-linked, D-glucopyranose monomers. The three main CD species include α, β, and γ-CD, indicating rings that contain six, seven, or eight glucose units, respectively. The CD molecule has a structure quite similar to a truncated cone, with primary hydroxyl groups (one from each glucose unit) circling the narrow opening and secondary hydroxyls (two per glucose unit) around the wider opening. An annotated snapshot of β-CD and a shorthand sketch representing its geometry are shown in Figure 3.1. The secondary hydroxyl groups around the β-CD's wide opening readily participate in inter-unit hydrogen bonding, adding to the molecule's stability. [214] In the experiment mentioned above, the rate of S_N2 reaction at the water/1-bromooctane was significantly increased by the addition of β-CD: faster than the reaction with no catalyst and faster than when α-CD was employed as catalyst. [217] Cyclodextrins have attracted considerable attention across many fields due to their stability, solubility, and ability to form interesting host-guest complexes due to CD's characteristic hydrophilic exterior and hydrophobic pore. [215, 8, 46] Several groups have used computer simulations to investigate the formation of host-guest complexes with CD molecules, including detailed studies that quantify the thermodynamic favorability of these complexes. [202, 203, 235, 87, 121] The β-CD variety receives considerable attention since the size of its cavity enables it to host many molecules of industrial and pharmaceutical interest. [141, 8, 125, 147, 122] The approximate dimensions of β-CD and its pore are noted in the sketch in Figure 3.1. CD host-guest complexes may impact reactions in ways other than simply facilitating transport. The CD host ef-

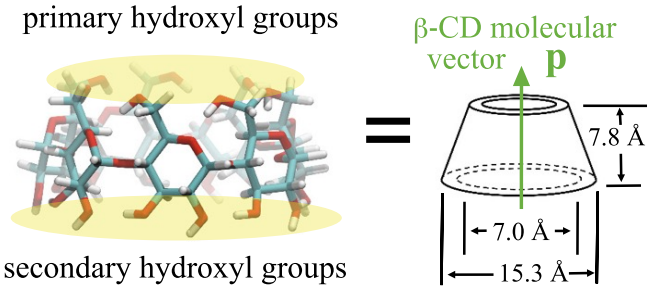

Figure 3.1: Left: β-CD, indicating the primary and secondary hydroxyl faces surrounding each opening. Right: a sketch of the β-CD molecule with approximate dimensions and the orientation and direction of the β-CD molecular vector, **p**.

fectively shields part of the guest molecule from reaction, which may be used to enhance selectivity. [46] In a similar fashion, CD molecules tethered to the inner walls of HPLC capillaries have demonstrated interesting separation capabilities, including the separation of pharmaceutical stereoisomers. [2] Open questions regarding the results presented by Trifonov and Nikiforov remain. How does the inclusion of β-CD increase the rate of interfacial reaction? Does β-CD only enhance transport of 1-bromooctane to the interfacial region? Or does the host/guest complex somehow increase the susceptibility of 1-bromooctane to nucleophilic attack?

Previous studies of a model S_N2 reaction in solvents of varying polarity, [14] at the water/organic interface, [158] and in the case of microhydration (1 - 5 water molecules near the reactive site) [156] reveal that the S_N2 reaction center is very sensitive to the presence of water. If the β-CD/1-bromooctane complex effectively "dehydrates" the reaction site, the reaction rate should increase. The purpose of the present work is to investigate the β-CD/1-bromooctane/water system using molecular dynam-

ics simulations and obtain molecular insight toward the IPTC mechanism. We recently reported molecular dynamics simulation results that surveyed a system similar to the Trifonov-Nikiforov experiment: β-CD at the water/1-bromobutane interface. [39] In our simulations, the β-CD molecule was quite surface active, its center of mass rarely more than 10 Å from the Gibbs dividing surface (GDS). The circular openings of the β-CD cavity were typically oriented parallel to the interface with approximately equal probability when β-CD was at the interface. The β-CD molecule was rotationally mobile, with a reorientational time constant of about 600 ps, considerably slower than when in bulk water, where $\tau_{rot} \approx 200$ ps. In the present work, we replace 1-bromobutane with 1-bromooctane to more precisely model the experimental system and consider several additional factors important for host/guest complexation at the liquid/liquid interface. The first aim of this work is to understand the molecular structure of the neat water/1-bromooctane liquid/liquid interface. To further understand this IPTC system, it is also imperative to understand the geometry and dynamics of the host/guest inclusion complexes. The move to a longer organic molecule complicates this analysis since, as guest, 1-bromooctane is longer than the β-CD pore: in this host/guest complex, presumably some of the guest molecules will protrude from the β-CD cavity. This suggests the third goal, understanding the impact of the β-CD host on the S_N2 reaction. In this S_N2 reaction, an aqueous nucleophile attacks the 1-bromooctane carbon atom that is bonded to the electron-withdrawing bromine atom. This alpha-carbon (αC) is the molecule's reactive site and is therefore of particular importance to the study of this system. The αC's geometry and dynamics while entering, leaving, and residing in the β-CD cavity

may provide evidence toward the exact utility and function of β-CD in the IPTC reaction. The rest of this manuscript is organized as follows: In section II we describe the details of our simulations and calculations used in the analysis. Section III presents the results and discusses this work in the context of understanding the S_N2 IPTC system. We begin by characterizing the liquid-liquid interface, then present equilibrium studies of β-CD in solution, and conclude by investigating dynamics and free energy involved in the host/guest complexes. In section IV we present summary and conclusions.

3.2 Systems and Methods

3.2.1 Force field and simulation details

Molecular dynamics simulations are performed using our in-house code. All intermolecular potentials are represented as the pairwise sum of Lennard-Jones and Coulomb terms,

$$U_{ij}(r) = \sum_{i<j} 4\epsilon_{ij} \left[\left(\frac{\sigma_{ij}}{r} \right)^{12} - \left(\frac{\sigma_{ij}}{r} \right)^{6} \right] + \frac{q_i q_j}{4\pi r \epsilon_0} \tag{3.1}$$

where r is the distance between atom centers i and j. Mixed interaction parameters are generated using standard Lorentz-Berthelot combining rules, $\sigma_{ij} = (\sigma_i + \sigma_j)/2$ and $\epsilon_{ij} = (\epsilon_i \epsilon_j)^{1/2}$. Water is modeled using a version of the flexible SPC force field [22] with intramolecular potentials as described by Kuchitsu and Morino. [109] The 1-bromooctane 'oil' phase consists of an OPLS united-atom alkane chain, terminated by

a bromine atom bearing a charge of -0.22e, which is balanced by an opposite change on the adjacent united-atom CH_2. [91, 149] We shall refer to this bromine-adjacent united-atom center as the alpha carbon (αC), as it represents the site of nucleophilic attack when 1-bromooctane participates in the S_N2 reaction mentioned in the introduction. The β-CD molecule is a fully-flexible, all-atom model with bonded and non-bonded parameters taken from the AMBER99SB-ILDN force field. [116] Several simulation geometries and systems are considered in this work. Liquid/liquid water/1-bromooctane interfacial systems are created by placing slabs of water and 1-bromooctane adjacent to each other in a rectangular box with the interface perpendicular to the z-axis. Periodic boundary conditions are applied in the x and y directions. Neat solvent environments use truncated octahedral symmetry. To study β-cyclodextrin in these systems, a β-CD molecule is inserted into the center of the simulation box and solvent molecules overlapping the β-CD are deleted. System compositions and sizes are summarized in Table 3.1. Assembled systems are briefly equilibrated to remove any high-energy, nonphysical configurations with short time steps ($\Delta t < 0.5$ fs). All starting configurations are equilibrated for a minimum of 1 ns of simulation time with a time step of 1 fs. Unless specified otherwise, data reported in this work is the ensemble average value over 20 ns of MD simulation time. These 20 ns consist of 20 independent starting configurations, each run for a 1 ns trajectory. Data was recorded every 20 steps, representing an average over 10^6 configurations. The equations of motion are integrated using the velocity Verlet algorithm [213] and all simulations are performed at 298K. All simulation snapshots shown in this work were generated using VMD. [81]

Table 3.1: Composition and size of simulated systems.

system	n_{BrOct}	$n_{\mathrm{H_2O}}$	$n_{\beta-\mathrm{CD}}$	x(Å)	y(Å)	z(Å)
A	1000	3944	0	62.58	62.58	300.0
B	380	0	1	60.0†	60.0†	60.0†
C	0	2111	1	50.0†	50.0†	50.0†
D	610	2400	1	50.0	50.0	300.0

† Dimensions refer to the cube that encloses systems with truncated octahedral symmetry.

3.2.2 Additional calculations

3.2.2.1 Solvents Spatial Distribution Functions

The radial distribution function $g(r)$ is useful for characterizing the spatial configuration of β-CD solvent systems where r is the distance between the β-CD center of mass and the solvent moiety of interest. This work will explore the β-CD host molecule at a level of detail where we must consider β-CD's non-spherical symmetry. As mentioned above, we approximate β-CD as a truncated cone (see Figure 3.1) and will use the cylindrical symmetry of this simplified description to help clarify our spatial analyses. In addition to $g(r)$, we also consider the two-dimensional pair correlation function $g(r,\theta)$ [201]

$$g(r,\theta) = \frac{1}{\eta_c}\left\langle \sum_{i=1}^{N} \delta(r - r_i)\cdot\delta(\theta - \theta_i) \right\rangle \tag{3.2}$$

where δ is the Dirac delta function, θ_i is the angle defined by the β-CD molecular vector $\mathbf{p}$ and the vector that begins at the β-CD center of mass and passes through the ith solvent particle of interest and r_i is the distance between this particle and the β-CD

center of mass. The normalization constant η_c is chosen so that the equivalent volume at bulk density has a value $g(r,\theta) = 1$. The β-CD molecular vector $\hat{\mathbf{p}}$ is a unit vector pointing in the direction from the center of mass of the 14 secondary hydroxyl oxygens (bottom base of the cone, see Figure 3.1) to the center of the primary hydroxyl face. The "center" of the primary face is the center of mass of the hexopyranose ethers and the adjacent carbons (14 atoms, 2 on each glucose ring) on the primary hydroxyl side of the β-CD molecule. $g(r,\theta)$ provides information about the orientational preference of solvent molecules around the perimeter of the β-CD molecule as well as a cross sectional view of the pore and volume occupied by the β-CD itself. To obtain complementary information we also consider the spatial distribution function $g(m,n)$. We define $\hat{\mathbf{m}}$ and $\hat{\mathbf{n}}$ as the unit vectors orthogonal to $\hat{\mathbf{p}}$ with $\hat{\mathbf{m}}$ passing through the center of mass of one of the β-CD glucose units. $g(m,n)$ represents the distribution of solvent particles relative to the β-CD center of mass, where m and n are values along the cartesian axes $\hat{\mathbf{m}}$ and $\hat{\mathbf{n}}$. This distribution $g(m,n)$ includes all particles located at $\pm$ 8 Å from the $\hat{\mathbf{m}}$-$\hat{\mathbf{n}}$ plane that passes through the β-CD center of mass and may be formally defined as

$$g(m,n) = \frac{1}{\eta_c}\left\langle \sum_{i=1}^{N} H\Big(8\mathring{A} - |\mathbf{r}_i \cdot \hat{\mathbf{p}}|\Big) \cdot \delta\Big(m - (\mathbf{r}_i \cdot \hat{\mathbf{m}})\Big) \cdot \delta\Big(n - (\mathbf{r}_i \cdot \hat{\mathbf{n}})\Big) \right\rangle \tag{3.3}$$

where H is the Heaviside step function. Cartoon sketches that illustrate the volume described by $g(m,n)$ for β-CD are included as Figures B.1 and B.2 in Appendix B.

3.2.2.2 Host/Guest Potential of Mean Force

The energetic favorability of a host/guest complex may be described quantitatively by considering the reversible work required to remove the guest from the host. We define a "reaction coordinate", γ, as the distance between the center of masses of the 1-bromooctane guest and β-CD host, projected onto the $\hat{\mathbf{p}}$ axis

$$\gamma = \left(\mathbf{r}_{\mathrm{BrOct}} - \mathbf{r}_{\beta-\mathrm{CD}}\right) \cdot \hat{\mathbf{p}} \tag{3.4}$$

where the positions $\mathbf{r}$ refer to the respective centers of mass. With this definition the β-CD center of mass is defined to be the origin of the γ-axis, i.e. when $\gamma = 0$ Å the host and tagged molecule's centers of mass overlap exactly on the p-axis. Because $\hat{\mathbf{p}}$ points toward the primary hydroxyl opening of the β-CD, $\gamma > 0$ indicates that the tagged center of mass is on the primary hydroxyl side of the β-CD center of mass and $\gamma < 0$ indicates that the tagged center of mass is on the secondary side. The local free energy of the guest molecule along the $\hat{\mathbf{p}}$ axis is given by

$$A(\gamma) = -k_B T \ln P(\gamma), P(\gamma) = \langle \delta(\gamma - \gamma\prime) \rangle \tag{3.5}$$

where k_B is the Boltzmann constant and $\gamma\prime$ is the instantaneous value of γ. $P(\gamma)$ is the probability of the host/guest complex to exist with center of mass separation γ. The reversible work required to change the host/guest center of mass distance from γ_1 to γ_2 would be $A(\gamma_1) - A(\gamma_2)$. To improve statistical sampling, the umbrella sampling

method is employed. [1, 34, 174] We construct a potential of mean force (PMF) curve describing the host/guest complex over the entire interval of interest by dividing the interval into K overlapping lamellae perpendicular to $\hat{\mathbf{p}}$. The PMF in each lamella is given by

$$A_k(\gamma) = -k_B T \ln P_k(\gamma) \tag{3.6}$$

where $P_k(\gamma)$ is the γ probability distribution within lamella k. In this work the lamella are 2.0 Å wide and overlap by 0.5 Å unless mentioned otherwise. γ is constrained to the lamella's desired range by a window potential (equal to 0 when γ within range and rises rapidly for γ values beyond the limits of the window) applied to the host and guest centers of mass through the course of all umbrella sampling trajectories. A similar study by Zheng et. al. constrained the host and guest centers of mass and also fixed the cyclodextrin position in simulation space by applying additional constraints to a subset of its atoms. [238] In this work, the only constraining force during the umbrella sampling is the window potential applied to the centers of mass; a brief derivation of these forces is included in Appendix B. The series of $A_k(\gamma)$ segments were combined by minimizing the distance between their overlapping regions to assemble a complete free energy profile over the region of interest. [110, 105] To accelerate the exploration of γ-space within a given lamella and improve sampling statistics, a biasing potential could be applied, if needed, to the centers of mass that define γ, modifying the host-guest interaction energy as

$$U^b_{\text{host/guest}} = U_{\text{host/guest}} - U_{\text{bias}}(\gamma) \tag{3.7}$$

where $U_{\text{bias}}(\gamma)$ was a quadratic function of γ so that the biasing potential approximated $A_k(\gamma)$. The free energy profile within a lamella with applied bias was then calculated as [1]

$$A_k^b(\gamma) = -k_B T \ln P_k(\gamma) + U_{\text{bias}}(\gamma) \tag{3.8}$$

3.3 Results and Discussion

3.3.1 The Neat Liquid/Liquid Interface

Figure 3.2a is a representative snapshot of the 1-bromooctane/water interface, highlighting that, in all biphasic simulations presented in this work, the simulation z-axis is the vector normal to the liquid/liquid interface. Although the two liquids are mostly immiscible, protrusions of water into the organic phase (and the organic into water, to a lesser extent) can be seen upon close inspection. These fluctuations and protrusions are typical of the liquid/liquid interface and the study of these fluctuations continues to attract significant attention. Theoretical studies of transport across the liquid/liquid interface suggest that these protrusions play a significant role. [107, 99] A density profile of the liquid/liquid interface is shown in Figure 3.2b. In all simulations with a liquid/liquid interface present, the Gibbs dividing surface (GDS, the position where the density of water is approximately half its bulk value) is located at $z = 0$. The positive direction is defined to be toward the organic phase and the water phase water is mostly located at $z < 0$ Å. The density profile of 1-bromooctane oscillates as it moves away from the liquid/liquid interface, potentially indicating surface layering.

Data presented for the neat liquid/liquid interface is the average of 800,000 configurations obtained during 8 ns of simulation time. The solid red and dashed purple curves in Figure 3.2b, representing the 1-bromooctane center of mass and α-carbon respectively, noticeably differ at the liquid/liquid interface. These features suggest that the interface is inducing order in the organic phase: the αC is generally closer to the aqueous phase than the 1-bromooctane's center of mass, resulting in a slight but well-defined reduction in αC density just beyond the GDS. This induced orientation may be compared with behavior at the 1-bromooctane liquid/vapor interface ($z \approx 75$ Å), where the center of mass density increases toward the interface, suggesting that the alkane tails preferentially aggregate near the liquid/vapor surface, immediately following an αC peak. In contrast, water monotonically approaches its bulk value from both the vapor/liquid water interface and the liquid/liquid interface when the density profile is examined at the scale presented by Figure 3.2b. To gain additional molecular insight into the liquid/liquid interface, we consider the orientation of the solvent molecules as a function of their position along the z-axis. The orientational distribution profile $P(\theta)$ for the water dipole vector is presented in Figure 3.3. θ is the angle between the dipole vector and a vector parallel to the z-axis and pointing toward the 1-bromooctane phase. In a bulk liquid, random orientation of molecules is expected when viewing a sample volume larger than a few molecular lengths. At the 1-bromooctane/water interface, water exhibits a definite orientational preference, with its dipole being mostly parallel to the interface. In Figure 3.3, the broad peak centered at $\cos\theta \approx 0$ flattens when considering distributions further from the interface and this interfacial orientational distribution is

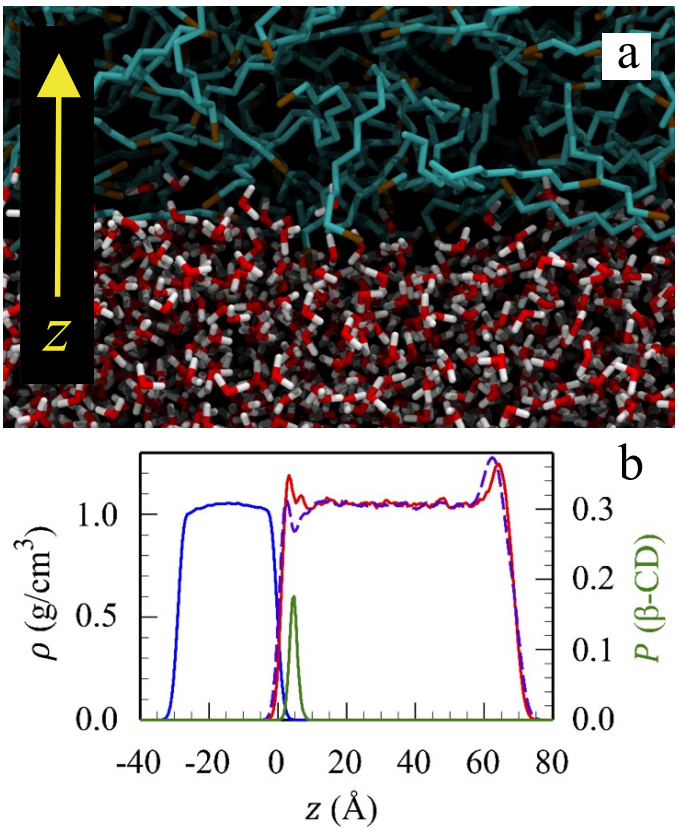

Figure 3.2: (a) Simulation snapshot of the 1-bromooctane/water interface. (b) Density profiles of water (blue), 1-bromooctane center of mass (red) and 1-bromooctane α-carbon (purple) in the neat solvent system. The location of β-CD's center of mass when at the liquid/liquid interface is shown as a probability distribution (green) on the right axis.

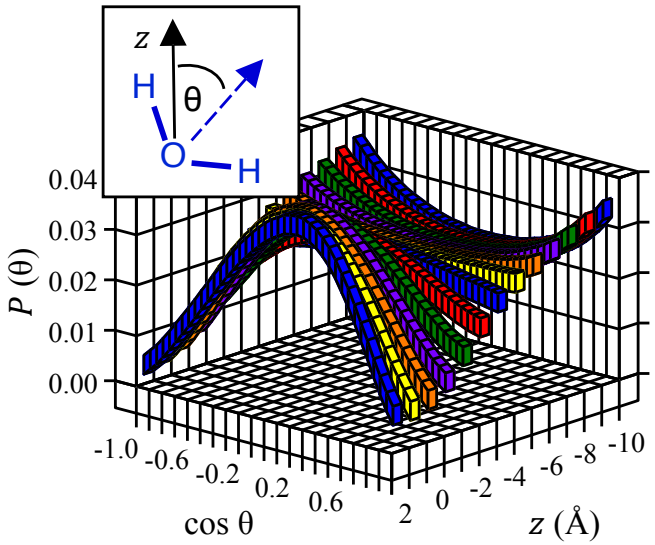

Figure 3.3: Orientational profile of the water dipole vector. θ is the angle between the water dipole vector and the vector normal to the interface (inset).

then seen to invert when approaching z = -10 Å. This inverted distribution suggests that the preferential orientation of water molecules at the interface induces further orientation in subsequent solvent layers. Figure 3.4 presents a similar analysis of the 1-bromooctane phase but uses four separate vectors to describe the orientation of these larger organic molecules. Figure 3.4a shows the orientational distribution profile of the molecular vector which points from the α-carbon to the bromine atom, describing the orientation of the charge-bearing head group and S_N2 reactive site. At the interface, the αC→Br vector is preferentially oriented toward the water phase. This preferred orientation persists for only a few angstroms into the organic phase. The distribution of the αC→Br vector is flat at a distance of 10 Å from the interface, indicating a random distribution. Figure 3.4b considers the vector defined by the fifth and fourth carbons in

the alkyl chain, C5→C4, which describes the center of the chain. The C5→C4 orientational distribution at the interface contains a broad peak centered at cos $\theta = 0.2$, the vector points slightly away from the interface toward the organic phase. Next, Figure 3.4c focuses on the end of the alkyl tail, the vector defined by C8→C7. At the interface the alkyl tail mostly lies parallel to the interface or points toward the organic phase and also displays a random orientation when $\approx$ 10 Å into the organic phase. Figure 3.4d shows the orientational preferences demonstrated by the entire alkane chain, defined by the C8→ αC vector. Orientational distributions of 1-bromooctane carbon chain orientations show a sharp peak centered at cos $\theta \approx 0$ when at the interface, suggesting that the 1-bromooctane molecules lie parallel to the liquid/liquid interface when in the interfacial region. Like the other molecular vectors studied by Figure 3.4, this orientational preference disappears when about 10 Å from the interface where random, bulk orientational behavior is reported. The orientation of 1-bromooctane molecules as a function of position on the z-axis is a useful parameter to consider when investigating the role of β-CD in IPTC. It has been reported by several groups that the β-CD molecule orients its cavity openings parallel to the interface when at the liquid/liquid interface and exhibits random orientation in the bulk. [203, 39] The combination of these results suggests a few mechanistic possibilities toward the IPTC utility of β-CD. The orientation of a β-CD/1-bromooctane host/guest complex at the interface may orient the reactive group toward the aqueous nucleophilic reactants. Solvent molecule orientation does not appear to favor insertion and exchange of interfacial 1-bromooctane guest molecules at the interface, since the 1-bromooctane molecules are predominantly perpendicular to

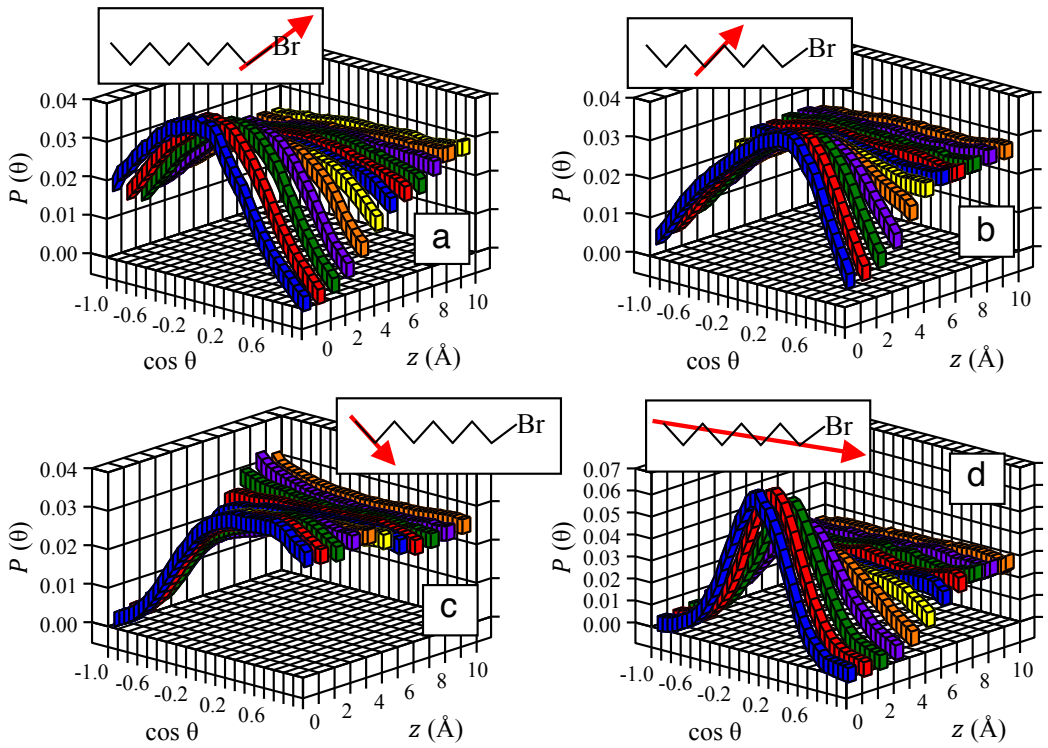

Figure 3.4: Orientational profile of 1-bromooctane molecular vectors defined by α-carbon$\rightarrow$Br (a), carbon 4$\rightarrow$carbon 5 (b), carbon 8$\rightarrow$carbon 7 (c), and carbon 8$\rightarrow\alpha$-carbon (d) versus the z-axis, normal to the interface. Inset cartoons illustrate the respective vectors.

and located outside of the β-CD truncated cone. However, β-CD at the interface may be positioned to accept or exchange 1-bromooctane guest molecules from the more disordered region toward the bulk organic. The actual energetics of host/guest exchange at the interface will be quantified later in this work. The characteristic interfacial orientation and cylindrical symmetry of the β-CD host suggest that the geometric parameter of interest when describing the interfacial solvent molecules in this system is the orientation of the 1-bromooctane alkyl chain, parallel or perpendicular to the liquid/liquid interface. We note that through these simulations no significant changes to the average 1-bromooctane radius of gyration [$R_g^2 = \frac{1}{N}\sum_{k=1}^{N}(\mathbf{r}_k - \langle\mathbf{r}\rangle)^2$] along the z-axis were observed, suggesting that the organic solvent molecules remain in similar intramolecular conformations whether near the interface or in bulk conditions.

3.3.2 β-Cyclodextrin in bulk solvents and at the liquid/liquid interface

To understand the behavior of β-CD at the interface, we first consider as a reference the solvation of β-CD in bulk water and in bulk 1-bromooctane. The solid blue curve in Figure 3.5a is $g(r)$, the radial distribution function (RDF) where r is the distance between the β-CD center of mass and the surrounding waters (oxygen). This curve agrees with previously published work, finding that water molecules are present in the pore but exhibit an affinity for the inner wall of the β-CD and are not likely to be located at the β-CD center of mass. The valley between $r \approx 4$ Å and $r \approx 8$ Å is the approximate region of space occupied by β-CD. The dashed blue line in Figure 3.5a is

the integral of the distribution function:

$$n(r) = \int_0^r 4\pi r^2 \rho g(r) dr \tag{3.9}$$

where $n(r)$ is the number of water molecules contained within a sphere of radius r centered at the β-CD center of mass and ρ is the bulk water density. From this integral we determine that between 7 and 8 water molecules reside within the β-CD pore, depending on the choice of r, in good agreement with previously reported experimental and simulation results. [115, 211, 112, 73, 33] To further understand the orientation of water molecules in and around the solvated β-CD, we present the water center of mass density in two dimensions, shown in Figures 3.5b and 3.5c. (Details of these spatial distribution functions are discussed in section II B.) In Figure 3.5b, which presents $g(m, n)$, the β-CD C_7 symmetry axis is clearly visible. Water molecules present in the pore are grouped into seven major clusters that correspond to the approximate location of the inward-pointing glycosidic ethers, characteristic of cyclodextrin molecules. The ability of these bridging ethers to accept hydrogen bonds from pore water molecules was detailed previously by Heine et. al. [73] We also note the 7-fold symmetry of water density on the outer surface of the β-CD molecule. The regions of high density lie approximately along the same radial axes as the high water density nodes within the β-CD pore. Figure 3.5c presents $g(r, \theta)$, where the angle θ is defined by the β-CD molecular vector $\hat{\mathbf{p}}$ (see Figure 3.1) and the vector that begins at the β-CD center of mass and ends at the water molecule's center of mass (see Section II A.) In these plots of $g(r, \theta)$ we take

$r < 12$ Å and $-\pi < \theta < \pi$. Because this view is perpendicular to the axis of cylindrical symmetry $\hat{\mathbf{p}}$, the region of water vacancy in the spatial distribution (SDF) reveals the torus-like volume occupied by the β-CD molecule. Along the outside of this region, the highest water density is clearly located along the inner wall of the β-CD pore, in agreement with the RDF in Figure 3.5a. A higher water-molecule density outlines the perimeter of the β-CD cross section, also in agreement with Figure 3.5a, and a region of higher density exists at $\theta \approx 15^\circ$ on the outside of the β-CD molecule, the approximate location of the bridging and hexopyranose (glucose ring) ethers. The hexopyrose ethers are assigned a smaller negative charge than the bridging ethers in most β-CD force fields, but the hexopyranose ether group is more sterically accessible to water molecules outside the β-CD molecule. These SDFs are particularly useful when considering a proper geometrical definition of the β-CD pore. For β-CD in the bulk organic solvent, we first present in Figure 3.6 several pair distribution functions, $g(r)$. In these plots, r represents the distance between the β-CD center of mass and several atomic sites on the 1-bromoctane molecule, since 1-bromooctane, is much larger in size than water. We present these distributions as a stacked plot where each pair distribution function is offset by adding 2 to the dimensionless value of $g(r)$. The red curve represents the atom center at the end of the alkane tail (C8) and thus $r = |\mathbf{r}_{\beta\text{-CD,CoM}} - \mathbf{r}_{\text{C8}}|$. This C8 RDF shows a very large peak, with a maximum value of more than 5, at $r \approx 2$ Å, indicating that the alkane tails of the 1-bromooctane have a very high density in the β-CD pore. The location of C8 within the 1-bromooctane molecule is shown in the cartoon on the right of Figure 3.6 as the red circle. The green curve (and green circle) represents the

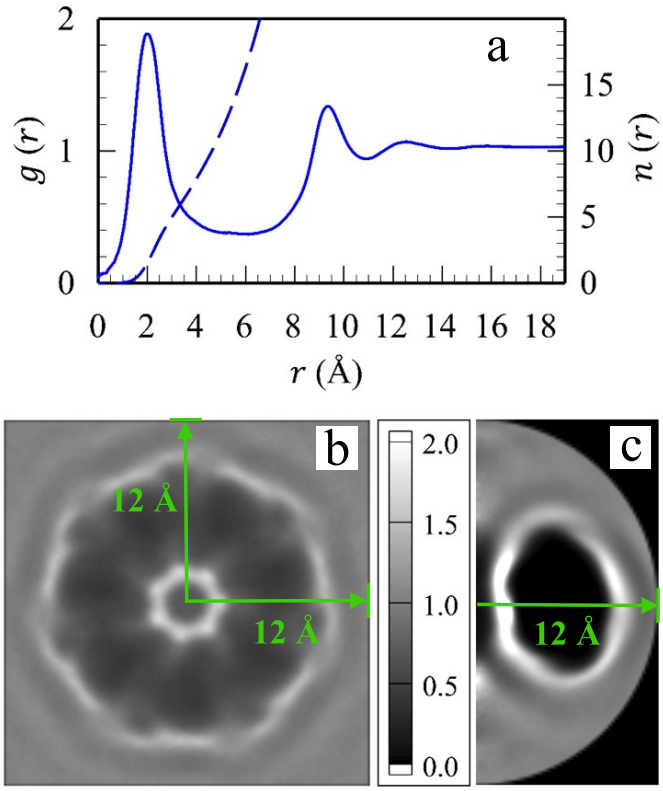

Figure 3.5: β-CD center of mass–water center of mass pair distribution functions: (a) $g(r)$, (b) $g(m, n)$, and (c) $g(r, \theta)$.

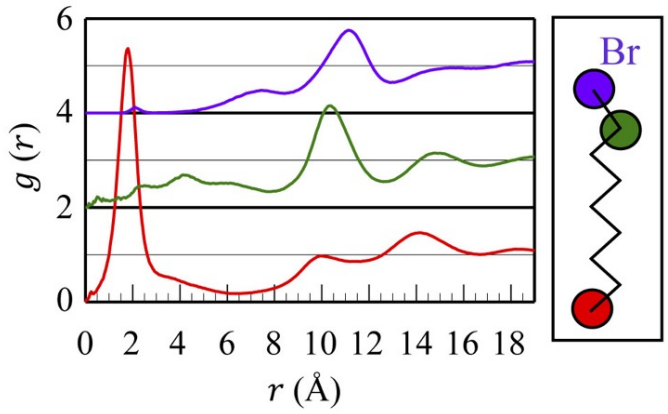

Figure 3.6: β-CD in 1-bromooctane, β-CD center of mass–1-bromooctane moiety pair distribution functions for C8 (red), αC (green), and bromine (purple). For clarity, the green abd purple curves were offset by adding 2 and 4, respectively, to the valuse of $g(r)$.

α-carbon (αC). This atom center is bonded to the bromine atom and is of particular importance since it is the site for the S_N2 reaction, the location of nucleophilic attack. The αC has little presence within the β-CD pore, with its first density peak at $r \approx 6$ Å and highest density at $r \approx 10$ Å. The bromine atom center, purple in Figure 3.6, is even less likely to be present in the pore than the αC. The RDFs in Figure 3.6 provide an initial insight into the behavior of the β-CD/1-bromooctane host/guest complex: the alkane tail appears to dock within the β-CD molecule leaving the reactive site, the αC, outside of the pore. With this general understanding of β-CD/1-bromooctane solvation, we further consider C8, the IPTC reactant's docking moiety, and the αC, the reactive site. Figure 3.7 displays spatial distribution functions that provide more detailed information. Figure 3.7a shows the $g(m, n)$, SDF of β-CD and the C8 atom center. C8's function as guest moiety in the β-CD pore is the most notable feature of

the SDF. We note here the symmetry of this density ring. The C8 guest does not appear to preferentially reside at any angular positions, quite unlike the behavior of water seen in Figure 3.5b. Density "nodes" as seen in the β-CD pore region in Figure 3.5b might indicate the presence of polar guest moieties and the absence of these nodes in Figure 3.7a suggests the entropic favorability of the 1-bromooctane guests versus water. In the C8 $g(r,\theta)$ SDF, Figure 3.7b, the C8 guest density peak is intense and localized, reaching a maximum value of 14 (well beyond the maximum value of 4.0 in the Figure 3.7 SDFs.) This peak is also considerably larger than that of C8 in β-CD's pore in Figure 3.6 because $g(r)$ averages over all θ values. This strong peak suggests that the 1-bromooctane C8 certainly has a preferred location within the β-CD pore. When we examined the SDFs representing the αC positions (Figures 3.7c,d), the αC was generally found to be less present in the pore, as expected. The $g(r,\theta)$ SDF (Figure 3.7d) suggests that the 1-bromooctane shows little preference as to which side of the β-CD molecule it enters when forming the host/guest complex because regions of high αC density are present at both the primary and secondary openings of the β-CD molecule. Understanding the behavior of β-CD in neat solvents establishes a baseline from which the behavior of β-CD at the liquid/liquid interface can be examined. The green curve in Figure 3.2b of section 3.1 is a probability distribution of the β-CD center-of-mass z location. The peak at 4.5 Å relative to the GDS indicates that the β-CD is surface active, with a tendency to be on the organic side of the interface. The surface activity of β-CD is due, in part, to the hydrogen bonding between the hydroxyl groups of one of the two pore faces and the aqueous phase, as discussed by Wipff and coworkers for different liquid/liquid

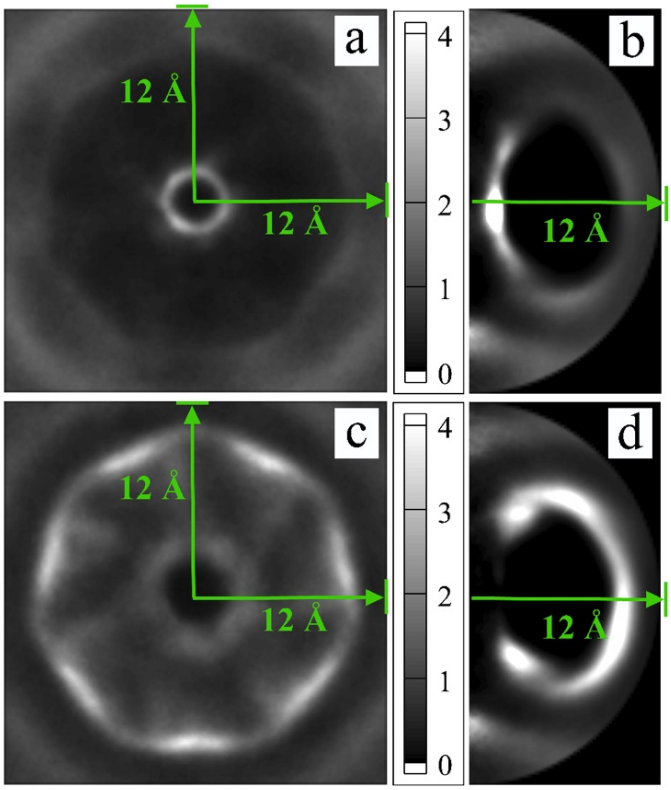

Figure 3.7: Spatial distribution functions for (a,b) β-CD center of mass–C8 [(a) $g(m,n)$ and (b) $g(r,\theta)$] and (c,d) β-CD center of mass–α-C [(c) $g(m,n)$ and (d) $g(r,\theta)$].

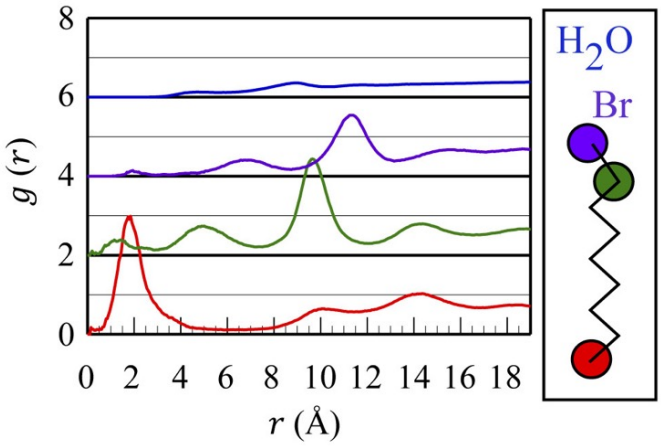

Figure 3.8: β-CD center of mass–solvent radial distribution functions for β-CD at the liquid/liquid interface. Shown are water (blue) and the 1-bromooctane bromine atom (purple), αC (green), and C8 (red). For clarity, the green, purple, and blue curves are offset by values of 2, 4, and 6, respectively, on the $g(r)$ axis.

systems. [202] Figure 3.8 shows pair distribution functions relative to the β-CD center of mass at the liquid/liquid interface [the g(r) curves are again offset by intervals of 2 for clarity]. The 1-bromooctane curves look similar in shape to those calculated in bulk 1-bromooctane (Figure 3.6) while their amplitudes (most notably as r approaches the bulk) are reduced by approximately a factor of 2 from the neat solvent values because of the geometry of the interfacial system. However, the likelihood of the β-CD molecule hosting a 1-bromooctane molecule remains similar to that in bulk 1-bromooctane. The integral of the RDF of the C8 atom center (red curve, Figure 3.8) through 4 Å only decreases from 1.1 (in Figure 3.6) to 0.9 at the liquid/liquid interface. We also note that the first peaks of the 1-bromooctane atom centers have shifted closer to $r = 0$ Å, indicating that the guest molecule is located further within the pore. During the course of these simulations, the 1-bromooctane guest molecule positions itself deeper within

the pore as the surrounding solvent polarity increases, a phenomenon that is discussed further in the next section. We conclude this section by providing additional detail on the pore guest populations. As mentioned earlier, our definition of the β-CD pore is cylindrical, as is clear from the SDF plots in Figures 3.5 and 3.7. Figure 3.9a contains a population histogram of water molecules (blue bars in Figure 3.9) within the β-CD pore when β-CD is in bulk water. The population distribution is approximately Gaussian in shape, with a maximum at nine water molecules in the pore. This peak is slightly higher than our previously reported value [39] and may be attributed to the less restrictive definition of the β-CD pore as a cylinder versus the spherical definition used in earlier work. Figure 3.9b shows the pore populations of selected 1-bromooctane moieties in bulk 1-bromooctane. This data complements the previous discussion in Figures 3.6 and 3.7 where the C8 tail (red bars in Figure 3.9) resides in the β-CD pore. Whereas one or two C8 moieties are likely to occupy the pore, the αC reactive site (green bars, Figure 3.9) is much less likely to do so, also in agreement with Figures 3.6 and 3.7. Figure 3.9c contains the pore population distributions at the liquid/liquid interface. One organic guest is likely to occupy the pore (if we simplify the definition by observing the C8 moiety), and the water population is greatly diminished, with rarely more than 1 water molecule in the pore region. The data described above and our previous MD studies of a model S_N2 reaction at interfaces, [14, 156] suggest that the presence (or absence) of water and β-CD hydroxyl groups in the vicinity of the αC should have a large impact on the reaction barrier. The precise locations of the reactive site relative to the β-CD and surrounding water molecules in the IPTC system is helpful for quantifying the β-CD

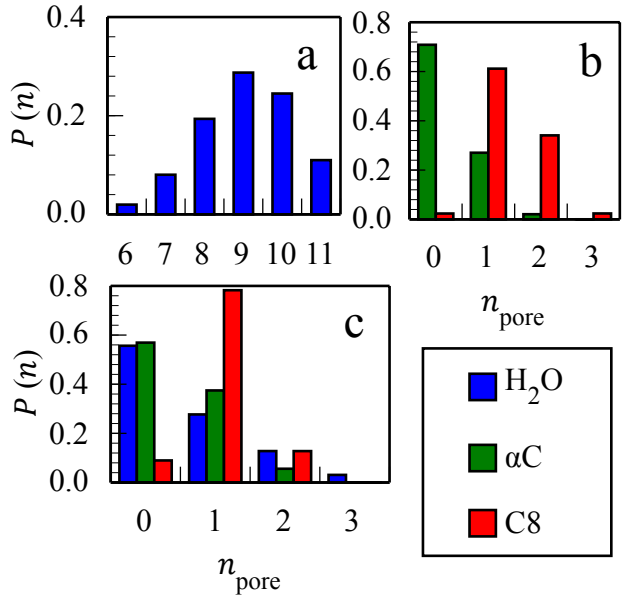

Figure 3.9: Pore guest probabilities when β-CD is in (a) neat water, (b) neat 1-bromooctane, and (c) at the liquid/liquid interface.

catalyst's potential enhancement of the S_N2 reaction rate.

3.3.3 Host/Guest Energetics and Dynamics

We now consider the 1-bromooctane/β-CD host/guest complex. In the preceding section the preferred orientation of 1-bromooctane molecules within the β-CD cavity was made clear: The alkane tail resides within the β-CD pore and the αC reactive site is near one of the pore openings. To act as a catalyst in the IPTC system, the host molecule must have an affinity for the guest reagent but not such an affinity that the guest molecule remains permanently in the cavity after reaction, "poisoning" the catalyst. The umbrella sampling technique described in Section II is used to determine the potential of mean force for moving a tagged 1-bromooctane molecule through the β-CD

pore for several solvent systems to quantify both the host-guest affinity and preferred docking position. We refer to the tracked 1-bromooctane molecule as "tagged" as opposed to "guest" since the molecule's position as β-CD's guest is likely to be occupied by another 1-bromooctane once the tagged molecule leaves the pore. PMF calculations and the window constraints as described in Section 2.2 reference the tagged 1-bromooctane's center of mass. This site is selected since constraint forces applied to a molecule's center of mass minimize disturbance to the molecular orientation. However, the atom center of physical interest in this work is the site of nucleophilic attack, the αC, not the center of mass, a virtual site. The curves in Figure 3.10 report the PMF along the αC projection onto the p-axis, $\gamma_{\alpha\mathrm{C}}$, a reaction coordinate that is much more relevant to the IPTC system than the center of mass. This coordinate is defined similarly to the definition given in equation 3.4 by

$$\gamma_{\alpha\mathrm{C}} = \langle (\mathbf{r}_{\alpha\mathrm{C}} - \mathbf{r}_{\beta\text{-CD}}) \cdot \hat{\mathbf{p}} \rangle_{\mathrm{bin}} \tag{3.10}$$

Note that, because the windows are defined with respect to the center of mass of 1-bromooctane, values of $\gamma_{\alpha\mathrm{C}}$ in this equation are determined by averaging the observed values in each bin. The tagged 1-bromooctane molecule may occupy the guest position in two distinct states, with the C8$\rightarrow$ αC vector pointing either in the direction of the smaller, primary hydroxyl opening or in the direction of the larger, secondary hydroxyl opening. Nomenclature introduced by Zheng et. al. [238] demarks the β-CD molecule as Δ, with the base of the triangle representing the larger pore opening, and the guest orientation defined as either $\uparrow$ or $\downarrow$, with the arrow's head indicating end of the tagged

molecule that contains the bromine atom and the αC reactive site. In neat solvent systems two such states are possible and we implement the shorthand $\Delta :\uparrow$ for "primary" and $\Delta :\downarrow$ for "secondary." These two guest states are illustrated by the cartoons in Figure 3.10a. The color convention of blue = $\Delta :\uparrow$ = primary and red = $\Delta :\downarrow$ = secondary is maintained for all PMF curves presented in this work. The range spanned by each PMF curve in Figure 3.10 represents the region of $\gamma_{\alpha C}$ where the tagged 1-bromooctane molecule remains in the specified state. Outside of the range of the presented curve, the tagged molecule either adopts a random orientation, $\langle(\mathbf{r}_{\alpha C} - \mathbf{r}_{C8}) \cdot \hat{\mathbf{p}}\rangle \approx 0$, or the tagged molecule switches to the other state (e.g., $\Delta :\uparrow \rightarrow \Delta :\downarrow$) In the former case, the tagged molecule is outside the influence of the β-CD molecule. In the former case, the "flipped" tagged molecule follows the PMF of its newly adopted state. We note that the $\Delta :\uparrow$ and $\Delta :\downarrow$ systems represent different systems because the reactive site of the 1-bromooctane guest interacts with a different pore opening in each case, thus illustrating the differences between the two faces. Figure 3.10b shows the host/guest PMF in vacuum. Both the primary and secondary orientations look energetically and spatially similar, with the 1-bromooctane reaching minima at $\gamma_{\alpha C} \approx \pm$ 4 Å, depending on whether the tagged molecule approaches from the primary or secondary side. In these PMF calculations, it is clear that the 1-bromooctane molecule preferentially enters the β-CD pore alkane-tail first with the charged αC–Br head group residing near the hydroxyl groups located at each pore opening. The tagged molecule will invert to achieve this desired orientation when it moves to the other side of the β-CD molecule but this reorientation dynamic is limited while inside the cavity. When β-CD is in water (Figure 3.10c), the PMFs look

similar to the one in vacuum, with the longer-ranged electrostatic interactions somewhat dampened by the presence of the polar solvent. The similarity of these two sets of curves suggests that the likelihood of host/guest complex separation in water is very similar to that in the gas phase. Representative snapshots of the 1-bromooctane/β-CD host/guest complex along the PMF curves in Figure 3.10c are provided in Figure B.3 in Appendix B. Figure 3.10d presents a very different set of curves. Host and guest are easily separated in the bulk 1-bromooctane. The energy required to extract the tagged molecules is approximately k_BT, suggesting easy, almost diffusion-limited guest molecule exchange. The organic solvent is a much more compatible solvent for the exiting tagged molecule than water or vacuum and more 1-bromooctane molecules are available to become the new guest. The PMF curves in Figure 3.10d end earlier when moving away from $\gamma = 0$ because the tagged molecules reorient themselves soon after the αC exits the pore. The ring of hydroxyl groups present at each β-CD pore opening easily dominates the weak electrostatic interactions within the organic phase and the bulk organic phase readily solvates the bromooctane's alkane tail. The total energetic cost of extracting the tagged molecule is less than 20% compared to when in bulk water. Although differences in hydrophobicity mostly explain the favorability of 1-bromooctane as guest, we also remind the reader of the SDFs shown in Figures 3.5b and 3.7a. These figures highlight the entropic favorability of the 1-bromooctane guest by illustrating the well-ordered 7 nodes of pore water density versus the smooth, circular density occupied by the bromooctane alkane tail. To discuss host/guest PMF at the liquid/liquid interface we introduce new nomenclature similar to that of Zheng et. al. [238] In systems where β-CD

is at the interface, we shall represent β-CD by either Δ or ∇, indicating its orientation relative to the interface. The symbol Δ refers to the narrow, primary hydroxyl rim pointing "up" toward positive z (the organic phase) and ∇ represents the reverse. The guest orientation again is either $\uparrow$ or $\downarrow$, which results in the four configurations considered by Figures 3.10e and 3.10f: Δ :$\uparrow$, Δ :$\downarrow$, ∇ :$\uparrow$, and ∇ :$\downarrow$. Figure B.4 in Appendix B contains representative simulation snapshots of these four system configurations. For consistency in these interfacial studies, the orientation of the β-CD is constrained so that $\hat{\mathbf{p}} \cdot \hat{\mathbf{z}} > 0.95$ if the β-CD is in the Δ position or $\hat{\mathbf{p}} \cdot \hat{\mathbf{z}} <$ -0.95 if β-CD is in the ∇ position. The derivation of this orientational constraint is analogous to the window potential derivation provided in Appendix B. Of course the host/guest system may freely rotate at the interface in practice, but this study is intended to describe behavior at the extreme case where location at the interface presumably has the most impact, where the inclusion complex is normal to the interface. The preceding studies of bulk solvent systems investigate the other extreme cases where the liquid/liquid interface has negligible impact. When β-CD is located at the liquid/liquid interface with one pore opening facing each phase, one might (wrongly) anticipate that when a 1-bromooctane guest exits to the organic side, it behaves like in neat 1-bromooctane and, when it exits to the water phase it behaves like in neat water. The PMF curves in Figures 3.10e and 3.10f demonstrate that this is not the case. To correctly interpret these curves, one needs to keep in mind that with $\hat{\mathbf{p}}$ normal to the interface, the pore opening near the interface is strongly tethered to the aqueous phase by the hydrogen bonds between the hydroxyl groups that surround the pore opening. Figure 3.10e shows the

cases where the tagged 1-bromooctane guest exits the pore toward the organic phase (Δ :↑ and ∇ :↑). The energetic penalty initially increases, similar to removing the guest *in vacuo* or in water since another organic molecule is not readily available to take its place in the β-CD pore. This lack of available replacement (which typically enters through the opposite pore in neat 1-bromooctane) explains the reluctance of the guest to exit in the direction of the organic phase, compared to extraction of the tagged molecule in bulk bromooctane. Extraction of the guest in either the Δ :↑ or ∇ :↑ configuration requires an energetic investment of about 3 kcal/mol. The curves truncate at different distances due to the two dissimilar faces. The PMF corresponding to exit from the more flexible primary hydroxyl end (Δ :↑, blue, Figure 3.10e) has a more gradual increase than the one corresponding to exit from the rigid secondary hydroxyl opening (∇ :↑, red, Figure 3.10e). Both curves end when the tagged molecule's alkane tail is free of the pore and the guest molecule adopts a random orientation relative to the β-CD molecule [$\langle(\mathbf{r}_{\alpha C} - \mathbf{r}_{C8}) \cdot \hat{\mathbf{p}}\rangle \approx 0$]. Perhaps surprisingly, we find that less energy is required to extract the tagged molecule toward the interface. In Figure 3.10f the energy to remove the tagged molecule is smaller than in 10e in all cases. When the tagged molecule is moved toward the interface, the pore facing the organic phase is able to receive a new guest organic molecule, similar to when the tagged molecule is removed in bulk 1-bromooctane. The energetic barrier to removal is small and the tagged molecule exits to the interface and reorients itself much earlier than when exiting toward the organic phase, presumably an orientation induced by the liquid/liquid interface. This result demonstrates the energetic importance of the

guest exchange itself. The availability of a new guest has a larger energetic impact than local solvent compatibility. We also note that, at the interface, exchange of the guest from the larger, more rigid secondary pore opening (red curves) requires less energy than the corresponding exchange through the narrower, more mobile primary hydroxyl opening (blue curves). Distinction between pore openings in not obvious in the bulk solvent PMF curves and is likely due to the geometric constraints on the β-CD while at the interface. The water–β-CD hydrogen bonds limit the overall mobility of the β-CD molecule, amplifying the differences between the pore openings. To summarize, the above PMFs suggest that insertion of the 1-bromooctane guest molecule into the β-CD cavity is quite facile in the bulk organic liquid but less so at the liquid/liquid interface. Once the complex drifts into the aqueous phase, the guest is more firmly locked in place. After a reaction in bulk water is complete, diffusion back to the liquid/liquid interface or into bulk organic is necessary to "unload" the product. With this survey of guest/host energetics in mind, we address the dynamics of the host/guest complex as it pertains to the IPTC system. The lifetime of a host/guest complex can be examined using the time correlation function (TCF) formalism

$$C(t) = \frac{\langle h(t)h(0)\rangle}{\langle h(0)h(0)\rangle} \tag{3.11}$$

where h represents a variable of interest. In the case of pore residence time, $C_r(t)$, we define h to be 1 if a given solvent moiety is within the pore and 0 if outside the pore. The ensemble average is calculated for all atom centers of interest and for all time origins.

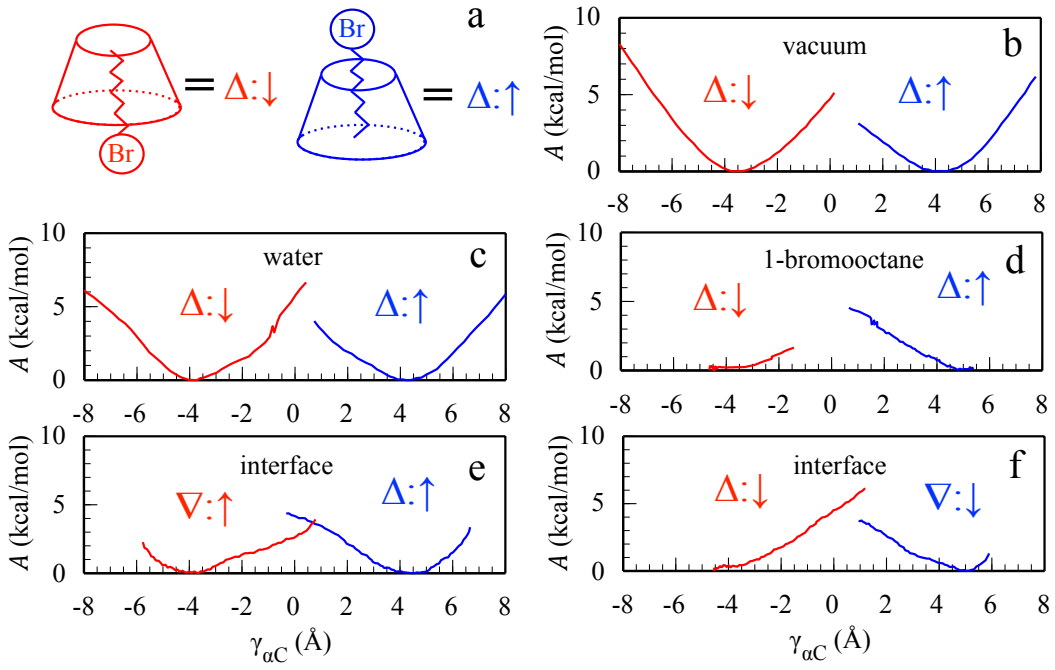

Figure 3.10: Potentials of mean force for a 1-bromooctane guest to approach and move through the β-CD pore when the host/guest complex is in (b) vacuum, (c) bulk water, (d) bulk 1-bromooctane, and (e, f) at the liquid/liquid interface. The red curve represents that the guest αC end faces the 2° hydroxyl side of the β-CD. In the blue curves, the αC side of the guest is toward the 1° hydroxyl opening, orientations are depicted by the cartoons in (a).

As a reminder, we define the β-CD pore as a cylinder of height 7.8 Å and radius 3.0 Å, centered about the β-CD center of mass and its axis of symmetry parallel to the $\hat{\mathbf{p}}$ vector. Figure 3.11 shows the lifetimes of several host/guest combinations in different solvent environments. Solid curves represent bulk solvent systems (water or 1-bromooctane) and dashed curves represent β-CD at the liquid/liquid interface. Water (blue curves) shows the greatest difference in lifetime between the bulk and interfacial systems. This result agrees with the description of β-CD's pore as a hydrophobic environment. Water may form a small, reasonably stable, hydrogen-bonded network in the β-CD pore in bulk aqueous solution, but water is a more transient guest when the more favorable species 1-bromooctane is present. The green curves represent the αC. At the liquid/liquid interface, 1-bromoocane molecules reside "deeper" in the β-CD pore, resulting in more instances where the αC atom center is considered a proper guest by the $C_r(t)$ algorithm's pore definition, and therefore a slightly longer residence time than the αC in neat 1-bromooctane. The alkane tail, C8, is represented by the red curves in Figure 3.11. The interface affects the lifetime of C8 negligibly, suggesting the stability of this guest moiety.

3.4 Conclusions

Molecular dynamics simulations of the β-CD/water/1-bromooctane system have provided molecular insights into the mechanism of inverse phase transfer catalysis in a unique system in which every interfacial liquid organic molecule is a potential

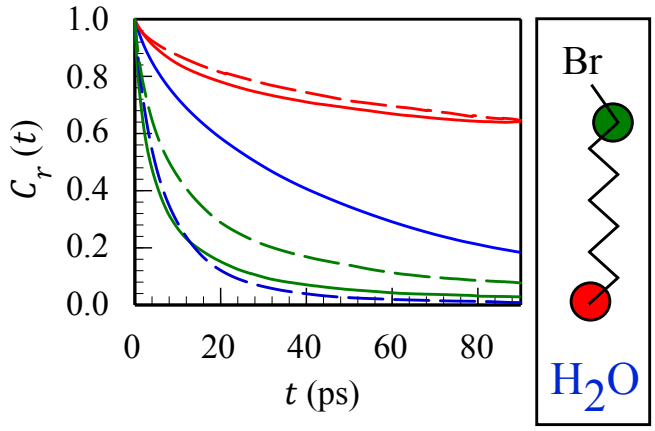

Figure 3.11: β-CD pore residence time correlation functions for water (blue) and the 1-bromooctane αC (green) and C8 (red) atom centers. Solid lines correspond to β-CD in bulk solvents and dashed lines correspond to β-CD at the liquid/liquid interface.

guest reactant. β-CD is a surface-active molecule that is capable of forming stable host-guest complexes with the organic reagent 1-bromooctane. Spatial distribution functions reveal preferred orientations of the 1-bromooctane guest, with the alkane tail inside the pore and with the C8 atom center near the inner wall of the pore. The guest's charged Br–αC head group resides near the hydroxyl groups located at one of the β-CD pore openings. The organic 1-bomomoctane is the preferred pore guest, but in bulk water the pore is occupied by a spatially well-defined group of pore waters. This spatial organization is seen as 7-fold symmetry in water-solvated β-CD SDFs. Potentials of mean force for the transfer of 1-bromooctane through the pore show that the 1-bromooctane guest is much more loosely bound to the β-CD when the complex is in the organic phase than when it is in water. The strongly bound host/guest complex in bulk water allows for the nucleophilic reaction to take place. The β-CD may then return to the organic

phase to exchange the organic product for a new guest reactant. This study reveals the mass transport utility of β-CD in the IPTC experiments of Trifonov and Nikiforov8 and also suggests future related studies. The calculated host/guest PMF curves also show the minimum energy locations of the 1-bromooctane guest's reaction center. Because the host molecule alters the local solvent environment, the reaction barrier can also be altered. Subsequent studies will probe the low-energy configurations of this host/guest complex with reactive molecular dynamics simulations to determine whether the β-CD molecule enhances the rate of S_N2 reaction.

Acknowledgment

This work is supported by the National Science Foundation through grant CHE-1363076.

Chapter 4

S_N2 reaction rate enhancement by β-cyclodextrin at the liquid/liquid interface

4.1 Introduction

Many chemical reactions of interest take place between reactants that are soluble in dissimilar phases, for example when a water-soluble polar molecule reacts with a nonpolar, oil-soluble molecule. [126] Since the reaction requires close contact between the reactants, this reaction can take place only at the water/oil interface, which, due to mass transport and geometrical constraints, significantly limits its rate. Phase transfer catalysts can enhance the rate by shuttling the polar reactant into the organic ("oil") phase (normal phase transfer catalysis, PTC) [126, 210, 72, 166] or by transferring the nonpolar reactant to the aqueous phase (inverse phase transfer catalysis, IPTC). [129, 29, 143] A

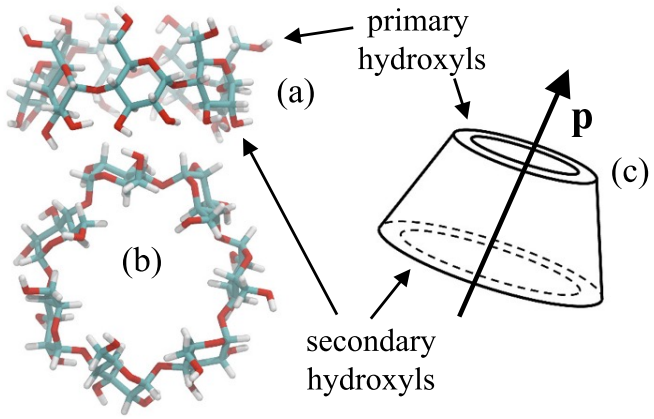

Figure 4.1: Representative structures of β-CD shown using "licorice" models, viewed perpendicular to (a) and looking into the pore (b). The general morphology of β-CD resembles a truncated cone (c).

well-known example of an inverse phase transfer catalyst is β-cyclodextrin (β-CD). The β-CD molecule is a cyclic sugar consisting of 7 glucose units, whose general geometry resembles a truncated cone. [215] Figure 4.1 provides a simulation snapshot and a cartoon representation for reference. The glucose hydroxyl groups surround both the large and small openings, resulting in an interesting electrostatic profile where the outside of the molecule has considerable polar character and its inner cavity is nonpolar. Because of this, β-CD readily forms host/guest complexes with nonpolar molecules. An important class of reactions subject to PTC or IPTC are nucleophilic substitution reactions (S_N2). The rate of S_N2 reactions is incredibly sensitive to the local environment surrounding the reacting species, reported in cases to decrease by 20 orders of magnitude when moving from the gas phase to bulk water. [82, 35, 84] These reactions are also faster by many orders of magnitude when carried out in nonpolar solvent instead of water. The surrounding polar solvent molecules provide greater stabilization to the charge-

localized reactant and product states than to the more diffused charge of the transition state (TS), significantly increasing the energy gap between reactant/product and TS, thus increasing the barrier to reaction. An interesting example of an S_N2 reaction catalyzed by β-CD that provides the motivation for our work is $CN^- + CH_3(CH_2)_7Br \longrightarrow CH_3(CH_2)_7CN + Br^-$ carried out at the interface between 1-bromooctane and water by Trifonov and Nikiforov, [217] who found that addition of β-CD increases the rate of the reaction by (only) a factor of 8. This result is puzzling given the significant enhancement in the rate expected when the reactants are located in nonpolar environments like the interior cavity of β-CD. This reaction is also unusual because each interfacial molecule of the nonpolar phase is a potential reactant, thus reducing the need for mass transport to the interface. We recently reported molecular dynamics simulation results on the stability of β-CD/1-bromooctane host/guest complexes in bulk 1-bromooctane, in bulk water, and at the interface of these two immiscible solvents. [102] We found little to no energetic barrier to host/guest complexation/dissociation in the organic phase or at the liquid/liquid interface but a substantial barrier to dissociation when in the aqueous phase. This host/guest interaction supports the idea of a phase transfer mechanism: the surface-active β-CD can easily form an inclusion complex with 1-bromooctane when at the interface. The complex diffuses to bulk water where the guest is effectively "locked" in place and where it is most likely to be exposed to the nucleophilic attack by CN^-. The product/β-CD complex diffuses to the interface where it dissociates and the cycle continues. However, the precise catalytic function and phase transfer mechanism of β-CD in this and other systems remain unclear. An alternative mechanism that has

been suggested is that the surface-active β-CD brings the organic guest molecule to the interface, exposing the reactive moiety to the aqueous phase at the interface, and allows the product species to diffuse away (as opposed to shuttling the guest into the aqueous phase). [203, 202] Our energy/stability studies are consistent with both mechanisms, since exchange of the 1-bromooctane guest at the interface toward the aqueous phase was seen to be quite facile, suggesting that β-CD may remain at the interface and serve primarily to orient the 1-bromooctane reactive site in a manner that facilitates reaction with species in the adjacent phase as suggested. The IPTC mechanism describes catalysis in the context of assisted mass transfer, where the role of the phase transfer catalyst is to reduce the physical distance between reactants and allow chemical reaction. However, it is possible that the IPTC catalyst also functions as a more traditional catalyst, and alters the electronic configuration of the chemical reaction along the reaction coordinate and lowers the energetic barrier to reaction. Indeed, β-CD's impact on chemical reactions has been well-studied. [143, 215, 6, 196, 148, 8, 57, 214] One interesting application of β-CD host/guest complexation involves reactive species with multiple reactive sites. In some cases, the geometry and polarity of β-CD allow it to form a host/guest complex that sterically hinders reaction at one of these sites, effectively shielding the "guest" site and directing the chemical reaction toward the site with which β-CD does not complex. [8] The IPTC mechanism in a β-CD catalyzed system like those studied by Trifonov and Nikiforov [217] may also benefit from the local volume excluded by the β-CD host in addition to enhanced mass transfer between the phases. If the β-CD host serves to exclude water from the reactive site, it may

result in decreased stabilization of the reactant/product states, effectively reducing the reaction barrier. The purpose of the present work is to more closely investigate these factors and focus on the chemical reaction in this IPTC system. To investigate this idea, we revisit the 1-bromooctane/water/β-CD system and include a chemical reaction in our simulation model. The experimental work on which we base our studies involves the S_N2 reaction between 1-bromooctane and an aqueous nucleophile, but in these initial studies we focus our attention on a simpler system, the symmetric S_N2 reaction $Cl^- + CH_3Cl \longrightarrow ClCH_3 + Cl^-$. This reaction has served as a benchmark system for the theoretical and computational study of solvent effects on chemical reaction thermodynamics and dynamics. [82, 130, 14, 67, 212] Implementation and use of this model reaction to probe the complex solvation environments in the β-CD IPTC system allows us to compare the results to the large body of theoretical and computational studies performed on this reaction. The free energy profile of this benchmark system has been studied in a wide range of molecular-level simulations in a variety of solvents of varying polarity, quantifying the impact of solvent polarity on the reaction barrier. We have previously reported studies of this reaction at the water-air interface, in small clusters of water within bulk organic solvent, and at the interface of two immiscible liquids. [14, 160, 158, 157] Here we briefly summarize two main points from our previous work that capture some of the insights relevant to this IPTC system. First, the presence of only a few molecules of water in an otherwise nonpolar environment has a dramatic effect on the free energy profile of this reaction. Molecules in the first solvation shell dominate the interaction potential between solute and solvent and are therefore mostly

responsible for the stabilization of the product/reactant states. Since this solvation shell typically consists of only a few solvent molecules, the significant impact of a single, polar solvent molecule within an otherwise nonpolar system may retard the rate of reaction by several orders of magnitude. Second, surprisingly, the rate of the benchmark reaction at the immiscible water/oil interface is slower than in bulk water. This is due to the fact that at the liquid/liquid interface the aqueous phase provides a stability of the highly charge-localized reactant and product states similar to that provided in bulk water. However, the interaction between the delocalized charges of the transition state and the surrounding solvents is quite weak and similar to that provided by the organic phase. The reduced stability of the transition state and the enhanced stability of the reactants (and products) result in a larger net barrier to reaction. [158] The proximity of the β-CD host molecule to the S_N2 reactive center makes the system considerably more complex since the β-CD may significantly alter the local solvation environment in ways besides simply limiting solvent molecule access to the reactive center. The structural fluctuations and localized protrusions of one phase into the adjacent phase inherent to the liquid/liquid interface significantly influence (and accompany) mass transfer at and between the phases. At the water/oil interface β-CD preferentially orients so that one of its circular openings is parallel to the interface, with the hydroxyl groups at that opening participating in hydrogen bonds with interfacial water molecules. This ring of hydrogen bonds should serve to isolate the β-CD pore from interfacial fluctuations, effectively causing the interfacial β-CD pore region to resemble a nonpolar membrane cavity. To quantify the influence of the β-CD host molecule on the benchmark S_N2

reaction, this work examines the free energy profile when the reactive system is located within the β-CD cavity. We consider both energetic and structural factors, the interaction potential and arrangement of molecules that surround the reaction site, to understand the influence of the β-CD host molecule. The results are discussed in the context of existing studies of the benchmark S_N2 reaction and their implications toward understanding inverse phase transfer catalysis. The rest of this work is organized a follows: Section II describes the details of our reactive molecular dynamics simulations and free energy calculations. Section III presents the results of these simulations and relevant analyses. Section IV summarizes and outlines future work.

4.2 Systems and Methods

4.2.1 Non-reactive force fields and simulation details

This work considers a model S_N2 reaction in several different solvent environments, including in bulk liquids, at the interface between two immiscible liquids, and within the pore of β-CD. The composition and geometries of these systems are listed in Table 1. The nonreactive force fields used to represent water, 1-bromooctane, and β-CD have been described recently [102] and are summarized here for convenience. Intermolecular potentials are the pairwise sum of Lennard-Jones and Coulomb terms

$$U_{ij}(r) = \sum_{i<j} 4\epsilon_{ij} \left[\left(\frac{\sigma_{ij}}{r} \right)^{12} - \left(\frac{\sigma_{ij}}{r} \right)^{6} \right] + \frac{q_i q_j}{4\pi r \epsilon_0} \tag{4.1}$$

where r is the distance between atom centers i and j. Standard Lorentz-Berthelot combining rules are used to generate mixed interaction parameters. Our water model is a version of the flexible SPC force field [22] with intramolecular potentials as described by Kuchitsu and Morino. [109] The oil phase (1-bromooctane) consists of a charged headgroup (q_{Br} = -0.22) [149] and an OPLS-UA alkane tail. [91] The united-atom 1-bromooctane model is employed to reduce computational complexity. Adding parameters beyond the charged headgroup and electrically neutral alkane tail would not provide any interesting additional physical insight into this work. The β-CD molecule is a fully flexible, all-atom representation with parameters taken from the AMBER ff99SB-ILDN force field. [116] Since this work is focused on the detailed effect of the β-CD on a model S_N2 reaction, its impact when functioning as a "molecular-reactor," [8, 57] we use the all-atom representation. All molecular dynamics simulations are performed using our in-house code that uses the velocity Verlet algorithm and a time-step of 0.5 fs to integrate the laws of motion. [222] All simulations are performed at 298 K. System snapshots are obtained using visual molecular dynamics (VMD.) [81]

Table 4.1: Composition and size of simulated systems.

system	n_{BrOct}	$n_{\mathrm{H_2O}}$	$n_{\beta-\mathrm{CD}}$	x(Å)	y(Å)	z(Å)
A	384	0	0	60.0†	60.0†	60.0†
B	0	999	0	39.11†	39.11†	39.11†
C	509	2030	0	45.0	45.0	300.0
D	0	2104	1	50.0†	50.0†	50.0†
E	610	2400	1	50.0	50.0	300.0

† Dimensions refer to the cube that encloses systems with truncated octahedral symmetry.

4.2.2 The empirical valence bond (EVB) model

To model the S_N2 reaction we use an EVB approach similar to the model first introduced by Warshel and co-workers. [82, 225] The EVB model describes a chemical reaction as a mixture of diabatic states, whose condensed-phase interaction potentials are equal to the gas-phase potentials plus the interaction between each state and its surrounding solvent (and the β-CD when present). The EVB method can describe the changing electronic configuration along the reaction coordinate while being computationally inexpensive enough to allow the simulation of a reactive system within large, condensed-phase molecular systems. We refer the reader to a previously published, detailed discussion of our implementation [14] and other works that present the EVB approach with greater depth. [224, 96] Here we briefly summarize the EVB model, focusing on the components relevant to the analysis presented later in this work. We use the simplest approach to consider the symmetric S_N2 reaction $Cl^- + CH_3Cl \longrightarrow CH_3Cl + Cl^-$ and assume that only two orthonormal valence states contribute to the total wave function: $\psi_1 = Cl^- + CH_3Cl$ and $\psi_2 = CH_3Cl + Cl^-$. [130, 14]

$$\Psi = c_1\psi_1 + c_2\psi_2, \langle\psi_1|\psi_2\rangle = \delta_{ij} \tag{4.2}$$

The total Hamiltonian is

$$\hat{H} = \begin{pmatrix} H_{11}(\mathbf{r}_i, \mathbf{r}_d, \mathbf{r}_s) & H_{12}(r_1, r_2, \theta) \\ H_{21}(r_1, r_2, \theta) & H_{11}(\mathbf{r}_i, \mathbf{r}_d, \mathbf{r}_s) \end{pmatrix} \tag{4.3}$$

where H_{11} and H_{22} are the Hamiltonians for the diabatic states ψ_1 and ψ_2

$$H_{11} = E_k + H_{11}^0(r_1, r_2, \theta) + U_{ss}(\mathbf{r}_s) + U_{si}(\mathbf{r}_s, \mathbf{r}_i) + U_{sd}(\mathbf{r}_s, \mathbf{r}_d) \tag{4.4}$$

which include E_k, the kinetic energy of all atoms, and H_{11}^0, the gas-phase Cl^- ion–CH_3Cl molecule interaction potential. U_{ss}, U_{si}, and U_{sd} represent the solvent–solvent, solvent–Cl^- (ion), and solvent–CH_3Cl (dipole) interaction potentials. Due to the symmetric nature of the reaction, H_{22} is of identical form and involves only changing the indices of the Cl atom centers. The off-diagonal terms in equation 4.3, H_{12} and H_{21}, are the electronic coupling terms used by Hynes and co-workers [130, 92]

$$H_{12} = -QS(r_1)S(r_2) \tag{4.5}$$

where $S(r)$ is the overlap integral for the σ orbital formed by the carbon 2p and chlorine 3p orbitals, determined using the approximations of Mulliken et al. [150] Q is a parameter fitted so that the correct gas-phase potential energy surface is obtained, set to 678.0 kcal/mol. Diagonalization of the Hamiltonian in equation 4.3 gives rise to the ground state adiabatic Hamiltonian H_{ad} used to propagate the reactive classical trajectories. We define a simple, geometric reaction coordinate to be the distance between the Cl and CH_3 atom centers, $\xi = r_1 - r_2$, where the reaction coordinate ξ is precisely zero at the transition state (TS) because of the symmetric nature of the reaction studied in

this work. To quantify the degree with which the solvent stabilizes the reactants versus the products, we define a "solvent coordinate" $s(\xi)$ at each value of ξ by considering the solute-solvent interaction potential's contribution to the energy gap $H_{11} - H_{22}$:

$$H_{11} - H_{22} = \Delta H^{\circ} + s \tag{4.6}$$

where ΔH° is the energy gap between the gas-phase diabatic states. Note that at the transition state $\langle s \rangle = 0$.

4.2.3 Reaction free energy profile calculations

We calculate the free energy profile of the model S_N2 reaction along the reaction coordinate ξ using umbrella sampling with overlapping windows and an applied biasing potential. Our implementation may be formally described by starting with the definition

$$\begin{aligned} W(\xi) &= -k_B T \ln\langle \delta(r_1 - r_2 - \xi) \rangle \\ &= -k_B T \ln \frac{\int \delta(r_1 - r_2 - \xi) e^{-H_{ad}/k_B T} d\Gamma}{\int e^{-H_{ad}/k_B T} d\Gamma} = -k_B T \ln P(\xi) \end{aligned} \tag{4.7}$$

where k_B is the Boltzmann constant and δ is the Dirac delta function. The free energy profile $W(\xi)$ over the interval $[\xi_0, \xi_N]$ may be calculated by dividing the interval into N overlapping subintervals, where the value of ξ in a window j is constrained to $[\xi_{j-1}, \xi_j]$ by window potentials applied as a function of r_1 and r_2. The resulting set of overlapping

$W_j(\xi)$ are stitched together by adding a constant C_j that minimizes the difference between the overlapping regions of $W_{j-1}(\xi)$ and $W_j(\xi)$. For improvement of sampling statistics and acceleration of the exploration of phase space, a biasing potential is added to the adiabatic Hamiltonian

$$H_{ad}^b = H_{ad} + U_b(\xi) \tag{4.8}$$

where U_b is a function of ξ and is of the form

$$U^b(\xi) = Ae^{-\alpha\xi^2} - Be^{-\beta|\xi|} \tag{4.9}$$

The parameters A, α, B, and β are chosen so that $U_b(\xi)$ approximates $W(\xi)$. The reported free energy profile is given by

$$W(\xi) = -k_B T \ln\langle\delta(r_1 - r_2 - \xi)\rangle_b - U_b(\xi) \tag{4.10}$$

noting that the ensemble average $\langle\ldots\rangle_b$ is obtained using the Hamiltonian modified by the applied biasing potential, H_{ad}^b. In this work all data is presented as a function of the reaction coordinate ξ and is obtained by sampling overlapping windows along ξ as mentioned above. Each window is 0.5 Å wide and overlaps the neighboring window by 0.2 Å. 1 ns of trajectory data is collected within each window.

4.3 Results and Discussion

4.3.1 Reactions in bulk liquids

As a useful reference we first consider our benchmark reaction in the bulk of the two liquids. Figure 4.2a shows the potential of mean force W along the reaction coordinate ξ for the $Cl^- + CH_3Cl \longrightarrow ClCH_3 + Cl^-$ reaction in bulk water, in 1-bromooctane, and in vacuum. The large differences in the free energy profiles and the activation free energies $\Delta A^{\ddagger}$ in these three systems are due to the changing solvation environment of the reactive system along ξ. The polar solvents stabilize the reactant and product states much more than the reaction's transition state due to the greater charge separation and magnitude in the reactant/product states than in the transition state. As a result, the barrier to the reaction increases by 10 kcal/mol in 1-bromooctane relative to vacuum and by an additional 15 kcal/mol in water relative to 1-bromooctane. We refer the reader to our earlier, more extensive survey and discussion of this reactive system in solvents of increasing polarity. [14] We also draw attention to the ion-dipole minima at $\xi = \pm 1.5$ Å. These minima are due to the electrostatic attraction between the Cl^- and the electrophilic end of the CH_3Cl dipole and are most prominent in vacuum and in nonpolar solvent environments. With increasing solvent polarity and thus stabilization of the product/reactant states, the ion-dipole minima diminish, effectively vanishing when in an aqueous environment. [14] The free energy barrier is defined as the difference between the free energy at $\xi = -\infty$ (free energy of reactants) and the maximum height of the free energy profile at the transition state ($\xi = 0$). The equilibrium value of the solvent coor-

dinate s_{eq} in each solvent is shown in Figure 4.2b. As described in equation 4.6, s_{eq} is the contribution of solvent-solute interaction energy to the energy gap between the two diabatic states, $H_{11} - H_{22}$, and serves as a useful quantitative probe of the reaction's local environment. The dependence of s_{eq} on ξ illustrates the solvent-solute coupling. The magnitude of s_{eq} when ξ is far from the transition state describes the solvation energy contribution to the barrier height. The slope of $s_{eq}(\xi)$ near the transition state describes the rate of preferential solvation of the reactant/product states as the charge separation increases with increasing $|\xi|$. [14, 66] The structure of local solvent molecules surrounding the reaction may be described as a function of ξ by considering the radial distribution function

$$g_{vl}(r) = \frac{1}{\eta_c} \langle \sum_{i=1}^{N} \delta(r - r_i) \rangle \tag{4.11}$$

where v is the Cl^-, CH_3, or Cl atom center; l is the representative atom center in the solvent molecule; and r_i is the distance between the atomic centers v and l. δ is the Dirac delta function, and N is the total number of pair distances. The normalization constant η_c is chosen so that $g_{vl}(r \to \infty) = 1$. For water, the oxygen molecule is the representative atom center, and for 1-bromooctane the united-atom CH_2 adjacent to the Br atom (αC) is selected as the representative atom center. Since this αC united atom bears a partial positive charge, its arrangement around the Cl^- will contribute most significantly toward the solvent-solute interaction potential and thus to s_{eq}. The local solvent structure around the ion, $g_{vl}(r)$, may be expressed as a function of ξ by extracting the maximum value of $g_{vl}(r)$ (g_{max}) from trajectories obtained during the umbrella sampling of the

reaction, with one data point obtained for each overlapping 0.5 Å wide window along ξ. The results of these calculations for the reaction $Cl^- + CH_3Cl \longrightarrow ClCH_3 + Cl^-$ in bulk water and bulk 1-bromooctane are shown in Figure 4.3. Three curves are obtained for each solvent for $v = Cl^-$, CH_3, and Cl. The two panels in Figure 4.3 correspond to solvents of very different size and polarity yet show a similar behavior. We may describe these curves by moving-along the reaction coordinate ξ from left to right. As the Cl nucleophile (green curve) approaches CH_3Cl, the ordering of its solvation shell rapidly decreases near the transition state at $\xi = 0$ Å. In a similar fashion, the solvation shell around the Cl leaving group (red curve) tightens and becomes more ordered as the charge on the leaving group increases immediately after crossing the TS and moving toward $+\xi$. The two panels are similar in overall shape but have significantly different g_{max} magnitudes. This difference largely reflects the normalization of $g_{vl}(r)$ to unit bulk density and the size difference between the two solvent molecules. If we define the population of the first solvation shell by integrating the first peak of $g_{vl}(r)$, the number of the solvent molecules surrounding the Cl ions is more similar, 7.7 water molecules and 6.2 1-bromooctane αC atom centers. In the case of both solvents, the CH_3 atom center (blue curve) shows little enhanced solvation, even in the regions near $\xi = 0$, where the values of gmax change dramatically for both the nucleophile and leaving group.

4.3.2 Reaction in aqueous host/guest complex

We next consider the benchmark reaction carried out within the interior of the β-CD cavity in bulk water. To help decide on the precise location for the reactants, we

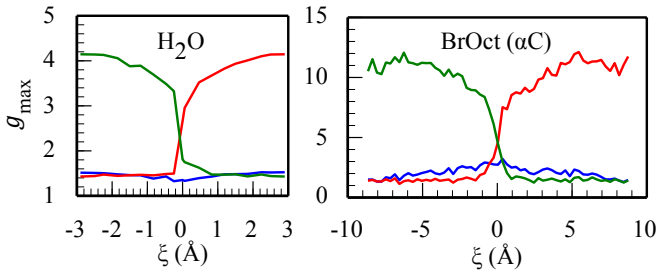

Figure 4.2: Solvation of the atom centers in the EVB reactive system. Curves represent the maximum value of $g_{vl}(r)$ for the respective atom center surrounding solvent molecules: the Cl^- nucleophile (green), the leaving Cl^- (red), and the CH_3 united atom (blue). The central solvent atoms are the water oxygen (left panel) and the 1-bromooctane α-carbon (right).

invoke our previous work where we examined the host/guest stability of the β-CD/1-bromooctane complex in bulk water, in bulk 1-bromooctane, and at the liquid/liquid interface. [102] Stability studies of the host/guest complex in bulk water showed that the minimum free energy (most-favored) location of the 1-bromooctane guest corresponds to having the reactive site (the carbon adjacent to the bromine atom, αC) near the hydroxyl groups at either opening and the alkane tail within the β-CD pore. Guided by this observation, we insert the benchmark system at these two energetically favored positions and obtain the potential of mean force curves along the reaction coordinate ξ in bulk water, while the reactants' center of mass is constrained to the given location. A third curve is also obtained by constraining the benchmark S_N2 reaction to the "center" of the β-CD pore. While this location is not physically relevant to the 1-bromooctane/β-CD host/guest complex, we include this in our effort to fully probe the impact of β-CD on this benchmark S_N2 reaction. All β-CD-reactive system constraints involve restricting the center of mass of the benchmark system with a windowing potential perpendicular

to the β-CD molecular vector **p** shown in Figure 4.1c (and therefore parallel to the β-CD pore openings). The cartoon in the upper right of Figure 4.4 illustrates the positions of the benchmark reaction for each corresponding free energy profile. The planar constraints, as distances from the β-CD center of mass along **p**, are 4.20 $\pm$ 0.25 Å at the small opening, -3.90 $\pm$ 0.25 Å at the large opening, and -1.0 $\pm$ 0.5 Å for the "center" of the pore. Figure 4.4a shows free energy profiles for the aqueous $Cl^- + CH_3Cl \longrightarrow CH_3Cl + Cl^-$ reaction/β-CD host/guest complex at various guest locations compared to the reaction in bulk water (blue curve). Surprisingly, all three host/guest configurations show a similar reaction barrier as the one in bulk water with no β-CD present. This is also reflected in the nearly identical variation of the solvent coordinate as a function of the reaction coordinate in the different locations shown in Figure 4.4b. Evidently the hydrophobicity of the β-CD interior must be counterbalanced by the water molecules remaining in the cavity and near the mouth of the pore as well as by the existence of many OH groups around each pore opening. All these species are able to provide enhanced stabilization of the reactants and product states that is only slightly reduced from that in bulk water while at the same time providing significantly less stabilization of the transition state than that in bulk water. This is similar to what has been observed in studies of this benchmark S_N2 system at water interfaces [160] and in water clusters within nonpolar solvents. [158] Figure 4.5 is a qualitative sketch of free energy diagrams, showing the relative stability of the transition state and products/reactants in different environments. In the β-CD pore, like at the neat liquid/liquid interface, the increase in barrier height is mostly due to reduced stabilization of the transition state. Support for

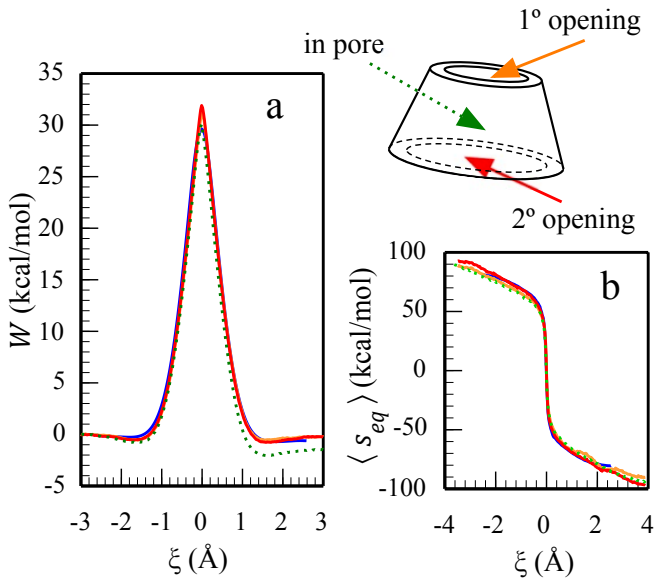

Figure 4.3: Free energy profiles (a) and equilibrium solvent coordinate values (b) for the reaction $Cl^- + CH3Cl \leftrightarrow CH_3Cl + Cl^-$ in bulk water (blue) and as guest in β-CD pore in water at three positions: at the small, primary hydroxyl opening (orange), at the larger, secondary hydroxyl opening (red), and near the β-CD's center of mass (green, dotted). The cartoon in the upper right shows the approximate location of the reactive system as guest in the β-CD molecule.

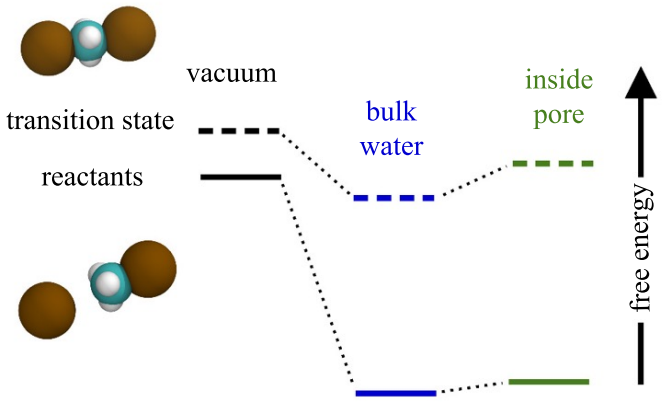

Figure 4.4: A cartoon depicting (not to scale) the free energy of the transition state (dashed lines) and the reactants (solid lines) in different environments.

the above explanation is provided by examination of the local structure around the S_N2 reaction. This can again be described by considering $g_{max}(\xi)$, the maximum value of $g_{vl}(r)$ in each umbrella-sampling window along ξ. However, to appropriately account for the presence of β-CD, the ability of its hydroxyl groups to solvate the S_N2 system must also be considered. As a first approximation we again apply equation 4.11 to construct pair distribution functions but count both water and β-CD hydroxyl group oxygens as the relevant solvent moiety (l) when calculating $g_{vl}(r)$. This assumption is reasonable since the β-CD hydroxyl hydrogens are assigned partial charges within $+0.01e$ of our water model's hydrogen charge of $+0.41e$, therefore providing similar stability to the negatively charged species in the benchmark system. Comparing the host/guest g_{max} plots in Figure 4.6 to the corresponding analysis performed in bulk water (Figure 4.3), it is seen that the reactant/product hydration shell populations are only slightly larger in the aqueous system without β-CD. The peak values of g at the transition states are smaller when the S_N2 system is within the β-CD molecule. The net effect of the cavity is to stabilize the reactants (and products) to a degree that is almost the same as that in bulk water while stabilizing the transition state to a degree that is much less than in bulk water. We conclude this section by noting the small asymmetry in the PMF when the reaction takes place in the middle of the β-CD pore. In this location the Cl-CH_3-Cl system is approximately locked in an orientation that gives rise to different local hydrations for the two Cl atoms, which results in breaking the symmetry of the reaction. This is evident from a comparison of the peak values of g for the two Cl atoms in Figure 4.6. While the two curves describing the hydration of the nucleophile and the

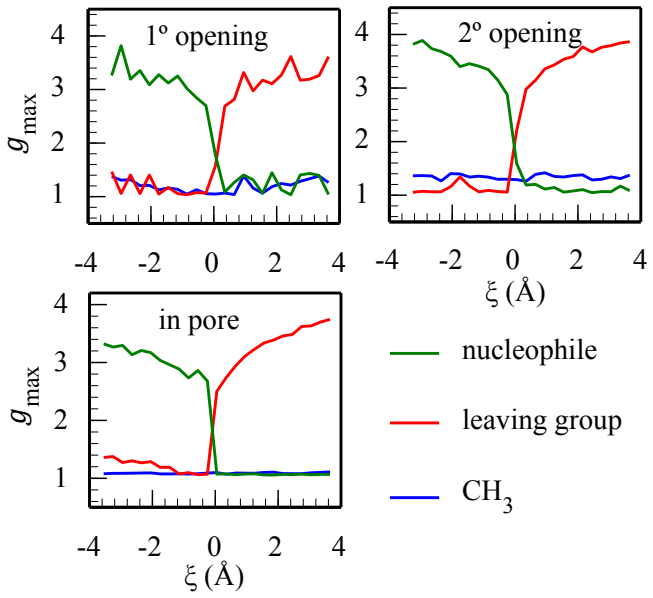

Figure 4.5: The maximum value of $g_{vl}(r)$ along ξ describes the solvation of the β-CD complexed reactive system atom centers in an aqueous system. Each panel represents the reactive system at a different location within the β-CD host molecule. Following ξ from left to right, the curves correspond to the Cl nucleophile (green), the CH_3 reaction center (blue), and the Cl leaving group (red). All g_{max} values represent the total solvation of the reactive system by water and β-CD hydroxyl groups (see text for details).

leaving groups at the two openings of the cavity are symmetrical, the corresponding curves are clearly nonsymmetrical when the reaction takes place in the center of the pore. Interestingly, each curve is similar to one of the curves at each of the two openings (compare the "in pore" green curve with the green curve at the 1° opening and the "in pore" red curve with the red curve at the 2° opening).

4.3.3 Reactions at the liquid/liquid interface

We next consider the more complicated situation when the host/guest complex is located at the liquid/liquid interface. We first define a simple nomenclature adapted from one introduced by Zheng et al. [238] In our simulations, the z-axis is normal to the interface, with the Gibbs dividing surface (GDS) located at approximately $z = 0$ Å, the 1-bromooctane phase located in the region of $z > 0$ Å, and the aqueous phase located at $z < 0$ Å. The surface-active β-CD molecule is located near the GDS, with its center of mass in the organic phase and one of the circular pore openings parallel to the interface (the vector p defined in Figure 4.1 is perpendicular to the interface). To simplify and clarify the discussion of the host/guest system at the liquid interface, we define the system where the β-CD is at the interface with the large opening near the GDS and the small opening pointing toward $+z$ (toward the bulk organic phase) as Δ or "up". Similarly, when the β-CD small opening is at the GDS and the large opening toward $+z$, we shall refer to this system as ∇ or "down". A cartoon schematic of this nomenclature is included in the upper right part of Figure 4.7. In each host/guest configuration the reactive system is confined to the minimum energy position of the

reactive site in a corresponding β-CD/1-bromooctane host/guest complex as determined in our preceding work. [102] The constraint on the position of the S_N2 system uses the same form as the constraints applied in the β-CD/S_N2/water system described in Section III.C, with the S_N2 system's center of mass confined to a plane parallel to the pore openings and separated from the β-CD center of mass by 4.20 $\pm$ 0.25 Å at the small opening and -3.90 $\pm$ 0.25 Å at the large opening. The arrows in the cartoon in Figure 4.7 indicate the approximate location of the S_N2 system center of mass at the liquid/liquid interface, and the colors of the arrows correspond to the respective free energy profiles. Figure 4.7a shows the free energy profile for the $Cl^- + CH_3Cl \longrightarrow ClCH_3 + Cl^-$ reaction at the neat interface (red curve) and when the reactive system is a guest within the β-CD molecule in the Δ (blue) and ∇ (green) positions. At the neat interface, the reaction barrier is approximately 32.2 kcal/mol, noticeably greater than in bulk water. This increase in barrier height at the interface due to diminished stabilization of the transition state has been described in earlier sections and discussed in detail in our previous work. [158] The two interfacial host/guest systems (blue and green) have nearly indistinguishable profiles, which again suggests that the difference between the two openings has little impact on the host reactive system. However, unlike in the aqueous systems in Section III.C , the interfacial host/guest systems have a lower barrier to reaction than the corresponding reactive system without the β-CD host molecule. The magnitudes of the host/guest reaction barriers at the interface are 29.8 kcal/mol for the Δ configuration and 28.8 kcal/mol for the ∇ configuration, both substantially lower than the value obtained at the neat interface. This result

has an important consequence with regard to the IPTC reaction: When β-CD hosts the reaction at the interface, it acts as a conventional catalyst by lowering the barrier to reaction relative to the corresponding system without β-CD present. This catalytic function of β-CD is provided by its shielding of the reactive system from some interfacial water molecules, resulting in less stabilization of the reactant and product states. If the reduction in barrier height were due to β-CD weakly binding to or locally distorting the reactive system itself to lower the reaction barrier, we should see a similar effect in the host/guest system in bulk water, an effect not seen in Figure 4.4a. The values of $s_{eq}(\xi)$ for the interfacial systems in Figure 4.7b agree with the free energy profile calculations. Moving away from the transition state ($\xi = 0$ Å), all curves rapidly increase in magnitude as charge separation increases. Away from the transition state the host/guest systems both have smaller magnitude values of s_{eq} than the neat interfacial system. In Figure 4.8 we again utilize $g_{max}(\xi)$ to describe the stabilization of the benchmark reactive system by the surrounding solvent. The top two panels describe solvation of the bare solute system at the liquid/liquid interface; the top left panel of Figure 4.8 refers to solvation by water, and the top right panel refers to solvation by 1-bromooctane, where the αC is again used as the atom center of reference due to its partial positive charge. These two panels describe a phenomenon reported earlier when this benchmark reactive system is observed at the immiscible water/organic interface. When away from the transition state, the charge-bearing Cl atom center is solvated by water, and the CH_3Cl "dipole" resides in the organic phase, solvated predominantly by the 1-bromooctane. The bottom two panels of Figure 4.8 show $g_{max}(\xi)$ for the interfacial host/guest Δ and

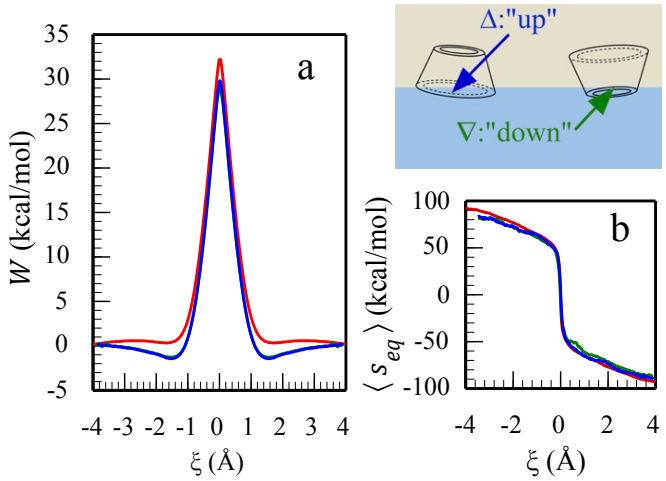

Figure 4.6: Free energy profile (a) and equilibrium value of the solvent coordinate (b) for the S_N2 system at the liquid/liquid interface. The blue and green curves represent the reactive system as guest within β-CD in the Δ ("up") and ∇ ("down") orientations, the red curve is the neat interface. The cartoon on the upper right shows the location of the reactive system and β-CD in each system. The light brown background represents the 1-bromooctane phase and the aqueous phase is light blue.

∇ configurations. Like in the case of the host/guest system in bulk water, the solute-solvent pair distribution functions contain the sum of both water and β-CD hydroxyl oxygen atoms as the solvent.

4.4 Conclusions

We have studied the effect of complexation with β-CD in various solvent environments on the benchmark symmetric S_N2 reaction $Cl^- + CH_3Cl \longrightarrow ClCH_3 + Cl^-$ by molecular dynamics simulations to gain insight into the mechanism of inverse phase transfer catalysis. In bulk water the reaction is almost unaffected by the complexation of the reactants with β-CD. Despite the hydrophobic nature of the β-CD cavity, wa-

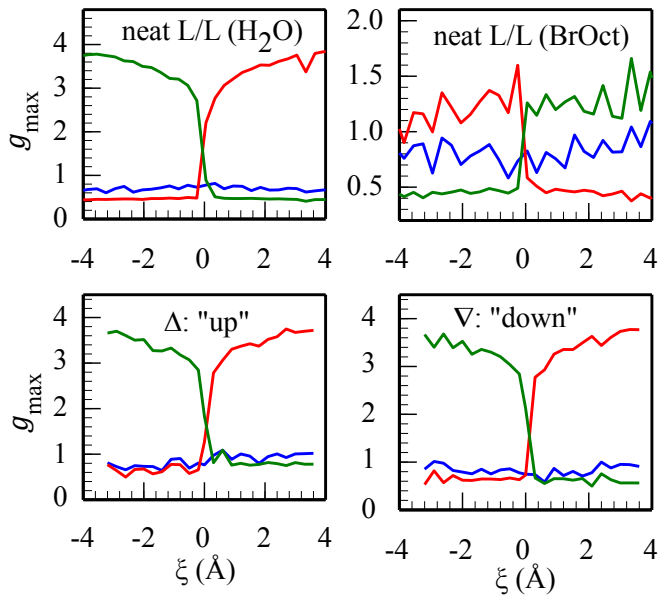

Figure 4.7: Solvation of the atom centers in the model S_N2 system at the liquid/liquid interface. The top panels represent the reactive system at the neat interface, solvated by water (left) and 1-bromooctane (right). The bottom panels represent the total solvation of the reactive system by water and β-CD hydroxyl groups (see text for details).

ter molecules remaining in the cavity and near the opening, along with the β-CD OH groups, provide a hydration environment close to that of bulk water. At the immiscible liquid/liquid interface the formation of an inclusion complex with β-CD reduces the barrier height relative to the reaction at the neat interface. This is due to the fact that at the interface the β-CD molecule resides mostly in the organic phase, with nonpolar species preferentially populating the pore. The β-CD host molecule partially restricts access of interfacial water molecules to the guest S_N2 system, resulting in a slightly reduced stabilization of the reactant/product states. This work suggests that β-CD may act as both a conventional catalyst (reducing the energetic barrier to reaction along the reaction coordinate) and phase transfer catalyst (facilitating mass transfer of one reactant to an adjacent, immiscible phase). It provides a qualitative explanation for the rate enhancement observed experimentally for the reaction $CN^- + CH_3(CH_2)_7Br \longrightarrow CH_3(CH_2)_7CN + Br^-$ at the water/1-bromooctane interface. [217] Work is in progress to develop a new EVB model that considers this specific reaction. The presence of an alkane tail directly adjacent to the reactive center (inside the cavity) may, upon first consideration, suggest additional local dehydration of the reactive site, further reducing the energetic barrier to reaction. However, as determined by earlier studies,13 the 1-bromooctane reactive site typically resides at the outer edge of the β-CD pore. Therefore, the alkane tail may have a negligible impact on the magnitude of stabilization provided by nearby solvent molecules. Insight gained from the present work will be useful for isolating the different factors that may (or may not) influence the rate in this more complex system.

Acknowledgments

This work is supported by the National Science Foundation through grant CHE-1363076.

Chapter 5

On the local intermolecular ordering and dynamics of liquid chloroform

5.1 Introduction

The intermolecular structure and ordering of neat liquids have been investigated with diffraction experiments and computer simulations for several decades [25, 79, 27, 50, 24, 37, 83, 111, 176, 234, 32]. Molecules with simple symmetry, like the nearly tetrahedral chloroform ($CHCl_3$), receive particular attention, as knowledge of their structure serves as a stepping-stone toward systems of greater complexity. Understanding intermolecular structure may also lead to insights toward chloroform's outstanding solvation properties that result in its widespread use in both research and manufacturing capacities despite chloroform's well-documented detrimental health effects and safety concerns [88, 239, 48, 228]. Understanding the precise nature of $CHCl_3$'s solvation abil-

ity could lead toward alternate solvents with similar properties. We shall not summarize decades of $CHCl_3$ structural research here, but instead direct readers toward the review recently published by Pusztai and co-workers [177]. The present work focuses on a long-standing orientational question related to the existence of the 'Apollo configuration.' In this Apollo configuration nearest-neighbor chloroform molecules have parallel, collinear dipoles with the hydrogen atom being located in the "hollow formed by three chlorine atoms" [23] of the neighboring $CHCl_3$, as illustrated by the cartoon in Figure 5.1a. The Apollo configuration has been dismissed by most researchers in the field [177, 123], but its possible existence as an important structural feature in $CHCl_3$ was suggested recently in the neutron diffraction (ND) experiments by Shephard et al. [201] In this work, the authors introduce 'polar stacking:' a quantitative definition of local dipole-dipole ordering in bulk liquid chloroform. The criteria for 'polar stacking' were defined as follows: A vector that begins at the C atom of the reference $CHCl_3$ molecule and points toward its H atom is defined. The neighboring $CHCl_3$ is in a polar stack with the reference $CHCl_3$ molecule if (1) its H atom is between 2.0 and 4.2 Å from the reference C atom and (2) and the H–C$\cdots$H angle is between 150° and 210°. Figure 5.1b is a cartoon schematic of this definition, where the green $CHCl_3$ molecule is in a polar stack with the reference molecule and the red $CHCl_3$ molecules are not. Analysis of ND data suggests that 29.3% of $CHCl_3$ molecules participate in these structures and that these head-to-tail dipole orientations may extend well beyond two neighboring $CHCl_3$ molecules to include 'polar stacks' that consist of up to 5 $CHCl_3$ molecules [201]. These stacks are further postulated to form 'super dipole' aggregates, which may enhance solvation and

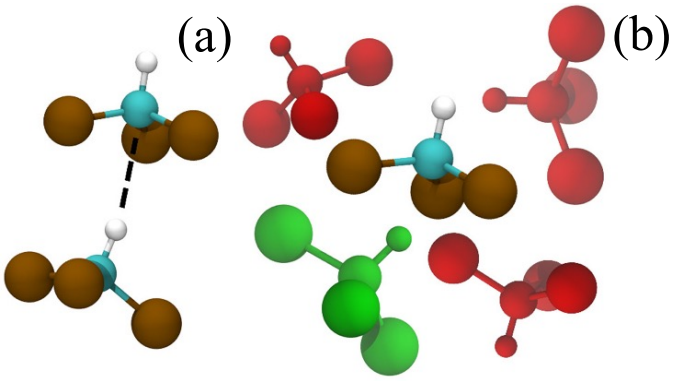

Figure 5.1: Cartoon schematics of (a) $CHCl_3$ molecules in the 'Apollo configuration' and (b) $CHCl_3$ molecules in a 'polar stack.' The molecule arranged in a 'stack' with the reference molecule is green, those not participating in the stack are red.

extraction properties. We note the distinction between 'polar stacking' and the Apollo configuration: The 'polar stacking' definition is based on three atomic centers (H, C, and the neighboring H) and is a measure of head-to-tail dipole vector configurations. Quantification of the 'Apollo configuration' requires an additional constraint regarding dipole-dipole collinearity or parallelism and is necessary for the existence of the "super dipole" aggregates. The present work uses computer simulations to search for and study the dynamics of these stacked structures as described by Shephard et al. In addition, by removing the electrostatic contribution from intermolecular potential energy functions we can gain insight into the role of electrostatic vs. packing effects in determining the existence of these structures. Disabling the electrostatics in MD simulations has been shown to have little effect on the local intermolecular ordering of liquid $CBrCl_3$, a molecule that shares $CHCl_3$'s C_{3v} symmetry and is also of similar size [175], although the magnitude of the $CBrCl_3$ dipole moment vector is much smaller than in liquid $CHCl_3$.

However, disabling some of the electrostatics in a system with much stronger coulombic interactions, a hydroxylated silica surface, results in a relatively dramatic change in the local ordering of an adjacent liquid alcohol phase [104]. This change in interfacial ordering is due to disruption of the local hydrogen-bonding network between the silica surface and the adjacent liquid phase. We also extend the analysis of $CHCl_3$ local structure to quantify a relationship between polar stacking and the Apollo configuration. Since $CHCl_3$ molecules participating in a 'polar stack' have their dipole moment vectors in a head-to-tail orientation, adding a dipole moment colinearity constraint will reveal the subset of 'polar stacked' $CHCl_3$ molecules that are also in the 'Apollo configuration.'

5.2 Simulation Details

We use a chloroform force field that gives rise to site-site radial distribution functions that are in good agreement with those calculated by other force fields and are in agreement with results of previous experiments. Classical molecular dynamics simulations of neat liquid chloroform are performed using our in-house code. We use an all-atom, 5-site, fully flexible, fixed-charge $CHCl_3$ model where the intermolecular interaction potential is the pairwise sum of Lennard-Jones and Coulombic terms

$$U_{ij}(r) = \sum_{i<j} 4\epsilon_{ij} \left[\left(\frac{\sigma_{ij}}{r} \right)^{12} - \left(\frac{\sigma_{ij}}{r} \right)^{6} \right] + \frac{q_i q_j}{4\pi r \epsilon_0} \tag{5.1}$$

where r is the distance between atom centers i and j. Standard Lorentz-Berthelot combining rules, $\sigma_{ij} = (\sigma_i + \sigma_j)/2$, $\epsilon_{ij} = (\epsilon_i \epsilon_j)^{1/2}$, are used to generate mixed interac-

tion parameters. Details of this model have been described elsewhere [12, 90] but for convenience we include a full listing of the inter and intramolecular potential energy parameters in Tables 5.1 and 5.2. The simulation box consists of 794 $CHCl_3$ molecules in a truncated octahedron whose enclosing cube has an edge length of 59.69 Å. The simulations in this work consist of only fixed-charge (non-polarizable) force fields and sample two extreme cases: the aforementioned fixed partial charges used in our previous studies ($\langle\mu\rangle$ = 1.4 D) and the nonphysical case of a zero-charge $CHCl_3$. All molecular dynamics simulation data presented in this work represents the ensemble average of 10^6 configurations obtained during 10 ns of simulation time. Simulations were performed at 298 K with an integration time step of 0.5 fs.

Table 5.1: Intermolecular potential parameters used in the $CHCl_3$ model.

Atom	$\sigma(\AA)$	ϵ(kcal/mol)	$q(e)$
C	3.20	0.101	0.32
Cl	3.50	0.348	-0.14
H	2.75	0.0266	0.10

Table 5.2: Stretch and bend equilibrium values and force constants.

Equilib. value	Force const. ($\times$ kcal/mol)
$r^{eq}_{\mathrm{CCl}} = 1.77$ Å	$k_{\mathrm{CCl}} = 630$ Å^{-2}
$r^{eq}_{\mathrm{CH}} = 1.07$ Å	$k_{\mathrm{CH}} = 725$ Å^{-2}
$\theta^{eq}_{\mathrm{ClCCl}} = 112.0°$	$k_{\mathrm{ClCCl}} = 149$ rad^{-2}
$\theta^{eq}_{\mathrm{ClCCl}} = 106.8°$	$k_{\mathrm{ClCCl}} = 95.6$ rad^{-2}

5.3 Results and Discussion

5.3.1 Survey of local structure: spatial distribution functions

When considering the molecular structure of a liquid composed of a nearly-spherical or pseudo-spherical species like chloroform, it is reasonable to expect the overall molecular arrangement to resemble a model of close-packed spheres, like the common textbook examples of liquid argon [34] or "Lennard-Jonesium" [144]. Following a standard approach, we may first quantitatively describe the structure of a bulk liquid using the radial distribution function, $g_{\text{A-B}}(r)$

$$g_{\text{A-B}}(r) = \frac{1}{\eta_c} \left\langle \sum_{i=1}^{N} \delta(r - r_i) \right\rangle \tag{5.2}$$

where A is the reference atom center ($CHCl_3$'s central C atom in this work), B is the atom center of interest in the neighboring molecules, η_c is a normalization constant selected so that $g_{\text{A-B}}(r \to \infty) = 1$, and the ensemble average is collected over all N molecules and N possible reference atoms. Figure 5.2 shows the $g(r)$ curves for bulk liquid $CHCl_3$ at 298 K. The first peak of $g_{\text{C–C}}(r)$ (blue curve) is located at 5.4 Å and the first minima at 7.5 Å, in good agreement with previous reports [27, 50, 37, 62]. The overall 'pseudo-spherical' shape of $CHCl_3$ does result in a $g_{\text{C–C}}(r)$ curve that resembles the radial distribution of close-packed spheres. The first two $g_{\text{C–C}}(r)$ peaks integrate to 8.9, indicating that the pseudo-spherical $CHCl_3$ is less tightly packed than actual close-packed spheres (like liquid argon or "Lennard-Jonesium"), whose first two peaks

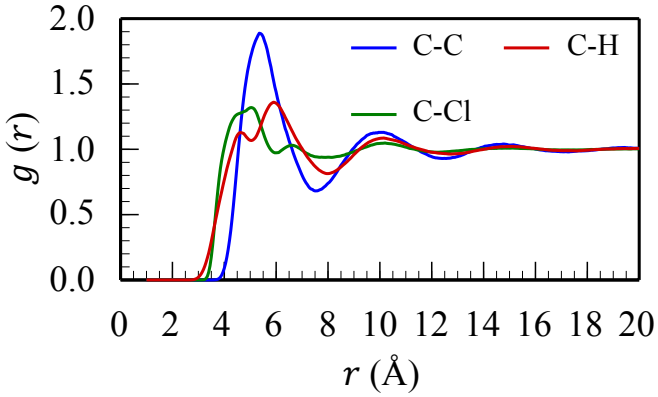

Figure 5.2: Radial distribution functions referencing the central carbon atom in bulk liquid $CHCl_3$. Curves are displayed for $g_{C-x}(r)$ where x = C (blue), x = Cl (green), and x = H (red).

integrate to about 12[34]. We also draw attention to the visible asymmetry of this first $g_{C–C}(r)$ peak, a feature that will be discussed at length later in this work. The green and red curves in Figure 5.2 are $g_{C–Cl}(r)$ and $g_{C–H}(r)$. These curves represent the distribution of the atoms bonded to the central carbon atom in a (nearly) tetrahedral arrangement. The symmetry of the radial distribution function is far less spherical when considering the arrangement of tetrahedral pendant atoms (like Cl in CCl_4) and even less so for the 'nearly tetrahedral' surrounding atoms in $CHCl_3$. In both cases, $g_{C–Cl}(r)$ and $g_{C–H}(r)$, the region of r spanned by the first peak of $g_{C–C}(r)$ is separated into multiple peaks due to the more complicated symmetry. Again, these radial distribution functions agree well with previously reported values from diffraction and simulation studies referenced above. To further the discussion of $CHCl_3$'s local structure, we expand the distribution function in Eq. (2) to include a 2-dimensional spatial distribution

function of the form

$$g_{\text{A-B}}(r) = \frac{1}{\eta_c}\left\langle \sum_{i=1}^{N} \delta(r - r_i) \cdot \delta(\theta - \theta_i) \right\rangle \tag{5.3}$$

where θ is defined to be the angle between two vectors that originate from the carbon atom of the reference $CHCl_3$ and point toward the reference H atom and the atom center of interest in surrounding $CHCl_3$ molecules. Figure 5.3a is schematic cartoon that illustrates this definition of the angle θ and distance r as used in $g_{\text{C–C}}(r, \theta)$ the calculation of $g_{\text{C–C}}(r, \theta)$. Figure 5.3b shows $g_{\text{C–C}}(r, \theta)$ for $CHCl_3$ juxtaposed with $g_{\text{C–C}}(r)$ to illustrate the additional structural insight provided by including the second dimension θ. Most notably, the first $g_{\text{C–C}}(r)$ peak transforms into a band in the $g_{\text{C–C}}(r, \theta)$ contour plot. The origin of the $g_{\text{C–C}}(r)$ peak's asymmetry is revealed by the non-circular shape and location of high g regions within this band, revealing significant ordering in θ-space. In the case of $g_{\text{C–C}}(r, \theta)$ the largest value of g in the first band is clearly centered around θ = 180° with a second, smaller region of high g centered around θ = 50°. This suggests that the carbon atoms of $CHCl_3$ molecules in the first solvation shell are primarily located near the center of the triangular face formed by the nearly tetrahedral reference molecule– with regions of high g located near the center of the face formed by the three chlorine atoms and at the center or edges of the Cl–Cl–H faces. The circular, dashed amber line in Figure 5.3b is centered at r = 0 and is included to serve as reference to and emphasize the non-spherical shape of the first solvation shell. Figure 5.4 shows the more complex case of $g_{\text{C–H}}(r, \theta)$, shown in juxtaposition with $g_{\text{C–H}}(r)$. As mentioned

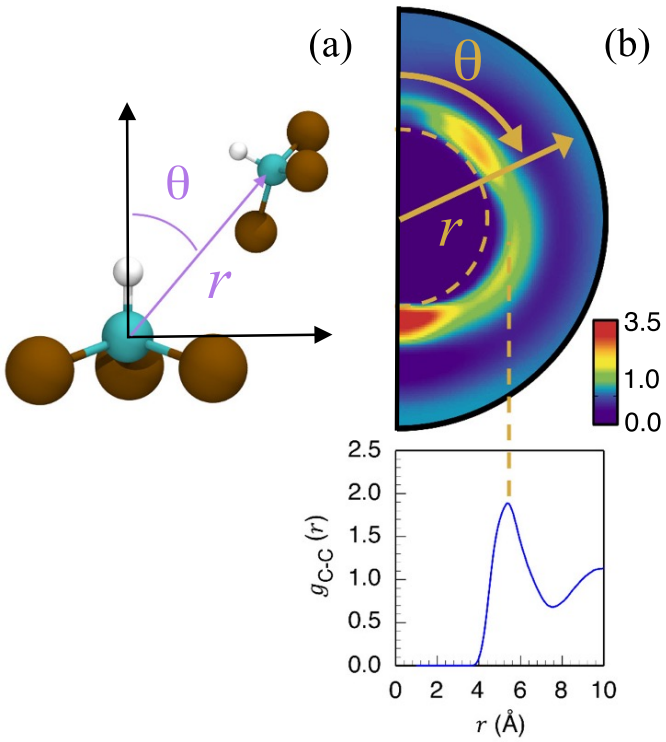

Figure 5.3: (a) Cartoon schematic of the variables r and θ, as used in $g_{\text{C–C}}(r, \theta)$. (b) The spatial distribution function $g_{\text{C–C}}(r, \theta)$ is presented in comparison with its one-dimensional projection onto $g_{\text{C–C}}(r)$.

above, the region of r-space that corresponds with the first peak of $g_{\text{C–C}}(r)$, $r < 8$ Å, is separated into two visible peaks in $g_{\text{C–H}}(r)$ due to the near-tetrahedral symmetry of $CHCl_3$, depending on whether the neighboring $CHCl_3$'s H atom points toward or away from the reference $CHCl_3$. These two peaks correspond to the two bands in $g_{\text{C–H}}(r, \theta)$. The difference between the 1- and 2-dimensional distribution functions is much more obvious in this case, where the innermost sub-layer (corresponding to the peak at $r \sim 4.6$ Å) does not span all values of θ, with no visible H population between $0° < \theta < 40°$. A circular, dashed amber line in $g_{\text{C–C}}(r, \theta)$, representing $r = 5$ Å and centered at $r = 0$ Å, is again included to emphasize the non-circular nature of the SDF bands. We also draw attention to the fact that,in Figure 5.4, the $g_{\text{C–H}}(r)$ peaks near $r = 4.6$ Å and $r = 6.0$ Å do not align with the corresponding $g_{\text{C–H}}(r, \theta)$ bands when vertical dashed lines are extended from the $g_{\text{C–H}}(r)$ peaks in Figure 5.4 to beyond $\theta = 90°$ in the SDF due to the non-circular shape of the bands. This characteristic non-circular structure will be discussed further when introducing the quantitative definition of polar stacking in liquid $CHCl_3$. After considering the local order of the central atoms with $g_{\text{C–C}}(r, \theta)$ and briefly introducing some of the more nuanced aspects present in SDFs of the tetrahedrally arranged outer atoms, we now compare MD simulation data with recently published experimental work. Figure 5.5 shows a side-by-side comparison of SDFs obtained by neutron diffraction experiment [201] and by our molecular dynamics simulations. In each circular SDF plot in Figure 5.5 the ND data is on the left half and MD data is on the right half. Separate scale bars are included for each hemisphere of SDF data for accuracy although efforts were made to replicate the color scale

used in Reference [201] to facilitate comparison between ND and MD data in Figure 5.5.[1] The leftmost SDF in Figure 5.5 shows the position of chlorine atoms in nearby $CHCl_3$ molecules, $g_{\text{C–Cl}}(r, \theta)$. The experimental and simulation data agree quite well, with the areas of high spatial density in the MD simulation located at similar r and θ. The general agreement is clear: neighboring Cl atoms are located in a well-defined first solvation shell with strong peaks centered at $\theta \approx 35°$ and $\theta \approx 180°$. We again note the non-circular nature of this band which corresponds to the broad, blunt peak in $g_{\text{C–Cl}}(r, \theta)$ centered near $r = 4.5$ Å. Examination of $g_{\text{C–Cl}}(r, \theta)$ reveals that this peak mostly consists of a merged doublet, with the $g_{\text{C–Cl}}(r, \theta)$ peak at $\theta = 180°$ corresponding to the smaller peak centered at $r = 4$ Å and the $\theta = 35°$ peak corresponding to the larger member of the doublet, centered at $r = 5$ Å. Upon further inspection, both ND and MD SDFs reveal that the first solvation shell consists of two subshells. The first subshell consists of the band at $r = 4$-5 Å. The second contains weak but certainly visible density peaks again centered at $\theta \approx 35°$ and $\theta \approx 180°$ located a few Å beyond the first subshell, at approximately $r = 6.8$ Å. This second shell is also visible in the $g_{\text{C–Cl}}(r)$ curve in Figure 5.3. The SDF plot in the right panel of Figure 5.5 considers the hydrogen atom, $g_{\text{C–H}}(r, \theta)$. Here the experimental and simulation data sets show a more noticeable difference. A well-defined first solvation shell consisting of two subshells is again present, but the spatial distribution of hydrogen differs. In the first subshell, closest to the central reference atom, the ND experiment reports a considerably more localized density of hydrogen located beneath the chlorine face, centered at $\theta = 180°$.

[1] Raw data corresponding to the ND contour plots in Figure 5.2 were not available at the time of publication (C. Salzmann, private conversation).

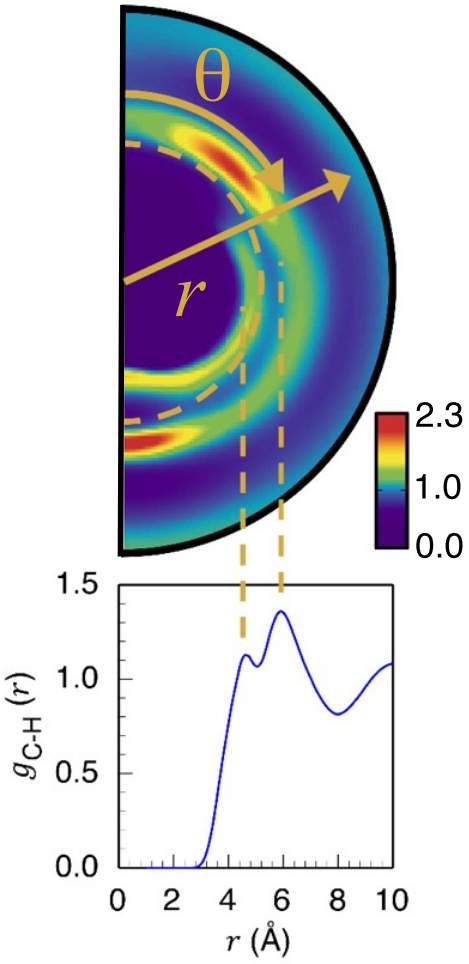

Figure 5.4: Spatial and radial distribution functions $g_{\mathrm{C–H}}(r, \theta)$ (top) and $g_{\mathrm{C–H}}(r)$ (bottom) for bulk liquid $CHCl_3$.

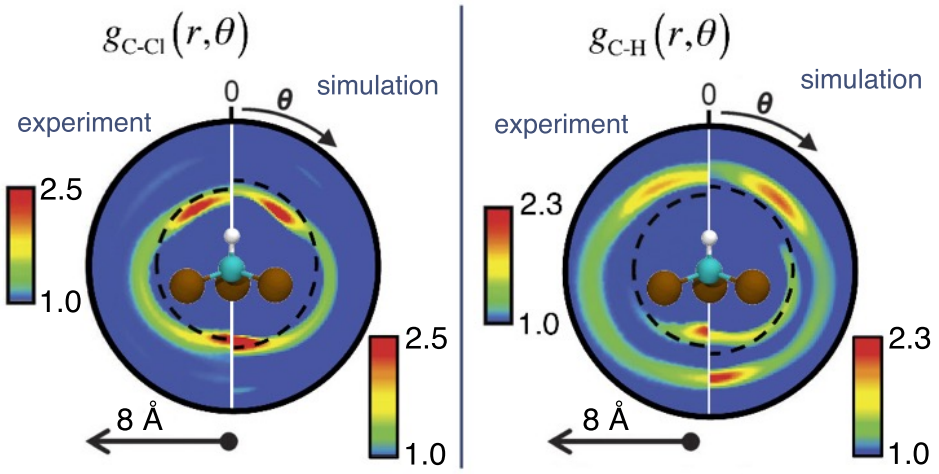

Figure 5.5: Side-by-side comparisons of spatial distribution functions obtained by neutron diffraction experiment and molecular dynamics simulations. These images consider the functions $g_{\text{C–Cl}}(r,\theta)$ (left) and $g_{\text{C–H}}(r,\theta)$ (right). Experimental data is adapted from Reference [201] with permission from The Royal Society of Chemistry.

The MD results found a similar but much more diffuse distribution of hydrogen atoms in this subshell. The second subshell is also different, with stronger peaks (more defined ordering) in the MD simulations, centered at $\theta \approx 45^\circ$ and $\theta \approx 180^\circ$. Both peaks in the second subshell band are centered at $r \approx 6$ Å.

5.3.2 Analysis, origin, and dynamics of 'polar stacking'

Overall, the 5-site fixed charge model reproduces the experimentally determined intermolecular ordering well enough to further investigate the 'polar stack' structures. We apply the definition of polar stacking as presented by Shephard et al. [201], where two chloroform molecules are considered to be members of a "stack" if their intermolecular C-H distance is between 2.0 Å and 4.2 Å and their H–C$\cdots$H angle is within the range $150^\circ < \theta < 210^\circ$. The dashed black circles in the experimental data shown

in Figure 5.5 describe this 4.2 Å radial cut-off. Our only modification to this definition was to increase this cut-off distance to 5.0 Å, which corresponds to the first minima of the first subshell in our calculated $g_{\text{C–H}}(r, \theta)$. These radial cut-offs are indicated by the dashed circular lines in the right hemisphere of each panel in Figure 5.5. Figure 5.6a compares polar stacking populations obtained by the ND experiment and our MD simulation. In the MD simulations 37.1% of the chloroform molecules take part in polar stacks of $n \geq 2$ as compared to 29.3% in the recent ND experiments. Additionally, the MD values for the binned stack lengths reported in Figure 5.6a are comparable but higher for all values of $n \geq 2$, some of the difference between MD and ND stacking populations is certainly due to our more liberal r cut-off value. This general agreement is interesting but leads us to the following, more general questions related to the local ordering in liquid chloroform: How much of this configuration is due to the presence of permanent dipoles? Do these structures result from the electrostatic interactions between neighbors? To answer these questions, we performed MD simulations again, leaving the Lennard-Jones parameters unchanged and setting the partial charges of all atom centers to zero. This simple change eliminates the permanent dipoles while maintaining the same intramolecular geometry[2] The resulting polar stacking populations for these zero-charge simulations are included as grey bars in Figure 5.6a. We find that eliminating the partial charges has a very small effect on the population of these polar stacks, reducing the molecules participating in polar stacks from 37.1% to 34.3%. Deletion of electrostatic contributions has a small effect, suggesting that these structures, as

[2]Setting partial charges on all atom centers to zero eliminates the electrostatic contribution but we also note that the Lennard-Jones term itself contains empirically determined cohesive factors (e.g. ϵ).

defined and detected, appear to be a function of geometrical packing, not dipole-dipole interaction. MD simulations also allow investigation into the dynamics of these structures, in particular the lifetime of the polar stacks. To calculate this lifetime, we track all detected groups of polar stacked $CHCl_3$ molecules and assign the variable h a value of 1 if the molecules are in a polar stack and a value of 0 if the stack has disassociated. We may then calculate the lifetime correlation function [31] as

$$C(t) = \frac{\langle h(t) \cdot h(0) \rangle}{\langle h(0) \cdot h(0) \rangle} \tag{5.4}$$

where $C(t)$ is calculated over all detected stacks and all time origins. Figure 5.6b contains a summary of the stack lifetimes from both the normal and zero-charge MD simulations. Lifetimes are presented for the case of all stacks ($n \geq 2$) and longer stacks ($n \geq 3$). As expected, longer stacks have a shorter lifetime and an ensemble of all detected stacks is longer lived. These lifetime correlation functions behave as double exponential decays, reflecting the contribution of both relatively fast reorientations and slower diffusion to the breakup of these structures. In longer stacks ($n \geq 3$) the short and long decay time constants are 0.085 ps and 0.75 ps. Averaging over all detected stacks ($n \geq 2$) the short and long time constants are 0.24 ps and 2.6 ps. Most importantly, these calculations show no significant decrease in lifetime when the electrostatic contribution to the intermolecular potential is removed. Similar lifetimes between normal and zero-charge stacks strongly suggest that the molecular dipoles do not make a significant contribution to the forces responsible for their presence. We also briefly

consider the effect of removing the electrostatics on intermolecular ordering. Figure 5.7 presents $g(r,\theta)$ data obtained from normal and zero-charge MD simulations in a format analogous to Figure 5.5. The left hand image in Figure 5.7 shows the spatial distribution of neighboring Cl atoms, $g_{\text{C–Cl}}(r,\theta)$. Differences between the normal and zero-charge contours are nearly imperceptible at this level of detail. The distributions of nearby H atoms show a more appreciable difference between the two simulations. The $g_{\text{C–H}}(r,\theta)$ contours most noticeably differ in the first solvation sub-shell. When electrostatics are active in the $CHCl_3$ model, nearby hydrogen atoms are mostly present near the Cl atoms and near the cavity formed by the three Cl atoms in the reference molecule. The population of H in the first subshell near the reference molecule H atom is essentially zero, presumably due to electrostatic repulsion. When electrostatics are disabled, the absence of this repulsion allows neighboring hydrogen atoms to populate the first subshell near the reference molecule's H atom center (at $\theta \approx 45°$). This increase in the value of $g_{\text{C–H}}(r,\theta)$ in this region of the first subshell is responsible for the accompanying decrease in the magnitude of the $g_{\text{C–H}}(r,\theta)$ peak in the second subshell, also located at $\theta \approx 45°$, which may be explained by a simple rotation of the surrounding $CHCl_3$ molecules. The difference between $g_{\text{C–H}}(r,\theta)$ data resulting from the normal and "no charge" simulations is also much more significant than the variation between the positional ordering of $CBrCl_3$ in normal and "no charge" simulations previously reported by Pothoczki, et al. [175] The difference between $g_{\text{C–H}}(r,\theta)$ and $g_{\text{C–Cl}}(r,\theta)$ is particularly noteworthy, since it suggests that electrostatic attraction or repulsion have little effect in regard to the ordering of the more massive and sterically hindered Cl (or Br)

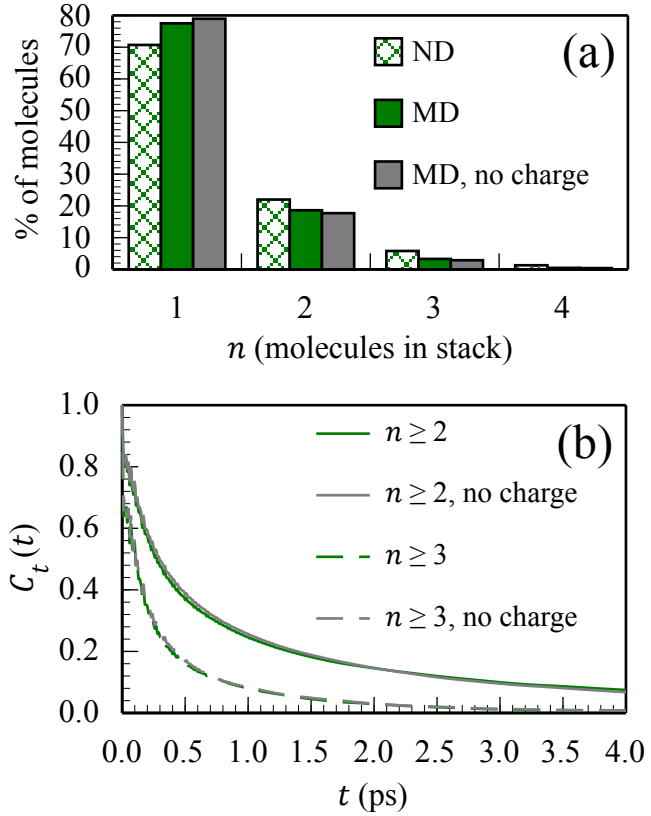

Figure 5.6: (a) Polar stacking populations from the experimental (patterned), MD (green), and zero-charge MD (grey) simulations. (b) Lifetime correlation functions, C_t, for polar stacks detected in the normal (green) and zero-charge (grey) MD simulations. Lifetime data is separated to describe both short (solid curves) and long (dashed curves) stacks.

atoms but that electrostatic repulsion appears to limit the proximity of the H atoms in neighboring $CHCl_3$ molecules. The 'polar stack' structures as defined by Shephard et al. are an interesting metric with which we may probe the local ordering of $CHCl_3$. Since these structures are defined by the C–H vector and position of neighboring H atoms, they quantify the population of $CHCl_3$ molecules with head-to-tail dipole arrangement. However, we again note that this definition only includes the position of three atoms

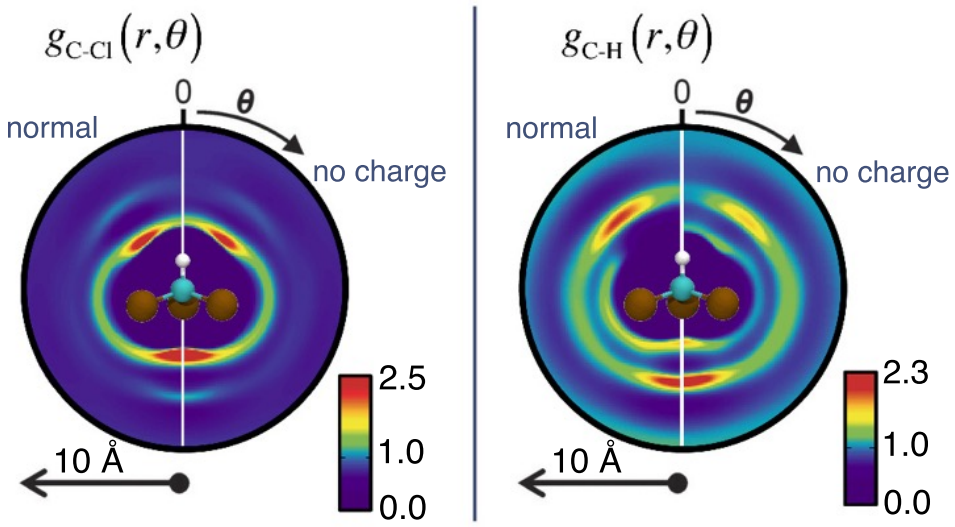

Figure 5.7: Spatial distribution functions obtained from MD simulations. These images consider the functions $g_{\text{C–Cl}}(r,\theta)$ (left) and $g_{\text{C–H}}(r,\theta)$ (right). The left side of each contour contains data obtained from a normal MD simulation of $CHCl_3$, the right side shows data from simulations where the electrostatic contributions have been removed ("no charge").

and does not comment on the collinearity of the head-to-tail dipoles it identifies, an important distinction to make when including these structures in the context of the larger discussion of the Apollo configuration [177]. To quantify $CHCl_3$ molecules in the Apollo configuration, we utilize the current polar stacking definition since it effectively identifies $CHCl_3$ molecules with head-to-tail dipole vectors. The angle ϕ is defined to be the angle formed by the dipole moment vectors of neighboring $CHCl_3$ molecules μ_i and μ_j in a polar stack, as illustrated by the cartoon inset in Figure 5.8. The green curve in Figure 5.8 shows the distribution of cos θ $(\hat{\mu}_i \cdot \hat{\mu}_j)$ for all $CHCl_3$ molecule pairs detected to be in a polar stack. The stacked molecules have a wide distribution of ϕ, with a peak at approximately 43°. The sub-population of polar-stacked $CHCl_3$ molecules that are

also in the Apollo configuration will depend on the choice of ϕ (a constraint on parallelism), which we define as 30°. The $\phi = 30°$ cut-off is indicated by the vertical dashed line in Figure 5.8 and, in these simulations, corresponds to 12.3% of the polar-stacked molecules being oriented in the Apollo configuration (by the definition described here). Since 37.1% of the total population is arranged in polar stacks, 4.6% of the total $CHCl_3$ population is in the Apollo configuration. Similarly, when the electrostatic contribution to the intermolecular potential energy is disabled (grey curve in Figure 5.8), 3.4% of the total population is in the Apollo configuration using this same definition. These values are close to 6.15%, the probability to obtain an analogue of the Apollo configuration when considering randomly oriented tetrahedral dice as calculated by Rey [180]. However $CHCl_3$ is not a perfect tetrahedral and the calculations in this work focus on only 1 of the 4 tetrahedral corners: the H atom. Therefore we may more appropriately compare our calculated values to 1.53% (6.15%/4) and note that our calculations differ by a few percent of the total population, which may be due to a real, beneficial geometric packing effect provided by the smaller H atom or (most likely) differences in our approach to this calculation. Regardless, the similarity of these disparately obtained values is another indication of the importance of geometrical packing considerations in the local intermolecular ordering of $CHCl_3$. As mentioned above, the grey curve in Figure 5.8 represents the angular distribution of polar stacked $CHCl_3$ molecules when the electrostatics are disabled. This distribution is very similar to the normal simulation (green curve), providing further evidence that the local intermolecular ordering in $CHCl_3$ is driven by geometric packing effects and does not result from electrostatic

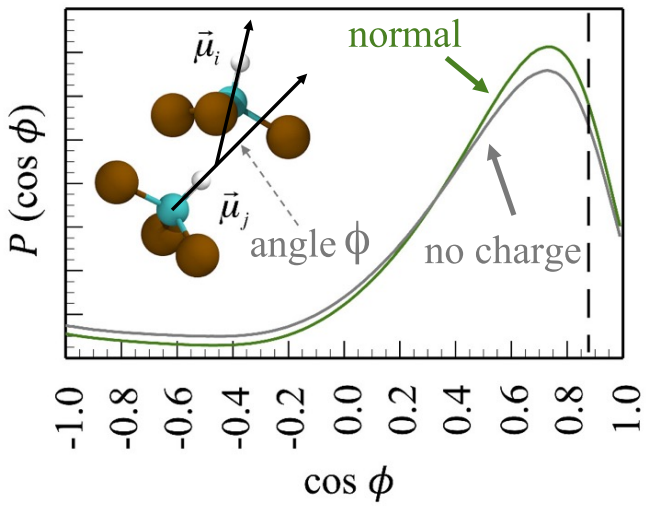

Figure 5.8: Distribution of angles between $CHCl_3$ dipole moment vectors for pairs of molecules participating in polar stacks. The green curve represents the distribution from the normal MD simulation and the grey curve represents the simulation run with the electrostatic contribution to the potential energy disabled.

effects.

5.4 Conclusions

In summary, our MD simulations do confirm the recently reported 'polar stacking' populations detected in ND experiments. However, by "turning off" the $CHCl_3$'s permanent dipole in the simulations, we find that the dipole has little impact on this aspect of intermolecular ordering of $CHCl_3$: The polar stacking populations are nearly unchanged when the electrostatic contributions to the potential energy are set to zero. Dynamic calculations also suggest nearly identical lifetimes of these polar stacks in the normal and zero-charge simulations, further diminishing the importance of the dipole in the self-assembly of these structures. This evidence leads us to believe that these 'polar

stacks' are the result of steric packing, not a cooperative ordering driven by the electrostatic interaction between neighboring dipoles. These findings do not necessarily rule out the 'polar stacks' of $CHCl_3$ as beneficial solvation agents, but suggest (if this assertion is correct) that it is the nearly-tetrahedral symmetry of $CHCl_3$ that contributes to its solvation ability, making $CHCl_3$ a superior solvent compared to species with similar dipole character but more complicated packing geometries. Extending the analysis of polar stacking, we find that a distribution of the angles formed by 'stacked' dipoles suggests that only about 12% of 'stacked' $CHCl_3$ molecules have reasonably collinear dipole moment vectors, further supporting previous assertions that the 'Apollo configuration' represents only a very small fraction of the total population in bulk liquid $CHCl_3$.

Acknowledgments

This work has been supported by the National Science Foundation through grant CHE-1363076. The authors would like to thank Professor C. G. Salzmann for providing information about his work and for valuable comments.

Chapter 6

Geometric and energetic considerations of surface fluctuations during ion transfer across the water-immiscible organic liquid interface

6.1 Introduction

Most of our current understanding of ion transfer across the interface between two immiscible liquids (typically water and a weakly polar solvent) is based on electrochemical measurements (see References [191, 139, 219] for recent reviews) and the corresponding theoretical and computational studies of the free energy change associated with this process (see References [55] and [18] for recent reviews). Considerably more challenging is the experimental determination and interpretation of the dynam-

ics of ion transfer. Specifically, while one can describe a voltage-current relationship for the transfer of ions across the interface in terms of first order rate constants, the published values of these rate constants over the last three decades seem to depend on the experimental method used. The various reasons provided for this situation include limitations in the instruments' time resolution, uncertainty in the value of the electric potential drop across the interface, and unclear separation between diffusion through the bulk phases and the crossing of the interface, among others. [139, 55] Putting aside the experimental uncertainty in the values of rate constants, development of a quantitative predictive theory for the rate of ion transfer requires a reasonable understanding of the mechanism by which an ion exchanges its solvation environment as it crosses the interface. Existing theoretical models such as those based on the Nernst-Planck equation (diffusion in an external field) have been successful in simulating experimentally observable cyclic voltammetry curves. [55] However, ion transfer rate constants derived from this description give values that are up to two orders of magnitude larger than measured. [55, 94] The slower rate constant suggests a barrier or some type of retardation effects. Better agreement with experiments can be obtained when the diffusion equation is numerically solved with a molecularly derived potential of mean force (PMF) as an input external force. [9] If the PMF exhibits a barrier, one could employ transition state theory to estimate the rate constant. [190] While the PMF calculated from a molecularly detailed model can be useful for some clues about the mechanism of ion transfer (and the nature of the barrier), it is an equilibrium mean field description in which the role of dynamic fluctuations is mostly ignored. Molecular dynamics sim-

ulations provide ample evidence that these fluctuations are critical for elucidating the mechanism of the transfer process. In particular, simulations suggest the importance of water molecules' protrusions (water "fingers") into the organic phase as a mechanism that, while necessary, results in slowing down the transfer rate into the organic phase and enhancing the reverse process by producing water protrusions in response to the approaching ion. [10, 194, 192, 45, 54, 76] Theoretical models based on this picture provide additional support for this mechanism. For example, Marcus has estimated the rate of ion attachment and detachment from a water "finger" and diffusion along it and concluded that the rate limiting step for ion transfer is the motion of an ion along a "solvation coordinate." [127] Urbakh, Kornyshev, and co-workers developed a coupled, two-dimensional Langevin equation model of ion transfer in which one degree of freedom describes the ion's motion and the second describes dynamic interfacial fluctuations modeled as capillary waves. [108, 221] Numerical solutions and the analytical expression derived for the rate constant suggests that ion-surface coupling can result in a slowing down of the ion motion relative to simple diffusion. In order to obtain molecular-level insight into the ion transfer process, it is useful to describe the collective ion–solvent interactions using a single (or a few) degree(s) of freedom "reaction coordinate(s)." In this paper, we utilize two independent collective coordinates and use them to examine both the thermodynamic and the dynamic fluctuations during the transfer of a hydrophilic Cl^- ion across the water/nitrobenzene interface. One of these coordinates, suggested by Schweighofer and Benjamin, [194] is based on the solvation energy of the ion. The other, recently proposed by Morita and co-workers, is geometrically based and attempts

to characterize the finger structure formed during the ion transfer. [106] The rest of the paper is organized as follows. In Section II, we describe the simulation details, the umbrella sampling free energy calculations with biasing potential, and the two reaction coordinate calculations. In Section III, we discuss the results of these calculations and in Section IV, we summarize this work and present our conclusions.

6.2 Systems and Methods

6.2.1 Simulation details

The water/nitrobenzene liquid/liquid interfacial system consists of two adjacent slabs of 986 water molecules and 252 nitrobenzene molecules in a 31.28 $\times$ 31.28 $\times$ 300.0 Å rectangular box. The liquid/liquid interface is located in the x-y plane at $z > 0$, with the water phase in the region of $z < 0$ and the nitrobenzene phase in the $z > 0$ region. Each liquid phase is in equilibrium with its respective vapor phase; only one liquid/liquid interface is present. Periodic boundary conditions are applied in all directions and a soft reflecting potential wall is located 5 Å from the simulation box boundaries in the z-direction to prevent molecules from crossing into the adjacent vapor phase. Intermolecular interaction potentials are represented as the pairwise sum of Lennard-Jones and Coulomb terms,

$$U_{ij}(r) = \sum_{i<j} 4\epsilon_{ij} \left[\left(\frac{\sigma_{ij}}{r} \right)^{12} - \left(\frac{\sigma_{ij}}{r} \right)^{6} \right] + \frac{q_i q_j}{4\pi r \epsilon_0} \tag{6.1}$$

where r is the distance between atom centers i and j. Standard Lorentz-Berthelot combining rules, $\sigma_{ij} = (\sigma_i + \sigma_j)/2$ and $\epsilon_{ij} = (\epsilon_i \epsilon_j)^{1/2}$, are used to generate Lennard-Jones parameters for all mixed interactions. For water, we use a version of the flexible simple point charge (SPC) model [22] with intramolecular potentials as described by Kuchitsu and Morino. [109] The nitrobenzene molecules are modeled using a 14-site all-atom model described previously. [136] In brief, this nitrobenzene model uses intramolecular parameters taken from the AMBER force field [226] and modified intermolecular parameters taken from *ab initio* calculations and reproduces the experimental dipole moment and enthalpy of vaporization. The chloride ion Lennard-Jones parameters ($\sigma = 3.934$ Å and $\epsilon = 0.832$ kcal/mol) were used in previous simulations and give reasonable agreement with the experimental hydration free energy. [15] Molecular dynamics simulations are performed with our in-house MD software that uses the velocity Verlet algorithm to integrate the equations of motion. Unless otherwise specified, all reported simulation data are averaged over 10 independently generated starting configurations, each run for 1 ns, for a total ensemble average over 10 ns of simulation time. All simulations were performed at 298 K and with an integration time step of 0.5 fs.

6.2.2 Free energy calculations

The local free energy of the single chloride ion is given by

$$A(z) = -k_B T \ln P(z), P(z) = \langle \delta(z - z_I) \rangle, \tag{6.2}$$

where δ is the Dirac delta function and z_I is the ion's position along the axis normal to the interface. $P(z)$ is the probability to find the ion at z and the ensemble average is calculated over all possible solvent configurations while the ion is located at $z_I = z$. The reversible work required to move the ion from position z_1 to z_2 would be $A(z_1) - A(z_2)$. While direct sampling of the ion position can theoretically be used to compute $A(z)$, in practice if at a given interval $A(z)$ varies significantly (more than 5 k_BT), and/or if significant structural relaxation of the solvents is necessary to sample equilibrium configurations (as is the case here with the formation of "water fingers"), a different approach is required. In the umbrella sampling method, [1, 34, 174] the interval of interest is divided into a series of N overlapping lamellae parallel to the liquid-liquid interface such that within each lamella a statistically meaningful sampling of z_I (using the 10 ns trajectory) can be obtained and used to calculate the corresponding $A_n(z)$,

$$A_n z = -k_B T \ln P_n(z), \tag{6.3}$$

where $P_n(z)$ is the chloride ion z coordinate probability distribution within lamella n. In the simulations described below, the lamellae are 3 Å wide, overlap by 1 Å, and span the simulation box from the region of bulk water to bulk nitrobenzene. The ion is constrained within a specified lamella by a window potential (which is zero when the ion is inside that window but rises rapidly when the ion attempts to escape the window) through the course of the 10 ns trajectory. The series of $A_n(z)$ segments ($n = 1, 2, \ldots, N$) is combined by using their overlapping regions [110, 105] to arrive

at the complete free energy profile for the entire interval of interest. If $A(z)$ varies rapidly in a given region, most often due to the water finger "pulling" the ion toward the aqueous phase, poor statistical sampling may arise. To accelerate the exploration of phase space and improve sampling statistics in this region, we apply a biasing potential $U_{bias}(z)$ to the ion, modifying the total ion-solvent interaction energy,

$$U_I^b = U_I - U_{bias}(z), \tag{6.4}$$

where $U_{bias}(z)$ is a function of the ion z position only and is typically of the form

$$U_{bias}(z) = \alpha \frac{(1 + \tanh[\lambda(z - \zeta)])}{2}, \tag{6.5}$$

where the constants α, γ, and ζ are selected (and given in Appendix D) so that the biasing potential approximates $A_n(z)$. The free energy profile in lamella with applied bias is therefore calculated as follows: [1]

$$A_n^b(z) = -k_B T \ln P_n(z) + U_{bias}(z). \tag{6.6}$$

6.2.3 Reaction coordinates

Quantitatively describing and tracking the transfer of a single ion from the aqueous phase to an adjacent immiscible phase has been challenging since early work. [151] The most obvious coordinate would be the ion's distance from the liquid/liquid interface along an axis normal to the interface. Extracting the ion's position in simulation z-space

is trivial, but assigning a reference z-coordinate value to a liquid/liquid interface is not particularly clear due to fluctuations inherent to the liquid/liquid interface, including interfacial distortion caused by the water finger itself. More importantly, describing the state of the system using a single coordinate assumes that the two solvents provide a mean field for the motion of the ion and ignores solvent fluctuations. A relatively simple approach to take into account these fluctuations is to add an additional coordinate describing the interface. For example, as mentioned in the Introduction, Urbakh, Kornyshev and co-workers proposed a geometrical coordinate describing interface deformation and fluctuations. In this paper, we consider in detail two coordinates: an energy based one introduced by Schweighofer and Benjamin [194] and a geometric one recently introduced by Morita and co-workers. [106] Both of these coordinates can be computed for instantaneous system configurations and represent, in some sense to be explained below, a complimentary description of the environment experienced by the ion.

6.2.3.1 Solvation coordinate

For a two-phase system we define a solvation coordinate for each solvent,

$$s_W = U_{I-W}/U_{I-W}^{bulk}, \tag{6.7}$$

$$s_{NB} = U_{I-NB}/U_{I-NB}^{bulk} \tag{6.8}$$

where the subscripts W and NB represent the water or nitrobenzene solvents, I represents the ion, U is the total intermolecular interaction potential energy between the ion and the specified solvent, and U^{bulk} is the average total ion- solvent interaction potential when the ion is in the bulk solvent at the same temperature. Values of U^{bulk} (U^{bulk}_{I-W} = -155.5 kcal/mol and U^{bulk}_{I-NB} = -89.39 kcal/mol) are calculated by molecular dynamics simulations of a single ion in the uniform bulk liquids using the same force fields and parameters described above. Additional details regarding U^{bulk} calculations are provided in Appendix D. The solvation coordinates consider both electrostatic and Lennard-Jones potentials between the ion and all solvent molecules present in the simulation. Note that s_W and s_{NB} are dimensionless and implicitly dependent on the ion's location z, in addition to the coordinates of all solvent molecules (although mainly sensitive to the solvent molecules in the nearest solvation shells). We expect the following: $s_W(z \rightarrow \text{bulk water}) = 1$, $s_W(z \rightarrow \text{bulkliquid}) = f$, where $f > 1$ represents the interaction of the ion with (mostly) the fraction of the hydration shell that was co-transferred to the organic phase ($f \approx 0$ for a hydrophobic ion).

6.2.3.2 Water protrusions coordinate

Recently, Kikkawa et al. employed mathematical graph theory to develop a new geometrical coordinate useful for describing ion transfer between water and an adjacent immiscible phase. [106] To calculate the "water finger coordinate," w, the ion and water molecules are treated as vertices in an undirected graph. The edges of the graph are the geometrical distances between the vertices. A connected path between the

ion and bulk water is defined by the requirement that all edges along the path are shorter than a threshold distance. At each system configuration, the coordinate w is equal to the minimum threshold distance that will give rise to a connected path. For example, a "naked" ion with $z = +10$ Å in a system where the interface is constrained at $z = 0$ Å would have $w \approx 10$ Å. If a water molecule was present with the same x and y coordinates as the ion and $z = 4$ Å, $w \approx 6$ Å.Our implementation of this algorithm varies slightly; we assign the position of the water oxygen molecule as the vertex representing each water molecule instead of the water molecule's center of mass. This assignment allows us to directly compare the water finger coordinate to the commonly used geometrical definition of water-water hydrogen bonds, where $r_{OO} < 3.4$ Å. [189, 135, 124] A hydrated (or partially hydrated) ion "connected" to the bulk water phase via an intact water finger would have a value of w less than or equal to this upper bound of 3.4 Å, which we shall refer to as $r_{OO}^{\max}$. For simplicity, we define the condition of "connected to bulk water" when the ion is connected to a water molecule whose oxygen molecule is located at $z < 0$. This is sufficient since finger breakup always occurs at $z > 0$. It is useful to note at this point several features of this coordinate: When the ion is in bulk water, $\langle w \rangle \approx$ peak position of the O–O radial distribution function (or ion–oxygen RDF peak position if longer) regardless of the position z_I of the ion. When the ion is in the organic phase connected via water finger to the aqueous phase, $w \approx$ O–O distance corresponding to the longest hydrogen bond. As the water finger breaks, w corresponds to the distance between the two nearest water molecules–one that belongs to the ion partial hydration shell and one to the water phase, regardless of the size of the ion's hydration shell. If

the ion in the organic phase is "naked," w is equal to the distance between the ion and the closest water molecule.

6.2.3.3 Ion transfer simulations across a molecularly sharp interface

To gain further insight into the role of solvent fluctuations during the ion transfer process, we also consider a system in which the water/nitrobenzene interface is constrained to be a molecularly sharp ("flat") interface. This is done by adding a soft reflecting potential in the x-y plane at $z = 0$ that acts on any water or nitrobenzene molecule whose center of mass attempts to cross the $z = 0$ plane. This external potential essentially restricts the water molecules to the $z < 0$ region and the nitrobenzene molecules to the $z > 0$ region and gives rise to a molecularly sharp interface, where capillary fluctuations are strongly dampened. The reflecting potential is a function of the distance from the center of mass of each molecule so that perturbations to the molecular orientational distribution are minimized. The implemented potential is of the form

$$\begin{aligned} U_n^W &= \gamma H(z_{COM}) z_{COM}^2 \\ U_n^{NB} &= \gamma H(-z_{COM}) z_{COM}^2 \end{aligned} \tag{6.9}$$

where U_n^W is the reflecting potential on water molecule n, whose center of mass is located at z_{COM} along the interface normal and $H(x)$ is the Heaviside step function ($H(x) = 0$ for $x < 0$; $H(x) = 1$ for $x \geq 0$). Similarly, U_n^{NB} is the reflecting potential on nitrobenzene molecule n. γ is a force constant whose exact value is not important. In the simulations described below we use $\gamma = 1200$ kcal mol^{-1} Å^2. The reflecting potential

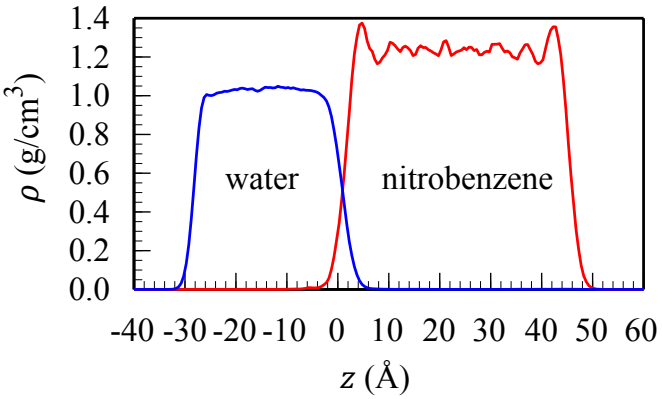

Figure 6.1: Density profiles of water (blue) and nitrobenzene (red) at T = 298K, averaged over 50,000 configurations recorded during 10 ns of simulation time.

prevents the ion from carrying any part of its hydration shell across the interface and prevents the formation of the water "finger."

6.3 Results and Discussion

Figure 6.1 shows the density profiles of water and nitrobenzene with the ion in bulk water, confined to a window 17.5 Å $< z_I <$ 14.5 Å. We chose $z = 0$ to be the location of the Gibbs Dividing Surface (GDS, the plane parallel to interface where the water density is approximately 50% of the bulk value. For the exact definition see Reference [184]). The interface region is quite narrow (the distance over which the density of water varies from 90% to 10% of the bulk value is 5 Å). The properties of the neat water/nitrobenzene interface have been described elsewhere. [136] The ion transfer equilibrium calculations described below are carried out with the ion location extending from the bulk water ($z = 15$ Å) to the bulk nitrobenzene regions ($z = 20$

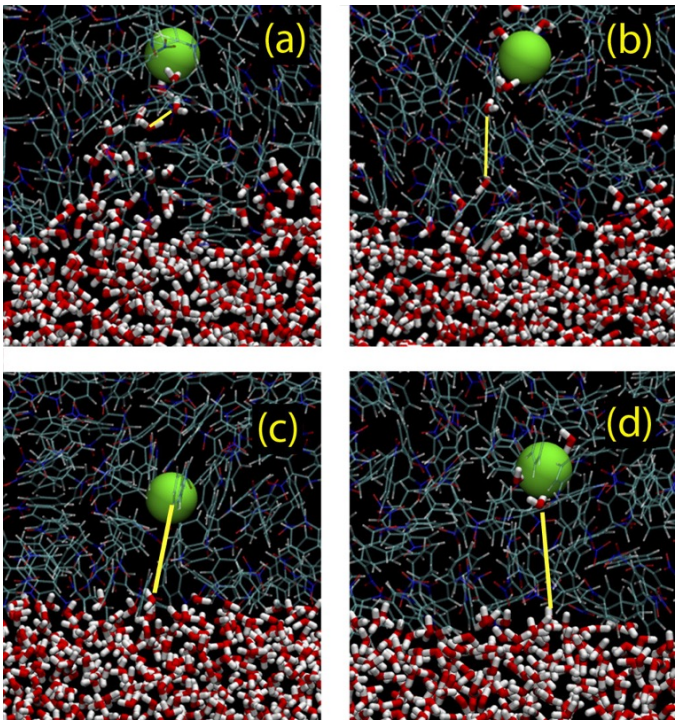

Figure 6.2: Representative snapshots of a single chloride ion (green sphere) interacting with the normal [(a) and (b)] and flat [(c) and (d)] water/nitrobenzene interface. The approximate value of the water protrusion coordinate, w, is illustrated by the yellow lines in each image.

Å). Figure 6.2 depicts several snapshots from the simulations, which illustrate some of the important structural considerations involved in the ion transfer process. In an unconstrained system (Figure 6.2(a)) as the chloride ion moves from the aqueous phase toward the nitrobenzene phase, it carries with it most of its hydration shell, which creates a local disturbance at the interface. Hydration shell water molecules remain hydrogen bonded to neighboring water molecules, and the ion remains tethered to the aqueous phase by the water "finger" structure. As the ion moves further into the organic phase, surface distortions are increased, the water "finger" elongates and finally

breaks, typically when it has extended about 1 nm into the organic phase, leaving the ion with a partial hydration shell (Figure 6.2(b)). In contrast, when the interface is constrained to be flat, the ion is transferred as a single species into the organic phase (Figure 6.2(c)). Panel d is a snapshot from a simulation in which the chloride ion and three water molecules $Cl(H_2O)_3$ are transferred across the flat interface, which is to be discussed below. The free energy profiles corresponding to the different ion transfer processes examined here are shown in Figure 6.3(a). These free energy profiles were calculated as explained in Section II B. Additional details, including the values of the biasing potentials used, are given in Appendix D. The free energy profile for the transfer of the chloride ion across the normal water/nitrobenzene interface has a shallow minimum at about $z = 2$ Å. From that point, it monotonically increases as the ion is transferred across the interface to bulk nitrobenzene. The net free energy of transfer is 12 ± 1 kcal/mol. We estimate the error in this calculation by considering the standard deviation of A values from 10 free energy profiles generated from each of the 10 independent initial configurations. Statistical fluctuations are additive as the adjacent windows are "stitched together" to form a continuous free energy profile. This approach to error estimation is therefore quite conservative since the curve reported in Figure 6.3(a) averages data from all 10 configurations within each lamella *before* consolidating them into one continuous curve describing the ion transfer event, dampening statistical fluctuations between the independent transfer events. This result may be compared with the estimated experimental value [197] of 9.5 ± 0.5 kcal/mol. The calculated value of A would presumably be lower and closer to experimental results with the implementation

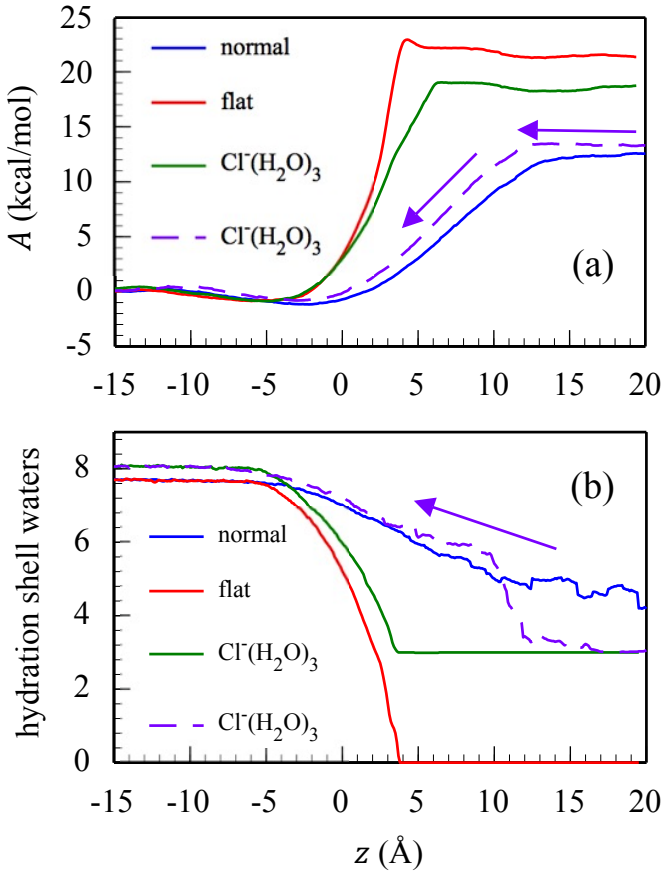

Figure 6.3: (a) Free energy profiles of the chloride ion across the water/nitrobenzene interface. (b) Average number of water molecules in the ion's solvation shell during the transfer event. Blue, red, and green solid lines correspond to the transfer across the normal interface, the flat interface, and to the transfer of $Cl^-(H_2O)_3$ across the flat interface, respectively. Dashed lines correspond to the "back" transfer of $Cl^-(H_2O)_3$ from nitrobenzene to water across the normal interface. $z = 0$ is the location of the Gibbs Dividing Surface (GDS).

of a polarizable nitrobenzene force field. Figure 6.3(b) depicts the corresponding average number of hydration shell water molecules (defined as the number of water molecules whose oxygen-chloride ion distance is less than the first minimum of the bulk O–Cl^- radial distribution function $r_{min} = 3.85$ Å). The change in the average hydration number as a function of z tracks the change in the free energy profile. The decline (relative to the bulk value of 7.70 ± 0.05) begins at around $z = 3$ Å and reaches the value of 4.7 ± 0.6 when the ion is located within the range 15 Å $< z <$ 18 Å. Within this region the water finger fluctuation has broken and the ion and its remaining hydration shell move toward the bulk organic phase. The increasing fluctuation in hydration shell population is due to the breakup and formation of the water finger, which is most likely to happen when the ion is near $z \approx 12$ Å when the finger is fully extended, as will be discussed below. When the interface is constrained to be molecularly sharp and the ion is transferred without any water molecules, the free energy profile is significantly different (red curve in Figure 6.3(a)): The shallow local minimum is gone, the rise in the free energy occurs at smaller values of z compared with the normal interface and the net free energy of transfer is significantly larger (23 ± 1 kcal/mol). Clearly, transferring the ion into the organic phase is much more favorable when some number of water molecules accompany the ion. Since the initial increase in the free energy correlates quite closely with the reduced number of hydration shell water molecules, we can attribute the steeper rise in the free energy to the more rapid decrease in the hydration number (green line in Figure 6.3(b)), made necessary by the constraint imposed on the interface. A continuum viewpoint of this process can be described by invoking the model of a sphere moving

toward a flat surface in a viscous fluid. [127] In this model, the resistance deviates from Stokes' formula when the sphere approaches the surface, increasing with $1/d$, where d is the distance between the sphere and the surface. In the normal, unconstrained system this additional resistance results in the distortion of the interface, caused by the approaching ion. In the unconstrained system this resistance of the surface to the ion's approach is considerably smaller than the approach toward a flat, solid surface since the unconstrained liquid/liquid interface may distort in response to the ion's motion. Since the water molecules are unable to cross the $z = 0$ plane, the ion must approach the interface as it would a solid surface (and then pass through it). The dramatically increased free energy requirement of the flat interface system in the region of -3 Å $> z > +3$ Å illustrates the energetic value of the surface distortion. These results demonstrate that, in the unconstrained ("normal") simulation, interfacial distortions caused by the approach of the ion to the interface significantly reduce the free energy required for ion transfer. With the flat interface constraint, we are able to gain some clues about the energetic benefit of interfacial fluctuations, surface distortion, and water finger formation during the ion transfer event. However, this constraint also completely strips the ion of its water solvation shell. Co-transfer of part of this hydration shell is a well-established phenomenon, witnessed in both experiment and simulation (for a recent review see Reference [18]) that should contribute toward the reduction of free energy in liquid/liquid ion transfer. [182] We can provide a partial account of this effect by considering the transfer of the ion with a fixed number n of water molecules across the constrained flat interface. In these simulations, we set $n = 3$, which is close to the

experimentally accepted number. [167] Oxygen atoms of the 3 water molecules assigned to the solvation shell are attached to the chloride ion using the interaction potential given by $\gamma H(x)x^2; x = |\mathbf{r}_{\mathrm{Cl}} - \mathbf{r}_{\mathrm{O}}| - r_{min}$, where the constant γ is 1200 kcal·mol^{-1}Å^{-2}, H is the Heaviside step function, and $r_{min} = 3.85$ Å is the location of the first minimum of the chloride-oxygen water radial distribution function. The three water molecules tethered to the ion are not influenced by the external potential that keeps the interface flat and therefore are allowed to cross into the organic phase with the ion. Thus, we are in fact considering the transfer of the stable species $Cl^-(H_2O)_3$ across the flat interface. The addition of this small solvation shell reduces the free energy of ion transfer across the flat, constrained interface by 17% compared to the transfer of the fully "naked" ion. The shape of the free energy curves is different as well (Figure 6.3(a)): When 3 water molecules accompany the ion, the free energy plateau begins slightly further into the organic phase due to the presence of hydration shell water. The hydration shell allows the ion to remain within hydrogen bonding distance to the aqueous phase by the length of an additional water-water hydrogen bond. This additional water-water hydrogen bond extends beyond the potential barrier imposed at $z = 0$. The second feature considers the small peak prior to the plateau, which we assign to the energetics of rearranging interfacial water molecules to interact with approaching or leaving ion. This peak is not readily present in the $Cl^-(H_2O)_3$ simulation, which is a reasonable result since the small solvation shell water molecules would require less energy to reintegrate with the aqueous phase than the naked chloride ion. Given the relatively long lifetime of water protrusions and other surface fluctuations and given

the uncertainty and variability in the number of water molecules that are co-extracted with the ion, it is reasonable to question whether the free energy curves depicted in Figure 6.3 describe true equilibrium behavior. To partially explore this issue and gain additional insight into the ion transfer process, we have also attempted to calculate the free energy profile for the back transfer of the ion from the nitrobenzene to the aqueous phase. The challenge here is to correctly select the initial state of the ion in the organic phase. One approach is to start from a configuration reached during the forward (water $\rightarrow$ organic) simulations. [45, 54] In reality, an ensemble average over properly weighted different hydration clusters, $Cl^-(H_2O)_n$, would be required to truly describe the reverse process. In Figure 6.3, we show the free energy profile calculated for the transfer of $Cl^-(H_2O)_3$ from the organic phase to the aqueous phase across the normal interface as the process with the most likely largest contribution. Indeed the free energy profile (dashed line Figure 6.3(a)) is quite close to the curve for the normal transfer of Cl^- from water to nitrobenzene. Note that the average hydration number for this reverse transfer (dashed line Figure 6.3(b)) increases as the $Cl^-(H_2O)_3$ approaches the interface due to the water surface fluctuations. The increase begins near $z = 12$ Å, which is the point identified earlier as the average maximum length of water fingers before breakup in the transfer from water to nitrobenzene. These results suggest that the energetics of interfacial ion transfer (for small ions) is largely dictated by surface distortion and the formation of the water finger structure. As the finger extends to near maximum length, just prior to breaking, the structure is typically a single chain of hydrogen-bonded water molecules surrounded by molecules of the adjacent immiscible

phase. Breaking the elongated water finger requires significantly less free energy than stripping the ion from the hydration shell as nitrobenzene molecules that surround the water finger interact and interfere with the increasingly fragile chain of hydrogen-bonded water. Simulations of the constrained surface do not allow the distortion of the surface of the random motion of nitrobenzene molecules to reduce the energetic cost of ion transfer. However when we allow a fixed number of water molecules to co-transfer with the water, we partially account for the energetic benefit of this co-transfer. Crossing the interface is quite similar in both flat-interface simulations, but the hydrated ion demonstrates an "easier" transition into the organic phase. Although these PMF curves are calculated using an equilibrium umbrella sampling technique with a single ion, we may use these results to comment on the observable dynamics of a macroscopic system. However, it should be again noted that the physical constraints applied in the flat and $Cl^-(H_2O)_3$ systems to deconstruct the energetics of this ion transfer do not have realistic experimental analogues. If equilibrated systems of these designs could exist, we should expect that they would have Boltzmann-weighted ion populations related to the free energy differences calculated above. Further, the flux of the chloride ions across the interface should be related to the free energy curves in Figure 6.3(a) by

$$j_I \propto e^{-\beta \Delta A}, \tag{6.10}$$

where j_I is the flux across the interface, β is $1/(k_B T)$, and ΔA is the difference between the lowest and highest values in the respective PMF curve. With this approach,

the flat interface constraint reduces ion flux by about a factor of 107. When the 3-water solvation shell is allowed to co-transfer in the $Cl^-(H_2O)_3$ simulation, the flux increases by about 2 orders of magnitude, about 105 times slower than in the unconstrained system. The description of the ion transfer process using only the ion's position along the interface normal averages out the detailed mechanistic picture qualitatively described above. As the mechanism of ion transfer is intimately connected with the deformation of the interface, formation of the water "finger," and the co-transfer of some hydration shell water molecules, additional coordinates to describe this information are required to develop a quantitative account of the transfer process. In general, for any generalized coordinate $\Gamma(\mathbf{r})$ (such as s_W, s_{NB}, or w defined above) where $\mathbf{r}$ represents all nuclear positions (including the ion location x_I, y_I, z_I), the local equilibrium average $\langle\Gamma\rangle(z)$ is given by where $f(\mathbf{r})$ is the normalized phase space density ($f(\mathbf{r}) = \exp(-\beta U(\mathbf{r}))/\int \exp(-\beta U(\mathbf{r}))d\mathbf{r}, U(r)$ is the total system potential energy, and $\beta = 1/k_BT$) and z_I is the ion's location along the interface normal. The equilibrium simulations in each of the overlapping windows provide statistically reliable data to compute these ensemble averages, which we examine next. The three panels in Figure 6.4 show the average values of the water solvation coordinate $\langle s_W\rangle$ and the nitrobenzene solvation coordinate $\langle s_{NB}\rangle$ as a function of the ion's z position for the three systems examined. Since most (about 70%) of the ion-water interaction energy is determined by the molecules in the first hydration shell, it is not surprising that the three $\langle s_W\rangle(z)$ curves in Figure 6.4(a) resemble the corresponding curves in Figure 6.3(b). Under normal conditions, $\langle s_W\rangle$ gradually decreases as the ion moves into the organic phase. The

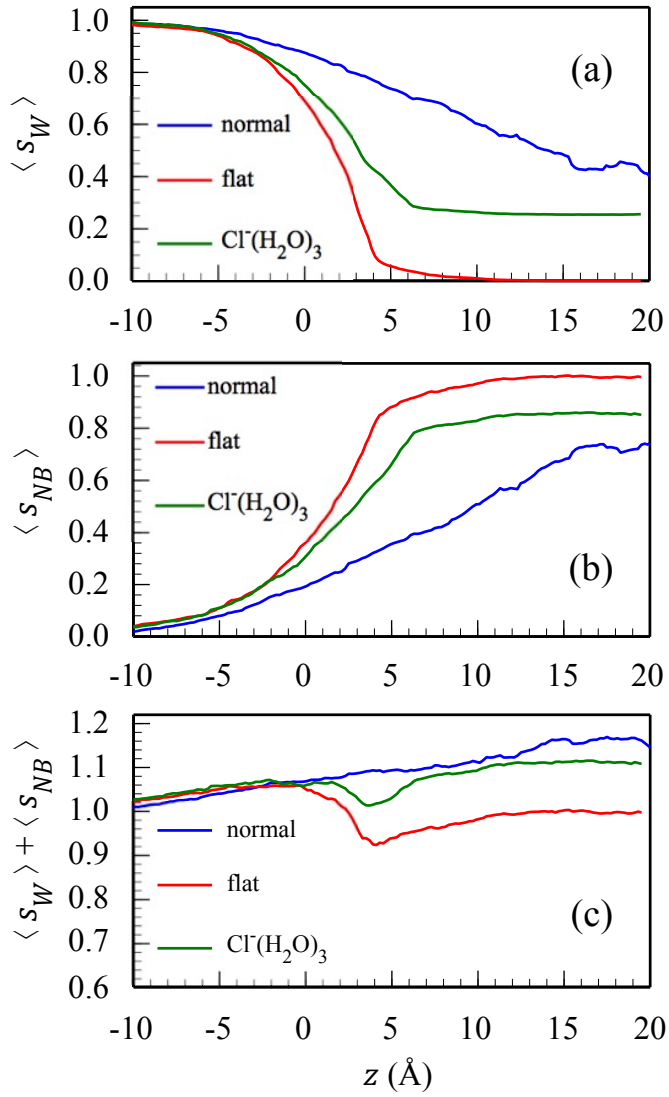

Figure 6.4: (a) The average water solvation coordinate s_W, (b) the average nitrobenzene solvation coordinate s_{NB}, and (c) $s_W + s_{NB}$ as a function of the ion's location along the normal to the water/nitrobenzene interface.

decrease is not dramatic since most ion-water interaction occurs between the ion and its solvation shell, which is mostly intact when the ion crosses the interface. The solvation coordinate continues to decrease as the ion moves into the organic phase and the average number of water molecules in the 1st hydration shell and contributions from the 2nd hydration shell and beyond decreases. In the flat-interface system, $\langle s_W \rangle$ decreases rapidly at the interface since the ion is stripped of its solvation shell water. The tail of the flat-interface curve represents the remaining ion-water long-range columbic attraction. The flat-interface, fixed hydration shell simulation ($Cl^-(H_2O)_n$) represents an intermediate behavior. Since three water molecules are always present in the vicinity of the chloride ion, the water solvation coordinate plateaus once the ion leaves the short-range influence of the aqueous phase. The nitrobenzene solvation coordinate is shown in Figure 6.4(b). In the normal, unconstrained system $\langle s_{NB} \rangle$ increases gradually as the ion moves to the organic phase. With the flat-interface constraint enabled, the ion is more exposed to the nitrobenzene phase as it approaches the interface since the constrained interface is unable to distort toward $+z$. When the naked ion crosses into the organic phase, $\langle s_{NB} \rangle$ increases rapidly and plateaus. With three solvation-shell water molecules tethered to the ion in the flat-surface system ($Cl^-(H_2O)_3$), the system plateaus at a lower value due to the presence of these solvation water molecules. It is interesting to examine the sum $\langle s_W \rangle + \langle s_{NB} \rangle$ for each of these systems. A fixed value of 1 for this sum, independent of z, would suggest that the interaction energy of the ion with the water is replaced on a relative basis with the interaction energy of the ion with the less polar organic liquid. This was found to be the case for the transfer of tetra-alkyl

ammonium ions and ion pairs across the water/chloroform interface. [17] Here, the small hydrophilic ion gives rise to a slightly different picture. While the sum does not vary much from 1 (only about 5%-15% total change depending on the system), the variations provide additional insight into the structure of the hydrated ion that is consistent with the discussion above. Thus, for the normal interface, $\langle s_W \rangle + \langle s_{NB} \rangle$ varies from 1 in bulk water to 1.15 in bulk nitrobenzene. The slight increase suggests that the decrease in the total ion-water interactions is slightly made up for by the fact that the water molecules in the first hydration shell are held more tightly together when the ion is in bulk nitrobenzene than when the ion is in bulk water. This is also confirmed by noting the increased water-ion interaction energy per water molecule in the hydration shell and the longer water-ion residence time when the hydrated ion is in the bulk organic phase. [16] The slight increase in $\langle s_W \rangle + \langle s_{NB} \rangle$ as the ion is transferred from water across the flat interface is initially the same as that of the normal interface until the ion reaches the Gibbs surface. At this point, the rapid drop in the ion-water interaction is seen as a sudden decrease in the sum of the solvation coordinates as the ion is stripped of its hydration shell. When the ion with a fixed hydration shell ($Cl^-(H_2O)_3$) crosses the interface (Figure 6.4(c), green curve), the interaction energy between the ion and the three tethered water molecules increases, similar to the behavior of the unconstrained system's hydration shell. The sum of the solvation coordinates approaches 1.1 as the ion and its fixed $n = 3$ shell move into the bulk nitrobenzene region. With this understanding of the nature of the solvation coordinates s_W and s_{NB}, it is useful to consider the dependence of the system's free energy on them. In general, the two-dimensional

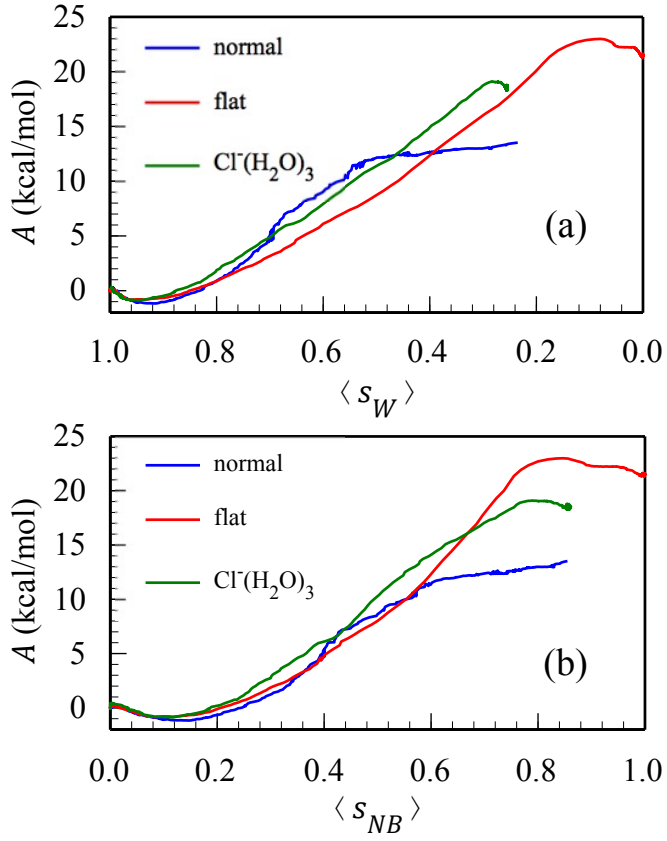

Figure 6.5: The free energy of ion transfer vs. the equilibrium (a) water solvation and (b) nitrobenzene solvation coordinates.

free energy $A(z, s)$ in which z and s (where s stands for s_W or s_{NB}) vary independently, would contain a relatively complete description of the ion transfer. In practice, computing $A(z, s)$ would be challenging because values of s significantly different from the equilibrium values are extremely rare and irrelevant to the process of electrochemical ion transfer. When the ion is located in the aqueous phase, the probability of observing a value of s_W significantly different from 1 (or s_{NB} different from 0) is essentially zero, corresponding to a very high value of the free energy. When the ion is at or near the GDS, relatively large fluctuations in the values of s_W and s N B are more likely, corresponding to lower free energy values. As the ion is moved to the organic phase, at each value of z the two-dimensional free energy $A(z, s)$ has an approximate parabolic dependence on s_W or s_{NB} with the minimum (equilibrium value) of A attained at $\langle s_W \rangle$ or $\langle s_{NB} \rangle$. This equilibrium value is plotted in Figure 6.5 as a function of $\langle s_W \rangle$ (Figure 6.5(a)) and $\langle s_{NB} \rangle$ (Figure 6.5(b)). The fact that the top panel (where s_W varies from 1 to 0) and the bottom panel (where s_{NB} varies from 0 to 1) are almost identical is a direct result of the relationshiphs $\langle s_W \rangle + \langle s_{NB} \rangle \approx 1$ mentioned above. They describe the free energy change when the ion is transferred from water to nitrobenzene when the solvation coordinates are allowed to reach equilibrium at each value of z. Unlike the significantly different behavior depicted in Figure 6.4 for the three systems, the similarity in the shape of the three curves in Figure 6.5 is quite striking, with the main difference being the final value of the free energy. This suggests that the local equilibrium free energy of the ion is more strongly correlated to its solvation state than to its location. The relatively small differences between the three curves in the region $0.5 < s_W < 0.7$

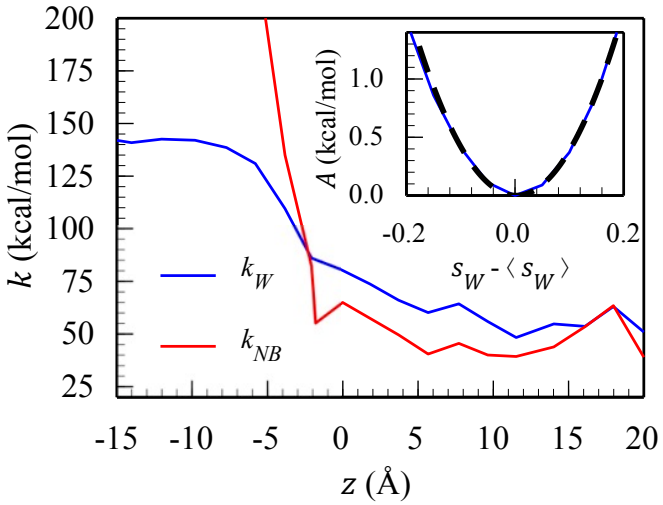

Figure 6.6: Solvent force constants k_W (blue) and k_{NB} (red) and a representative fit of free energy variation about the corresponding equilibrium solvent coordinate value (inset). The dashed curve represents the parabolic fitting function.

(more clearly observed in the top panel) suggest that significant contribution to the free energy of transfer is the deformation of the interface and the creation of the water finger, but that this is less than the "cost" of transferring a "naked" ion. While Figure 6.5 suggests that solvation coordinate is highly correlated with the position of the ion, it is interesting to examine in some detail the parabolic dependence of the free energy $A(z, s)$ on the solvation coordinate s. Specifically, for small deviations from equilibrium,

$$\begin{aligned} A(z, s_W) &= A_{eq} + \frac{k_W}{2}(s_W - \langle s_W \rangle)^2, \\ A(z, s_{NB}) &= A_{eq} + \frac{k_{NB}}{2}(s_{NB} - \langle s_{NB} \rangle)^2. \end{aligned} \tag{6.11}$$

Figure 6.6 shows the values of the "solvent force constants" k_W and k_{NB} determined from a parabolic fit of the fluctuations in the solvent coordinates about their equilibrium

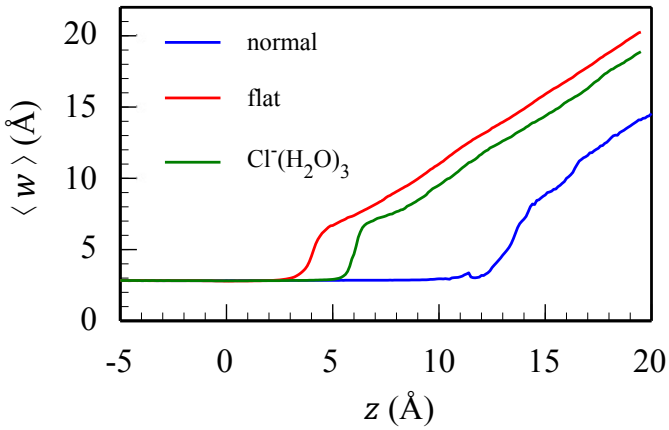

Figure 6.7: The water finger coordinate, w, as a function of the ion's location along the normal to the water/nitrobenzene interface.

values. A large value of the force constant indicates a tighter solvation environment, which requires larger free energy to deform. An example of this parabolic relation is shown in the inset of Figure 6.6. Here $A(z, s_W)$ of an ion confined to a window defined by -1.5 Å $< z <$ 1.5 Å and the parabolic fit from which k_W is obtained (dashed curve) are shown. As the ion is transferred from the aqueous phase to the organic phase the decrease in the k_W force constant corresponds to the large fluctuations in the hydration energy caused by the depletion of the hydration shell and the formation of the water finger. In contrast, k_{NB} is mostly constant when the ion is in the organic phase, with a rapid increase as the ion sheds the solvating nitrobenzene molecules upon entering the interface region and moving toward the aqueous phase. We should point out that when the ion is in the organic phase and the water finger is broken, several hydration shell structures as well as different finger structures may contribute to the fluctuations in s_W and these fluctuations are no longer well described by a single parabola. We next

consider the variation in the water finger coordinate w as the ion is transferred through the interface. Figure 6.7 shows the average $\langle w \rangle$ as a function of the chloride ion's z position, calculated by averaging the values of w in 0.1 Å bins along z. As long as the ion is attached to the bulk water phase via an unbroken network of water molecules, $\langle w \rangle$ is near the O–O distance corresponding to a water-water hydrogen bond (about $r_{OO} =$ 2.75 Å, which corresponds to the peak value of the bulk water O–O radial distribution function). The value of z at which $\langle w \rangle$ begins to significantly increase beyond $r_{OO}^{\max}(3.4\mathring{A}$, see Section II-C-2) is the point where the ion breaks away from the aqueous phase. In the constrained surface systems, this separation from the bulk water begins at $z \approx 3$ Å for the transfer of the naked ion and at $z \approx 5$ Å for the transfer of $Cl^-(H_2O)_3$ across the flat interface. The difference of about 2 Å between the two constrained systems is attributed to an additional hydration water between the ion and the aqueous phase during the transfer of $Cl^-(H_2O)_3$. When the ion breaks free of the interface, the last interacting water remaining at the interface is no longer pulled toward the $+z$ direction, and it recedes into the aqueous phase, resulting in the rapid increase in $\langle w \rangle$ seen in both of the constrained simulations ($z \approx 4$ Å and $z \approx 6$ Å). As the ion moves away from the flat constrained surface, $\langle w \rangle$ increases linearly with the ion's z position and in this region, to a good approximation, $\langle w \rangle = z$ for the naked ion and $\langle w \rangle = z - z_{OCl}$ for the transfer of $Cl^-(H_2O)_3$, where z_{OCl} is the projection along the interface normal of the position of the peak Cl–O radial distribution function, about 3.2 Å. The average shortening of $\langle w \rangle$, when compared to the naked ion at the same z position, is approximately 2.5 Å due to the intervening of slightly less than a single water molecule (on average) between

the ion and the flat interface. In the unconstrained, normal system, the water finger appears to break when the ion is approximately at $z = 12$ Å. Examination of individual trajectories (see below) suggests that the breakup follows elongation of the water finger and significant water surface fluctuations, which make the initial rise not as sharp as in the constrained systems. As the water finger elongates, the water finger structure changes from a more conical morphology to a linear chain of water molecules, finally resulting in the breakup of a hydrogen bond between a hydration shell water molecules and the other water molecules in the finger. Additional insight into the utility of the water finger coordinate for describing the mechanism of ion transfer is provided in Figure 6.8, which shows the local equilibrium free energy of the ion plotted against the equilibrium value of the water finger coordinate. The nearly step-like behavior of the three systems suggests that, in all systems examined, by the time the last hydrogen bond is broken (when $\langle w \rangle \approx 3.4$ Å, the commonly used maximum oxygen-oxygen distance when geometrically defining the existence of water-water hydrogen bonds), most of the free energy change has been accounted for, especially when surface fluctuations are suppressed. This is more clearly observed in the normalized free energy change in the bottom panel, where ΔA_t is the net free energy of transfer from water to nitrobenzene. This behavior is consistent with our earlier discussion, which assigns most of the free energy change to the creation and elongation of the water finger in the normal system or the stripping of the water hydration shell in the constrained systems. The fact that $\langle w \rangle$ does not appreciably change during this critical phase of the finger formation and elongation reduces its utility for understanding the mechanism of the transfer (except

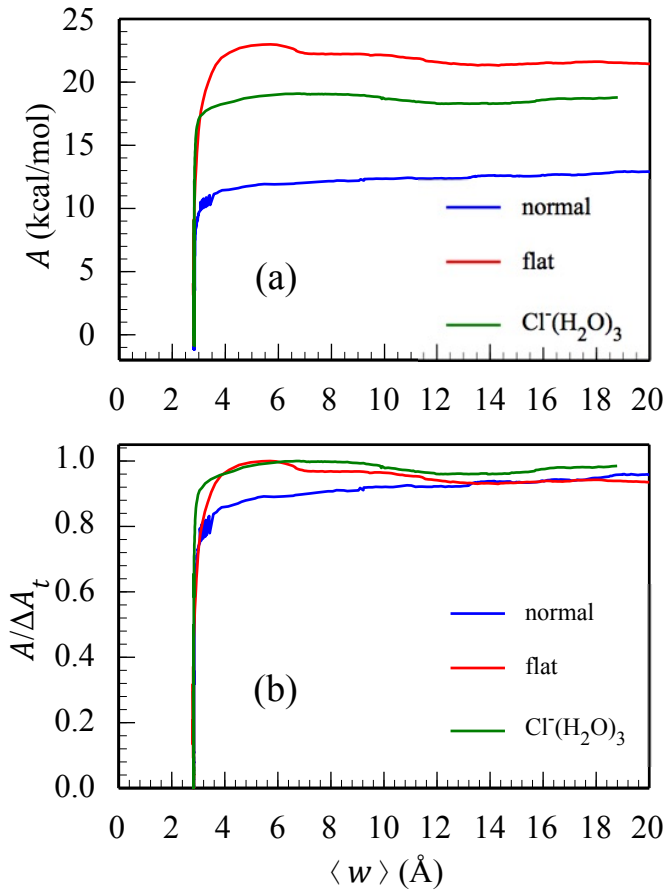

Figure 6.8: (a) The free energy of ion transfer vs. the equilibrium water finger coordinate (b) Normalized free energy vs. the equilibrium water finger coordinate.

for the obvious observation that transfer via formation of a water finger is much more energetically favorable). Because the water finger coordinate w is (loosely speaking) a measure of the longest oxygen-oxygen distance, it may be used to monitor the integrity of the water finger. This is demonstrated in Figure 6.9, which depicts z, w, s_W and s_{NB} vs. time for a selected 0.8 ns trajectory of the unconstrained system. In this particular simulation, the ion is constrained within the window 8.5 Å $> z >$ 11.5 Å (in the organic phase). The relatively flat line near $w \approx 3$ Å indicates the region with an intact water finger, where the ion is tethered to the aqueous phase by at least a chain of hydrogen bonded water molecules with a maximum r_{OO} of approximately 3.4 Å. At 0.27 ns the water finger breaks, w increases to over 10 Å, and remains broken with rapid fluctuations for the next 0.3 ns until it reforms at $t = 0.62$ ns and remains intact for the rest of the trajectory. This spontaneous formation and breakup of the water finger while the ion is held above the interface quantitatively demonstrate the harpoon or "protrusion"-based transfer mechanisms suggested in earlier work. [10, 127] Figure 6.9 also reveals the statistical fluctuations of the solvation and water finger coordinates during the most erratic part of the transfer process: separation of the ion from the water phase. The solvation coordinates s_W and s_{NB} have a fairly consistent standard deviation of 0.1 in the MD trajectory observed in Figure 6.9. The water finger demonstrates a significantly different behavior in regard to fluctuation, with a standard deviation of 0.07 Å when the water finger structure is intact (0.0 ns $< t <$ 0.2 ns) and 1 Å when the water finger has broken (0.3 ns $< t <$ 0.6 ns). This difference in σ_w values reflects the nature of the coordinate. When the water finger is intact, fluctuations in w

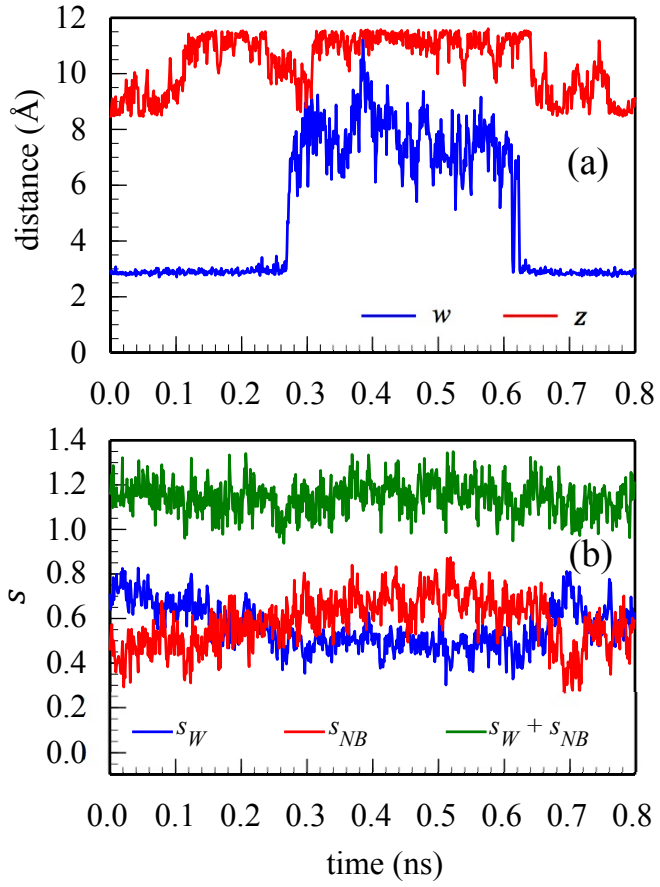

Figure 6.9: (a) Instantaneous water finger coordinate (w) and ion position (z) versus simulation time (t) for a selected trajectory. (b) Corresponding instantaneous values of the solvation coordinates and their sum.

are essentially fluctuations in hydrogen bond distances. When broken, fluctuations in w largely describe geometric fluctuations of the liquid-liquid interface. Several interesting points can be gleaned from Figure 6.9. When the finger is intact ($t < 0.27$ or $t > 0.62$ ns), the ion is able to explore the whole range of z values, suggesting that the water finger is able to keep up and fluctuate accordingly. When the finger is broken, w experiences large fluctuations while the ion is mostly near the "upper" ($z \approx 11$ Å) edge

of the window. Without the anchor provided by the water finger, the ion is more likely to drift towards the bulk of the organic phase due to the applied biasing potential. This is also reflected by the variations observed in the values of the solvation coordinates (bottom panel): s_{NB} increases and s_W decreases during this time frame (while the sum fluctuates around a fixed average of 1.1). The large fluctuations in w correspond to large surface water deformation. For example at $t \approx 0.4$ ns we see that $w \approx z \approx 11$ Å corresponding to a situation where the ion's partial hydration shell points away from the interface while the interface is locally flat.

6.4 Conclusions

Characterizing liquid surface fluctuations during ion transfer across the interface between water and an immiscible organic solvent and taking into account the partial co-transfer of the ion hydration shell are crucial for correctly describing the mechanism of this important process. Our free energy calculations for the transfer of Cl^- across the water/nitrobenzene interface show that a major contribution to the ion's free energy of transfer from the aqueous to the organic phase is in the deformation of the interface and the creation of water molecules protrusions ("finger") into the organic phase. However, a significant "savings" in free energy is gained by the co-transfer of several water molecules with the ion. The ion solvation energy with each of the two liquids (normalized by the corresponding bulk values) gives crucial information about the local thermodynamic state of the ion and is strongly correlated with the ion local free energy

and position. In contrast, the geometric coordinate w does not appreciably change during the critical phase of the water finger formation and elongation. This coordinate is useful for monitoring the integrity of the water "finger" and for identifying the onset of the "harpoon"-like mechanism for the ion transfer.

Acknowledgments

We are grateful for several illuminating discussions with professor Morita. J.J.K. also thanks L. Wang, N. Kikkawa, and the Morita group for their hospitality. Financial support from the National Science Foundation through Grant No. CHE-1363076 is acknowledged.

Chapter 7

Miscibility at the immiscible liquid/liquid interface: A molecular dynamics study of thermodynamics and mechanism

7.1 Introduction

It is well known that water is sparingly soluble in even the most nonpolar liquids. Water will, in very small amounts, penetrate into the adjacent "immiscible" phase when a nonpolar liquid is in contact with water vapor or liquid water. A small concentration of water in a nonpolar environment can have a significant impact by initiating corrosion, inhibiting particle growth, poisoning catalytic sites, occupying active sites, or dramatically increasing the energetic barrier to chemical reactions. [233, 35, 82, 170, 164]

For these reasons the quantification and removal of trace water in organic solvents continues to attract attention in several fields. [233, 64, 161] The equilibrium concentration of water dissolved in nonpolar solvents has been quantified experimentally and, to a limited extent, studied by computer simulation. [181, 85, 5, 3] However the thermodynamics and, in particular, mechanism of water's dissolution into an adjacent, immiscible liquid phase remain open questions. In this work we focus on the transfer of water from a bulk liquid water phase to a bulk liquid organic phase at the immiscible water/liquid interface. Our initial intuitive understanding of this transfer event may draw from studies of ion transfer across that interface. [127, 10, 194, 99, 106, 107, 45, 179] In ion transfer, the ionic species moves across the interface and drags with it a portion of its hydration shell. The ion remains tethered to the aqueous phase by an extruded protrusion of hydrogen bonded water molecules that may extend over 1 nm beyond the Gibbs Dividing Surface into the organic phase. When the final water-water hydrogen bond breaks, the ion and part of its hydration shell (typically 1-4 water molecules) diffuses into the organic phase. However, water-water hydrogen bonding interactions are typically significantly weaker than ion-water electrostatic interactions and this mechanism may not accurately explain the dissolution of water in an organic solvent. A second logical basis of comparison is the evaporation of water. Water evaporation is also the transfer of water from a bulk liquid phase into a medium of much lower relative permittivity (a vacuum) and therefore may share thermodynamic or mechanistic aspects with the transfer of water into a nonpolar liquid phase. A series of recent theoretical studies have revealed interesting details regarding the evaporation of water. [220, 153, 152] Bonn and co-workers [153] found that

the evaporation of water involves two main steps: (1) A final collision, where the transferring water is close to a hydrogen-bonded surface water molecule and (2) the formation of a new hydrogen bond between the non-transferring water and another nearby water just prior to this final collision. They suggest that this mechanism acts as a "Newton's cradle," where the formation of the new hydrogen bond imparts sufficient energy to the transferring water molecule to break its last remaining water-water hydrogen bond, ejecting it from the liquid/vapor interface. Sakaguchi and Morita also investigated the evaporation of water through Langmuir-Blodgett films of n-alcohols, reporting that the alcohols slightly reduce the net free energy required for water evaporation or condensation through the monolayer. [188] Presence of a short-chain alcohol monolayer (butanol) has a very small effect on the monotonic Free Energy Profile (FEP) of water evaporation but long-chain n-alcohols (decanol and hexadecanol) introduce a free energy barrier of a few kcal/mol due to a significant decrease in the mass accommodation coefficient. The FEPs of evaporation through long-chain film resemble the transfer of an ion across the immiscible liquid/liquid interface when the interface is constrained to a flat plane by an externally applied potential. [99] This relationship is interesting since both the interface constraint and the intra-monolayer Van der Waals forces effectively flatten the interface, suppressing fluctuations. Sakaguchi and Morita report that the transport of water through the monolayer is facilitated by a "water finger" protrusion, further strengthening the link to liquid/liquid ion transfer. To investigate the water dissolution process we first use equilibrium molecular dynamics simulations to derive the FEP, also known as the Potential of Mean Force (PMF), for the transfer of water molecule(s) across the

interface. These calculations provide a mean field description and thus largely ignore the importance of dynamic fluctuations at the liquid/liquid interface. However, as in the case of ion transfer, the FEP could provide evidence that these fluctuations are important to transport across these adjacent phases. We recently studied the free energy of transfer of a chloride ion across the water/nitrobenzene interface, finding that when interfacial fluctuations are suppressed (a flat interface constraint is implemented but co-transfer of the water's solvation shell is permitted) the net free energy of transfer increases by approximately 60%. [99] In the case of ion transfer, these and other computer simulations [10, 194, 106, 107, 45] strongly support and quantify the "water finger" or protrusion mechanism. Also in the present work these equilibrium FEP calculations are accompanied by a few suggested "reaction coordinates": Collective variables that attempt to describe the transfer event using a few degrees of freedom. We then complement these equilibrium studies with a set of 487 molecular dynamics trajectories, each having captured an independent dissolution event of water into nitrobenzene. Our analysis of these dissolution events is similar to the water evaporation studies recently performed by Bonn and coworkers, [153] which allows for easy mechanistic comparison between water/vapor (evaporation) and liquid/liquid (dissolution) water transfer. The rest of this paper is organized as follows: In Section II we describe and analyze the thermodynamics calculations performed on the interfacial systems. Section III analyzes the collected dissolution events to investigate the mechanism and dynamics of water transferring from bulk water to nitrobenzene. Section IV summarizes and concludes.

7.2 Thermodynamics

7.2.1 Methods

7.2.1.1 Systems and force fields

Molecular dynamics simulations of water/nitrobenzene, water/hexane, and water liquid/vapor systems were performed using our in-house code. The liquid/liquid systems consist of two adjacent slabs of immiscible liquids in a 31.28 × 31.28 × 300.0 Å rectangular box with the liquid/liquid interface located in the x-y plane at $z \approx 0$ Å. The aqueous phases, consisting of 986 water molecules, are located at $z < 0$ and the organic phases, either 252 nitrobenzene molecules or 250 hexane molecules, are in the $z > 0$ region. Each liquid phase is in equilibrium with its respective vapor phase with soft reflecting potential walls located 5 Å from the simulation box boundaries in the z direction to prevent vapor phase molecules from crossing into the adjacent vapor phase. The water liquid/vapor system consists of a slab of 986 water molecules in equilibrium with its own vapor contained within a rectangular box with the same dimensions and soft reflecting walls near the z boundaries as the liquid/liquid systems. All intermolecular interaction potentials are the pairwise sum of Lennard-Jones and Coulomb terms

$$U_{ij}(r) = \sum_{i<j} 4\epsilon_{ij} \left[\left(\frac{\sigma_{ij}}{r} \right)^{12} - \left(\frac{\sigma_{ij}}{r} \right)^{6} \right] + \frac{q_i q_j}{4\pi r \epsilon_0} \tag{7.1}$$

where r is the distance between atom centers i and j. Lennard-Jones parameters for mixed interactions are generated using Lorentz-Berthelot combining rules, $\sigma_{ij} = (\sigma_i +$

$\sigma_j)/2$ and $\epsilon_{ij} = (\epsilon_i \epsilon_j)^{1/2}$. The nitrobenzene model has been described previously [136] and reproduces the experimental dipole moment and enthalpy of vaporization. For hexane, we use the OPLS united atom model. [91] Our water model is a version of the flexible simple point charge (SPC) model [22] with intermolecular potentials as described by Kuchitsu and Morino. [109] These particular combinations of water and organic models produce liquid/liquid and liquid vapor interfacial properties (surface tension, density profiles, and orientational distributions) that agree well with experiment. [10, 159, 18, 193] Starting configurations were first constructed manually and equilibrated by performing MD simulations with short time steps ($t < 0.1$ fs) to remove any high energy, nonphysical configurations. Prior to production runs all starting configurations were run for at least 1 ns of simulation time with a time step of 0.5 fs to ensure equilibration (e.g. convergence of average total energy, density profiles, etc.) and verify that all applied constraints conserve energy.

7.2.1.2 free energy calculations

We use umbrella sampling [1, 34, 174] with an applied biasing potential to calculate the free energy profile of a water molecule transferring from bulk water into the adjacent phase. Our implementation of this technique has recently been described in detail [99] and here we briefly summarize it. To calculate the free energy profile of this water transfer process, we first select a single water molecule of interest: the "tagged" water. The interval of interest along the z-axis spans the region from bulk water to the bulk organic liquid, -10 Å $> z_w >$ 17 Å, where z_w is the position of the transferring

water molecule's center of mass along the z-axis and the liquid/liquid interface is located at approximately $z = 0$ Å. We divide this interval into a series of N overlapping lamellae that are parallel to the x-y plane (parallel to the liquid/liquid interface.) The local free energy in each lamella is

$$A_n(z_w) = -k_B T \ln P_n(z_w) + C_n \tag{7.2}$$

where $P_n(z_w)$ is the probability distribution of z_w within lamella n and C_n is a constant. The An segments are combined by selecting C_n to minimize the difference between A_n and A_{n+1} in the overlapping regions [110, 105] to create a complete free energy profile which spans the entire interval of interest. Poor statistical sampling of a given lamella may occur if the value of $A(z_w)$ varies by a large amount. We apply a biasing potential, $U_{bias}(z_w)$, to the tagged water to accelerate the exploration of phase space and improve sampling statistics. This modifies the interaction between the tagged water molecule and the surrounding solvent molecules U_{wx} as follows:

$$U^b_{wx} = U_{wx} - U_{bias}(z_w) \tag{7.3}$$

where $U_{bias}(z_w)$ is a function of the position of the tagged water molecule's center of mass along the z-axis and is of the form

$$U_{bias}(z_w) = \alpha \frac{(1 + \tanh[\lambda(z_w - \zeta)])}{2} \tag{7.4}$$

where the constants α, γ, and ζ are selected so that the biasing potential approximates $A(z_w)$. The free energy profile within a lamella is determined from the biased probability distribution $P_n^b(z_w)$ by

$$A_n(w_z) = -k_B T \ln P_n^b(w_z) + U_{bias}(z_w) \tag{7.5}$$

The simulations in this work use lamellae that are 3 Å wide and overlap by 1 Å. The tagged water is confined within the specified lamella by a window potential that is zero within the boundaries of the lamella along the z-axis and rises rapidly if the tagged water attempts to exit the lamella. All equilibrium data presented in this work represents 10 ns of sampling within each of the overlapping lamella and all simulations are performed at 298 K.

7.2.2 Results and discussion

Figure 7.1 shows the density profiles of the two liquid/liquid systems. Obviously water is immiscible with each of these adjacent organic phases. In each system the Gibbs Dividing Surface (GDS) is located at $z_{GDS} = 0$ Å. The exact definition of the Gibbs Dividing Surface is the plane parallel to the interface where the excess density of one liquid on one side exactly matches the deficit on the other side relative to a step function profile. [184] However, at the liquid/liquid interface, one may define the GDS with respect to each liquid and get a slightly different value, which to a good approximation is the location where the density of water is 50% of the bulk value. The interface region of

the water/nitrobenzene system (Figure 7.1a) is noticeably wider than the water/hexane interface (Figure 7.1b.) The distance over which the water density varies from 90% to 10% of the bulk value is approximately 5 Å in the water/nitrobenzene system and 3 Å in the water/hexane system. This difference in interface width can be directly related to the surface tension of two interfaces: $\sigma = 51$ dyn/cm for water/hexane [187] and $\sigma =$ 25 dyn/cm for water/nitrobeneze. [95] The interface width is a result of thermal averaging over capillary fluctuations of a molecularly sharp interface. [184, 172] All phases achieve bulk density when only a few molecular diameters away from the liquid/liquid interface. The miscibility of water in the two organic liquids is determined by energetic and entropic contributions but is roughly related to the relative permittivity of the two liquids: $\epsilon_r \approx 6$ for hexane and $\epsilon_r = 34.8$ for nitrobenzene at 298 K. The exact value can be obtained from the net difference in free energy as determined by the FEP calculations. Figure 7.2a shows the FEP of a water molecule transferring from the bulk aqueous phase to the bulk region of the adjacent phase in each of the three interfacial systems, calculated using the umbrella sampling method described in Section II.A.2. As the tagged water molecule moves from bulk water toward the organic (in the $+z$ direction) each free energy curve increases monotonically and plateaus in the organic region. The water/nitrobenzene FEP (blue curve) begins to rise at $z \approx$ -3 Å (about one water layer before the GDS), exhibits a slight and broad maxima at $z \approx 7$ Å, and reaches a plateau at $z \approx 10$ Å. The net free energy of transfer is 3.8 kcal/mol. The experimentally determined solubility of nitrobenzene in water, 0.178 M, [85] corresponds to a net free energy of transfer of 2.36 kcal/mol. This difference in net free energy is not large in

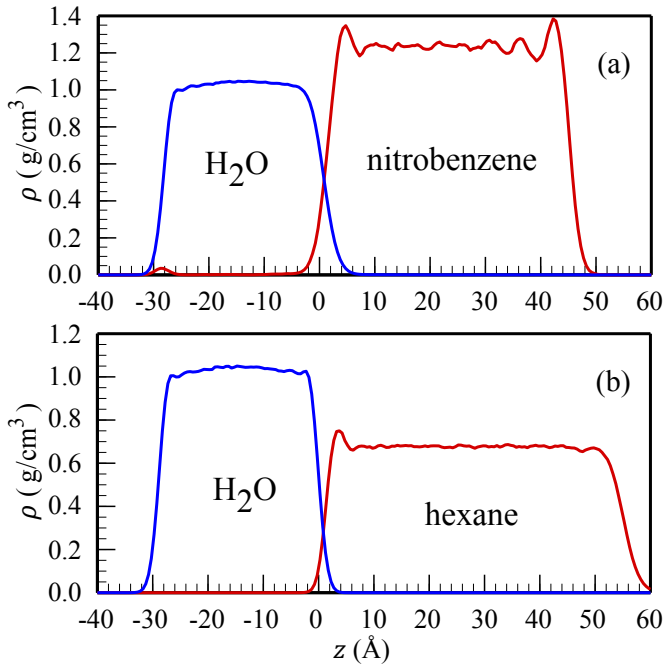

Figure 7.1: Density profiles of the (a) the water/nitrobenzene and (b) water/hexane liquid/liquid systems obtained from molecular dynamics simulations. In each panel the blue curve represents the aqueous phase and the red curve represents the organic phase. Data shown from each system is the average of 50,000 configurations collected over 10 ns of simulation time.

magnitude but is a significant percentage of the actual value. The water/hexane FEP (red curve) plateaus at $z \approx 7$ Å and had the largest net free energy of transfer, 7.6 kcal/mol. The experimental solubility data, 0.0362 M water in hexane at 298 K, [181] corresponds to a net free energy of transfer of 4.54 kcal/mol, significantly lower than the value determined by our simulations. Lastly, the green curve in Figure 7.2a represents evaporation of water, the transfer of a tagged water molecule from bulk water into an adjacent water vapor phase, also plateau at $z \approx 7$ Å. The net free energy of transfer for evaporation is 6.5 kcal/mol, which compares well to the experimentally determined value of 6.32 kcal/mol. [3] The difference between the water/hexane liquid/liquid net free energy in Figure 7.2a and the corresponding value determined from solubility data reflects a recent and ongoing discussion regarding the accuracy of the force fields used in water/alkane simulations. Chapman and co-workers [5] identified the poor performance of fixed-charge force fields and Lorentz-Berthelot combining rules when studying the solubility of water in alkanes, noting that the water-alkane interactions are dramatically underestimated. This work was followed by commentary by McDaniel and Yethiraj [131] and a similar report (with similar findings) by Panagiotopoulos and coworkers [89] on water/CO_2 and water/n-alkane mixtures. Recently, subsequent work by Chapman and co-workers [3] confirmed that the electrostatic and induction effects between water and alkanes are critical components to consider when considering this extreme case of water's solubility in alkanes. Our water/hexane free energy profile in Figure 7.2a agrees with the underestimation of water's solubility in an alkane. The solubility of water in nitrobenzene is also underestimated but to a much lesser extent. Since

nitrobenzene (unlike hexane) is significantly polar, the electrostatic interaction energy between nitrobenzene and water at the liquid/liquid interface is much larger than the interaction energy resulting from the induced dipoles when water and nitrobenzene are in close contact. As a result, it is possible to account for the total energy using fixed empirical parameters. The calculated net free energy of transfer of our non-polarizable water across the liquid/vapor interface compares very well with experimental values. This thermodynamic result agrees with the mechanistic simulations performed by Bonn and co-workers, who directly compared the performance of a nonpolarizable SPC water model with an *ab initio* based polarizable water force field. [153] They reported that their conclusions hold equally well regardless of force field. Figure 7.2b shows the average number of water molecules in the solvation shell of the transferring water. We define surrounding water molecules to be a member of the tagged water molecule's solvation shell if the oxygen-oxygen distance is less than 3.4 Å, which is the first minimum of $g_{OO}(r)$ in bulk water. In bulk water the tagged water has about 5 water molecules in its solvation shell. This population decreases quite rapidly as the tagged water moves to the interface and eventually reaches zero when the final water-water hydrogen bond breaks and the transferring water is "dissolved" in the adjacent phase. The blue curve, representing the water/nitrobenzene phase, maintains a nonzero population deeper into the adjacent phase than in the hexane and water vapor systems, which parallels the behavior of the FEP curves shown in the top panel. The more polar nitrobenzene phase allows the transferring water to drag neighboring waters further into the organic phase, suggesting that the transfer of water into an adjacent, immiscible, weakly polar phase

is accompanied by a larger local protrusion of the aqueous phase into the organic phase. This protrusion appears to be larger than in the case of water/nitrobenzene than in water/hexane or water/water vapor but much smaller than the protrusions or "water fingers" that accompany the transfer of a small ion across the immiscible water/organic interface. [10, 99, 106] The rapid decay to zero suggests that, in all systems, the transfer of a single water molecule is energetically favored over the simultaneous transfer of several waters. This is the same behavior as in the case of evaporation [128, 153] but is in marked contrast with the transfer of negative or positive ions, [99, 45] which keep part of their hydration shell due to strong water-ion electrostatic forces. Nonzero solvation shell values in the region of $z \approx 15$ Å exist in the water/nitrobenzene system but are not due to co-transferred water. In these cases, other water molecules have dissolved into the nitrobenzene phase and "found" the transferred water molecule. To further support the notion of one-at-a-time transfer of water in the water/nitrobenzene system, we computed the FEP for the transfer of a water "dimer" ($(H_2O)_2$) and a water "trimer" ($(H_2O)_3$). In each of these co-transfer simulations, we tethered one or two of the surrounding water molecules to the tagged water by implementing a spherical, harmonic restraining potential around the tagged water's center of mass that kept the center of masses of the tethered and tagged waters within 3.4 Å of each other. (We note that the restraining potential is applied to the centers of mass and not e.g. the oxygen atom centers so that the orientation of the molecules is not affected by the introduction of a tethering force.) Figure 7.3a shows the free energy of transfer along the z-axis for the unconstrained (solid curve, same as the blue curve in Figure

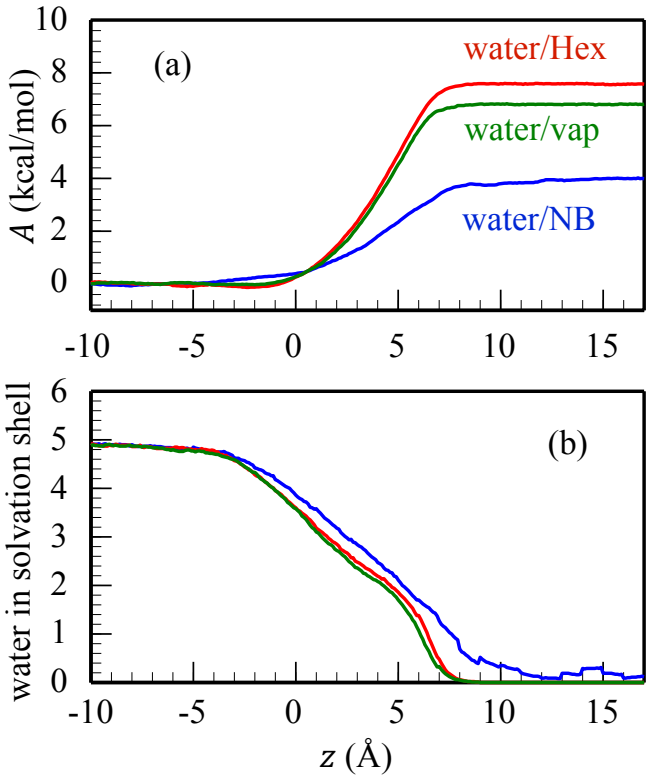

Figure 7.2: (a) Free energy profiles and (b) average number of water molecules in the first solvation shell of the transferring water molecule. The curves correspond to an H_2O molecule transferring from bulk water into bulk nitrobenzene (blue), bulk hexane (red), and an adjacent vapor phase (green.)

7.2a), $(H_2O)_2$ "dimer" (dashed curve), and $(H_2O)_3$ "trimer" (dotted curve). The results confirm that the transfer of a single water molecule is preferred since the addition of co-transferred waters increases the net free energy of transfer. As mentioned earlier, the net free energy of transfer for water across the water/nitrobenzene interface is 3.8 kcal/mol. This value increases to 5.9 with the co-transfer of 1 solvation shell water and further increases to 7.4 with the co-transfer of 2 solvation shell water molecules. Figure 7.3b shows the corresponding average number of water molecules in the transferring water's hydration shell. In bulk water the restraining potential results in a noticeably larger solvation shell population in the $(H_2O)_2$ and $(H_2O)_3$ systems. Aside from this artifact, the solvation shell populations of the $(H_2O)_2$ and $(H_2O)_3$ systems gradually reduce toward 1 and 2 respectively, indicating that even the imposition of an artificial solvation shell does not result in the co-transfer of additional water molecules. At the simplest level, the observation that water dissolves one molecule at a time and does not co-transfer additional water molecules like ions do, can be attributed to the much weaker water-water vs. water-ion electrostatic interactions. However, the increase in free energy of transfer from 3.8 kcal/mol to 5.9 kcal/mol represents a more complicated balance of energy and entropic contributions, which a detailed molecular theory could provide. A major component of the free energy of transfer is the interaction energy between the single water molecule and the rest of the system. We denote by $U_W(z)$ and $U_O(z)$ the average interaction energy between the tagged water molecule at the location z and the rest of the water (W) and organic solvent (O), respectively. The bulk values are denoted by $U_W^{bulk} = U_W(\infty)$; $U_O^{bulk} = U_O(\infty)$; all considered at the same

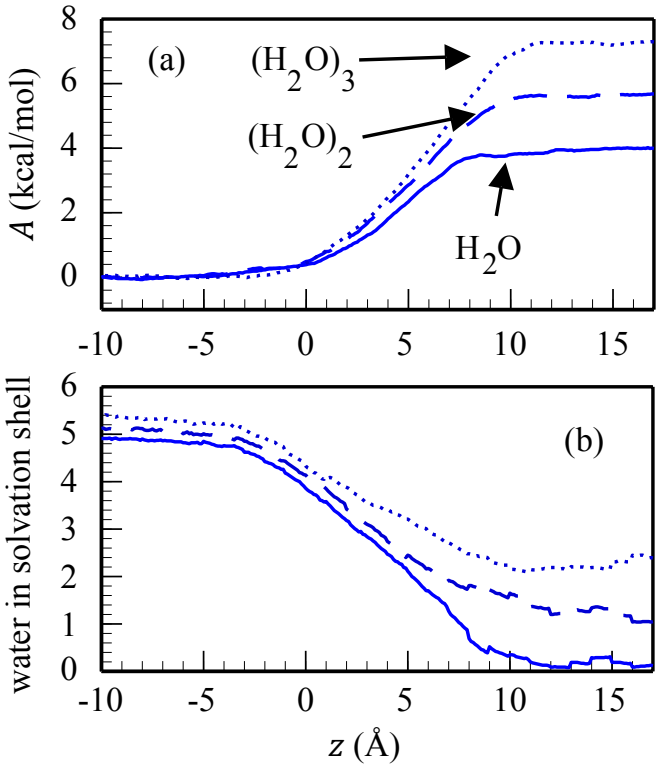

Figure 7.3: (a) Free energy profiles and (b) average number of water molecules in the first solvation shell of H_2O transferring from bulk water into bulk nitrobenzene. The solid curve (labeled "H_2O" in the top panel) represents the unconstrained system, the dashed curve represents the transfer of a "dimer" $(H_2O)_2$, and the dotted curve a water "trimer" $(H_2O)_3$.

temperature. These are determined by molecular dynamics simulations of a single water molecule in the uniform bulk liquid using the same force field parameters described in Section II.A.1. We find: U_W^{bulk} = -24.5 kcal/mol, U_{Hex}^{bulk} = -2.0 kcal/mol, and U_{NB}^{bulk} = -9.8 kcal/mol. These values suggest that for transfer to nitrobenzene: $\Delta U_{W\rightarrow NB}$ = -9.8 - (-24.5) = 14.7 kcal/mol, $\Delta S_{W\rightarrow NB} = (\Delta U_t - \Delta A_t)/T$ = 37 cal/K. For transfer to Hexane: $\Delta U_{W\rightarrow Hex}$ = -2.0 - (-24.5) = 22.5 kcal/mol, $\Delta S_{W\rightarrow Hex} = (\Delta U_t - \Delta A_t)/T$ = 50 cal/K. The entropy increase corresponds to the much greater translational freedom of the water molecules in the organic solvents than in bulk water. The smaller value in nitrobenzene compared with hexane is due to the ordering imposed by the water-nitrobenzene hydrogen bonding. For the interaction of $(H_2O)_2$ with the two bulk phases we find U_{D-W}^{bulk} = -42.3 kcal/mol and U_{D-NB}^{bulk} = -17.18 kcal/mol, values that are slightly less negative than twice the single water molecule values. For the trimer we get U_{D-T}^{bulk} = -60.0 kcal/mol and U_{T-NB}^{bulk} = -20.4 kcal/mol. These values suggest that for transfer of $(H_2O)_2$ to nitrobenzene: $\Delta U_{D-W\rightarrow D-NB}$ = -17.18 - (-42.3) = 25.1 kcal/mol, $\Delta S_{D-W\rightarrow D-NB} = (\Delta U_t - \Delta A_t)/T$ = 64 cal/K. For the transfer of $(H_2O)_3$ to nitrobenzene: $\Delta U_{T-W\rightarrow D-NB} = \Delta U_t - \Delta A_t)/T$ = -20.4 - (-60.0) = 39.6 kcal/mol, $\Delta S_{T-W\rightarrow T-NB} = (\Delta U_t - \Delta A_t)/T$ = 108 cal/K. As additional water molecules are co-transferred the increase in the unfavorable energy change outweigh the favorable increase in entropy leading to increase in the free energy of transfer. As the tagged water molecule is transferred across the interface, U_W and U_O vary. While the number of water molecules in the first hydration shell of the tagged water molecule provides useful information about the change in the local environment experienced by this wa-

ter, a more accurate indicator utilizes the total interaction energy defined above. To this end we define a solvation coordinate s for the transferred water molecule in each solvent [194, 99]

$$s_W = U_W / U_W^{bulk} \tag{7.6}$$

$$s_O = U_O / U_O^{bulk} \tag{7.7}$$

where O is "NB" for nitrobenzene and "Hex" for hexane. Figure 7.4a shows the value of s_W for all simulated systems where $\langle \ldots \rangle$ indicates the ensemble average value collected as a function of the tagged water's position along the simulation z-axis. Since the first solvation shell constitutes most (about 70%) of the solvent-solute interactions, the curves in Figure 7.4a closely track the corresponding solvation shell population curves shown in Figures 7.2b and 7.3b. For all systems the value of $\langle s_W \rangle$ begins at 1 while the tagged water molecule is in the bulk aqueous region and decreases as it moves into the adjacent phase. For the systems without imposed co-transfer of additional water molecules (solid curves) this decrease is quite dramatic once the tagged molecule crosses the interface since the tagged molecule is effectively stripped of its solvation shell waters. In the cases of $(H_2O)_2$ and $(H_2O)_3$ the decrease is more gradual and the value of $\langle s_W \rangle$ plateaus at a value significantly higher than zero, indicating the large contribution to interaction energy made by solvation shell waters. For example, in the case of $(H_2O)_3$, two solvation shell waters are present at approximately $z = 12$ Å and $\langle s_W \rangle \approx 0.5$. This indicates that the strength of the interaction between these two solvation shell waters and the tagged water is about half of the total tagged water-solvent interaction energy in

a bulk water environment. Figure 7.4b shows $\langle s_O \rangle$ along the simulation z-axis for each of the liquid/liquid systems. For all systems $\langle s_O \rangle$ begins at zero in the bulk aqueous phase and increases monotonically, approximately linearly, until the tagged water has transferred into the organic phase. In the water/nitrobenzene systems (blue curves) the early part of this increase (in the region of -4 Å $< z <$ 3 Å) is very similar regardless of the co-transferring water constraint. In the water/hexane system (red curve) the increase of $\langle s_O \rangle$ begins earlier along the z-axis because the hydration shell is stripped from the transferring water earlier (along the z-axis) than in the water/nitrobenzene system. To gain geometric insight into the perturbation of the water structure during the transfer we also describe the transfer process using the "water finger" coordinate w, introduced recently by Morita and co-workers, [106] in the study of ion transfer across the immiscible water/organic liquid/liquid interface. Here we slightly modify the definition of the water finger coordinate to adapt it for the water transfer event. The coordinate w is an instantaneous measure of the transferring species' connectivity to the aqueous phase. Its value is the largest distance that must be traversed if one were to start at the transferring species and move to the bulk aqueous phase, where the only allowable moves are "hops" to other water molecule oxygen atoms. To calculate this coordinate, an undirected mathematical graph is defined in which each water oxygen atom is a vertex and the distances between the oxygens are the edges. The coordinate w is the minimum threshold distance required to give a connected path between the transferring water and the aqueous phase. Figure 7.5a and 7.5b show the distance described by w (yellow) in representative system snapshots. When the transferring water

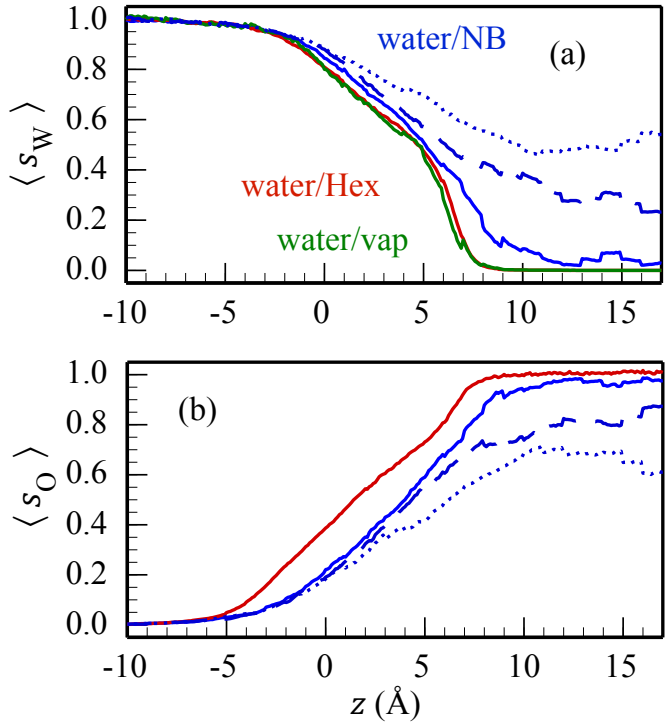

Figure 7.4: Variation of the solvation coordinates (a) s_W and (b) s_O along the simulation z-axis. s_O is s_{NB} for water/nitrobenzene and s_{Hex} for water/hexane. The blue curves represent the transfer of H_2O from water to nitrobenzene (dashed $\rightarrow$ dimer, dotted $\rightarrow$ trimer), the red curve represents water/hexane, and the green curve represents water liquid/water vapor (evaporation.)

is connected to the aqueous phase by a network of water-water hydrogen bonds (Figure 7.5a), the value of w is approximately the O–O distance of a water-water hydrogen bond. After the last water-water hydrogen bond breaks (Figure 7.5b), the value of w increases rapidly. We refer the reader to References [99, 106, 107] and Appendix E for more detailed, technical discussions of w. Figure 7.5 shows the ensemble-averaged values of w as a function of the tagged water's z position for the interfacial systems. Since the transfer of water occurs one-at-a-time, the value of w in the region of $z > 5$ Å (tagged water moving into the organic phase) is equal to the length of the final water-water hydrogen bond (when intact) and, after this last bond breaks, w increases rapidly, approximately linearly with the tagged water molecule's z position. The most obvious feature distinguishing the systems in Figure 7.5 is the spatially delayed increase of $\langle w \rangle$ in the water/nitrobenzene system (blue curve). This corresponds to the tagged water molecule separating from the aqueous phase further into the adjacent phase (recalling that the GDS is located at $z \approx 0$ Å.) Larger interfacial protrusions ("water fingers") accompany water transfer in the water/nitrobenzene system due to the lower interfacial surface tension and the final water-water hydrogen bond breaks when the tagged water is at approximately $z = 6.5$ Å, as opposed to $z = 5.9$ Å in the case of the water/hexane and water/vapor interfaces. This suggests that water transferring into nitrobenzene does so from a larger protrusion than in the other systems and this will be considered further in Section III.

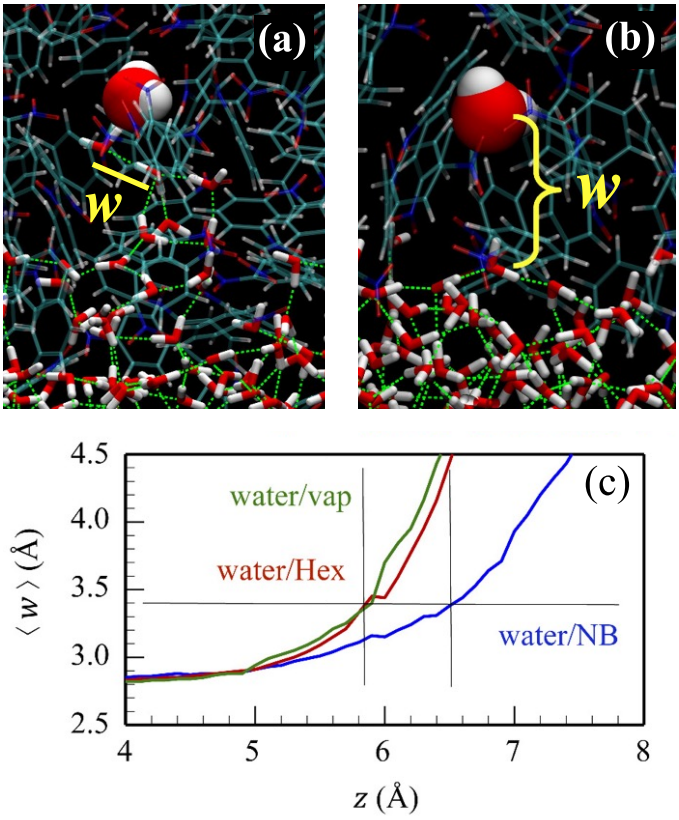

Figure 7.5: Simulation snapshots illustrating the length of the water finger coordinate (w) when the transferring water is (a) connected to the bulk by a hydrogen-bonded "finger" of water and (b) shortly after the breakup of the last water-water hydrogen bond. Panel (c) shows $\langle w \rangle$ as measured during the umbrella sampling simulations. Curves represent the dissolution or transfer of a water molecule from bulk water into an adjacent phase of liquid nitrobenzene (blue), liquid hexane (red), or water vapor (green). The grey lines are included to guide the eyes to $\langle w \rangle = 3.4$ Å, the cutoff distance for water-water hydrogen bonding.

7.3 Dynamics and mechanism

7.3.1 Methods and nonequilibrium simulation details

To study the dynamics and mechanism of dissolution of water into nitrobenzene, we use an approach similar to the one used by Mason [128] and Bonn and co-workers [153] to study water evaporation. We select 43 independent, equilibrated water/nitrobenzene configurations, ensuring that each starting configuration contains no water molecules dissolved in the nitrobenzene phase. Trajectories are run at constant total energy for 100 ps from each starting configuration by selecting random velocities from a Boltzman distribution and storing the positions and velocities of the 200 water molecules with the highest z position and 100 nitrobenzene molecules with the lowest z position every 4.0 fs. This selection captures the interfacial region of interest, approximately -6 Å $< z <$ 17 Å in the simulation box ($z_{GDS} \approx 0$). A dissolution event is defined whenever any water molecule reaches $z >$ 10 Å and the nearest water molecule is over 6 Å away, at which point the trajectory is terminated. These cutoffs ensure that the transferring water has diffused into the organic phase. In the case of no detected dissolution event within the 100 ps interval, new random velocities were selected and the process repeats. In total, 487 dissolution events were collected from 5302 trajectories, which correspond to a total of 507 ns of simulation time. Our analysis of the collected dissolution events employs a methodology similar to that used by Bonn and co-workers. [153] In the final configuration of the recorded trajectories the "dissolved" water molecule that has transferred into the nitrobenzene phase is labeled 'A.' We then travel backwards in time

in the trajectory to locate the last water-water interaction prior to the dissolution into nitrobenzene. When the distance between the oxygen atoms of water A and another water is less than 3.3 Å and this water-water distance is the minimum for at least 50 fs while moving backwards through the acquired trajectory we define this configuration to be $t = 0$, the moment of the last water-water interaction, and define water B: the last water molecule to 'interact' with water A prior to dissolution. This procedure ensures that we do not misinterpret O-O bond "vibrations" as the actual final breakup. The vector pointing from O_B to O_A at time zero, $\mathbf{r}_0$, and the midpoint of the O_B-O_A line segment at time zero, $\mathbf{M}$, are stored and are used as reference points for the dynamics of the dissolution events. Figure 7.6 is a representative snapshot of a dissolution event, indicating the positions of water molecules A and B. Figure 7.6a was acquired just prior to the breakup of the A-B hydrogen bond (green dotted line). In Figure 7.6b, 40 fs later, the molecules have moved and the hydrogen bond is no longer intact.

7.3.2 Results and discussion

Before discussing the dissolution mechanism in detail, a brief comment concerning the dissolution rate is warranted. Since 487 dissolution events were collected in a total of 507 ns trajectories, the rate of dissolution we observed is 0.961 water molecules/ns, which, given the simulation box cross section of $(3.128\ \text{nm})^2$, corresponds to a dissolution flux of 163 $\text{mol}\cdot\text{m}^{-2}\cdot\text{s}^{-1}$. This may be compared with the evaporation flux by using the fact that, at equilibrium, the number of evaporating water molecules is equal to the number of collisions of vapor phase molecules with the surface. The later

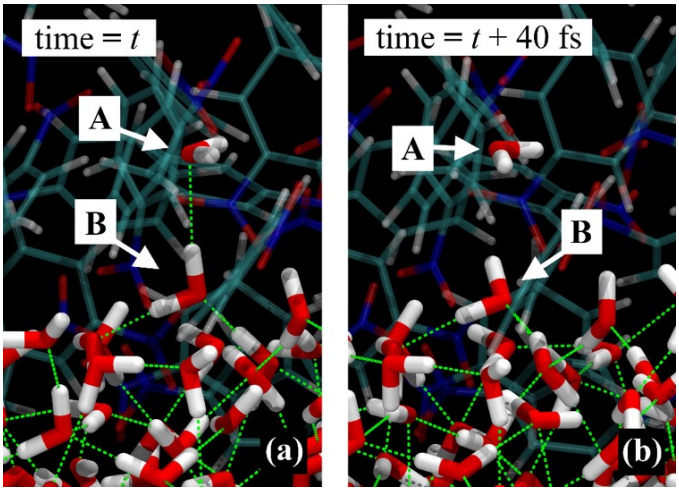

Figure 7.6: The dissolution of a water molecule into nitrobenzene. In panel (a) the transferring water molecule A is still tethered to bulk water by a hydrogen bond to B. In panel (b), 40 fs later, the hydrogen bond has broken and the transferring water has begun to diffuse into the adjacent organic phase.

is given by $\rho\langle v\rangle/4$, [132] where ρ is the water vapor density (approximately equal to p_{vap}/RT with p_{vap} being the vapor pressure at temperature T) and $\langle v\rangle = (8RT/\pi M)^{1/2}$ is the average molecular velocity. [132] Using the experimental vapor pressure of water at 298 K, $p_{vap} = 23.8$ torr, we find $\rho = 1.28$ mol·m^{-3} and the average velocity $\langle v\rangle =$ 592 m/s and thus an evaporation flux of 189 mol·m^{-2}·s^{-1} at 298 K. This is surprisingly similar to the dissolution flux given the difference between the free energy barrier to evaporation (6.5 kcal/mol) and dissolution (3.8 kcal/mol). It is possible that our dissolution flux is underestimated because of our conservative definition of the dissolution event, which requires that the transferred water diffuse a few Å into the organic phase. The low dissolution flux can also be due to recrossings of the transition state barrier caused by collisions with nearby solvent molecules, a much less likely event for evapora-

tion. To examine the dissolution mechanism we begin by considering several kinematic parameters that allow a direct comparison with the mechanism of water evaporation described in Reference [153]. Figure 7.7a is a cartoon schematic showing some of the relevant geometrical coordinates and panels b-d show the time dependence of several parameters characterizing the kinematics of the "last collision" before dissolution during the time interval $t = 0 \pm 100$ fs. In all panels the red curves represent water A (the dissolving water) and the blue curves represent water B (the last water molecule to interact with A). The error bars represent one standard deviation of 487 dissolution events. Figure 7.7b shows the angle $\theta_A(t)$ between the instantaneous center of mass velocity vector of A, denoted by $v_A(t)$, and $\mathbf{r}_0$, defined above (red curve) and same for molecule B (blue curve). The curves in 7b confirm the collision of waters A and B at time zero and show behavior quite similar to the final water-water collision in the evaporation of water. [153] About 20 fs prior to the collision, each molecule approaches the $\mathbf{r}_0$ vector about 30° from normal, they collide, moving past the $\theta = 90°$ point and exit the collision at nearly the same angle at which the other water entered, resulting in a nearly symmetrical region at $t = 0 \pm 20$ fs. Figure 7.7c shows the total kinetic energy ($E_k = \sum_i m_i |\mathbf{v}_i|^2/2$, where the sum is over the three water atoms) of each water molecule during the final collision. On average water B enters with more kinetic energy and appears to transfer part of this energy to water A during the collision. In this regard the E_k curves are similar in shape to related data obtained for the evaporation of water in Reference [153]. The main difference between the evaporation and dissolution E_k curves is that, on average, water B's kinetic energy remains constant (near the minimum

value) after the evaporation collision but water B's kinetic energy is partially restored after the dissolution collision. This 'recovery' of B's average E_k partially reflects a major mechanistic difference between evaporation and dissolution. In evaporation, water A is 'launched' into the vapor phase from the surface by a final collision event occurring near the GDS and water B remains near the GDS. In contrast, as our equilibrium calculations suggested and will further shown below, dissolution into nitrobenzene is accompanied by larger interfacial protrusion of water into the nitrobenzene phase. The pendant water molecule at the 'tip' of this protrusion is essentially inserted or deposited into the organic phase and the final water-water interaction exists somewhere between two possible extremes: (1) Water A is ejected from the tip of the protrusion by the final collision. (2) The protrusion retracts, leaving behind water A. It is between these two extremes that we see the average kinetic energy behavior as shown in Figure 7.7c. In (1) E_k of B would remain constant after the collision while A would gain significantly and in (2) E_k of A would remain constant after this final collision while E_k of B somewhat increases. Figure 7.7d shows the average distance of waters A and B from the collision midpoint M during the final collision. Both water A and water B are further from the collision midpoint at +100 fs (after the collision) than they were at -100 fs (water A much more noticeably). We again compare these results with the evaporation data in Reference [153] where water A, the transferring water is much further from M at +100 fs but water B is considerably closer to M at +100 fs than at -100 fs. This reveals further mechanistic insight: In the evaporation collision water B stays near the collision site, having 'launched' A into the vapor phase. In the dissolution event both waters B

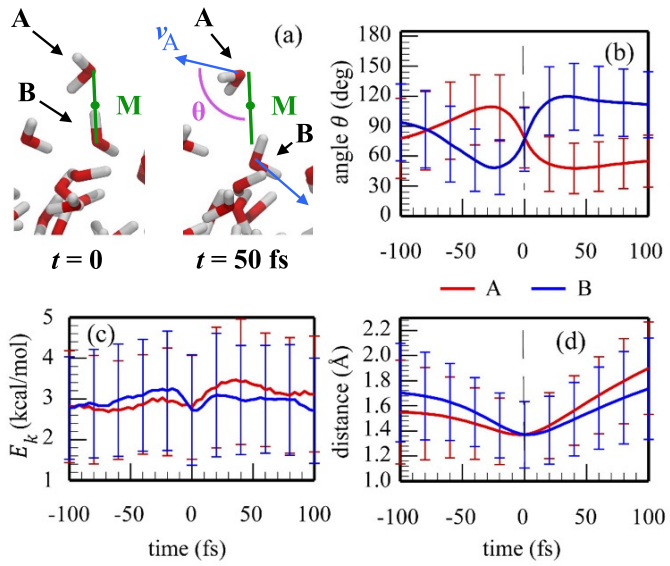

Figure 7.7: (a) Cartoon schematics of the $\mathbf{r}_0$ vector (green line) at time of collision ($t = 0$), center of collision M (green dot), and θ (pink), which is the angle defined by $\mathbf{r}_0$ and the post-collision velocity vector (e.g. v_A, blue.) Nitrobenzene molecules have been omitted for clarity. Averaged time dependence (487 dissolution events) of selected dynamical variables before and after collision of water molecules A and B: (b) Angle of center of mass velocity vectors, (c) kinetic energies of the molecules, and (d) distance from M, the center of the collision vector. The red curves represent A, the transferring water molecule, and the blue curves represent B, the last water molecule that A interacted with before the dissolution event. The error bars represent ± 1 standard deviation.

and A recoil from the collision at speeds greater than their approach, A having gained momentum from B and B being pulled back into the aqueous phase by its neighbors in the retracting water protrusion (to which B remains hydrogen bonded.) We next examine in detail the hydrogen bonding involved in the dissolution process. As outlined in Section I, Bonn and co-workers recently reported on the importance of water-water hydrogen bonding dynamics in water evaporation. [153] In their simulations water B forms a new hydrogen bond with a nearby water molecule at ∼44 fs before the final

collision ($t = 0$). The energy released by the formation of this new hydrogen bond is transferred to the A-B hydrogen bond, the breakup of which results in the evaporation of water A. We use a similar approach in our analysis and also include for the possibility of weak water-nitrobenzene hydrogen bonding. For water-water hydrogen bonds, we use a common geometrical definition where a hydrogen bond is present if the oxygen-oxygen distance is less than 3.4 Å and the H–O$\cdots$O angle is less than 30°. [99] Note that this definition is more restrictive than the condition for dissolution, which only considers the oxygen-oxygen distance. Figure 7.8 shows the time variation of average hydrogen bond populations around the time of the final water-water collision. The green curve in figure 8 represents the hydrogen bond between waters A and B. Since at time t the A-B hydrogen bond either exists ($h(t) = 1$) or does not ($h(t) = 0$), this curve represents the ensemble average $\langle h(t) \rangle$ during the 487 dissolution trajectories. The curve is relatively flat for several hundred fs prior to the detected collision and begins to rapidly decay to zero after about 40 fs. The red and blue curves are the average number of hydrogen bonds between waters A and B and all other water molecules, respectively (not counting A-B hydrogen bonds). The average number of water hydrogen bonds with water A is near zero, indicating that the transferring water only has a strong interaction with water B and suggesting that the predominant final configuration has water A tethered to the aqueous phase by 1 hydrogen bond. Water B participates in an average of 1.8 hydrogen bonds with other water molecules and this number slightly increases after the dissolution of the A-B hydrogen bond. Figure 7.8 also considers hydrogen bonding between waters A and B and the surrounding nitrobenzene molecules. For water-nitrobenzene

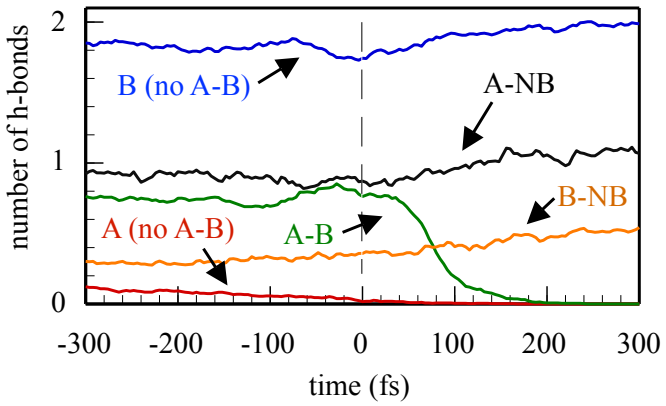

Figure 7.8: Average hydrogen bond populations during the dissolution event. The green curve represents hydrogen bonds between waters A and B. The red curve is the average number of hydrogen bonds between A and other water molecules, not counting A-B hydrogen bonds. Similarly, the blue curve represents the average number of hydrogen bonds between B and other waters, excluding A-B. A-nitrobenzene and B-nitrobenzene hydrogen bonds are represented by the black and orange curves, respectively. All populations are averaged over the 487 dissolution events.

hydrogen bonds we use the same definition as water-water hydrogen bonds above, where nitrobenzene may participate as hydrogen bond acceptor. The hydrogen bond population of nitrobenzene-water A (black curve) increases slightly as water A is transferred into the organic phase and able to form the bond more freely. At the same time the water B-nitrobenzene hydrogen bond population (orange curve) also slightly increase due to the increased exposure of water B to the nitrobenzene phase. The hydrogen bonding populations in Figure 7.8 suggest a rather simple mechanism. Water A is tethered to the aqueous phase by a single hydrogen bond with water B, this hydrogen bond dissociates, and A diffuses into the nitrobenzene phase. As the final A-B hydrogen bond elongates and breaks it may adopt two configurations: water A may act as either hydrogen bond donor or acceptor. The top two panels in Figure 7.9 show representative snapshots at

$t = 0$, where water A is acting as hydrogen bond acceptor (Figure 7.9a) or donor (Figure 7.9b). Hydrogen bonds are indicated by the green dotted lines and nitrobenzene molecules are made invisible so that the difference in the two configurations is clear. Figure 7.9c shows the average number of A-B hydrogen bonds during the final collision and dissolution event (green curve, same as the green curve in Figure 7.8) and the role of water A in the A-B hydrogen bond is specified by red (acceptor) and blue (donor) curves. We find that the transferring water is the acceptor in about 63% of the final A-B hydrogen bonds. The fact that twice as many dissolving water molecules break an acceptor bond than a donor bond may be attributed to the interaction of water A with nitrobenzene. When A acts as acceptor, its two positively charged hydrogen atoms face the nitrobenzene phase where they may interact with the negatively charged nitro groups, whereas when A acts as a donor, only one hydrogen atom is interacting with the negative end of the nitro group. Figure 7.10 provides further support for the mechanism described above by examining some of the relevant distances between the dissolved water and other nearby molecules. Figure 7.10a shows the shortest distance between water A's oxygen and the nearest water oxygen (blue curve) and the shortest distance between a water A hydrogen and the nearest water hydrogen atom (red curve). Both the O-O and H-H distances remain rather constant as the collision event is approached, forming a minimum at $t = 0$ (an artifact of the way the collision is defined, as explained above), and then monotonically increasing, signaling the breakup of the hydrogen bond and subsequent diffusion of the water molecule. The other curves in Figure 7.10a focus on the interactions with the organic liquid. The green and black

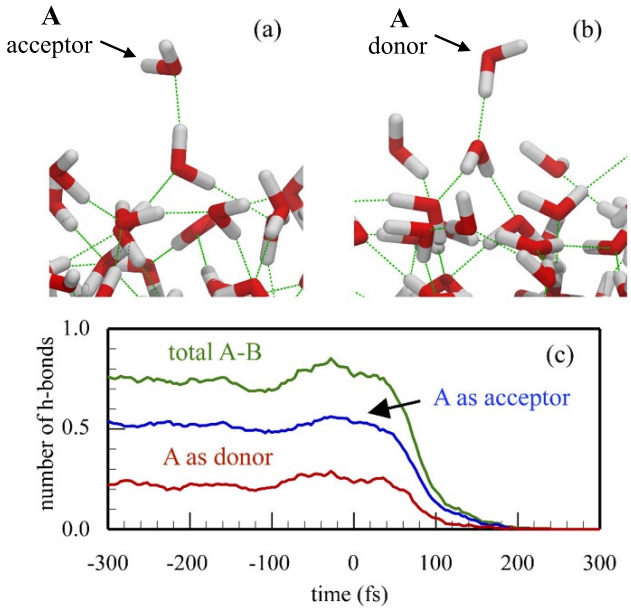

Figure 7.9: Panels (a) and (b) are simulation snapshots illustrating water A as acceptor (a) or donor (b) in the A-B hydrogen bond. The green dotted lines indicate water-water hydrogen bonds. Nitrobenzene molecules have been deleted for clarity. In (c) the average number of A-B hydrogen bonds during the transfer event is shown as the green curve (same as the green curve in Figure 7.8). Molecule A's role in this A-B hydrogen is shown by the blue (acceptor) and red (donor) curves.

curves depict the distance between the transferring water molecule's oxygen atom and the nearest nitrobenzene oxygen and any nitrobenzene atom, respectively. These curves are flat, indicating that the surrounding nitrobenzene molecules do not appear to engage water A during its final collision and dissociation. The water-nitrobenzene curves also indicate that the negatively charged nitro oxygen atoms are not the nitrobenzene moiety nearest to the transferring water as may be expected when considering the partial charges used in our model. Finally, in Figure 7.10b we provide the justification for the assertion that the transferring water emerges from a tip of a water finger. This figure shows the average position of the water A oxygen on the z-axis (red curve) and the distance between waters A and B (blue curve) around the time of the final collision. Again using 3.4 Å as the oxygen-oxygen cutoff distance for both hydration shell membership and maximum water-water hydrogen bond length, we find (average of the 487 transfer events) that the transferring water separates from the bulk at approximately 95 fs after the final collision and at an average z position of 6.0 ± 0.3 Å. This location is only slightly closer to the GDS than the location where the average finger coordinate reaches the cutoff of 3.4 Å: $z(\langle w\rangle$ =3.4 Å) = 6.5 Å in our equilibrium calculations (see Figure 7.5). The fact that these two locations are comparable in value is not surprising since in a simple, single-water transfer event $w \approx r_{OO}$ = 3.4 Å when the transfer is nearly complete (blue curve, Figure 7.8b). Symbolically: $\langle z(w = 3.4 \text{ Å})\rangle = 6.0 \pm 0.3$ Å $\approx z(\langle w\rangle = 3.4 \text{ Å}) = 6.5$ Å. Thus, the breakup of the water molecule from bulk water during the non-equilibrium dissolution trajectories is taking place from a protrusion's tip whose location, on average, is very similar to the breakup position as determined by

the equilibrium free energy transfer calculations.

7.4 Conclusions

The transfer of water from the aqueous phase to an adjacent, immiscible liquid phase has not received much attention, but the thermodynamics and mechanism of this transfer event share features with two more well-studied systems: water evaporation and ion transfer across the liquid/liquid interface. Our molecular dynamics simulations show that, like evaporation, water prefers to transfer to the adjacent phase one-at-a-time: The net free energy of transfer for co-transfer with a single member of its hydration shell (an $(H_2O)_2$ dimer) is larger than single water transfer by about 3.5 k_BT. In addition to the transferring water's position relative to the GDS, the normalized solvation energies may be used as reasonable reaction coordinates that correlate strongly with position-based free energy profiles. Dynamic studies that focused on the interaction between the dissolving water molecules and other interfacial water molecules prior to the transfer event show that the local structure surrounding the transferring water is more similar to a transferring ion than evaporating water. The transfer from water to nitrobenzene occurs via a protrusion into the organic phase, with the last water-water hydrogen bond breaking at about 6 Å beyond the GDS. This breakup occurs approximately 95 fs after the last strong water-water interaction and (unlike in the evaporation of water) involves the dissolution of a pendant water molecule from a water protrusion into the organic phase and retraction of the protrusion.

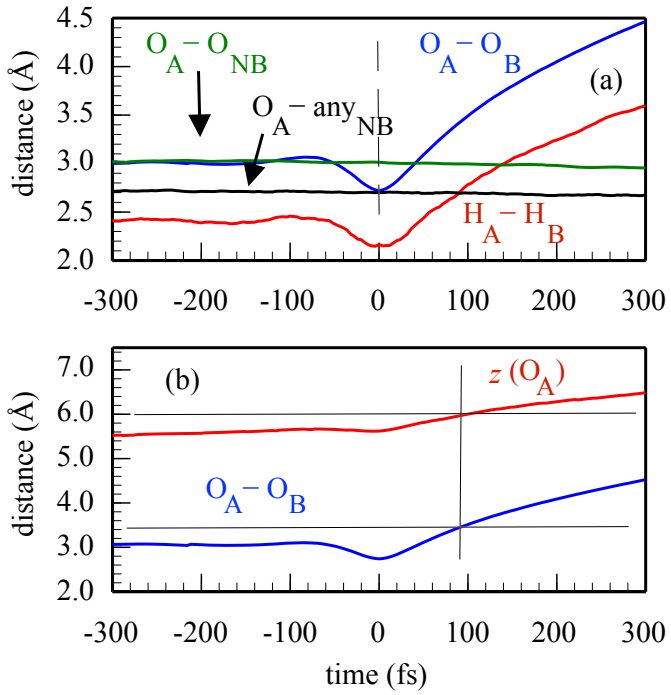

Figure 7.10: Panel (a): Distances from the transferring water to nearest solvent moiety. The blue curve represents water oxygen-oxygen distances and the red is water hydrogen-hydrogen distances. The black and green curves represent the shortest distance from the transferring water oxygen to the nearest nitrobenzene oxygen (black) or any nitrobenzene atom (green.) Panel (b): Average distance between the oxygen atoms of waters A and B (blue, same as panel a) and position of water A's oxygen (O_A) on the simulation z-axis (red.) The vertical and horizontal lines guide the eye to r_{AB} = 3.4 Å, where the A-B hydrogen bond is broken and the corresponding value of $z(O_A)$ = 6.0 Å, which occurs at t = 95 fs.

Acknowledgments

This work is supported by the National Science Foundation through grant CHE-136076. J.J.K. also acknowledges R. J. Vigna for helpful discussions and the University of California, Santa Cruz Chancellor's Dissertation Year Fellowship for financial support.

Bibliography

[1] M. P. Allen and D. J. Tildesley. *Computer Simulation of Liquids*. Clarendon, Oxford, 1987.

[2] D. W. Armstrong, T. J. Ward, R. D. Armstrong, and T. E. Beesley. Separation of drug stereoisomers by the formation of β-cyclodextrin inclusion complexes. *Science*, 232(4754):1132–1135, 1986.

[3] D. Asthagiri, A. Valiya Parambathu, D. Ballal, and W. G. Chapman. Electrostatic and induction effects in the solubility of water in alkanes. *J. Chem. Phys.*, 147(7):074506, 2017.

[4] C. D. Bain. Sum-frequency vibrational spectroscopy of the solid/liquid interface. *J. Chem. Soc., Faraday Trans.*, 91(9):1281–1296, 1995.

[5] D. Ballal, P. Venkataraman, W. A. Fouad, K. R. Cox, and W. G. Chapman. Isolating the non-polar contributions to the intermolecular potential for water-alkane interactions. *J. Chem. Phys.*, 141(6):064905, 2014.

[6] A. Banerjee and P. K. Sengupta. Encapsulation of 3-hydroxyflavone and fisetin

in β-cyclodextrins: Excited state proton transfer fluorescence and molecular mechanics studies. *Chem. Phys. Lett.*, 424(4–6):379–386, 2006.

[7] A. L. Barnette and S. H. Kim. Coadsorption of n-Propanol and Water on SiO2: Study of Thickness, Composition, and Structure of Binary Adsorbate Layer Using Attenuated Total Reflection Infrared (ATR-IR) and Sum Frequency Generation (SFG) Vibration Spectroscopy. *J. Phys. Chem. C*, 116(18):9909–9916, 2012.

[8] L. Barr, P. G. Dumanski, C. J. Easton, J. B. Harper, K. Lee, S. F. Lincoln, A. G. Meyer, and J. S. Simpson. Cyclodextrin molecular reactors. *J. Incl. Phenom. Macrocycl. Chem.*, 50(1-2):19–24, 2004.

[9] I. Benjamin. Dynamics of ion transfer across a liquid–liquid interface: A comparison between molecular dynamics and a diffusion model. *J. Chem. Phys.*, 96(1):577–585, 1992.

[10] I. Benjamin. Mechanism and Dynamics of Ion Transfer Across a Liquid-Liquid Interface. *Science*, 261(5128):1558–1560, 1993.

[11] I. Benjamin. Vibrational Spectrum of Water at the Liquid/Vapor Interface. *Phys. Rev. Lett.*, 73(15):2083–2086, 1994.

[12] I. Benjamin. Photodissociation of ICN in liquid chloroform: Molecular dynamics of ground and excited state recombination, cage escape, and hydrogen abstraction reaction. *J. Chem. Phys.*, 103(7):2459–2471, 1995.

[13] I. Benjamin. Chemical Reactions and Solvation at Liquid Interfaces: A Microscopic Perspective. *Chem. Rev.*, 96, 1996.

[14] I. Benjamin. Empirical valence bond model of an S_N2 reaction in polar and nonpolar solvents. *J. Chem. Phys.*, 129(7):074508, 2008.

[15] I. Benjamin. Structure and dynamics of hydrated ions in a water-immiscible organic solvent. *J. Phys. Chem. B*, 112(49):15801–15806, 2008.

[16] I. Benjamin. Molecular dynamics study of hydrated alkali and halide ions in liquid nitrobenzene. *J. Electroanal. Chem.*, 650(1):41–46, 2010.

[17] I. Benjamin. Recombination, Dissociation, and Transport of Ion Pairs across the Liquid/Liquid Interface. Implications for Phase Transfer Catalysis. *J. Phys. Chem. B*, 117(16):4325–4331, 2013.

[18] I. Benjamin. Reaction Dynamics at Liquid Interfaces. *Annu. Rev. Phys. Chem.*, 66(1):165–188, 2015.

[19] I. Benjamin. Reactivity and Dynamics at Liquid Interfaces. In A. L. Parrill and K. B. Lipkowitz, editors, *Reviews in Computational Chemistry Volume 28*, pages 205–313. John Wiley & Sons, Inc, Hoboken, NJ, USA, 2015.

[20] I. Benjamin, P. F. Barbara, B. J. Gertner, and J. T. Hynes. Nonequilibrium free energy functions, recombination dynamics, and vibrational relaxation of I_2^- in acetonitrile: Molecular dynamics of charge flow in the electronically adiabatic limit. *J. Phys. Chem.*, 99(19):7557–7567, 1995.

[21] I. Benjamin, M. A. Wilson, A. Pohorille, and G. M. Nathanson. Scattering of water from the glycerol liquid-vacuum interface. *Chem. Phys. Lett.*, 243(3):222–228, 1995.

[22] H. J. C. Berendsen, J. P. M. Postma, W. F. Van Gunsteren, and J. Hermans. Interaction models for water in relation to protein hydration. In B. Pullman, editor, *Intermolecular Forces*, page 331. D. Reidel, Dordrecht, 1981.

[23] H. Bertagnolli and P. Chieux. The complete set of atom pair correlation functions of liquid chloroform as obtained from a final neutron scattering experiment with H/D isotopic substitution. *Mol. Phys.*, 51(3):617–631, 1984.

[24] H. Bertagnolli, K. Goller, and H. Zweier. Structure investigations of liquid chloroform by statistical-mechanical calculations and reverse Monte Carlo simulation. *Berichte Bunsenges. Für Phys. Chem.*, 99(10):1168–1178, 1995.

[25] H. Bertagnolli, D. O. Leicht, M. D. Zeidler, and P. Chieux. A neutron diffraction study of liquid chloroform. *Mol. Phys.*, 36(6):1769–1777, 1978.

[26] O. Björneholm, M. H. Hansen, A. Hodgson, L.-M. Liu, D. T. Limmer, A. Michaelides, P. Pedevilla, J. Rossmeisl, H. Shen, G. Tocci, E. Tyrode, M.-M. Walz, J. Werner, and H. Bluhm. Water at Interfaces. *Chem. Rev.*, 116(13):7698–7726, 2016.

[27] H. J. Böhm, C. Meissner, and R. Ahlrichs. Molecular dynamics simulation of

liquid CH_3F, CHF_3, CH_3Cl, CH_3CN, CO_2 and CS_2 with new pair potentials. *Mol. Phys.*, 53(3):651–672, 1984.

[28] G. C. Bond and D. T. Thompson. Catalysis by Gold. *Catal. Rev.*, 41(3-4):319–388, 1999.

[29] B. Boyer, A. Hambardzoumian, J.-P. Roque, and N. Beylerian. Reaction in biphasic water/organic solvent system in the presence of surfactant: Inverse phase transfer catalysis versus interfacial catalysis. *Tetrahedron*, 56(2):303–307, 2000.

[30] M. R. Brindza and R. A. Walker. Differentiating solvation mechanisms at polar solid/liquid interfaces. *J. Am. Chem. Soc.*, 131(17):6207–14, 2009.

[31] A. Burshtein and S. Temkin. *Spectroscopy of Molecular Rotation in Gases and Liquids*. Cambridge University Press, 2005.

[32] N. B. Caballero, M. Zuriaga, M. A. Carignano, and P. Serra. Molecular kinetics of solid and liquid $CHCl_3$. *Chem. Phys. Lett.*, 585:69–73, 2013.

[33] C. Cézard, X. Trivelli, F. Aubry, F. Djedaïni-Pilard, and F.-Y. Dupradeau. Molecular dynamics studies of native and substituted cyclodextrins in different media: 1. Charge derivation and force field performances. *Phys. Chem. Chem. Phys.*, 13(33):15103–15121, 2011.

[34] D. Chandler. *Introduction to Modern Statistical Mechanics*. Oxford University Press, 1 edition, 1987.

[35] J. Chandrasekhar, S. F. Smith, and W. L. Jorgensen. S_N2 reaction profiles in the gas phase and aqueous solution. *J. Am. Chem. Soc.*, 106(10):3049–3050, 1984.

[36] T.-M. Chang and L. X. Dang. Recent Advances in Molecular Simulations of Ion Solvation at Liquid Interfaces. *Chem. Rev. 10641305-1322*, 106(4), 2006.

[37] T.-M. Chang, L. X. Dang, and K. A. Peterson. Computer simulation of chloroform with a polarizable potential model. *J. Phys. Chem. B*, 101(17):3413–3419, 1997.

[38] S. M. Chemtob and G. R. Rossman. Timescales and mechanisms of formation of amorphous silica coatings on fresh basalts at Kīlauea Volcano, Hawai'i. *J. Volcanol. Geotherm. Res.*, 286:41–54, 2014.

[39] J. Chief Elk and I. Benjamin. β-Cyclodextrin at the water/1-bromobutane interface: Molecular insight into reverse phase transfer catalysis. *Langmuir*, 31(18):5086–5092, 2015.

[40] I. Chorny, I. Benjamin, and G. M. Nathanson. Scattering, Trapping, and Ionization of HCl at the Surface of Liquid Glycerol. *J. Phys. Chem. B*, 108(3):995–1002, 2004.

[41] A. Cimas, F. Tielens, M. Sulpizi, M.-P. Gaigeot, and D. Costa. The amorphous silica-liquid water interface studied by ab initio molecular dynamics (AIMD): Local organization in global disorder. *J. Phys. Condens. Matter*, 26(24):244106, 2014.

[42] H. A. Claessens and M. A. van Straten. Review on the chemical and thermal

stability of stationary phases for reversed-phase liquid chromatography. *J. Chromatogr. A*, 1060(1):23–41, 2004.

[43] M. P. Collings, V. L. Frankland, J. Lasne, D. Marchione, A. Rosu-Finsen, and M. R. S. McCoustra. Probing model interstellar grain surfaces with small molecules. *Mon. Not. R. Astron. Soc.*, 449(2):1826–1833, 2015.

[44] E. R. Cruz-Chu, A. Aksimentiev, and K. Schulten. Water-silica force field for simulating nanodevices. *J. Phys. Chem. B*, 110(43):21497–508, 2006.

[45] L. X. Dang. A Mechanism for Ion Transport across the Water/Dichloromethane Interface: A Molecular Dynamics Study Using Polarizable Potential Models. *J. Phys. Chem. B*, 105(4):804–809, 2001.

[46] E. M. M. Del Valle. Cyclodextrins and their uses: A review. *Process Biochem.*, 39(9):1033–1046, 2004.

[47] L. P. Dempsey, J. A. Faust, and G. M. Nathanson. Near-interfacial halogen atom exchange in collisions of Cl_2 with 2.7 M NaBr–glycerol. *J. Phys. Chem. B*, 116(40):12306–12318, 2012.

[48] A. Dettling, K. Stadler, C. Eisenbach, G. Skopp, and H. T. Haffner. Systemic inflammatory response due to chloroform intoxication—an uncommon complication. *Int. J. Legal Med.*, 130(2):401–404, 2016.

[49] U. Diebold. The surface science of titanium dioxide. *Surf. Sci. Rep.*, 48(5):53–229, 2003.

[50] W. Dietz and K. Heinzinger. Structure of liquid chloroform. A comparison between computer simulation and neutron scattering results. *Berichte Bunsenges. Für Phys. Chem.*, 88(6):543–546, 1984.

[51] M. Digne, P. Sautet, P. Raybaud, P. Euzen, and H. Toulhoat. Hydroxyl Groups on γ-Alumina Surfaces: A DFT Study. *J. Catal.*, 211(1):1–5, 2002.

[52] F. Ding, Z. H. Hu, Q. Zhong, K. Manfred, R. R. Gattass, M. R. Brindza, J. T. Fourkas, R. A. Walker, and J. D. Weeks. Interfacial organization of acetonitrile: Simulation and experiment. *J. Phys. Chem. C*, 114(41):17651–17659, 2010.

[53] J. W. Dolan, J. R. Gant, and L. R. Snyder. Gradient elution in high-performance liquid chromatography : II. Practical application to reversed-phase systems. *J. Chromatogr. A*, 165(1):31–58, 1979.

[54] D. J. V. A. dos Santos and J. A. N. F. Gomes. Molecular dynamics study of the calcium ion transfer across the water/nitrobenzene interface. *ChemPhysChem*, 3(11):946–951, 2002.

[55] R. A. W. Dryfe. The electrified liquid-liquid interface. *Adv. Chem. Phys.*, 141:153–215, 2009.

[56] Q. Du, E. Freysz, and Y. Shen. Vibrational spectra of water molecules at quartz/water interfaces. *Phys. Rev. Lett.*, 72(2):238–241, 1994.

[57] C. J. Easton. Cyclodextrin-based catalysts and molecular reactors. *Pure Appl. Chem.*, 77(11):1865–1871, 2009.

[58] A. Eftekhari-Bafrooei and E. Borguet. Effect of surface charge on the vibrational dynamics of interfacial water. *J. Am. Chem. Soc.*, 131(34):12034–5, 2009.

[59] A. Eftekhari-Bafrooei and E. Borguet. Effect of hydrogen-bond strength on the vibrational relaxation of interfacial water. *J. Am. Chem. Soc.*, 132(11):3756–61, 2010.

[60] K. B. Eisenthal. Liquid Interfaces Probed by Second-Harmonic and Sum-Frequency Spectroscopy. *Chem. Rev.*, 96(4):1343–1360, 1996.

[61] C. Escudero and M. Salmeron. From solid–vacuum to solid–gas and solid–liquid interfaces: In situ studies of structure and dynamics under relevant conditions. *Surf. Sci.*, 607:2–9, 2013.

[62] M. W. Evans. A review and computer simulation of the structure and dynamics of liquid chloroform. *J. Mol. Liq.*, 25(3):211–260, 1983.

[63] J. A. Faust, L. P. Dempsey, and G. M. Nathanson. Surfactant-promoted reactions of Cl_2 and Br_2 with Br^- in glycerol. *J. Phys. Chem. B*, 117(41):12602–12612, 2013.

[64] L. A. Frink and D. W. Armstrong. Determination of trace water content in petroleum and petroleum products. *Anal. Chem.*, 88(16):8194–8201, 2016.

[65] S. H. Garofalini. Molecular dynamics computer simulations of silica surface structure and adsorption of water molecules. *J. Non-Cryst. Solids*, 120(1-3):1–12, 1990.

[66] B. J. Gertner, J. P. Bergsma, K. R. Wilson, S. Lee, and J. T. Hynes. Nonadiabatic

solvation model for S_N2 reactions in polar solvents. *J. Chem. Phys.*, 86(3):1377–1386, 1987.

[67] B. J. Gertner, R. M. Whitnell, K. R. Wilson, and J. T. Hynes. Activation to the transition state: Reactant and solvent energy flow for a model S_N2 reaction in water. *J. Am. Chem. Soc.*, 113(1):74–87, 1991.

[68] E. A. Gobrogge and R. A. Walker. Binary solvent organization at silica/liquid interfaces: Preferential ordering in acetonitrile–methanol mixtures. *J. Phys. Chem. Lett.*, 5(15):2688–2693, 2014.

[69] E. A. Gobrogge, B. L. Woods, and R. A. Walker. Liquid organization and solvation properties at polar solid/liquid interfaces. *Faraday Discuss.*, 167:309, 2013.

[70] M. Grün, A. A. Kurganov, S. Schacht, F. Schüth, and K. K. Unger. Comparison of an ordered mesoporous aluminosilicate, silica, alumina, titania and zirconia in normal-phase high-performance liquid chromatography. *J. Chromatogr. A*, 740(1):1–9, 1996.

[71] U. Guenther, I. Smirnova, and R. H. H. Neubert. Hydrophilic silica aerogels as dermal drug delivery systems – Dithranol as a model drug. *Eur. J. Pharm. Biopharm.*, 69(3):935–942, 2008.

[72] M. Halpern. Phase-Transfer Catalysis. In *Ullmann's Encyclopedia of Industrial Chemistry*. Wiley-VCH Verlag GmbH & Co. KGaA, 2000.

[73] T. Heine, H. F. Dos Santos, S. Patchkovskii, and H. A. Duarte. Structure and

dynamics of β-cyclodextrin in aqueous solution at the density-functional tight binding level. *J. Phys. Chem. A*, 111(26):5648–5654, 2007.

[74] P. Hemström and K. Irgum. Hydrophilic interaction chromatography. *J. Sep. Science*, 29(12):1784–1821, 2006.

[75] M. C. Henry, L. K. Wolf, and M. C. Messmer. In situ examination of the structure of model reversed-phase chromatographic interfaces by sum-frequency generation spectroscopy. *J. Phys. Chem. B*, 107(12):2765–2770, 2003.

[76] N. Holmberg, M. Sammalkorpi, and K. Laasonen. Ion transport through a water–organic solvent liquid–liquid interface: A simulation study. *J. Phys. Chem. B*, 118(22):5957–5970, 2014.

[77] A. J. Hopkins, C. L. McFearin, and G. L. Richmond. Investigations of the solid–aqueous interface with vibrational sum-frequency spectroscopy. *Curr. Opin. Solid State Mater. Sci.*, 9(1):19–27, 2005.

[78] K. Horie, T. Kamakura, T. Ikegami, M. Wakabayashi, T. Kato, N. Tanaka, and Y. Ishihama. Hydrophilic interaction chromatography using a meter-scale monolithic silica capillary column for proteomics LC-MS. *Anal. Chem.*, 86(8):3817–3824, 2014.

[79] C. S. Hsu and D. Chandler. RISM calculation of the structure of liquid chloroform. *Mol. Phys.*, 37(1):299–301, 1979.

[80] Z. Hu and J. D. Weeks. Acetonitrile on silica surfaces and at its liquid-vapor

interface: Structural correlations and collective dynamics. *J. Phys. Chem. C*, 114(22):10202–10211, 2010.

[81] W. Humphrey, A. Dalke, and K. Schulten. VMD: Visual molecular dynamics. *J. Mol. Graph.*, 14(1):33–38, 1996.

[82] J. K. Hwang, G. King, S. Creighton, and A. Warshel. Simulation of free energy relationships and dynamics of S_N2 reactions in aqueous solution. *J. Am. Chem. Soc.*, 110(16):5297–5311, 1988.

[83] A. Idrissi. Effect of the local anisotropy on the structural and dynamical properties in liquid chloroform: A molecular dynamics analysis. *J. Mol. Liq.*, 107(1):29–39, 2003.

[84] C. K. Ingold. *Structure and Mechanism in Organic Chemistry*. Cornell University, Ithaca, NY, 2nd edition, 1969.

[85] T. Iwachido, M. Kimura, and K. Tôei. The coextraction of water into nitrobenzene with alkali metal salts of hexanitrodiphenylamine in the presence of dibenzo-18-crown-6. *Chem. Lett.*, 5(10):1101–1104, 1976.

[86] Y. Iwasawa. *Catalysis by Metal Complexes*, volume 7. D. Reidel Publishing Company, Dordecht, Holland, 1986.

[87] M. Jana and S. Bandyopadhyay. Molecular dynamics study of β-cyclodextrin-phenylalanine (1:1) inclusion complex in aqueous medium. *J. Phys. Chem. B*, 117(31):9280–9287, 2013.

[88] D. Jayaweera, S. Islam, N. Gunja, C. Cowie, J. Broska, L. Poojara, M. S. Roberts, and G. K. Isbister. Chloroform ingestion causing severe gastrointestinal injury, hepatotoxicity and dermatitis confirmed with plasma chloroform concentrations. *Clin. Toxicol.*, 55(2):147–150, 2017.

[89] H. Jiang, I. G. Economou, and A. Z. Panagiotopoulos. Phase equilibria of water/CO_2 and water/n-alkane mixtures from polarizable models. *J. Phys. Chem. B*, 121(6):1386–1395, 2017.

[90] M. L. Johnson and I. Benjamin. Photodissociation of ICN at the water/chloroform interface. *J. Phys. Chem. A*, 113(26):7403–11, 2009.

[91] W. L. Jorgensen, J. D. Madura, and C. J. Swenson. Optimized intermolecular potential functions for liquid hydrocarbons. *J. Am. Chem. Soc.*, 106(22):6638–6646, 1984.

[92] J. Juanos i Timoneda and J. T. Hynes. Nonequilibrium free energy surfaces for hydrogen-bonded proton-transfer complexes in solution. *J. Phys. Chem.*, 95(25):10431–10442, 1991.

[93] J.-J. Jwo. In A. G. Volkov, editor, *Interfacial Catalysis*, pages 227–284. Marcel Dekker, New York, 2003. Chapter title: Phase Transfer Catalysis: Fundamantals and Selected systems.

[94] T. Kakiuchi. Current—potential characteristic of ion transfer across the inter-

face between two immiscible electrolyte solutions based on the Nernst—Planck equation. *J. Electroanal. Chem.*, 322(1–2):55–61, 1992.

[95] T. Kakiuchi, M. Nakanishi, and M. Senda. The electrocapillary curves of the phosphatidylcholine monolayer at the polarized oil–water interface. I. Measurement of interfacial tension using a computer-aided pendant-drop method. *Bull. Chem. Soc. Jpn.*, 61(6):1845–1851, 1988.

[96] S. C. L. Kamerlin and A. Warshel. The empirical valence bond model: Theory and applications. *Wiley Interdiscip. Rev. Comput. Mol. Sci.*, 1(1):30–45, 2011.

[97] Y. Kanda, T. Nakamura, and K. Higashitani. AFM studies of interaction forces between surfaces in alcohol–water solutions. *Colloids Surf. Physicochem. Eng. Asp.*, 139(1):55–62, 1998.

[98] J. J. Karnes and I. Benjamin. Mechanism and dynamics of molecular exchange at the silica/binary solvent mixtures interface. *J. Phys. Chem. A*, 119(50):12073–12081, 2015.

[99] J. J. Karnes and I. Benjamin. Geometric and energetic considerations of surface fluctuations during ion transfer across the water-immiscible organic liquid interface. *J. Chem. Phys.*, 145(1):014701, 2016.

[100] J. J. Karnes and I. Benjamin. On the local intermolecular ordering and dynamics of liquid chloroform. *J. Mol. Liq.*, 248(Supplement C):121–126, 2017.

[101] J. J. Karnes and I. Benjamin. S_N2 reaction rate enhancement by β-cyclodextrin at the liquid/liquid interface. *J. Phys. Chem. C*, 121(35):19209–19217, 2017.

[102] J. J. Karnes and I. Benjamin. Structure and dynamics of host/guest complexation at the liquid/liquid interface: Implications for inverse phase transfer catalysis. *J. Phys. Chem. C*, 121(9):4999–5011, 2017.

[103] J. J. Karnes and I. Benjamin. Miscibility at the immiscible liquid/liquid interface: A molecular dynamics study of thermodynamics and mechanism. *J. Chem. Phys.*, 148(3):034707, 2018.

[104] J. J. Karnes, E. A. Gobrogge, R. A. Walker, and I. Benjamin. Unusual structure and dynamics at silica/methanol and silica/ethanol interfaces—a molecular dynamics and nonlinear optical study. *J. Phys. Chem. B*, 120(8):1569–1578, 2016.

[105] J. Kästner. Umbrella sampling. *Wiley Interdiscip. Rev. Comput. Mol. Sci.*, 1(6):932–942, 2011.

[106] N. Kikkawa, L. Wang, and A. Morita. Microscopic barrier mechanism of ion transport through liquid–liquid interface. *J. Am. Chem. Soc.*, 137(25):8022–8025, 2015.

[107] N. Kikkawa, L. Wang, and A. Morita. Computational study of effect of water finger on ion transport through water-oil interface. *J. Chem. Phys.*, 145(1):014702, 2016.

[108] A. A. Kornyshev, A. M. Kuznetsov, and M. Urbakh. Coupled ion–interface dy-

namics and ion transfer across the interface of two immiscible liquids. *J. Chem. Phys.*, 117(14):6766–6779, 2002.

[109] K. Kuchitsu and Y. Morino. Estimation of anharmonic potential constants. II. Bent XY_2 molecules. *Bull. Chem. Soc. Jpn.*, 38(5):814–824, 1965.

[110] S. Kumar, J. M. Rosenberg, D. Bouzida, R. H. Swendsen, and P. A. Kollman. Multidimensional free-energy calculations using the weighted histogram analysis method. *J. Comput. Chem.*, 16(11):1339–1350, 1995.

[111] G. Lamoureux, J. D. Faraldo-Gómez, S. Krupin, and S. Y. Noskov. Polarizable model of chloroform based on classical Drude oscillators. *Chem. Phys. Lett.*, 468(4–6):270–274, 2009.

[112] L. Lawtrakul, H. Viernstein, and P. Wolschann. Molecular dynamics simulations of β-cyclodextrin in aqueous solution. *Int. J. Pharm.*, 256(1–2):33–41, 2003.

[113] S. H. Lee and P. J. Rossky. A comparison of the structure and dynamics of liquid water at hydrophobic and hydrophilic surfaces—a molecular dynamics simulation study. *J. Chem. Phys.*, 100(4):3334, 1994.

[114] S. Leroch and M. Wendland. Simulation of forces between humid amorphous silica surfaces: A comparison of empirical atomistic force fields. *J. Phys. Chem. C*, 116(50):26247–26261, 2012.

[115] K. Lindner and W. Saenger. Crystal and molecular structure of cycloheptaamylose dodecahydrate. *Carbohydr. Res.*, 99(2):103–115, 1982.

[116] K. Lindorff-Larsen, S. Piana, K. Palmo, P. Maragakis, J. L. Klepeis, R. O. Dror, and D. E. Shaw. Improved side-chain torsion potentials for the AMBER ff99SB protein force field. *Proteins Struct. Funct. Bioinforma.*, 78(8):1950–1958, 2010.

[117] D. Lis, E. H. G. Backus, J. Hunger, S. H. Parekh, and M. Bonn. Liquid flow along a solid surface reversibly alters interfacial chemistry. *Science*, 344(6188):1138–1142, 2014.

[118] S. Liu and J. T. Fourkas. Orientational time correlation functions for vibrational sum-frequency generation. 3. Methanol. *J. Phys. Chem. C*, 119(10):5542–5550, 2015.

[119] W. Liu, L. Zhang, and Y. R. Shen. Interfacial layer structure at alcohol/silica interfaces probed by sum-frequency vibrational spectroscopy. *Chem. Phys. Lett.*, 412(1-3):206–209, 2005.

[120] X.-Y. Liu and P. Bennema. The relation between macroscopic quantities and the solid–fluid interfacial structure. *J. Chem. Phys.*, 98(7):5863–5872, 1993.

[121] Y. Liu, C. Chipot, X. Shao, and W. Cai. Threading or tumbling? Insight into the self-inclusion mechanism of an *altro*-α-cyclodextrin derivative. *J. Phys. Chem. C*, 118(33):19380–19386, 2014.

[122] T. Loftsson, Í. B. Össurardóttir, T. Thorsteinsson, M. Duan, and M. Másson. Cyclodextrin solubilization of the antibacterial agents triclosan and triclocarban:

Effect of ionization and polymers. *J. Incl. Phenom. Macrocycl. Chem.*, 52(1-2):109–117, 2005.

[123] L. J. Lowden and D. Chandler. Theory of intermolecular pair correlations for molecular liquids. Applications to the liquids carbon tetrachloride, carbon disulfide, carbon diselenide, and benzene. *J. Chem. Phys.*, 61(12):5228–5241, 1974.

[124] A. Luzar and D. Chandler. Hydrogen-bond kinetics in liquid water. *Nature*, 379(6560):55–57, 1996.

[125] X. Ma, B. Yang, Y. Zhao, H. Xie, and X. Gong. Host-guest inclusion system of scutellarin with polyamine-β-cyclodextrin: Preparation, characterisation, and anti-cancer activity. *Aust. J. Chem.*, 68(6):946–955, 2015.

[126] M. Makosza and M. Fedoryński. Phase transfer catalysis. *Catal. Rev.*, 45(3-4):321–367, 2003.

[127] R. A. Marcus. On the theory of ion transfer rates across the interface of two immiscible liquids. *J. Chem. Phys.*, 113(4):1618–1629, 2000.

[128] P. E. Mason. Molecular dynamics study on the microscopic details of the evaporation of water. *J. Phys. Chem. A*, 115(23):6054–6058, 2011.

[129] L. J. Mathias and R. A. Vaidya. Inverse phase transfer catalysis. First report of a new class of interfacial reactions. *J. Am. Chem. Soc.*, 108(5):1093–1094, 1986.

[130] J. R. Mathis, R. Bianco, and J. T. Hynes. On the activation free energy of the Cl^- + CH_3Cl S_N2 reaction in solution. *J. Mol. Liq.*, 61(1–3):81–101, 1994.

[131] J. G. McDaniel and A. Yethiraj. Comment on "Isolating the non-polar contributions to the intermolecular potential for water-alkane interactions" [J. Chem. Phys. 141, 064905 (2014)]. *J. Chem. Phys.*, 144(13):137101, 2016.

[132] D. A. McQuarrie and J. D. Simon. *Physical Chemistry: A Molecular Approach*. University Science Books, USA, 1997.

[133] S. M. Melnikov, A. Höltzel, A. Seidel-Morgenstern, and U. Tallarek. A molecular dynamics study on the partitioning mechanism in hydrophilic interaction chromatography. *Angew. Chem. Int. Ed.*, 51(25):6251–6254, 2012.

[134] S. M. Melnikov, A. Höltzel, A. Seidel-Morgenstern, and U. Tallarek. Evaluation of aqueous and nonaqueous binary solvent mixtures as mobile phase alternatives to water–acetonitrile mixtures for hydrophilic interaction liquid chromatography by molecular dynamics simulations. *J. Phys. Chem. C*, 119(1):512–523, 2014.

[135] M. Mezei and D. L. Beveridge. Monte Carlo studies of the structure of dilute aqueous sclutions of Li^+, Na^+, K^+, F^-, and Cl^-. *J. Chem. Phys.*, 74(12):6902–6910, 1981.

[136] D. Michael and I. Benjamin. Molecular dynamics simulation of the water—nitrobenzene interface. *J. Electroanal. Chem.*, 450(2):335–345, 1998.

[137] S. Minakata and M. Komatsu. Organic reactions on silica in water. *Chem. Rev.*, 109(2):711–724, 2009.

[138] P. B. Miranda and Y. R. Shen. Liquid interfaces: A study by sum-frequency vibrational spectroscopy. *J. Phys. Chem. B*, 103(17):3292–3307, 1999.

[139] M. V. Mirkin and M. Tsionsky. In J. A. Bard and M. V. Mirkin, editors, *Scanning Electrochemical Microscopy*, page 191. CRC Press, 2012.

[140] M. Mizukami, M. Moteki, and K. Kurihara. Hydrogen-bonded macrocluster formation of ethanol on silica surfaces in cyclohexane. *J. Am. Chem. Soc.*, 124(43):12889–12897, 2002.

[141] E. Monflier, G. Fremy, Y. Castanet, and A. Mortreux. Molecular recognition between chemically modified β-cyclodextrin and dec-1-ene: New prospects for biphasic hydroformylation of water-insoluble olefins. *Angew. Chem. Int. Ed. Engl.*, 34(20):2269–2271, 1995.

[142] E. Monflier, S. Tilloy, E. Blouet, Y. Barbaux, and A. Mortreux. Wacker oxidation of various olefins in the presence of per(2,6-di-*o*-methyl)-β-cyclodextrin: Mechanistic investigations of a multistep catalysis in a solvent-free two-phase system. *J. Mol. Catal. Chem.*, 109(1):27–35, 1996.

[143] E. Monflier, S. Tilloy, Y. Castanet, and A. Mortreux. Chemically modified β-cyclodextrins: Efficient supramolecular carriers for the biphasic hydrogenation of water-insoluble aldehydes. *Tetrahedron Lett.*, 39(19):2959–2960, 1998.

[144] A. Morsali, E. K. Goharshadi, G. Ali Mansoori, and M. Abbaspour. An accurate

expression for radial distribution function of the Lennard-Jones fluid. *Chem. Phys.*, 310(1–3):11–15, 2005.

[145] R. D. Mountain. Microstructure and hydrogen bonding in water-acetonitrile mixtures. *J. Phys. Chem. B*, 114(49):16460–4, 2010.

[146] R. D. Mountain. Molecular dynamics simulation of water–acetonitrile mixtures in a silica slit. *J. Phys. Chem. C*, 117(8):3923–3929, 2013.

[147] E. F. Muhammad, R. Adnan, M. A. M. Latif, and M. B. A. Rahman. Theoretical investigation on insulin dimer-β-cyclodextrin interactions using docking and molecular dynamics simulation. *J. Incl. Phenom. Macrocycl. Chem.*, 84(1-2):1–10, 2015.

[148] M. Mukhopadhyay, D. Banerjee, and S. Mukherjee. Proton-transfer reaction of 4-methyl 2,6-diformyl phenol in cyclodextrin nanocage. *J. Phys. Chem. A*, 110(47):12743–12751, 2006.

[149] T. Müller, T. L. Werblowsky, G. M. Florio, B. J. Berne, and G. W. Flynn. Ultra-high vacuum scanning tunneling microscopy and theoretical studies of 1-halohexane monolayers on graphite. *Proc. Natl. Acad. Sci. U. S. A.*, 102(15):5315–5322, 2005.

[150] R. S. Mulliken, C. A. Rieke, D. Orloff, and H. Orloff. Formulas and numerical tables for overlap integrals. *J. Chem. Phys.*, 17(12):1248–1267, 1949.

[151] I. Nadler, D. Mahgerefteh, H. Reisler, and C. Wittig. The 266 nm photolysis of ICN: Recoil velocity anisotropies and nascent E,V,R,T excitations for the CN+I($^2P_{3/2}$) and CN+I($^2P_{1/2}$) channels. *J. Chem. Phys.*, 82(9):3885–3893, 1985.

[152] Y. Nagata, T. Ohto, E. H. G. Backus, and M. Bonn. Molecular modeling of water interfaces: From molecular spectroscopy to thermodynamics. *J. Phys. Chem. B*, 120(16):3785–3796, 2016.

[153] Y. Nagata, K. Usui, and M. Bonn. Molecular mechanism of water evaporation. *Phys. Rev. Lett.*, 115(23):236102, 2015.

[154] M. A. Natal-Santiago and J. A. Dumesic. Microcalorimetric, FTIR, and DFT studies of the adsorption of methanol, ethanol, and 2,2,2-trifluoroethanol on silica. *J. Catal.*, 175(2):252–268, 1998.

[155] J. Nawrocki, C. Dunlap, A. McCormick, and P. W. Carr. Part I. Chromatography using ultra-stable metal oxide-based stationary phases for HPLC. *J. Chromatogr. A*, 1028(1):1–30, 2004.

[156] K. V. Nelson and I. Benjamin. Microhydration effects on a model S_N2 reaction in a nonpolar solvent. *J. Chem. Phys.*, 130(19):194502, 2009.

[157] K. V. Nelson and I. Benjamin. A molecular dynamics-empirical valence bond study of an S_N2 reaction at the water/chloroform interface. *J. Phys. Chem. C*, 114(2):1154–1163, 2010.

[158] K. V. Nelson and I. Benjamin. A molecular dynamics/EVB study of an S_N2 reaction in water clusters. *Chem. Phys. Lett.*, 492(4-6):220–225, 2010.

[159] K. V. Nelson and I. Benjamin. Effect of a phase transfer catalyst on the dynamics of an S_N2 reaction. A molecular dynamics study. *J. Phys. Chem. C*, 115(5):2290–2296, 2011.

[160] K. V. Nelson and I. Benjamin. A model S_N2 reaction 'on water' does not show rate enhancement. *Chem. Phys. Lett.*, 508(1-3):59–62, 2011.

[161] H. Niu, D. Huang, and C. Niu. Time-gated fluorescence sensor for trace water content determination in organic solvents based on covalently immobilized europium ternary complex. *Sens. Actuators B Chem.*, 192(Supplement C):812–817, 2014.

[162] C. D. Norton and W. H. Thompson. On the diffusion of acetonitrile in nanoscale amorphous silica pores. Understanding anisotropy and the effects of hydrogen bonding. *J. Phys. Chem. C*, 117(37):19107–19114, 2013.

[163] C. D. Norton and W. H. Thompson. Reorientation dynamics of nanoconfined acetonitrile: A critical examination of two-state models. *J. Phys. Chem. B*, 118(28):8227–8235, 2014.

[164] T. Okuhara. Water-tolerant solid acid catalysts. *Chem. Rev.*, 102(10):3641–3666, 2002.

[165] S. Ong, X. Zhao, and K. B. Eisenthal. Polarization of water molecules at a

charged interface: Second harmonic studies of the silica/water interface. *Chem. Phys. Lett.*, 191(3):327–335, 1992.

[166] T. Ooi and K. Maruoka. Recent advances in asymmetric phase-transfer catalysis. *Angew. Chem. Int. Ed.*, 46(23):4222–4266, 2007.

[167] T. Osakai. The Role of Water Molecules in Ion Transfer at the Oil/Water Interface. In A. G. Volkov, editor, *Interfacial Catalysis*, pages 53–82. Marcel Dekker, New York, 2003. Chapter title: Phase Transfer Catalysis: Fundamantals and Selected systems.

[168] V. Ostroverkhov, G. A. Waychunas, and Y. R. Shen. New Information on Water Interfacial Structure Revealed by Phase-Sensitive Surface Spectroscopy. *Phys. Rev. Lett.*, 94(4):046102, 2005.

[169] S. K. Parida, S. Dash, S. Patel, and B. K. Mishra. Adsorption of organic molecules on silica surface. *Adv. Colloid Interface Sci.*, 121(1):77–110, 2006.

[170] J.-Y. Park, Z.-M. Wang, D.-K. Kim, and J.-S. Lee. Effects of water on the esterification of free fatty acids by acid catalysts. *Renew. Energy*, 35(3):614–618, 2010.

[171] A. G. Pelmenschikov, G. Morosi, A. Gamba, A. Zecchina, S. Bordiga, and E. A. Paukshtis. Mechanisms of methanol adsorption on silicalite and silica: IR spectra and ab-initio calculations. *J. Phys. Chem.*, 97(46):11979–11986, 1993.

[172] J. K. Percus and G. O. Williams. The Intrinsic Interface. In C. A. Croxton, editor, *Fluid Interfacial Phenomena*, pages 1–44. Wiley, New York, 1986.

[173] K. Piradashvili, E. M. Alexandrino, F. R. Wurm, and K. Landfester. Reactions and polymerizations at the liquid–liquid interface. *Chem. Rev.*, 2015.

[174] A. Pohorille and M. A. Wilson. Viewpoint 9 — Molecular structure of aqueous interfaces. *J. Mol. Struct. THEOCHEM*, 284(3):271–298, 1993.

[175] S. Pothoczki, A. Ottochian, M. Rovira-Esteva, L. C. Pardo, J. L. Tamarit, and G. J. Cuello. Role of steric and electrostatic effects in the short-range order of quasitetrahedral molecular liquids. *Phys. Rev. B*, 85(1):014202, 2012.

[176] S. Pothoczki, L. Temleitner, and L. Pusztai. Detailed intermolecular structure of molecular liquids containing slightly distorted tetrahedral molecules with C_{3v} symmetry: Chloroform, bromoform, and methyl-iodide. *J. Chem. Phys.*, 134(4):044521, 2011.

[177] S. Pothoczki, L. Temleitner, and L. Pusztai. Structure of neat liquids consisting of (perfect and nearly) tetrahedral molecules. *Chem. Rev.*, 115(24):13308–13361, 2015.

[178] K. L. Prime and G. M. Whitesides. Self-assembled organic monolayers: Model systems for studying adsorption of proteins at surfaces. *Science*, 252(5009):1164–1167, 1991.

[179] B. Qiao, J. V. Muntean, M. Olvera de la Cruz, and R. J. Ellis. Ion transport mechanisms in liquid–liquid interface. *Langmuir*, 33(24):6135–6142, 2017.

[180] R. Rey. Quantitative characterization of orientational order in liquid carbon tetrachloride. *J. Chem. Phys.*, 126(16):164506, 2007.

[181] J. W. Roddy and C. F. Coleman. Solubility of water in hydrocarbons as a function of water activity. *Talanta*, 15(11):1281–1286, 1968.

[182] D. Rose and I. Benjamin. Free energy of transfer of hydrated ion clusters from water to an immiscible organic solvent. *J. Phys. Chem. B*, 113(27):9296–303, 2009.

[183] M. Roskosz and H. Leroux. A significant amount of crystalline silica in seturned cometary samples: Bridging the gap between astrophysical and meteoritical observations. *Astrophys. J. Lett.*, 801(1):L7, 2015.

[184] J. S. Rowlinson and B. Widom. *Molecular Theory of Capillarity*, volume 88. Clarendon Press, Oxford, 1984.

[185] D. Roy, S. Liu, B. L. Woods, A. R. Siler, J. T. Fourkas, J. D. Weeks, and R. A. Walker. Nonpolar adsorption at the silica/methanol interface: Surface mediated polarity and solvent density across a strongly associating solid/liquid boundary. *J. Phys. Chem. C*, 117(51):27052–27061, 2013.

[186] M. Rutigliano, P. Gamallo, R. Sayós, S. Orlandini, and M. Cacciatore. A molec-

ular dynamics simulation of hydrogen atoms collisions on an H-preadsorbed silica surface. *Plasma Sources Sci. Technol.*, 23(4):045016, 2014.

[187] J. Saien, A. Rezvani Pour, and S. Asadabadi. Interfacial tension of the n-hexane–water system under the influence of magnetite nanoparticles and sodium dodecyl sulfate assembly at different temperatures. *J. Chem. Eng. Data*, 59(6):1835–1842, 2014.

[188] S. Sakaguchi and A. Morita. Mass accommodation mechanism of water through monolayer films at water/vapor interface. *J. Chem. Phys.*, 137(6):064701, 2012.

[189] M. G. Sceats and S. A. Rice. The entropy of liquid water from the random network model. *J. Chem. Phys.*, 72(5):3260–3262, 1980.

[190] W. Schmickler. A model for ion transfer through liquid—liquid interfaces. *J. Electroanal. Chem.*, 426(1–2):5–9, 1997.

[191] F. Scholz. Recent advances in the electrochemistry of ion transfer processes at liquid–liquid interfaces. *Annu. Rep. Prog. Chem., Sect. C: Phys. Chem.*, 102(0):43–70, 2006.

[192] K. Schweighofer and I. Benjamin. Transfer of a tetramethylammonium ion across the water-nitrobenzene interface: potential of mean force and nonequilibrium dynamics. *J. Phys. Chem. A*, 103(49):10274–10279, 1999.

[193] K. J. Schweighofer and I. Benjamin. Dynamics of ion desorption from the liquid—vapor interface of water. *Chem. Phys. Lett.*, 202(5):379–383, 1993.

[194] K. J. Schweighofer and I. Benjamin. Transfer of small ions across the water/1,2-dichloroethane interface. *J. Phys. Chem.*, 99(24):9974–9985, 1995.

[195] D. Seddon. Reformulated gasoline, opportunities for new catalyst technology. *Catal. Today*, 15(1):1–21, 1992.

[196] S. Sen, D. Sukul, P. Dutta, and K. Bhattacharyya. Slow solvation dynamics of dimethylformamide in a nanocavity. 4-Aminophthalimide in β-cyclodextrin. *J. Phys. Chem. A*, 105(47):10635–10639, 2001.

[197] Y. Shao and S. G. Weber. Direct observation of chloride transfer across the water/organic Interface and the transfer of long-chain dicarboxylates. *J. Phys. Chem.*, 100(35):14714–14720, 1996.

[198] Y. R. Shen. Surface properties probed by second-harmonic and sum-frequency generation. *Nature*, 337(6207):519–525, 1989.

[199] Y. R. Shen. Surfaces probed by nonlinear optics. *Surf. Sci.*, 299–300:551–562, 1994.

[200] Y. R. Shen and V. Ostroverkhov. Sum-frequency vibrational spectroscopy on water interfaces: Polar orientation of water molecules at interfaces. *Chem. Rev.*, 106(4):1140–54, 2006.

[201] J. J. Shephard, A. K. Soper, S. K. Callear, S. Imberti, J. S. O. Evans, and C. G. Salzmann. Polar stacking of molecules in liquid chloroform. *Chem. Commun.*, 51:4770–4773, 2015.

[202] N. Sieffert and G. Wipff. Adsorption at the liquid-liquid interface in the biphasic rhodium catalyzed hydroformylation of olefins promoted by cyclodextrins: A molecular dynamics study. *J. Phys. Chem. B*, 110(9):4125–4134, 2006.

[203] N. Sieffert and G. Wipff. Importance of interfacial adsorption in the biphasic hydroformylation of higher olefins promoted by cyclodextrins: a molecular dynamics study at the decene/water interface. *Chem. Eur. J.*, 13(7):1978–90, 2007.

[204] A. R. Siler and R. A. Walker. Effects of solvent structure on interfacial polarity at strongly associating silica/alcohol interfaces. *J. Phys. Chem. C*, 115(19):9637–9643, 2011.

[205] A. A. Skelton, P. Fenter, J. D. Kubicki, D. J. Wesolowski, and P. T. Cummings. Simulations of the quartz$(10\bar{1}1)$/water interface: A comparison of classical force fields, ab initio molecular dynamics, and x-ray reflectivity experiments. *J. Phys. Chem. C*, 115(5):2076–2088, 2011.

[206] I. Smirnova, S. Suttiruengwong, and W. Arlt. Feasibility study of hydrophilic and hydrophobic silica aerogels as drug delivery systems. *J. Non-Cryst. Solids*, 350:54–60, 2004.

[207] I. Smirnova, S. Suttiruengwong, and W. Arlt. Aerogels: Tailor-made Carriers for Immediate and Prolonged Drug Release. *KONA Powder Part. J.*, 23:86–97, 2005.

[208] R. K. Smith, P. A. Lewis, and P. S. Weiss. Patterning self-assembled monolayers. *Prog. Surf. Sci.*, 75(1):1–68, 2004.

[209] L. R. Snyder, J. W. Dolan, and J. R. Gant. Gradient elution in high-performance liquid chromatography : I. Theoretical basis for reversed-phase systems. *J. Chromatogr. A*, 165(1):3–30, 1979.

[210] C. M. Starks, C. L. Liotta, and M. E. Halpern. Phase-Transfer Catalysis: Fundamentals I. In *Phase-Transfer Catalysis*, pages 23–47. Springer Netherlands, 1994.

[211] T. Steiner and G. Koellner. Crystalline β-cyclodextrin hydrate at various humidities: Fast, continuous, and reversible dehydration studied by x-ray diffraction. *J. Am. Chem. Soc.*, 116(12):5122–5128, 1994.

[212] L. Sun, W. L. Hase, and K. Song. Trajectory studies of S_N2 nucleophilic substitution. 8. central barrier dynamics for gas phase Cl^- + CH_3Cl. *J. Am. Chem. Soc.*, 123(24):5753–5756, 2001.

[213] W. C. Swope, H. C. Andersen, P. H. Berens, and K. R. Wilson. A computer simulation method for the calculation of equilibrium constants for the formation of physical clusters of molecules: Application to small water clusters. *J. Chem. Phys.*, 76(1):637–649, 1982.

[214] J. Szejtli. Introduction and general overview of cyclodextrin chemistry. *Chem. Rev.*, 98(5):1743–1754, 1998.

[215] K. Takahashi. Organic reactions mediated by cyclodextrins. *Chem. Rev.*, 98(5):2013–2034, 1998.

[216] S. Tilloy, H. Bricout, and E. Monflier. Cyclodextrins as inverse phase transfer catalysts for the biphasic catalytic hydrogenation of aldehydes: A green and easy alternative to conventional mass transfer promoters. *Green Chem.*, 4(3):188–193, 2002.

[217] A. Z. Trifonov and T. T. Nikiforov. Cyclodextrins as phase-transfer catalysts in a nucleophilic displacement reaction. *J. Mol. Catal.*, 24(1):15–18, 1984.

[218] Z. Ulker and C. Erkey. An emerging platform for drug delivery: Aerogel based systems. *J. Controlled Release*, 177:51–63, 2014.

[219] S. Vallejo, L. J, J. M. Ovejero, R. A. Fernández, and S. A. Dassie. Simple Ion Transfer at Liquid—Liquid Interfaces. *Int. J. Electrochem.*, pages 1–34, 2012.

[220] P. Varilly and D. Chandler. Water evaporation: A transition path sampling study. *J. Phys. Chem. B*, 117(5):1419–1428, 2013.

[221] C. G. Verdes, M. Urbakh, and A. A. Kornyshev. Surface tension and ion transfer across the interface of two immiscible electrolytes. *Electrochem. Commun.*, 6(7):693–699, 2004.

[222] L. Verlet. Computer "Experiments" on classical fluids. I. Thermodynamical properties of Lennard-Jones molecules. *Phys. Rev.*, 159(1):98–103, 1967.

[223] J. Vieceli and I. Benjamin. Adsorption at the interface between water and self-assembled monolayers: Structure and electronic spectra. *J. Phys. Chem. B*, 106(32):7898–7907, 2002.

[224] A. Warshel. *Computer Modeling of Chemical Reactions in Enzymes and Solutions*. Wiley, 1991.

[225] A. Warshel and R. M. Weiss. An empirical valence bond approach for comparing reactions in solutions and in enzymes. *J. Am. Chem. Soc.*, 102(20):6218–6226, 1980.

[226] S. J. Weiner, P. A. Kollman, D. T. Nguyen, and D. A. Case. An all atom force field for simulations of proteins and nucleic acids. *J. Comput. Chem.*, 7(2):230–252, 1986.

[227] M. K. Weldon, P. Uvdal, C. M. Friend, and J. G. Serafin. Decoupling of vibrational modes as a structural tool: Coverage-induced reorientation of methoxide on Mo(110). *J. Chem. Phys.*, 103(12):5075–5084, 1995.

[228] A. Wennberg and D. Ørstavik. Evaluation of alternatives to chloroform in endodontic practice. *Dent. Traumatol.*, 5(5):234–237, 1989.

[229] G. M. Whitesides and P. E. Laibinis. Wet chemical approaches to the characterization of organic surfaces: Self-assembled monolayers, wetting, and the physical-organic chemistry of the solid-liquid interface. *Langmuir*, 6(1):87–96, 1990.

[230] R. M. Whitnell and K. R. Wilson. Computational molecular dynamics of chemical reactions in solution. In K. B. Lipkowitz and D. B. Boyd, editors, *Reviews in Computational Chemistry*, pages 67–148. John Wiley & Sons, Inc., 1993.

[231] R. Wischert, P. Florian, C. Copéret, D. Massiot, and P. Sautet. Visibility of Al

surface sites of γ-alumina: A combined computational and experimental point of view. *J. Phys. Chem. C*, 118(28):15292–15299, 2014.

[232] H. A. Wittcoff and B. G. Reuben. *Industrial Organic Reactions*. J. Wiley, New York, 1996.

[233] L. Xie, D. K. Harris, M. G. Bawendi, and K. F. Jensen. Effect of trace water on the growth of indium phosphide quantum dots. *Chem. Mater.*, 27(14):5058–5063, 2015.

[234] C.-C. Yin, A. H.-T. Li, and S. D. Chao. Liquid chloroform structure from computer simulation with a full ab initio intermolecular interaction potential. *J. Chem. Phys.*, 139(19):194501, 2013.

[235] H. Zhang, W. Feng, C. Li, Y. Lv, and T. Tan. A model for the shuttle motions of puerarin and daidzin inside the cavity of β-cyclodextrin in aqueous acetic acid: Insights from molecular dynamics simulations. *J. Mol. Model.*, 18(1):221–227, 2011.

[236] L. Zhang, W. Liu, Y. R. Shen, and D. G. Cahill. Competitive molecular adsorption at liquid/solid interfaces: A study by sum-frequency vibrational spectroscopy. *J. Phys. Chem. C*, 111(5):2069–2076, 2007.

[237] X. Zhang, W. H. Steel, and R. A. Walker. Probing solvent polarity across strongly associating solid/liquid interfaces using molecular rulers. *J. Phys. Chem. B*, 107(16):3829–3836, 2003.

[238] X. Zheng, D. Wang, Z. Shuai, and X. Zhang. Molecular dynamics simulations of the supramolecular assembly between an azobenzene-containing surfactant and α-cyclodextrin: Role of photoisomerization. *J. Phys. Chem. B*, 116(2):823–832, 2012.

[239] I. Zimoch and E. Łobos. Evaluation of health risk caused by chloroform in drinking water. *Desalination Water Treat.*, 57(3):1027–1033, 2016.

Appendix A

Methanol-silica hydrogen bond lifetime correlation function.

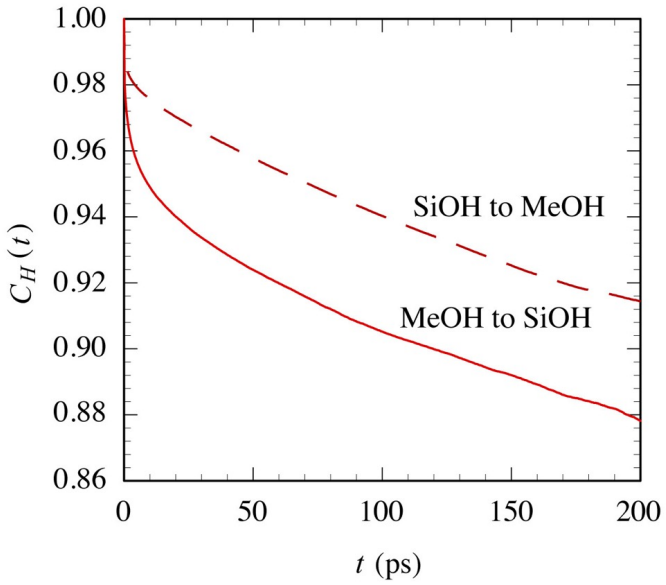

Figure A.1: Methanol-silica hydrogen bond lifetime correlation function. Methanol acts as hydrogen bond donor in the solid curve and as hydrogen bond acceptor in the dashed curve. $C_H(t)$, is defined as $C_H(t) = \frac{\langle h(t)h(0)\rangle}{\langle h(0)h(0)\rangle}$, where h is equal to 1 if a hydrogen bond exists and 0 if no bond exists. The ensemble average is calculated over all time origins.

Appendix B

Structure and dynamics of host/guest complexation at the liquid/liquid interface: Implications for inverse phase transfer catalysis

B.1 Umbrella sampling constraining forces

Host/guest PMF curves were generated by constraining the tagged molecule within a specified window along the p-axis. For a window of width w_w centered at $\gamma = w_c$, the applied constraining energy is

$$U = k\zeta^3, \zeta = |\gamma - w_c| - w_w/2 \tag{B.1}$$

where k is a constant (selected to be1200 kcal mol^{-1}Å^{-3}). We define the tagged molecule's center of mass as

$$\mathbf{r}_{\mathrm{BrOct}} = \frac{\sum_i m_i \mathbf{r}_i}{M_{\mathrm{BrOct}}} \tag{B.2}$$

where m_i and M_{BrOct} are the individual atom-center masses and total mass of the tagged molecule. The force on a 1-bromooctane atom center in the x-direction is then

$$f_{i,x} = -\frac{\partial U}{\partial x_i} = -3k\zeta^2 \frac{\partial \gamma}{\partial x_i} \mathrm{sgn}(\gamma - w_c) \tag{B.3}$$

where

$$\frac{\partial \gamma}{\partial x_i} = \frac{\partial \mathbf{r}_{\mathrm{BrOct}}}{\partial x_i} \cdot \hat{\mathbf{p}} = \frac{m_i}{M_{\mathrm{BrOct}}} \hat{\mathbf{i}} \cdot \hat{\mathbf{p}} \tag{B.4}$$

where $\hat{\mathbf{i}}$ is a unit vector along the x-axis and similarly for the y and z-directions.

The functional form differs when considering β-CD atoms since the definitions of $\hat{\mathbf{p}}$ and the β-CD center of mass, rβ-CD, share atoms. We formally define $\hat{\mathbf{p}}$ as

$$\hat{\mathbf{p}} = (\mathbf{r}_S - \mathbf{r}_L)/|\mathbf{r}_S - \mathbf{r}_L| \tag{B.5}$$

where $\mathbf{r}_S$ and $\mathbf{r}_L$ are the centers of the large and small pore openings, defined as centers of mass of a subset of β-CD atoms at each opening

$$\mathbf{r}_S = \frac{\sum_i m_i \mathbf{r}_i}{M_S} \tag{B.6}$$

where M_S is the total mass of the atoms which define $\mathbf{r}_S$. The force in the x-direction

on β-CD atoms that do not contribute to the definition of $\hat{\mathbf{p}}$ is

$$f_{i,x} = -\frac{\partial U}{\partial x_i} = -3k\zeta^2 \frac{\partial \gamma}{\partial x_i} \mathrm{sgn}(\gamma - w_c) \tag{B.7}$$

where the form of $\partial\gamma/\partial x_i$ similar to above

$$\frac{\partial \gamma}{\partial x_i} = \frac{\partial \mathbf{r}_{\beta\text{-CD}}}{\partial x_i} \cdot \hat{\mathbf{p}} = \frac{m_i}{M_{\beta\text{-CD}}} \hat{\mathbf{i}} \cdot \hat{\mathbf{p}} \tag{B.8}$$

A different force must be applied when considering a β-CD atom used in the definition of the $\hat{\mathbf{p}}$. Consider an atom center j where j is used to define $\mathbf{r}_S$. The applied force in the x-direction is

$$f_{j,x} = -\frac{\partial U}{\partial x_j} = -3k\zeta^2 \frac{\partial \gamma}{\partial x_j} \mathrm{sgn}(\gamma - w_c) \tag{B.9}$$

where

$$\frac{\partial \gamma}{\partial x_j} = -\frac{\partial \mathbf{r}_{\beta\text{-CD}}}{\partial x_j} \cdot \hat{\mathbf{p}} + (\mathbf{r}_{\mathrm{BrOct}} - \mathbf{r}_{\beta\text{-CD}}) \cdot \frac{\partial \hat{\mathbf{p}}}{\partial x_j} \tag{B.10}$$

and

$$\frac{\partial \hat{\mathbf{p}}}{\partial x_j} = \frac{\partial [(\mathbf{r}_S - \mathbf{r}_L)/|\mathbf{r}_S - \mathbf{r}_L|]}{\partial x_j} \tag{B.11}$$

Application of the chain rule again gives

$$\frac{\partial \hat{\mathbf{p}}}{\partial x_j} = \frac{m_j}{|\mathbf{r}_S - \mathbf{r}_L| M_S} [\hat{\mathbf{i}} - (\hat{\mathbf{i}} \cdot \hat{\mathbf{p}}) \hat{\mathbf{p}}] \tag{B.12}$$

which is substituted into Equation 3.21 to obtain

$$\frac{\partial \gamma}{\partial x_j} = -\frac{m_n}{M_{\beta\text{-CD}}}\hat{\mathbf{i}} \cdot \hat{\mathbf{p}} + \frac{m_n}{M_S|\mathbf{r}_{\text{BrOct}} - \mathbf{r}_{\beta\text{-CD}}|}[(\mathbf{r}_{\text{BrOct}} - \mathbf{r}_{\beta\text{-CD}}) \cdot \hat{\mathbf{i}} - \gamma(\hat{\mathbf{i}} \cdot \hat{\mathbf{p}})] \qquad \text{(B.13)}$$

Similar results are obtained for forces in the y and z-directions and the same approach is applied to find the appropriate forces on β-CD atoms which contribute to the definition of $\mathbf{r}_L$ and thus $\hat{\mathbf{p}}$.

B.2 Visualizing $g(m, n)$

We introduce the 2-dimensional spatial distribution function (SDF) $g(m, n)$ in the main text and here include further information to aid in visualizing the resultant data. This SDF views the β-CD molecule by 'looking through the pore,' and results in data that projects the surrounding solvent's density onto a plane parallel to the pore openings (orthogonal to the vector $\mathbf{p}$) and passing through the β-CD center of mass. Figure S1 is similar to Figure 5b in the main text, with a snapshot of the β-CD molecule overlaid for additional clarity. This 'top view' SDF considers all solvent molecules within ± 8 Å from the plane passing through the β-CD center of mass. The volume of solvent described by $g(m, n)$ is shown by the cartoon in Figure S2.

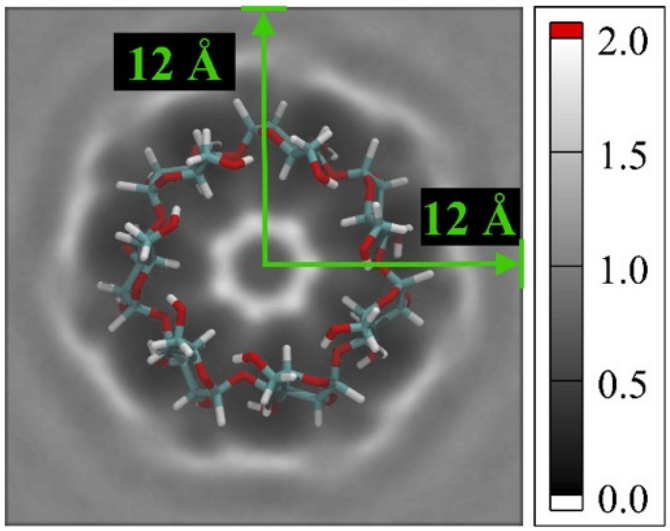

Figure B.1: $g(m, n)$, indicating the approximate position of the β-CD molecule.

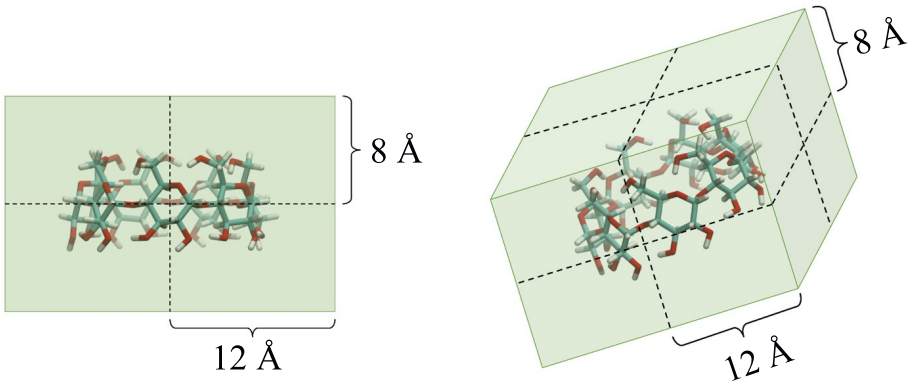

Figure B.2: Shaded green regions indicate the region of $g(m, n)$, as viewed from the side (left) and askew (right).

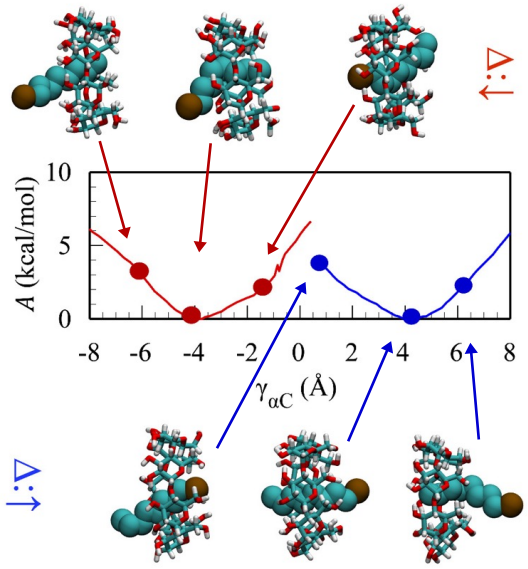

Figure B.3: $g(m, n)$, indicating the approximate position of the β-CD molecule.

B.3 Host/guest configurations in water

Representative configurations of the 1-bromooctane/β-CD host/guest complex along the PMF curves for the system in bulk water (see Figure 10c in main text) are shown in Figure S3. In the snapshots that accompany the plot, β-CD is shown using the "licorice" representation (sticks / lines) and the 1-bromooctane guest is shown in the "VdW" representation (large spheres for each atom center) using the VMD software.1 Each snapshot shown in Figure S3 is oriented so that the β-CD secondary hydroxyl opening is on the left and the β–CD primary hydroxyl opening is on the right. The arrow/delta notation used in the text is rotated to match the relevant snapshots. Surrounding water molecules have been deleted for clarity.

B.4 Host/guest complexes at the liquid/liquid interface

Figure S4 presents representative snapshots of the four different host/guest complexes at the 1-bromooctane/water interface studied in Figures 10d and 10e in the main text. The host/guest complex in the snapshots uses the same representation as in Figure S3 above. In all images, the organic phase is on the top (1-bromooctane molecules are mostly blue) and the aqueous phase is on the bottom. The corresponding notation introduced in the main text (Δ :↑, ∇ :↑, Δ :↓, ∇ :↓) is superimposed on each image.

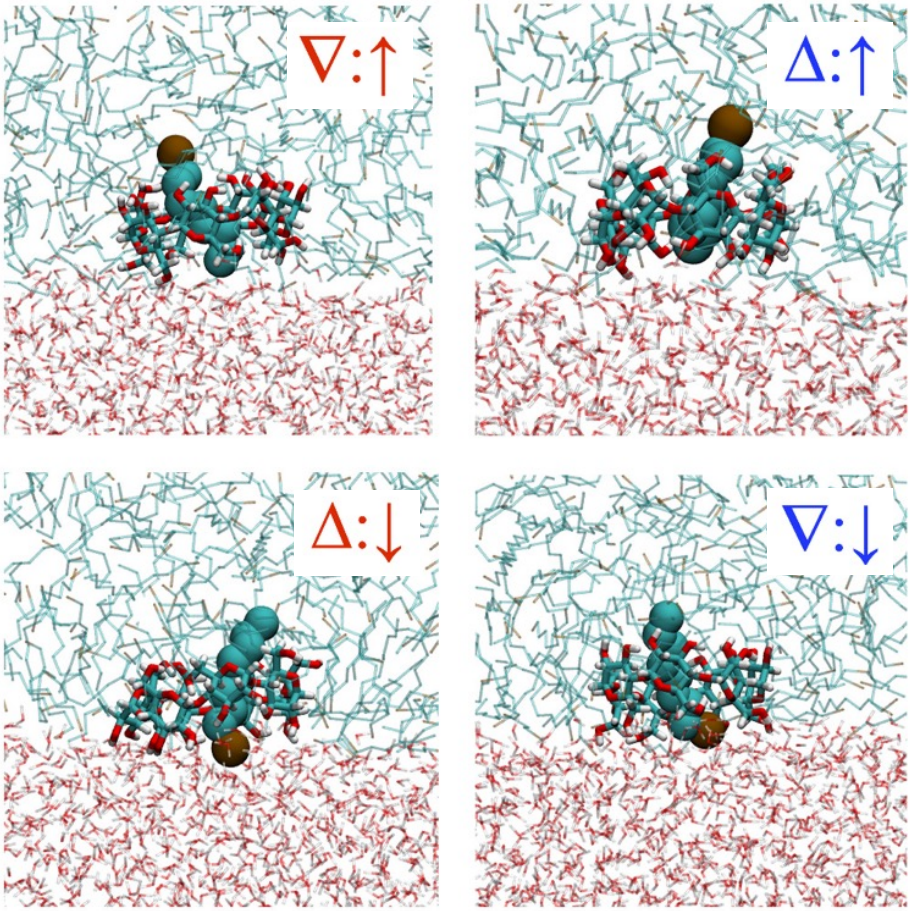

Figure B.4: Representative configurations of the host/guest complex along the related PMF curves for 1-bromooctane/β-CD in bulk water.

Appendix C

S_N2 reaction rate enhancement by β-cyclodextrin at the liquid/liquid interface

C.1 Supplementary Information

The following simulation snapshots are provided to aid in the visualization of the simulations performed in the main text. The solvent molecules, 1-bromooctane and water, are represented as thin stick models, β-cyclodextrin is represented using a thicker 'licorice' stick model, and the model 3-site S_N2 reactive system is represented as spheres. All simulation snapshots are generated using VMD 1.9.3 [81]

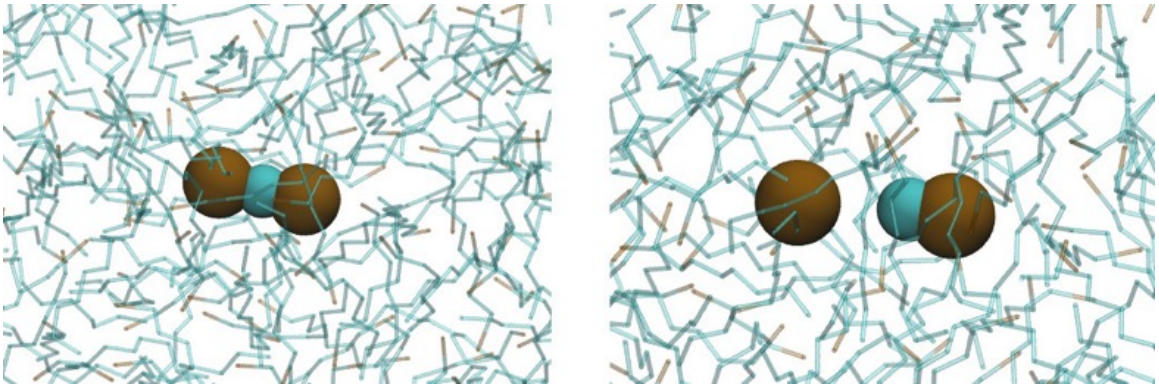

Figure C.1: The model S_N2 system near the transition state (left) and as ion and dipole (right) in neat 1-bromooctane.

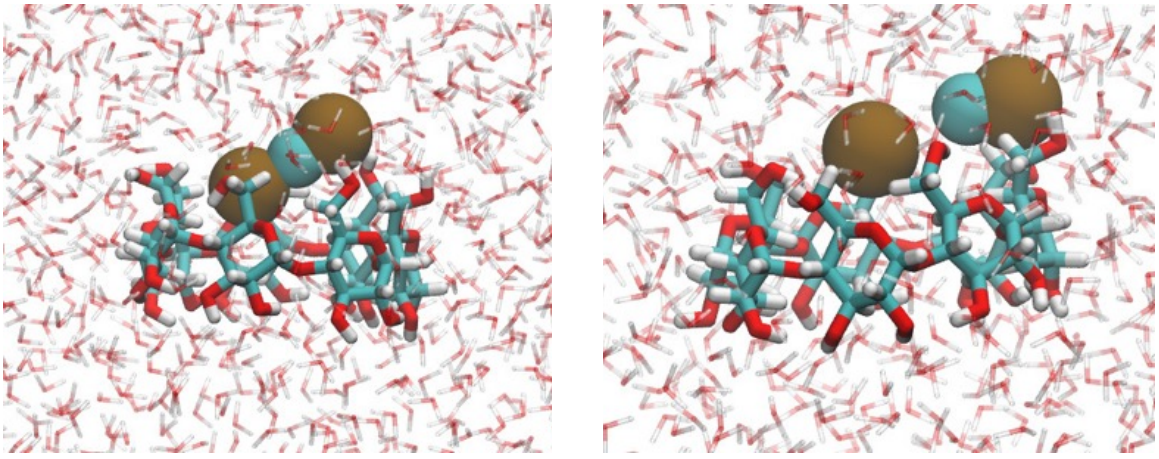

Figure C.2: The model S_N2 system near the transition state (left) and as ion and dipole (right) at the primary hydroxyl opening of β-cyclodextrin in bulk water.

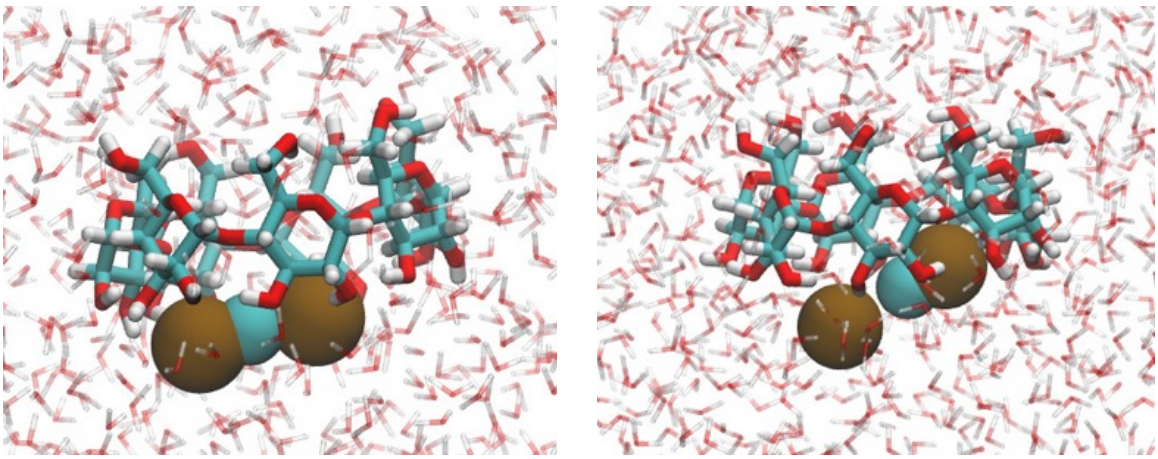

Figure C.3: The model S_N2 system near the transition state (left) and as ion and dipole (right) at the secondary hydroxyl opening of β-cyclodextrin in bulk water.

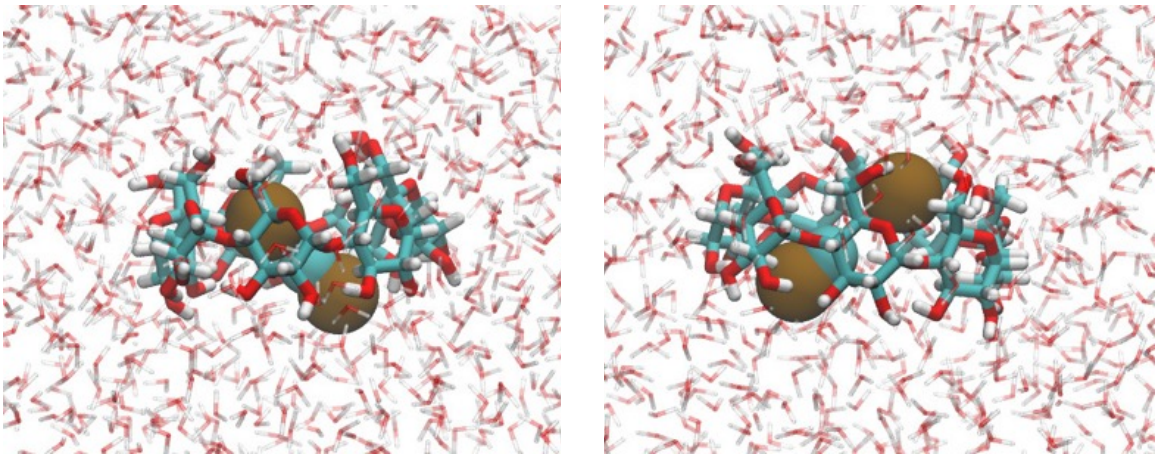

Figure C.4: The model S_N2 system near the transition state (left) and as ion and dipole (right) located "in the pore" of the β-cyclodextrin molecule in bulk water. See main text for details.

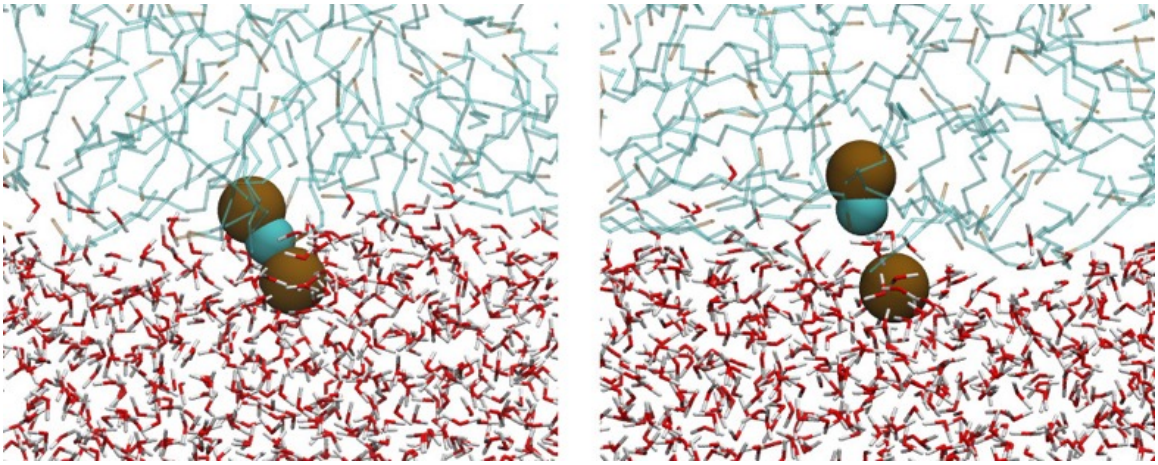

Figure C.5: The model S_N2 system near the transition state (left) and as ion and dipole (right) when located at the neat 1-bromooctane/water liquid/liquid interface.

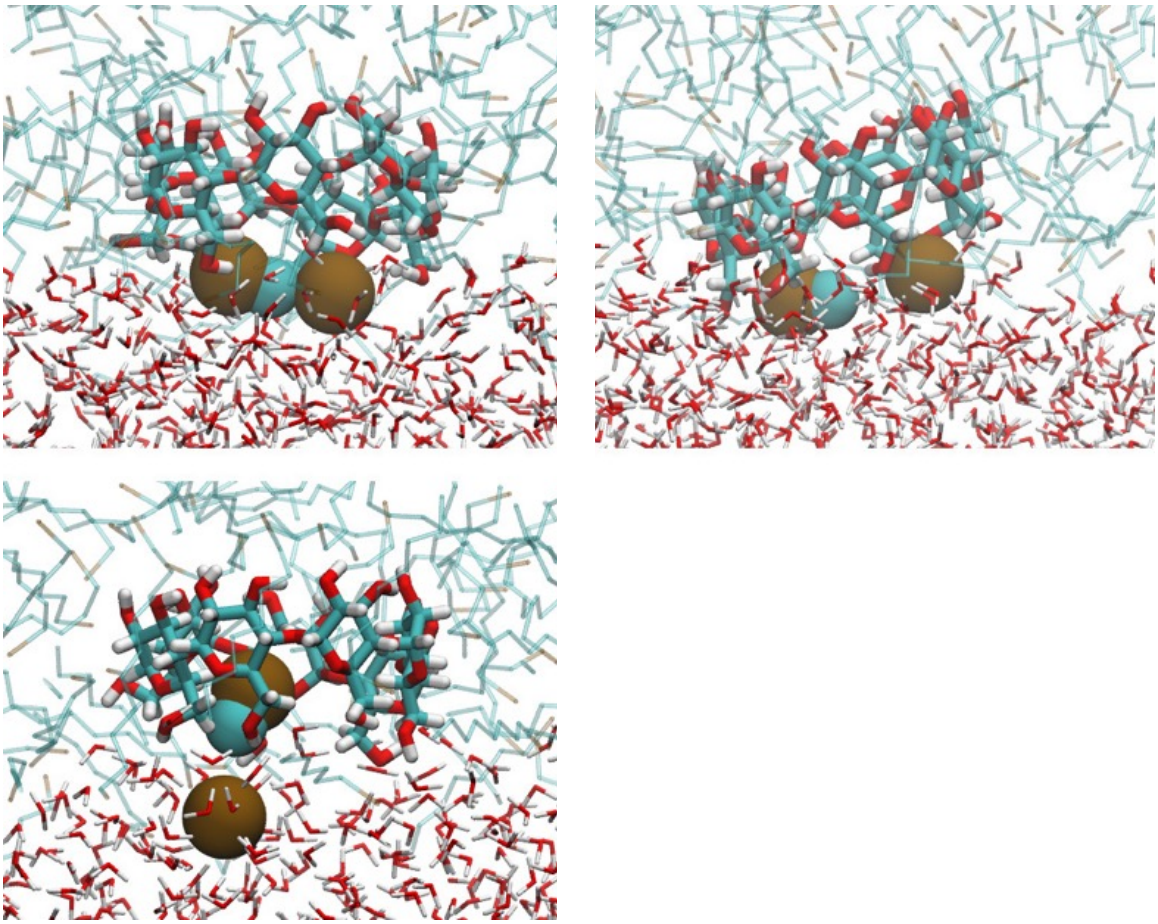

Figure C.6: The model S_N2 system near the transition state (top left) and as ion and dipole (top right and bottom) when located primary hydroxyl opening of β-cyclodextrin at the 1-bromooctane/water liquid/liquid interface.

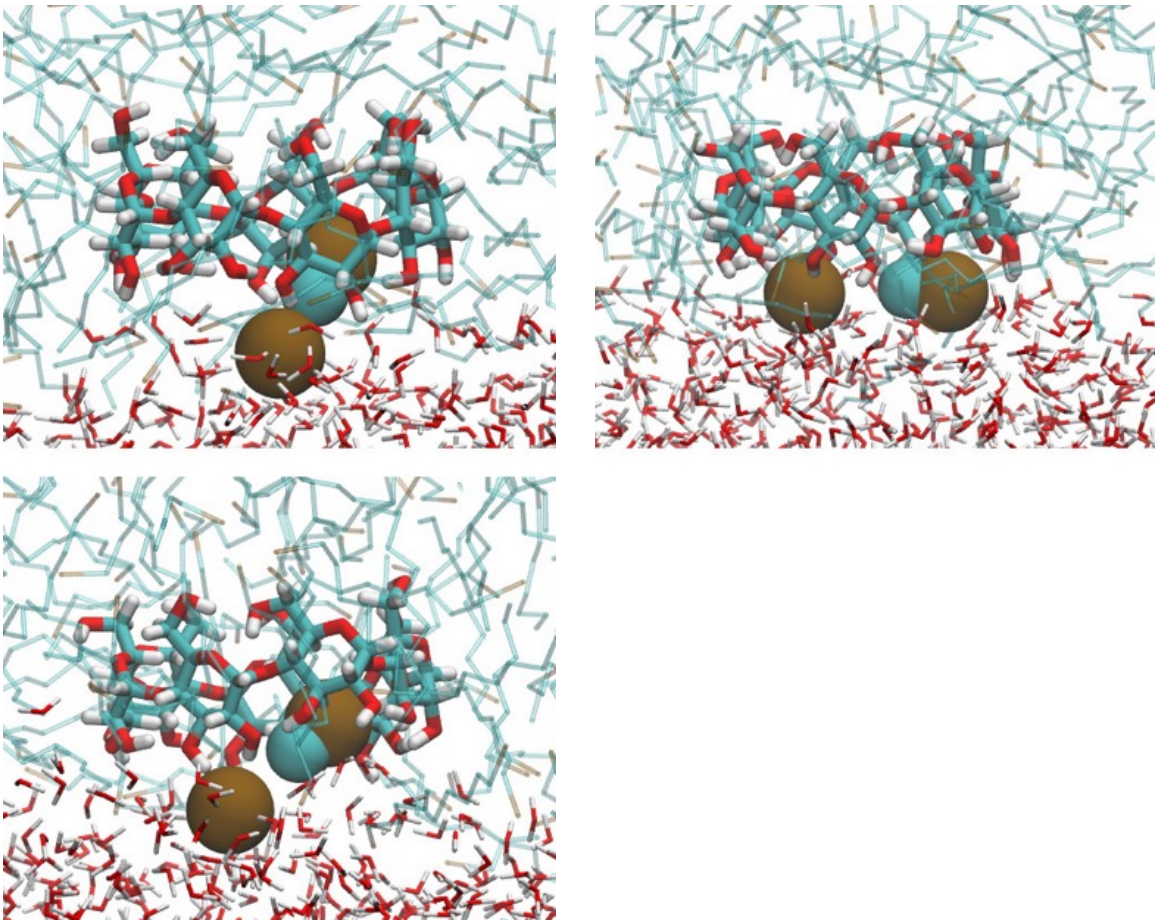

Figure C.7: The model S_N2 system near the transition state (top left) and as ion and dipole (top right and bottom) when located secondary hydroxyl opening of β-cyclodextrin at the 1-bromooctane/water liquid/liquid interface.

Appendix D

Geometric and energetic considerations of surface fluctuations during ion transfer across the water-immiscible organic liquid interface

D.1 Normalization of the solvation coordinates

For a two-phase system we define a solvation coordinate for each solvent s by

$$s_W = U_{I-W}/U_{I-W}^{bulk}, \tag{D.1}$$

$$s_{NB} = U_{I-NB}/U_{I-NB}^{bulk} \tag{D.2}$$

where the subscripts W and NB represent the water or nitrobenzene solvents, I represents the ion, U is the total intermolecular interaction potential energy between the ion and the specified solvent, and U_{bulk} is the total ion-solvent interaction potential when the ion is in the bulk solvent. Values of U^{bulk} (U^{bulk}_{I-W} = -155.531 kcal/mol and U^{bulk}_{I-NB} = -89.395 kcal/mol) are calculated by molecular dynamics simulations using the same force fields and parameters described in the main text. The solvation energy for the ion in bulk water, U^{bulk}_{I-W}, is calculated as the ensemble average value of 10 independent starting configurations, each run for 1 ns of simulation time (total ensemble average over 10 ns of MD simulation time). The configurations consist of the water/nitrobenzene system described in the main body of this work, with the ion confined well within the bulk region of the aqueous phase, -17.5 Å $< Z_I <$ -14.5 Å. In the case of bulk nitrobenzene, we place the ion in a truncated octahedral box containing 177 nitrobenzene molecules and the bare chloride ion. The value of U^{bulk}_{I-NB} is the ensemble average of the ion-nitrobenzene interaction potential over 10 independent configurations of this nature, each run for 1 ns of simulation time.

D.2 Biasing potentials

Below we list the applied biasing potentials for the normal, "flat" (no capillary fluctuations) , and $Cl^-(H_2O)_3$ systems. Due to the rapid increase in free energy observed in the constrained ("flat" and $Cl^-(H_2O)_3$) systems, it is necessary to use smaller windows to adequately sample some regions. Window ranges along the Z-axis

refer to a system center of mass located at $Z = 0$. The aqueous phase is located in the -Z direction. Ranges of Z not listed in the following tables obtained good sampling statistics without the use of an applied biasing potential. The biasing potentials follow one of three equations:

1. $U_{bias}(Z_I) = \alpha \dfrac{(1 + \tanh[\lambda(Z_I - \zeta])}{2}$

2. $U_{bias}(Z_I) = \alpha Z_I + \lambda(Z_I - \zeta)^2$

3. $U_{bias}(Z_I) = \alpha Z_I + \lambda Z_I^2 + \zeta Z_I^3$

with parameters given as follows:

Table D.1: Normal system

Window range (Å)	Eqn.	α	λ	ζ
-1.5 < Z < 1.5	1	11.0	0.18	7.0
0.5 < Z < 3.5	1	11.0	0.18	7.0
2.5 < Z < 5.5	1	11.0	0.18	7.0
4.5 < Z < 7.5	1	11.0	0.18	7.0
6.5 < Z < 9.5	1	11.0	0.18	7.0
8.5 < Z < 11.5	1	11.0	0.18	7.0
10.5 < Z < 13.5	1	11.0	0.18	7.0
12.5 < Z < 15.5	1	11.0	0.18	7.0
14.5 < Z < 17.5	1	11.0	0.18	7.0
16.5 < Z < 19.5	1	11.0	0.18	7.0

Table D.2: "Flat" system

Window range (Å)	Eqn.	α	λ	ζ
-3.5 $< Z <$ -0.5	1	22.0	0.36	1.5
-1.5 $< Z <$ 0.0	2	1.75	0.0	0.0
-0.5 $< Z <$ 1.0	2	2.30	0.0	0.0
0.5 $< Z <$ 2.0	2	3.0	0.0	0.0
1.5 $< Z <$ 3.0	2	0.0	1.45	0.3
2.5 $< Z <$ 4.0	2	0.0	-3.4	4.3
3.5 $< Z <$ 5.0	3	2.9	-40.8	189.4

Table D.3: $Cl^{-}(H_2O)_3$ system, "flat interface"

Window range (Å)	Eqn.	α	λ	ζ
-3.5 $< Z <$ 0.5	1	21.5	0.30	2.0
-1.5 $< Z <$ 1.5	1	20.0	0.30	2.0
0.5 $< Z <$ 3.5	1	22.0	0.30	2.0
2.5 $< Z <$ 5.5	1	23.0	0.35	2.5
4.5 $< Z <$ 6.0	1	19.0	0.60	4.2
5.5 $< Z <$ 7.0	1	23.5	0.80	4.0

Appendix E

Miscibility at the immiscible liquid/liquid interface: A molecular dynamics study of thermodynamics and

mechanism

E.1 Representative simulation snapshots

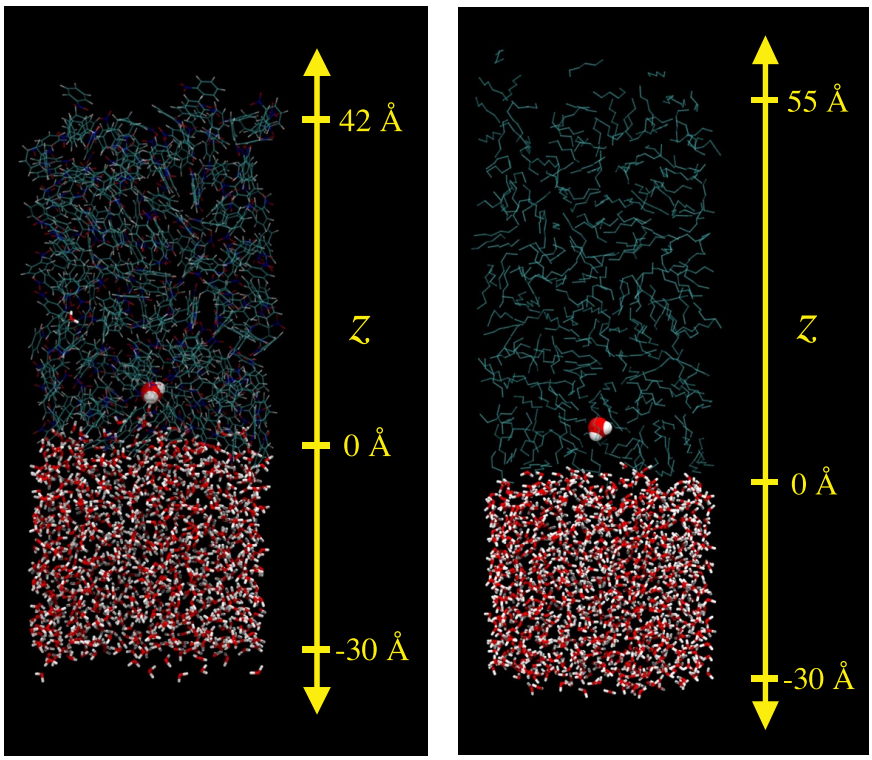

Figure E.1: Representative snapshots of the water/nitrobenzene (left) and water/hexane (right) liquid/liquid simulation boxes. Water and the organic solvents are shown using the 'licorice' representation. The tagged water is represented by its Van der Waals surface.

E.2 Water finger coordinate calculation

For convenience, we include an abbreviated algorithm for the calculation of the water finger coordinate w but also refer the interested reader to the initial work of Morita and co-workers. [106, 107]

1. Define an undirected mathematical graph
    a. Vertices are the water oxygen atoms
    b. Edges are the distances between the vertices
    c. Sort these edges into an ascending list
2. Perform a binary search of this list to find the minimum threshold value (w) that connects the transferring water to bulk water.
    a. Start with the middle distance in the list. Use this distance as the threshold distance and perform a breadth-first search using the transferring water as the tree root (or 'search key') to see if bulk water can be reached.
    b. Depending whether the answer is 'yes' or 'no,' bisect the list (discarding the half of the list that is entirely too short or entirely too long) and continue the binary search for the cutoff distance.

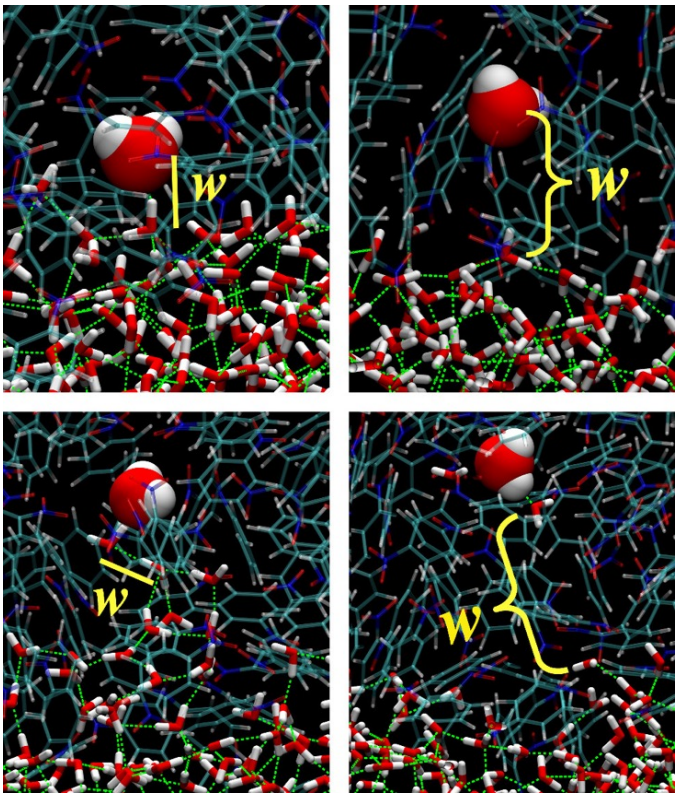

Figure E.2: An illustration of w in several different system configurations. In the left-hand panels w is approximately the O–O distance of a water-water hydrogen bond since the transferring water (shown as Van der Waals surface) is tethered to the aqueous phase by hydrogen bonded waters. In the right-hand panels, w is increasing rapidly as the dissolved water diffuses into to the nitrobenzene. In the lower right panel, note that the trimer constraint results in w being defined by a solvation shell water, not the "tagged" water.